Transactions of the ASME®

Journal of Turbomachinery

Published Quarterly by The American Society of Mechanical Engineers

VOLUME 109 • NUMBER 3 • JULY 1987

TECHNICAL PAPERS

BOOK REVIEWS

ANNOUNCEMENTS

Technical Editor
ARTHUR J. WENNERSTROM
Senior Associate Editor
G. K. SEROVY
Associate Editors
Advanced Energy Systems
S. I. FREEDMAN
Environmental Control
H. E. HESKETH
Fuels and Combustion Technologies
R. E. BARRETT
Gas Turbine
S. KUO
Internal Combustion Engine
K. J. SPRINGER
Nuclear Engineering
S. M. CHO
Power
R. W. PORTER

BOARD ON COMMUNICATIONS
Chairman and Vice-President
K. N. REID, JR.

Members-at-Large
J. T. COKONIS
M. FRANKE
M. KUTZ
F. LANDIS
J. R. LLOYD
T. C. MIN
R. E. NICKELL
R. E. REDER
R. ROCKE
F. W. SCHMIDT
W. WEINER

President, **R. ROSENBERG**
Executive Director,
D. L. BELDEN
Treasurer, **ROBERT A. BENNETT**

PUBLISHING STAFF
Mng. Dir., Publ., **J. J. FREY**
Dep. Mng. Dir., Pub.,
JOS. SANSONE
Managing Editor,
CORNELIA MONAHAN
Sr. Production Editor,
VALERIE WINTERS
Editorial Prod. Asst.,
MARISOL ANDINO

Transactions of the ASME, Journal of Turbomachinery (ISSN 0889-504X) is published quarterly (Jan., Apr., July, Oct.) for $85 per year by The American Society of Mechanical Engineers, 345 East 47th Street, New York, NY 10017. Second-class postage paid at New York, NY and additional mailing offices. POSTMASTER: Send address change to The Journal of Turbomachinery, c/o The AMERICAN SOCIETY OF MECHANICAL ENGINEERS, 22 Law Drive, Box 2300, Fairfield, NJ 07007-2300."

CHANGES OF ADDRESS must be received at Society headquarters seven weeks before they are to be effective. Please send old label and new address.

PRICES: To members, $24.00, annually; to nonmembers, $85.00.
Add $6.00 for postage to countries outside the United States and Canada.

STATEMENT from By-Laws. The Society shall not be responsible for statements or opinions advanced in papers or ... printed in its publications (B 7.1, para. 3).

COPYRIGHT © **1987** by the American Society of Mechanical Engineers. Reprints from this publication may be made on condition that full credit be given the TRANSACTIONS OF THE ASME – JOURNAL OF TURBOMACHINERY, and the author, and date of publication be stated.

INDEXED by Engineering Information

Downloaded 01 Jun 2010 to 171.66.16.52. Redistribution subject to ASME license or copyright; see http://www.asme.org/terms/Terms_Use.cfm

Unducted Fan Aerodynamic Design

L. H. Smith, Jr.
Aircraft Engine Business Group,
General Electric Company,
Cincinnati, OH 45215-6301

A method being used to design unducted fans, which are counterrotating propellers with unusually high disk loadings, is described. The quasi-three-dimensional approach employed is similar to that used for ducted fan designs; it consists of a circumferential-average flowfield analysis followed by cascade designs that include secondary flow and sweep effects. The open-tip condition enters as a significant secondary flow contribution. Blade shapes defined by this process are analyzed by a three-dimensional Euler solver and final adjustments are made as necessary. Examples of application of the method are presented to elucidate the magnitudes of the phenomena involved.

1 Introduction

Modern turbofan engines have bypass ratios from 4 to 8 with fan total-pressure ratios in the range from 1.55 to 1.8 at their top-of-climb sizing point. It has long been recognized that a higher bypass, lower pressure ratio combination would yield higher propulsive efficiency with the potential for reduced fuel consumption, but the drag and weight of the large nacelle needed and the need for a high-horsepower gearbox has discouraged advancement in this direction. Single-rotation propfans avoid the nacelle problem, but their low disk loadings, necessary to avoid high swirl losses, limit them to very low total-pressure ratios (around 1.06) and therefore large diameters that cause installation penalties. The use of counterrotation eliminates swirl losses and allows a total-pressure ratio of about 1.12, which is still low enough to provide a substantial propulsive efficiency improvement compared to today's turbofans, while substantially reducing the large diameter of the propfan. The name "unducted fan" has been given to this type of design.

Figure 1 shows an unducted fan engine. Here the counterrotating fan blades are driven by a multistage counterrotating turbine. The relative speed between adjacent blade rows in the turbine is comparable to that between the rotors and stators in a conventional turbofan turbine, and therefore the number of blade row pairs (stages) can be comparable for the same aerodynamic loading and turbine efficiency. Also, the multistage counterrotating arrangement assures that the two fan rotors each receive nearly the same torque, which virtually eliminates fan exit swirl losses automatically.

The practical disk loading of an unducted fan is ultimately limited by Mach-related losses, particularly in the aft rotor. The fact that the flowfield is vented to ambient pressure means that the total pressure added by the blading manifests itself primarily as an increase in Mach number, and this can lead to specific flow rates close to the critical value. For example, at a flight Mach number of 0.8 and a fan total-pressure ratio of 1.12, the downstream jet has a Mach number of 0.91 and a specific flow rate only 0.7 percent less than critical. The general tendency is for the meridional (through-flow) Mach number to increase uniformly toward this value as it passes through the blading, and although relatively thin airfoils can be employed, their thickness blockage in the inner part of the span presents a significant problem, particularly in the aft rotor. This can be mitigated by carefully designing the hub contour to interact favorably with the blading flowfield to prevent choking, and this is an important part of the design process. The aft rotor also has its Mach number increased by the swirl imparted by the forward rotor with the result that its flow is transonic over most of its span.

When executing an unducted fan aerodynamic design, primary attention is focused on the top-of-climb design point. This is where the blading Mach numbers are the highest and therefore where the need for design precision is the greatest. Generally, it is also the sizing point of the engine. At this con-

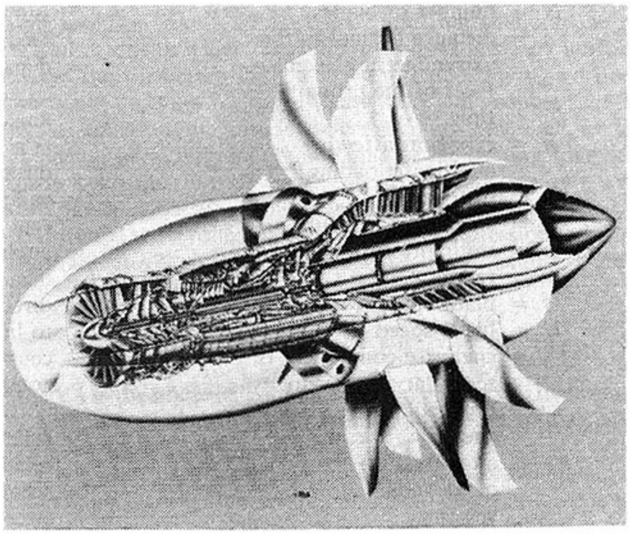

Fig. 1 Unducted fan propulsion system

Contributed by the Gas Turbine Division of The American Society of Mechanical Engineers and presented at the 32nd International Gas Turbine Conference and Exhibit, Anaheim, California, May 31–June 4, 1987. Manuscript received at ASME Headquarters February 19, 1987. Paper No. 87-GT-233.

dition, the spanwise loading distribution should be near the so-called optimum distribution that minimizes induced drag. Optimum distributions for counterrotating propellers with up to six blades were identified by Theodorsen [1]; they are characterized by the maximum blade circulation occurring at the hub. Blade lift coefficients will typically be higher at takeoff than at top-of-climb, and chord lengths may be set by takeoff requirements. Acoustic considerations also may influence the design; these generally drive the design toward increased blade number, increased sweep, and increased spacing between rotors as well as decreased lift coefficients and decreased thicknesses. Blades designed for the optimum circulation distribution at top-of-climb will typically run less heavily loaded toward the tip at part-power cruise conditions and more heavily loaded toward the tip at takeoff. The present paper deals only with aerodynamic design point analyses where the loading distribution is near the optimum one.

2 Design Approach

The design approach adopted here is essentially the same as that employed for ducted turbomachines in most design offices at this time. The actual three-dimensional flow is built up by superposing two or more basically two-dimensional solutions to yield what has been called a quasi-three-dimensional flowfield. The first and principal solution is a through-flow analysis which treats the circumferential-average flow; mathematically, it is axisymmetric and out of it come axisymmetric streamsurfaces.

The airfoils are designed on these streamsurfaces using blade-to-blade analyses or cascade concepts. In general, the airfoil designs need to recognize changes in lamina thickness and changes in radius of the streamsurfaces from leading edge to trailing edge as well as the effects of blade sweep and secondary flows.

Airfoils designed by this process are stacked to generate the blades. It is generally necessary to iterate the blade design with the circumferential-average analysis to assure that the latter contains proper blade force and blockage distributions.

A final check on the design is accomplished by employing a fully three-dimensional Euler analysis for each blade row, and the blade shapes are altered if necessary to achieve desirable surface Mach number distributions.

The several steps of this process will be described in greater detail in the following sections.

3 Circumferential-Average Flow

This flowfield is intended to represent, on a circumferential-average basis, all of the features of the complete flow. An example is shown in Fig. 2. The computation grid is fine enough to allow proper representation of the chordwise and spanwise distributions of aero loading, thickness blockage, and loss in the blade regions as well as the hub and nacelle contours. An important feature of this flow is the high level of through-flow (meridional) Mach numbers indicated by the contour lines, particularly inside the blade regions where blade thickness blockage is significant. The design of the hub contour is done

Nomenclature

a = blade wake spacing normal to wakes
C = absolute velocity relative to propelled craft
$c_\perp$ = blade chord projection in ζ plane
DW = downwash velocity
h = blade height
I = stagnation rothalpy
J' = advance ratio of the ultimate wake
k_p = ratio of spanwise static pressure gradient in the primary flow after/before the aft blade row
M = Mach number
N = number of blades
n = distance normal to the axisymmetric streamsurfaces of the primary flow
n = exponent affecting chordwise loading distribution
P = stagnation pressure
p = static pressure
r = radius
s = blade spacing
U = blade speed
V_s = spanwise component of secondary flow velocity on suction side of wake sheet
V_x = cross-passage component of secondary flow velocity
$\Delta \bar{V}_x$ = strength of tip-circle vortex sheet in the primary flow and in the secondary flow
W = velocity relative to a blade row
$W_\perp$ = W projection in ζ plane
x = cross-passage coordinate in Trefftz plane
y = spanwise coordinate in Trefftz plane
z = axial coordinate
β = angle between relative velocity and meridional direction
Γ = blade circulation for the primary flow
Γ_A = actual blade circulation (sum of primary and secondary flows)
δ = departure angle, see equation (6)
ζ = angle in ζ plane between relative velocity and direction perpendicular to line connecting adjacent blade axes
ζ^* = angle in ζ plane between meanline direction and direction perpendicular to line connecting adjacent blade axes
$\zeta_\perp$ = component of absolute vorticity in the primary flow perpendicular to the relative velocity vector
ζ_s = secondary vorticity
λ = sweep angle
ξ = fraction of chord measured from leading edge
ρ = fluid density
σ = cascade solidity in ζ plane

Subscripts

h = at hub
j = in jet (ultimate wake)
m = in meridional direction
o = ambient conditions
PS = pressure side
SS = suction side
s = secondary flow component
sw = sweep-end-effects component
TE = at trailing edge
t = at tip
u = circumferential component
x = in cross-passage direction
1, 2, . . . = locations and row identifications; see Fig. 9 (note: location 1 is also ambient)
2D = from two-dimensional analysis with varying radius and lamina thickness
∞ = vector mean of upstream and downstream conditions

Superscripts

$'$ = relative to a blade row
$\bar{}$ = average

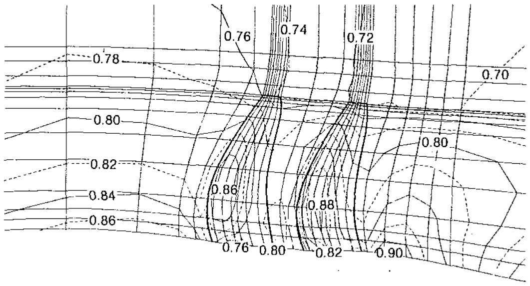

Contours of Meridional Mach Number

Fig. 2 Circumferential-average flowfield; $M_0 = 0.72$

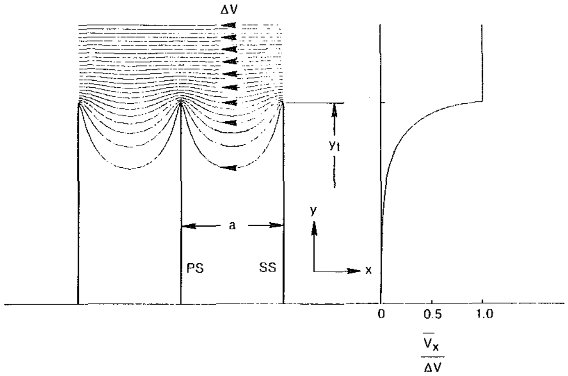

Fig. 3 Prandtl flow across blade tips

with this analysis, the shape being chosen to reduce the Mach numbers where the blade thickness blockage is the greatest.

The outer boundary condition on the circumferential-average flow is that the velocity approach the freestream velocity and the flow angle approach zero at an infinite distance. To meet these conditions economically, the flowfield is divided into an "inner" and an "outer" region. Flow properties in the inner region are calculated by the streamtube curvature technique, and the flow properties in the outer region are calculated by a simplified Douglas–Neumann procedure [2, 3]. Using this procedure, the outer boundary can be relatively close to the tip. The mass flow through the inner region is typically taken as five times the mass flow through the blading.

In an earlier treatment of circumferential-average flow [4], the author showed that when averages are taken of the various terms in the three-dimensional momentum equation, terms are generated that represent the differences between averages of products and products of averages. These were named *G*-functions, and it was pointed out that they are analogous to the Reynolds stresses of turbulent flow analysis. It was shown that their magnitudes are minor in an example of a ducted fan. It does not follow, however, that they are minor in the highly three-dimensional flowfield near the tip of a propeller.

Consider the flow in the ideal ultimate wake of a counter-rotating propeller. For this case, the circumferential-average meridional streamlines are straight and parallel, and there is no circumferential-average swirl. Therefore, our usual analysis without *G*-functions would yield the result that the circumferential-average pressure is constant across the flowfield. However, Theodorsen [1] has shown that the static pressure is higher inside the slipstream. For a large number of blades, this pressure difference is given by:

$$p_j - p_0 = \frac{\rho}{2}(C_j - C_0)^2 \tag{1}$$

which is not entirely negligible for unducted fans.

The reason for the increased static pressure in the slipstream is best illustrated with an example. Prandtl calculated the two-dimensional flow across the tips of a linear cascade; the streamline pattern is shown in Fig. 3 (see [5]). Since the stagnation pressure is uniform throughout the flowfield, the static pressure deep inside the blading is higher than that above the blade tips by $(\rho/2)(\Delta V)^2$. When a uniform flow out of the paper is added, the static pressure is not changed and the result is an exact three-dimensional solution for the slipstream flow for such a cascade. The velocity ΔV is Γ_h/a, where Γ_h is the blade circulation far removed from the tip and a is the wake spacing.

In order to approximate this effect in the circumferential-average flow analysis, the following approach is recommended. We first approximate the spanwise variation in circumferential-average static pressure for the flowfield in Fig. 3 with

$$\bar{p} = p_h - \frac{\rho}{2}\bar{V}_x^2 \tag{2}$$

(This overestimates the average pressure somewhat at and very near the tip.) For the Prandtl flowfield [5]

$$\bar{V}_x = \frac{\Gamma_h}{a}\left(1 - \frac{2}{\pi}\text{ arc cos } e^{-\pi\frac{y_t - y}{a}}\right) \tag{3}$$

From equation (2)

$$\frac{1}{\rho}\frac{\partial \bar{p}}{\partial y} = -\bar{V}_x \frac{\partial \bar{V}_x}{\partial y} \tag{4}$$

Since the circumferential-average streamlines are straight and parallel, and since there is no centrifugal field, the right-hand side of equation (4) is then considered to be the *G*-function associated with propeller-type flows. Although it was derived for a linear cascade, we assume that its magnitude is applicable for rotor applications, and it is, therefore, added to the circumferential-average radial momentum equation, to be used together with equation (3). For the forward rotor, Γ_h in equation (3) is taken as the maximum blade circulation along the span, which usually occurs at or near the hub. For the aft rotor, a fictitious Γ_h is chosen such that the contributions from both rotors will equal the full amount of slipstream pressure increase given by equation (1) at the aft rotor trailing edge. For stations inside each rotor, the *G*-function magnitude is specified to build up from leading edge to trailing edge proportional to its circulation. The a values for both rotors are taken near their tips.

It has been pointed out by Schouten [6] that the static pressure field that we have been discussing here depends on the existence of stable blade wake vortex sheets capable of sustaining a radial force at their outer edges. Schouten proposes that this flow model is unrealistic and that it should be replaced by one in which the static pressure is basically uniform across the slipstream except near the blade trailing vortices. We adopt this view for the ultimate wake and propose that the full *G*-function magnitude determined as described in the preceding paragraph be applied only at the trailing edge of a blade row and that it be decreased to zero linearly with distance downstream to the point where the vortex sheets can be expected to be rolled up. The following expression, adapted from Kaden [7], is used to obtain the axial distance from a trailing edge to the rollup location:

$$\Delta z = 0.56\, h \frac{Wh}{\Gamma_h} \cos\beta \tag{5}$$

where h is the blade height and W and β are the relative velocity and flow angle (measured from axial) at the trailing edge near the tip.

When more experience from unducted fans is available, it is planned to include flow mixing in the circumferential-average analysis as has been done by Adkins and Smith [8] for ducted turbomachines.

4 Blade-to-Blade Flow

The circumferential-average flow solution yields a distribution of circumferential-average flow angle that varies from leading edge to trailing edge on each of the axisymmetric streamsurfaces. Airfoil meanline angles can also be defined on these surfaces, and the difference between the flow angle and the meanline angle is defined as the *departure angle*. In compressors, then, the departure angle at the leading edge is known as incidence angle and at the trailing edge is known as deviation angle. Custom tailored airfoil shapes are defined by specifying distributions of departure angle from leading edge to trailing edge together with thickness distributions.

It was shown by Smith and Yeh [9] that when sweep is present, it is preferred to view the airfoils in a projection that recognizes only the velocity components perpendicular to a blade axis that follows the blade plan form (say the line that connects airfoil centroids) since velocity components parallel to this axis do not contribute to the blade turning action. This is depicted in Fig. 4, where the cut lies along an axisymmetric streamsurface and the viewing direction is parallel to the blade axis. The circumferential-average flow angle in this view is ζ, measured from a direction perpendicular to the line connecting adjacent blade axes, and this view is referred to as the ζ plane although it is not, strictly speaking, a plane. The blade meanline angle in the ζ plane is ζ^* and the departure angle is

$$\delta = \zeta - \zeta^* \tag{6}$$

An equation giving ζ in terms of other flow angles and blade axis angles is given in [9].

In concept, two-dimensional blade-to-blade flow solutions are carried out in the ζ plane with variations of lamina thickness (in the blade axis direction) and radius properly accounted for. Preferably, an inverse design method is used with the input blade circulation and thickness distributions chosen to correspond to those of the circumferential-average flow solution of Section 3. Circumferential-average flow angles from these ζ plane solutions and the resulting blade meanline angles are then used to yield the departure angles of the blade-to-blade solutions. These departure angles are then perturbed for secondary flow effects and sweep end effects, determined as described in the following sections, to yield the complete departure angles to be used with the circumferential-average flow angles of Section 3 to define the final blade shape.

In practice, available blade-to-blade inverse or even direct analysis codes may encounter numerical difficulties at the high Mach number levels of some unducted fan cascades, particularly those of the aft rotor near midspan. In such cases, the approach being employed here has the advantage that the departure angles that must, in such cases, be assumed, are relatively small in magnitude, and errors in their specification should therefore be of small consequence.

5 Secondary Flow

Secondary flow as defined here is that which, when added to a basically two-dimensional primary flow, yields the full three-dimensional flow. It represents the spanwise and cross-passage flowfield components that are associated with spanwise variations of the turning action of a blade row, including the effects of vorticity in the inflow, if any. Along a blade trailing edge, it is the jump in the spanwise velocity component of the secondary flow flowfield that constitutes the shed vortex sheet. For the open-tip rotors of unducted fans and propellers, this flowfield is quite intense near the tip, intense in its cross-passage velocities as well as its spanwise velocities. These cross-passage velocities lead to the need for positive departure angles at the tip even though the actual blade circulation is zero there.

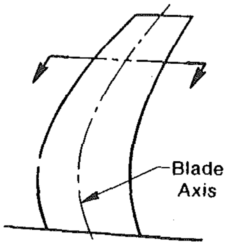

Fig. 4 Blade-to-blade flow viewing direction; view seen is called ζ plane

As described by Smith [10] and elsewhere, secondary flows are analyzed in a Trefftz surface, nominally located at downstream infinity but practically located near a blade row trailing edge. The secondary flow flowfield is determined in the Trefftz surface by integrating a Poisson equation for secondary flow streamfunction, where the right-hand side of the Poisson equation is secondary vorticity. The secondary vorticity is made up of two parts, that due to the reorientation of the inlet vorticity vectors as they pass through the blade row, and that due to the spanwise variation of the blade circulation of the primary flow in which the fluid is turned to the direction of the blade wake sheets in the ultimate wake [10]

$$\zeta_s = \frac{1}{a}\left[W_1 \zeta_{\perp 1} \frac{\Gamma_A}{W_\infty^2} + \frac{d\Gamma}{dn_1}\right]\frac{dn_1}{dn_2} \tag{7}$$

For a single-rotation propeller with irrotational inflow and an optimum loading distribution, Glauert [5] (after Betz) showed that the primary flow circulation (i.e., without tip effects) is given by

$$\Gamma = \text{const}\ \frac{\tan^2\beta_w}{1+\tan^2\beta_w} \tag{8}$$

where $\beta_w(r)$ is the angle that the wake sheet, which is a pure helix for an optimum single-rotation propeller, makes with the axial direction. If Γ_t is the primary flow circulation at the tip radius r_t, then this can be written

$$\Gamma = \Gamma_t \left(\frac{r}{r_t}\right)^2 \frac{1+\tan^2\beta_{w_t}}{1+\tan^2\beta_{w_t}\left(\frac{r}{r_t}\right)^2} \tag{9}$$

For this case with irrotational inflow equation (7) becomes

$$\zeta_s = \frac{1}{a}\frac{d\Gamma}{dr} \tag{10}$$

At the tip, the primary flow circulation Γ_t drops to zero discontinuously, so the secondary vorticity $\zeta_s = -\infty$ at that location and we must instead speak of a tip "secondary vortex sheet" whose strength is

$$\Delta \bar{V}_x = -\frac{\Gamma_t}{a_t} \tag{11}$$

The Trefftz surface is shown in Fig. 5. The distance between adjacent wake sheets is

$$a = \frac{2\pi r}{N}\cos\beta_w \tag{12}$$

We will now show by numerical example that the present approach employing secondary flow yields the classical optimum distribution of circulation. We choose six blades and an advance ratio in the ultimate wake of

$$J' = \pi \cot\beta_{w_t} = 2 \tag{13}$$

Numerically determined secondary flow streamlines are shown in Fig. 6, and the grid employed can also be seen there. For this example, the tip vortex sheet was represented by large but finite vorticity acting over a slab having a thickness of 0.01

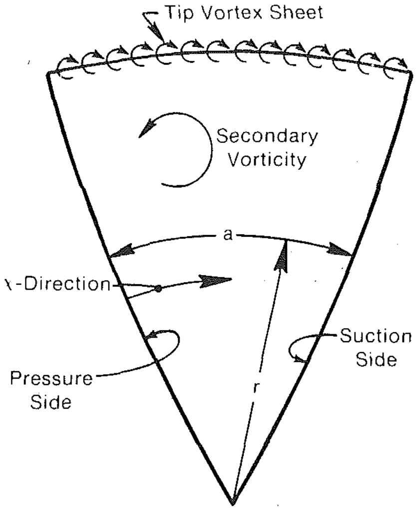

Fig. 5 Trefftz surface employed for secondary flow analysis

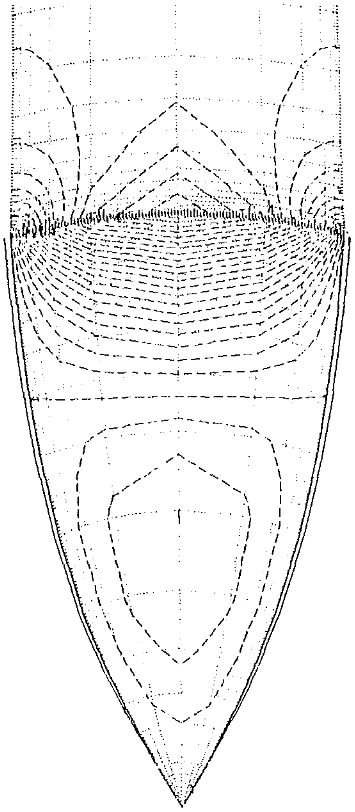

Fig. 6 Secondary flow streamlines for single-rotation propeller; $N = 6$, $J' = 2$

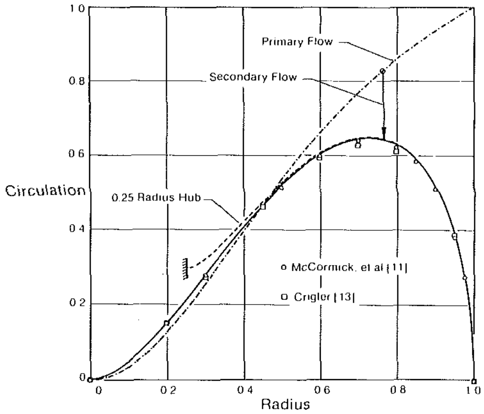

Fig. 7 Circulation distributions for single-rotation propeller; $N = 6$, $J' = 2$

percent r_t. The resulting circulation distribution is shown in Fig. 7. Excellent agreement is seen with values taken from McCormick et al. [11] based on the work of Eckhardt and Morgan [12]. Values from Crigler [13] after Theodorsen are also seen to be in good agreement. Calculations were also made for a case with a nonzero hub radius, and the result, also shown in Fig. 7, has the expected zero gradient at the hub.

For counterrotating propellers, it is to be expected that the optimum loading distribution has constant circulation along the span except for the tip falloff. This is expected because in this case neither rotor would have a shed vortex sheet, and hence there would be no induced losses except near the tip. This is also consistent with the optimum loading distributions found by Theodorsen [1]. Theodorsen's model is simplified in that the two rotors are located at the same axial position, the wake sheets both trail at the same angles, and the sheets from the forward rotor are continuous (not chopped as they would be if the aft rotor had finite loading). The author is not aware that finite axial spacing with finite loading has been treated, and if so, how the Theodorsen optimum distributions might be affected by these effects. It is clear, however, that such a treatment could only be carried out with a finite hub radius, because otherwise the swirl velocity at the axis between the rotors would be infinite.

In this paper we will not attempt to find optimum loading distributions, but one interesting comparison with Theodorsen's results for infinitesimal loading will be made. Suppose we consider the rotors to be far apart, and since the circulation near the inner radii must be radially constant, let us assume that the primary flow circulation is constant all along the span. We can then easily solve for the secondary flow, which is now induced entirely by the secondary vortex sheet at the tip because elsewhere, according to equation (7), the secondary vorticity is zero. We then add this to the primary flow as before to produce the actual circulation, This has been done for three examples having six blades and $J' = 2$, 3, and 5. The results are shown in Fig. 8 compared with Theodorsen's optimum distributions [1]. At $J' = 3$, which is representative of unducted fan designs, agreement is remarkably good. With a larger number of blades (ten is representative of unducted fan designs), agreement should be even better. From a practical point of view, without further information, we accept the radial distribution of circulation from the secondary flow method to be adequate for unducted fan design purposes. The shape of a wake sheet from the forward rotor, with its radially constant primary flow circulation, should then follow the direction of that from a free-vortex rotor.[1]

The treatment of the aft rotor is more complex than that of the forward rotor. Consistent with our general approach, the aft rotor receives an axisymmetric flow that is the circumferential average of the forward rotor discharge flow, and it therefore contains absolute vorticity that is parallel in direction to the forward rotor exit relative velocity. This vorticity has a component perpendicular to the aft rotor inlet relative velocity, and the first term in equation (7) is nonzero. Also, the primary flow circulation is generally not constant along the span of the aft rotor. The aft rotor's function is to remove the swirl imparted by the forward rotor. The shape of one of its wake sheets, then, must follow the direction of that from a free-vortex rotor, at least over its inner part. The wake sheet should be shaped over its outer part such that the resulting

---

[1] It is worth mentioning here that the wake sheets (except for very light loading) are not true helical surfaces as they are for optimum single-rotation propellers, and therefore the Trefftz surface is skewed differently at different locations downstream. This is also generally true for blade rows in ducted turbomachines, and it introduces second-order errors in the analysis. In practice, the Trefftz surface is assumed to be symmetric as shown in Fig. 5.

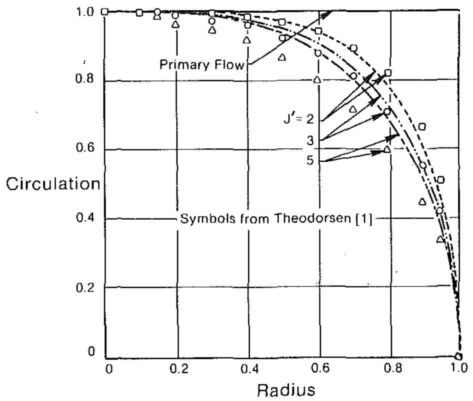

Fig. 8 Forward rotor circulation based on constant primary flow circulation; $N = 6$

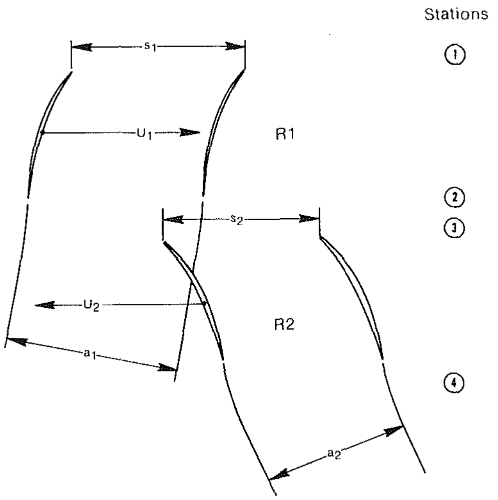

Fig. 9 Translating linear cascades

primary plus secondary flows remove the swirl imparted by the forward rotor. As an initial approximation, we can let the sheet be that from a free-vortex rotor over the whole span. We will show in the following subsection that this approximation is not quite correct. But a numerical example given in Section 8 will demonstrate that it is adequate for design purposes.

Translating Linear Cascade Example

In order to gain a clearer understanding of these concepts, we will now apply them to a simplified example. Instead of counterrotating rotors, consider translating linear cascades in incompressible inviscid flow. Let the cascades be far enough apart axially so that the aft cascade acts on the ultimate wake of the forward cascade. Figure 9 shows the cascades R1 and R2 and defines stations.

In Fig. 10, the solid vectors apply at the blade "hubs," i.e., far removed from the tips. All quantities are positive as shown. Although the figure is drawn with the blade speeds equal, this is not necessary and the following analysis will employ:

$$\bar{U}=\frac{1}{2}(U_1+U_2) \tag{14}$$

Note that a right angle is indicated at the end of the W_2 vector. The forward cascade in this example is one for which Prandtl's classical solution [5] applies exactly. The wake sheet has the angle β_2 from hub to tip, and the three-dimensional flow is obtained by adding a uniform flow in that direction to Prandtl's flow perpendicular to it. In our analysis, the primary flow direction is β_2 all along the span and changes discontinuously to $\beta_{2_0} = \beta_t$ above the tip. The primary flow circulation is therefore constant along the span at the value $s_1\Delta C_{u_h}$. The actual circulation is given by Prandtl's formulation

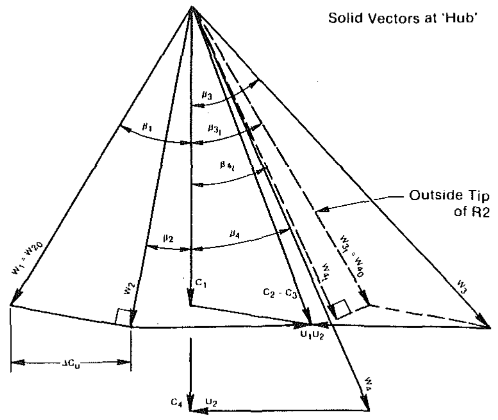

Fig. 10 Vector diagram for translating linear cascades

$$s_1\Delta C_u = s_1\Delta C_{u_h}\,\frac{2}{\pi}\,\arccos e^{-\pi\frac{y_t-y}{a}} \tag{15}$$

It should be pointed out here that there is a discontinuity in static pressure in the primary flow at the tip corresponding to the downward jump in relative velocity from W_{2_0} to W_2. The tip vortex sheet acts like a bound sheet rather than a free sheet. Since there is no such pressure jump in the actual flow, which is the sum of the primary and secondary flows, there is a corresponding but opposite jump in the secondary flow. This is consistent with the Trefftz surface solution, such as was shown in Fig. 6, with the higher velocities and lower pressures occurring on the inside of the vortex sheet.

We now proceed to deduce the primary flow for R2, which will be needed to conduct its secondary flow analysis using equation (7). The inlet flow to R2 is the circumferential average of the flow leaving R1; its relative velocity varies smoothly from W_{3_h} to W_{3_t}. In order to construct the R2 exit vector diagram it is first necessary to determine C_{4_h}. To do this we apply the Bernoulli equation

$$\frac{p_{4_h}}{\rho}+\frac{1}{2}\,C_{4_h}^2=\frac{p_1}{\rho}+\frac{1}{2}\,C_1^2+\frac{1}{\rho}(P_{4_h}-P_1) \tag{16}$$

the Euler equation of turbomachinery

$$\frac{1}{\rho}(P_{4_h}-P_1)=(U_1+U_2)\Delta C_{u_h} \tag{17}$$

and the Theodorsen expression for wake static pressure previously given in Section 3

$$\frac{1}{\rho}(p_{4_h}-p_1)=\frac{1}{2}(C_{4_h}-C_1)^2 \tag{18}$$

Equations (14) and (16)-(18) may be solved to yield

$$C_{4_h}=\frac{1}{2}\left(C_1+\sqrt{C_1^2+8\bar{U}\Delta C_{u_h}}\right) \tag{19}$$

Then

$$\beta_{4_h}=\arctan\frac{U_2}{C_{4_h}} \tag{20}$$

This is the angle of the wake sheet at the hub. For the initial approximation mentioned previously, β_4 would remain constant along the span since that is the linear cascade equivalent of a free-vortex rotor. For generality, however, we will keep the β_4 distribution as an input variable to be examined later.

With β_4 specified, it now remains to find the magnitude of the W_4 vector along the span so that its tangential component, which affects the primary flow circulation, can be determined.

The stagnation pressure relative to R2, P_3', can be deduced from the absolute stagnation pressure at its inlet using

$$\frac{P_3'}{\rho}=\frac{P_3}{\rho}+\frac{1}{2}(W_3^2-C_3^2) \tag{21}$$

Using the Euler equation of turbomachinery and vector diagram geometry, this becomes

$$\frac{P_3'}{\rho}=\frac{P_1}{\rho}+\frac{1}{2}\,U_2^2+2\bar{U}\Delta C_u \tag{22}$$

and W_4 can be found from

$$W_4^2=\frac{2}{\rho}(P_3'-p_4) \tag{23}$$

since there is no change in relative stagnation pressure through R2 in this example. Now, at first glance we might think that p_4 is uniform along the span (except for being discontinuous at the tip) in our primary flow solution, but recall from Section 3 that at the exit of R1, and hence at the inlet of R2, the G-functions of the circumferential-average flow cause a spanwise static pressure variation (equation (2)), which in the present context is

$$p_3=p_{3_h}-\frac{\rho}{2}\left[\sec\beta_2(\Delta C_{u_h}-\Delta C_u)\right]^2 \tag{24}$$

It is expected that the "axisymmetric" turning action of the R2 primary flow will modify this somewhat, but the magnitude of the modification is not immediately clear. Let

$$k_p=\frac{p_{4_h}-p_4}{p_{3_h}-p_3} \tag{25}$$

it being understood that p_3 and p_4 apply to the same streamline upstream and downstream of R2. The value of k_p is then determined by applying the condition that at the tip, the pressure jump across the vortex sheet in the primary flow should be

$$\begin{aligned} p_{4_t}-p_1&=\frac{\rho}{2}(W_{4_0}^2-W_{4_t}^2)\\ &=\frac{\rho}{2}(C_1^2+U_2^2)\sin^2(\beta_{3_t}-\beta_{4_t}) \end{aligned} \tag{26}$$

the second equality coming from the geometry of the vector diagram in Fig. 10. Equations (26) and (18) then combine to yield

$$p_{4_h}-p_{4_t}=\frac{\rho}{2}\left[(C_{4_h}-C_1)^2-(C_1^2+U_2^2)\sin^2(\beta_{3_t}-\beta_{4_t})\right] \tag{27}$$

Applying this and equation (24) at the tip where $\Delta C_u = 0$ to equation (25) gives

$$k_p=\frac{(C_{4_h}-C_1)^2-(C_1^2+U_2^2)\sin^2(\beta_{3_t}-\beta_{4_t})}{(\Delta C_{u_h})^2\sec^2\beta_2} \tag{28}$$

Combination of equations (22)-(28) plus (17), (18) and vector diagram geometry yields

$$W_4=\sqrt{W_{4_h}^2-4\bar{U}\left(1-\frac{\Delta C_u}{\Delta C_{u_h}}\right)\Delta C_{u_h}+\left(1-\frac{\Delta C_u}{\Delta C_{u_h}}\right)^2\left[(C_{4_h}-C_1)^2-(C_1^2+U_2^2)\sin^2(\beta_{3t}-\beta_{4_t})\right]} \tag{29}$$

where $\beta_{3_t} = \arctan(U_2/C_1)$.

The primary flow circulation for R2 is[2]

$$\begin{aligned} \Gamma_2&=s_2(W_{u_3}-W_{u_4})\\ &=s_2[U_2+\Delta C_u-W_4\sin\beta_4] \end{aligned} \tag{30}$$

At the tip where $\Delta C_u=0$ this reduces to

$$\Gamma_{2_t}=s_2\sqrt{C_1^2+U_2^2}\,\sin(\beta_{3_t}-\beta_{4_t})\cos\beta_{4_t} \tag{31}$$

which can also be deduced from the vector diagram geometry. The tip secondary vortex sheet strength in the Trefftz plane is then

$$\Delta\bar{V}_{x_2}=-\frac{\Gamma_{2_t}}{a_{2_t}}=-\sqrt{C_1^2+U_2^2}\,\sin(\beta_{3_t}-\beta_{4_t}) \tag{32}$$

Equations (32) and the spanwise derivative of equation (30) provide information for the evaluation of the second term in equation (7). To evaluate the first term, we use Crocco's equation

$$\begin{aligned} W_3\zeta_{\perp 3}&=|\nabla I_3|\\ &=\frac{d}{dn_3}\left(\frac{P_3'}{\rho}-\frac{1}{2}\,U_2^2\right) \end{aligned} \tag{33}$$

Using equation (22) with (33) yields

$$W_3\zeta_{\perp 3}=2\bar{U}\,\frac{d\Delta C_u}{dn_3} \tag{34}$$

Using

$$\Gamma_{A_2}=s_2\Delta C_u \tag{35}$$

which presumes reasonable success in having ΔC_u of R2 equal that of R1, and approximating W_∞^2 with W_4^2, the first term in equation (7) becomes

$$W_3\zeta_{\perp 3}\,\frac{\Gamma_A}{W_\infty^2}=\frac{2s_2\bar{U}\Delta C_u}{W_4^2}\,\frac{d\Delta C_u}{dn_3} \tag{36}$$

This term is negative, meaning that it augments the secondary flow caused by the tip vortex sheet.

For the present case the streamtube contraction term in equation (7) is

$$\frac{dn_3}{dn_4}=\frac{W_{m_4}}{W_{m_3}} \tag{37}$$

From the forward blade row velocity diagram shown in Fig. 10, it can be seen that

$$W_{m_3}=C_1+\Delta C_u\tan\beta_2 \tag{38}$$

and further application of its geometry yields

$$W_{m_3}=\frac{1}{2}\left[C_1+\sqrt{C_1^2+4\Delta C_u(U_1-\Delta C_u)}\right] \tag{39}$$

W_{m_4} can be found from equation (29) using

$$W_{m_4}=W_4\cos\beta_4 \tag{40}$$

Recapitulating, the primary flow circulation distribution for R2 needed for the second term in equation (7) is obtained from equation (30) using W_4 from (29). The first term in equation (7) is obtained from (36). In these expressions, ΔC_u is obtained from (15) at R2 inlet. The streamtube contraction term in (7) is obtained from (37) using (39) and (40). For the simplified example being considered here, we wish to determine if the specification of a constant wake sheet angle β_4 will result in R2 removing the swirl imparted by R1. Realizing that the penetration of secondary flow effects from the tip is proportional to the wake spacing a, and recognizing that the streamtube contraction effect of equation (37) tends to reduce this penetration, we account for this in an approximate way by letting

$$a_2=a_1\,\frac{W_{m_{3_h}}}{W_{m_{4_h}}} \tag{41}$$

in equation (7) and in the subsequent Trefftz plane analysis.

The above analysis is now applied to an example representative of current unducted fan designs. Let

$$U_2=U_1=C_1 \text{ and } \Delta C_{u_h}=0.125\,U_1$$

This leads to

---

[2] Here we follow the sign conventions of [10]; the circulation is positive.

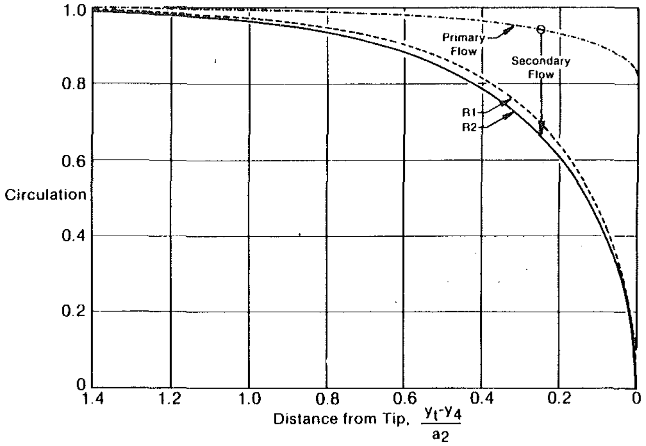

Fig. 11 Aft cascade circulation; $U_2 = U_1 = C_1, \Delta C_{u_h} = 0.125U_1$, constant β_4

$$\beta_1=45, \quad \beta_2=38.51, \quad \beta_{3_h}=45.66, \quad \beta_{3_t}=45, \quad \beta_{4_h}=39.64,$$

$$a_2/a_1=0.911, \quad \text{and } J'=\pi C_{4_h}/U_1=3.79.$$

Let us also assume that β_4 is constant along the span. The R2 primary flow and actual circulation distributions are shown in Fig. 11 in the dash-dot and solid lines, respectively. These are plotted versus spanwise position on the downstream side. Also shown for comparison is the circulation distribution of R1 (dashed line); its spanwise positions have been plotted accounting for streamtube contraction. Agreement between the two distributions is not perfect, but probably acceptable for engineering purposes. Agreement can be made nearly perfect by setting β_{4_t} 1.1 deg lower than β_{4_h} with the variation between hub and tip following the formula

$$\tan\beta_4=\tan\beta_{4_h}-0.3\,\frac{\Delta C_{u_h}}{C_{4_h}}\left(1-\frac{\Delta C_u}{\Delta C_{u_h}}\right) \tag{42}$$

Thus, the wake sheet from an aft rotor should not quite follow the direction of that from a free-vortex rotor, but should be slightly more axial at the tip.

It has been shown [10] that the strength of the vortex sheet shed from a blade row is

$$2V_s=\left[\zeta_{\perp 1}W_1\frac{\Gamma_A}{W_\infty^2}+\frac{d\Gamma_A}{dn_1}\right]\frac{dn_1}{dn_2} \tag{43}$$

which has the form of (7) but employs the actual circulation in its second term. Neglecting stream-tube contraction effects, both blade rows have the same (negative) second term, but R2 receives a (negative) contribution from the first term also. Therefore, the aft blade row's shed vortex sheet is stronger. It does not follow that the cross-passage secondary velocities are necessarily stronger in the aft row; the secondary flow contribution shown in Fig. 11 is less than that of R1 (although it is increased somewhat if the primary flow circulation is raised by opening the tip 1.1 deg).

The means for deducing secondary flow departure angle perturbations from these results will be presented in Section 8.

6 Sweep End Effects

As pointed out in Section 4, the principal effect of sweep is already taken into account by conducting blade-to-blade flow analyses in the ζ plane. However, as was shown by Smith and Yeh [9], when a swept blade intersects an endwall, the endwall constrains spanwise flow movements with the result that blade shape modifications are necessary at and near the endwall if the free-stream chordwise loading distribution is to be maintained. A method for calculating this shape modification was given in [9] for an elliptical chordwise loading distribution, and this yields departure angle perturbations of the order of −5 deg for sweeps around −25 deg and loadings typical of unducted fan hub conditions.

Since no such analysis was available for open rotor tips, the author engaged Prof. J. P. Sullivan of Purdue University to provide one. The resulting effort, carried out under NASA sponsorship, resulted in the work of Alsip and Sullivan [14]. Here several of the assumptions are similar to those of [9]: The blade array is linear rather than angular, the airfoils are thin and the loading is light, the flow is inviscid and subsonic compressibility corrections are incorporated. The input variables are cascade solidity, stagger, and sweep. Dihedral has been assumed to be zero, but chord taper has been included. The spanwise loading distribution is that of Prandtl, previously given herein. In addition to the elliptical chordwise distribution, it is also possible to specify

$$\Gamma_{A_\xi}=\Gamma_A\left[\sin\left(\xi\frac{\pi}{2}\right)\right]^n \tag{44}$$

where Γ_{A_ξ} = bound circulation encompassed between the leading edge and a point along the chord at the spanwise position; Γ_A = total bound circulation at the spanwise position; ξ = fraction of chord. Selection of n = 1.15 gives a distribution representative of modern designs; this will be shown in Section 8. The analysis is carried out using the vortex lattice method. The blades have a finite span; the aspect ratio can be input. At the inner end, the constraint is similar to that of an endwall, so results should be the same as those obtained from the method of [9]. A numerical example has demonstrated that this is indeed true.

The principal output of the Purdue lifting surface analysis is the spanwise and chordwise downwash distribution given as the difference between the full downwash and that of the circumferential-average flow. This is transferred into a sweep-end-effects downwash distribution by subtracting the same quantity for an unswept configuration having cascade properties seen in the ζ plane of the swept configuration. The resulting sweep-end-effects downwash perturbations DW_{sw} lead to sweep-end-effects departure angle perturbations

$$\delta_{sw}=\frac{180}{\pi}\frac{DW_{sw}}{W_\perp} \tag{45}$$

Here $W_\perp$ is the relative velocity in the ζ plane.

To demonstrate the magnitudes involved, the following cases, representative of unducted fan tip and hub conditions, have been calculated (Table 1). Results are shown in Fig. 12. The two blade ends were calculated independently assuming in each case that the local end values of sweep angle and chord remain constant with distance from the end.

The departure angle perturbations are seen to be negative at both blade ends, meaning that the local blade segment angles of attack must be lowered to account for this effect. This counteracts the secondary flow contribution at the tip. Locally at the hub, the linear theory predicts infinite values.

The results shown were calculated at zero Mach number; the tip calculation was repeated at M = 0.95 and the results were approximately 20 percent larger in magnitude. This relatively small effect of Mach number over a wide range of (subsonic) Mach number was also observed by Smith and Yeh [9].

7 Three-Dimensional Euler Analysis

The availability of large computers has made practical the solution of the three-dimensional equations of motion for compressible flow using time-marching methods. Codes in this class handle transonic flow nicely and generally are robust, meaning that the designer has assurance that a solution for his design will be obtained. The accuracy of the solution depends on the discretization approach used and the type and fineness of the grid. Errors are introduced by the need for smoothing

Table 1 Representative properties of unducted fan blade ends

	Tip	Hub
Sweep, λ, deg	45	−27
Solidity, σ	0.15	0.71
Stagger, ζ, deg	32	19
Loading, $\Gamma_h/c_\perp W_\perp$	0.68	0.35
Chordwise loading exponent, n	1.15	1.15
Local aspect ratio, h/c	6.0	2.5

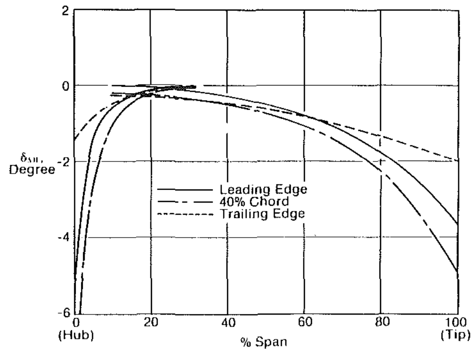

Fig. 12 Sweep-end-effects departure angle perturbations for representative unducted fan rotor

and artificial viscosity in some form or other, and the quality of the code depends on the skill of its developers. The code employed at General Electric was developed by Holmes and Tong [15] and is of good quality.

Codes of this type are generally direct, meaning that a flow solution is found for an input geometry. In the two-row code of Celestina et al. [16] the three-dimensional flow is solved for each rotor while the other is represented on a circumferential-average basis, and iteration back and forth between the rotors is carried out until convergence. The General Electric code has been generalized by Holmes to include also two-row capability, but in this case, since the code is intended for use in the design process, the "other row" is represented by source terms from the circumferential-average solution of Section 3 that are held fixed with design intent distributions. An example obtained using this method is shown in Fig. 13. In this case the three-dimensional solution has been obtained for the aft rotor.

When trimming a design, changes in the blade shape are accomplished by modifying the departure angle distribution that relates the blade shape to the circumferential-average flow angle, as described in Section 4.

8 Application to Blade Design

In this section the design approach described above will be applied to two examples. These are academic in nature; they are chosen to demonstrate certain features of the flow and to compare results from the different computer codes employed. They also provide information on how the secondary flow flowfield calculated downstream of a blade row affects the flow inside the blade row.

In order to permit use of the Purdue lifting surface code [14], which is limited to subsonic linear cascades, the examples will employ a hub/tip radius ratio of 0.99 and profiles with infinitesimal thickness and zero loss. Basic parameters will be the same as those used in the example in Section 5, with the Mach number level selected to keep blade surface Mach numbers subsonic.

8.1 Example No. 1, Isolated Blade Row. Let

$$U_h = C_0, \quad \Delta C_{u_h} = 0.125 U_h, \quad \sigma_h = 0.4, \quad M_0 = 0.5$$

This leads to a hub lift coefficient of about 0.44. Let the blade span equal twice the wake spacing (h/a = 2); this will be sufficient to assure that the Prandtl tip loading distribution (which is input far downstream) will not be constrained by the hub boundary. The resulting blade aspect ratio is about 3.8. The chordwise loading distribution is given by equation (44) with n = 1.15. This is shown in Fig. 14 together with the departure angles for the hub condition. These departure angles were obtained from the Purdue code serving as a two-dimensional inverse design procedure.

Figure 15 shows the circumferential-average flow streamlines with isobars superposed. Radial grid lines have not been shown, but there are six of them between the leading and trailing edge stations. This grid density is rapidly decreased with distance away from the blade row.

We now proceed to determine the departure angle distribution over the blade surface. As explained in Section 4, this is done by adding a perturbation for secondary flow to the basic two-dimensional cascade departure angle distribution. The two-dimensional distribution has already been given in Fig. 14 at the hub. At other spanwise positions it is simply scaled down proportional to the local circulation for this high-radius-ratio case. This is shown as δ_{2D} in Fig. 16, which applies at the trailing edge.

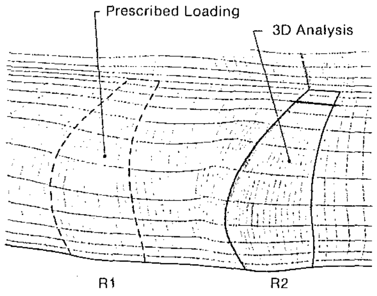

(a) Grid

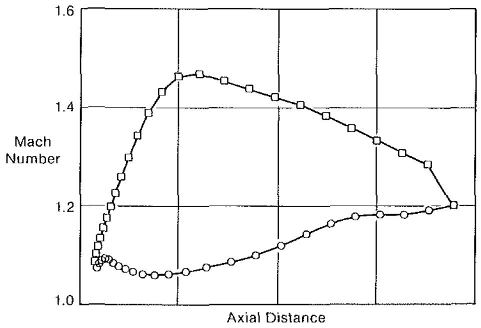

(b) Blade Mach Number Distribution at 92% Span

Fig. 13 Example of two-row Euler analysis, aft row analyzed

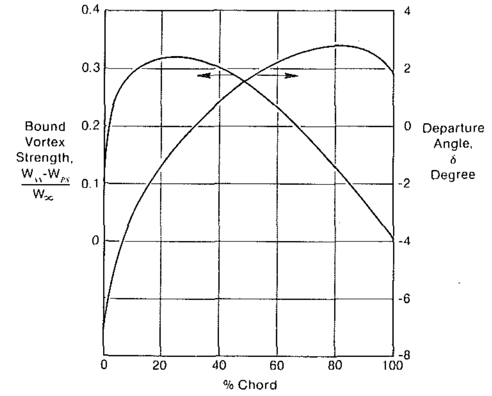

Fig. 14 Chordwise loading and departure angle distributions for the hub cascade

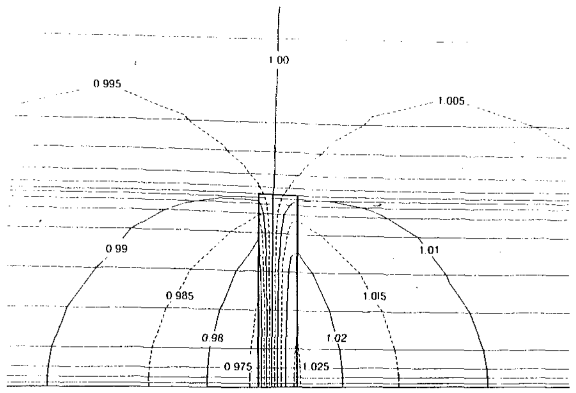

Contours of Static Pressure

Fig. 15 Circumferential-average static pressure field; example No. 1

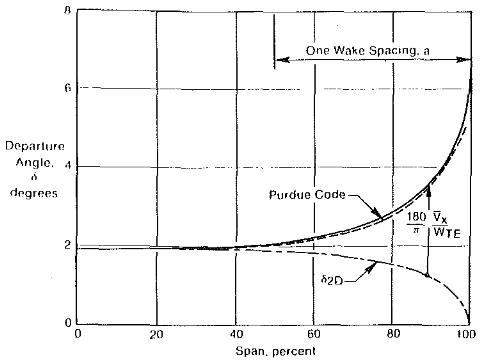

Fig. 16 Departure angle distributions at the trailing edge; example No. 1

The departure angle perturbation for secondary flow is related to the flow in the downstream Trefftz plane. Secondary vorticity for this example is limited to the tip secondary vortex sheet whose strength is

$$\Delta \bar{V}_x = -\frac{\Gamma}{a} = -\Delta C_{u_h} \sec \beta_2 \qquad (46)$$

The $\bar{V}_x$ distribution obtained from the Trefftz plane solution is converted into a departure angle perturbation as shown in Fig. 16, using the relative velocity at the trailing edge from the circumferential-average solution. Also shown in Fig. 16 is the trailing edge departure angle distribution obtained directly from the Purdue code. Agreement is seen to be good. The small difference could be explained by numerical or physical inaccuracies in any of the codes involved, but a more likely explanation is that near-field effects, beyond those already accounted for in the circumferential-average solution, account for the difference. To recognize this we will use only 90 percent of the Trefftz plane $\bar{V}_x$ when calculating the secondary flow departure angle perturbation at the trailing edge.

The secondary flow departure angles at other chordwise positions must depend upon the chordwise loading distribution. The Purdue code can be called upon to provide guidance here. In Fig. 17 values of the local secondary flow departure angles have been normalized by values at the trailing edge. The different symbols indicate different distances from the tip. Here the secondary flow departure angles have been obtained by subtracting from the total departure angles those of the two-dimensional flow, which are proportional to the blade circulation at that spanwise position. It is seen that all of the data can be represented reasonably well with one curve, which is then used.

Departure angles calculated by this means over the whole blade planform have been subtracted from the circumferential-average flow angles of the solution shown in Fig. 15 to obtain blade meanline angles; these are shown in Fig. 18. For

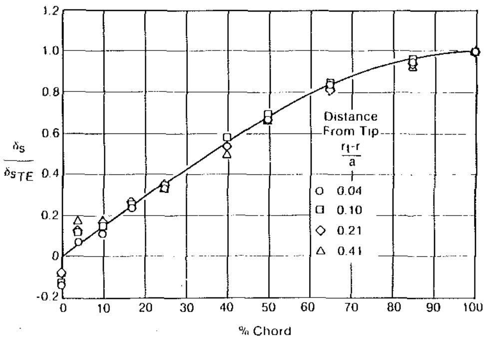

Fig. 17 Chordwise distribution of secondary flow departure angles

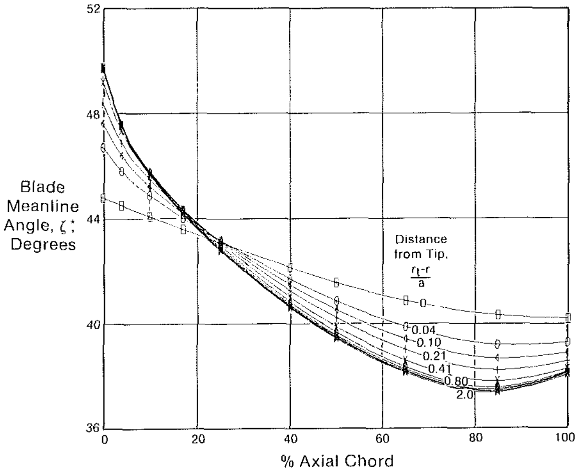

Fig. 18 Blade meanline angles for example No. 1

this constant-chord blade, the tip section is seen to be closed at the trailing edge and opened at the leading edge compared to the hub section.

The three-dimensional Euler code has been employed to analyze this blade shape, and results are presented in the next two figures. For these calculations the hub radius has been assigned the value 985, and the tip radius is therefore around 995, decreasing slightly from leading edge to trailing edge. The hub blade speed is 558.5.

Figure 19(*a*) shows circumferential-average angular momentum values at the leading edge and trailing edge stations compared to those of the circumferential-average analysis. Considering that several different codes have been employed, agreement is quite good. At and above the tip the Euler analysis has calculated a small angular momentum change; for this all-subsonic potential flow case Kelvin's theorem tells us that this is not correct. The very large gradient occurring in this region combined with the finite grid employed (the spanwise distance from the tip grid line to the next grid line on either side of it is 2.8 percent of the wake spacing) are believed to be responsible for this inaccuracy. Circumferential-average flow angles are shown in Fig. 19(*b*). The turning angle is seen to be negative at the tip. The higher angular momentum near the tip in the Euler solution noted in Fig. 19(*a*) is seen to be reflected in the trailing edge flow angle. Figure 19(*c*) displays the circumferential-average static pressure distributions. Generally, agreement is good. The local depression in the Euler result very near the tip at the trailing edge is a proper consequence of the strong radial flow components that are not fully accounted for in the *G*-function formulation; see equation (2).

Figure 20 shows airfoil surface relative Mach number distributions at four locations along the span. The loading distribution of Fig. 14 is seen to have been obtained reasonably well although the distribution for the section closest to the tip shows some variation.

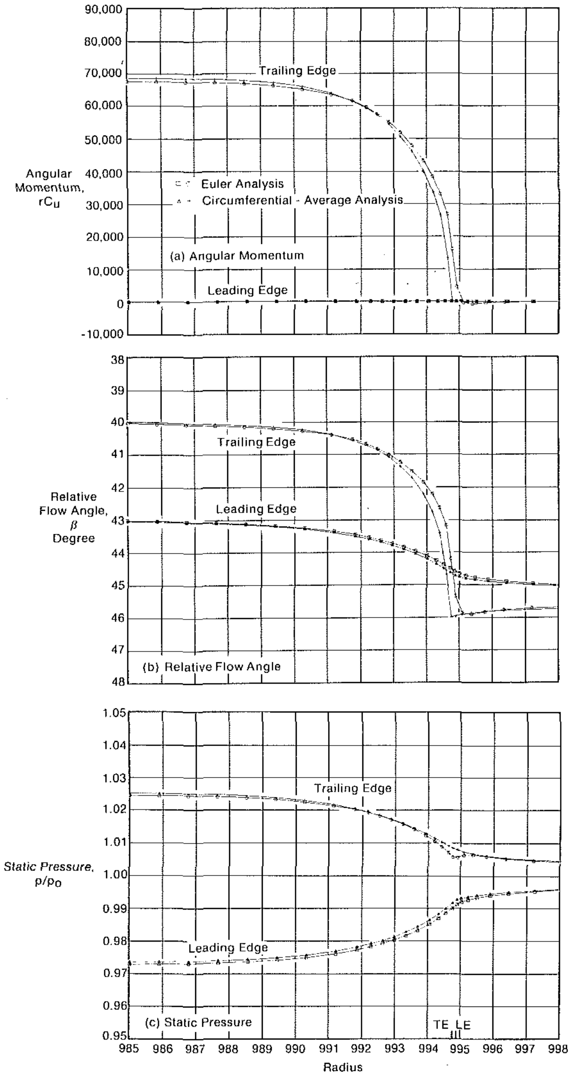

Fig. 19 Comparison of Euler analysis of Section 7 with circumferential-average analysis of Section 3; example No. 1

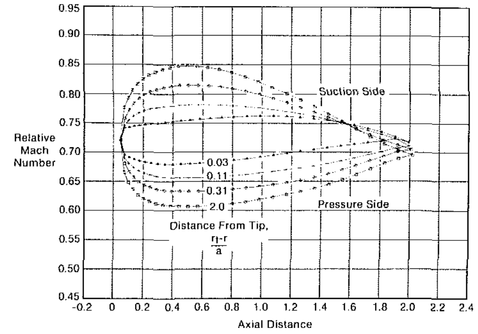

Fig. 20 Relative Mach number distributions from Euler analysis; example No. 1

8.2 Example No. 2, Aft Blade Row. In this two-row example the work input of the forward row is the same as that prescribed for example No. 1. The aft row has been designed to accept the same mass flow as that passing through the forward row and to remove the swirl imparted by it.

Pressure contours from the circumferential-average analysis are shown in Fig. 21. Comparison with Fig. 15 shows that the forward row flowfield has been affected by the presence of the aft row as expected; the blade design of the forward row would therefore have to be different from that shown in Fig. 18 to produce the desired loading.

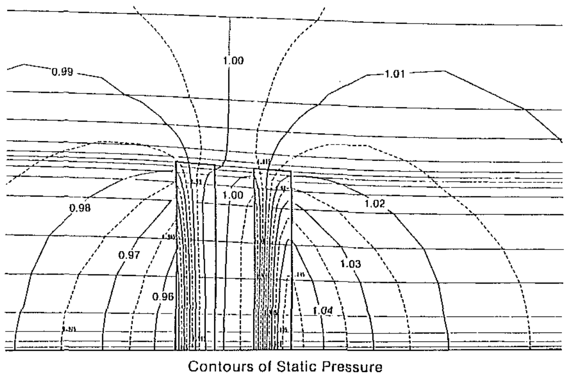

Fig. 21 Circumferential-average static pressure field; example No. 2

We specify the speed, solidity, and wake spacing of the aft row to be the same as those of example No. 1. Although the blade stagger angles will be about 2 deg higher and the hub inlet relative Mach number is increased from 0.75 to 0.79, the same δ_{2D} distribution will be employed as was used for example No. 1. *The secondary vorticity was calculated from equation* (7) using, for the second term, equations (30) and (32) with radially constant β_4, the value of which was chosen to produce the design hub circulation. The first term in equation (7) was evaluated using a computer subroutine for it that was adapted from Adkins and Smith [8]. The Trefftz plane analysis yielded cross-passage velocities that were about 85 percent as large as those of example No. 1, and the 90 percent factor was again applied before using them to calculate trailing edge secondary flow departure angle perturbations. The line in Fig. 17 was again used, departure angles over the whole planform were obtained, and these were subtracted from the circumferential-average flow angles to define the blade shape.

Results from the two-row Euler analysis for the second row are compared with those from the circumferential-average analysis in the next two figures. In Fig. 22(*a*) we see that the design intent angular momentum from the forward row has been nicely matched in the Euler solution. The distributions at the trailing edge show that R2 overturns slightly over most of the span, and Fig. 22(*b*) shows that this is the result of a departure angle inaccuracy of only about 0.1 deg. Very near the tip the discrepancy is larger, some of which is probably again caused by the very large gradients in the Euler analysis. Figure 22(*c*) again shows generally good agreement in the pressure distributions.

The surface Mach number distributions shown in Fig. 23 again look reasonable, except for a crossover near the trailing edge for the tip-most section. This is the result of a small amount of artificial viscosity generated by the Euler code affecting the relative total pressure; the static pressure is actually slightly lower on the suction side than on the pressure side at that location as it should be.

9 Conclusions

1 The same quasi-three-dimensional approach used to design ducted turbomachines can be successfully adapted to the design of unducted fans. With this method, custom-tailored airfoil shapes are designed by specifying distributions of departure angle, which relate the blade meanline angles to the flow angles from a circumferential-average analysis. The primary changes required are modifications of the secondary-flow and sweep-end-effects models to account for the open-tip condition.

2 An accurate circumferential-average flow analysis that recognizes radial and chordwise distributions of blade thickness blockage, loading, and loss is an important element in the design process. It serves as the design tool for shaping the hub contour. At the high meridional Mach numbers of un-

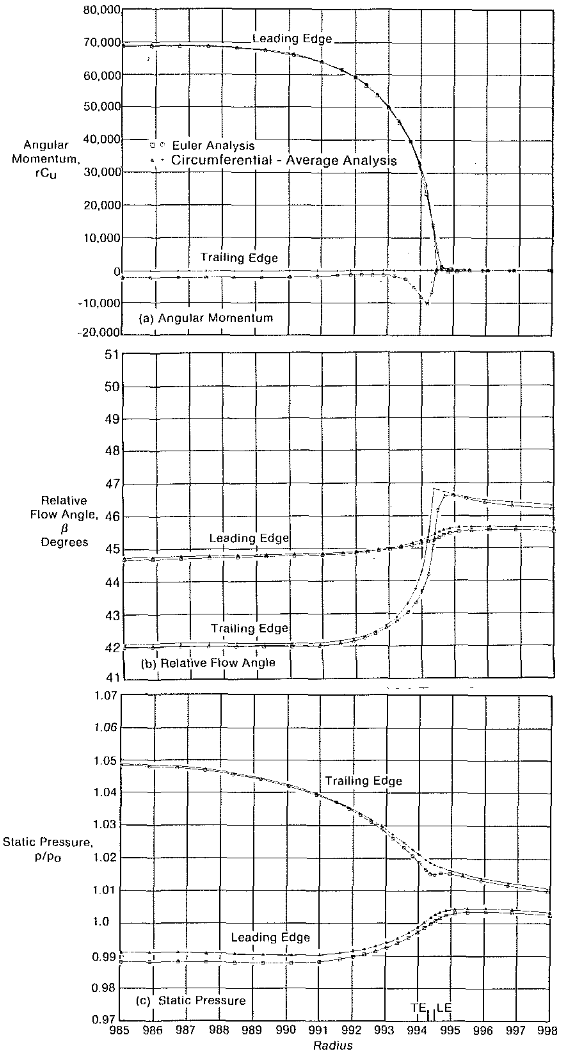

Fig. 22 Comparison of Euler analysis with circumferential-average analysis; aft blade row; example No. 2

ducted fans, proper hub contouring is vital if choking, where the blades are the thickest, is to be avoided.

3 The highly three-dimensional nature of the flow near the blade tips requires the addition of a Reynolds-stress-type term in the radial momentum equation used in the circumferential-average flow analysis. This term, which causes an increase in the pressure in the slipstream, dissipates downstream as the shed vortex sheet rolls up and dissipates.

4 The secondary flow approach employed was shown to predict proper optimum spanwise loading distributions for single-rotation propellers. For counterrotating propellers, a simple approach for treating the forward rotor was also shown to give a reasonable approximation to Theodorsen's optimum distributions for J' values of interest to unducted fan designers, but proper optimum solutions for cases with finite axial spacing and finite loading are unknown to the author.

5 A method was given for relating the cross-passage secondary flow velocities calculated in a Trefftz plane to the design departure angles. It was shown that the shed vortex sheet, which is given by the spanwise secondary flow velocities, must be stronger on the aft rotor of an unducted fan than on the forward rotor because of a contribution from the vorticity shed from the forward rotor. This does not necessarily mean that the cross-passage velocities of the aft rotor are larger, however.

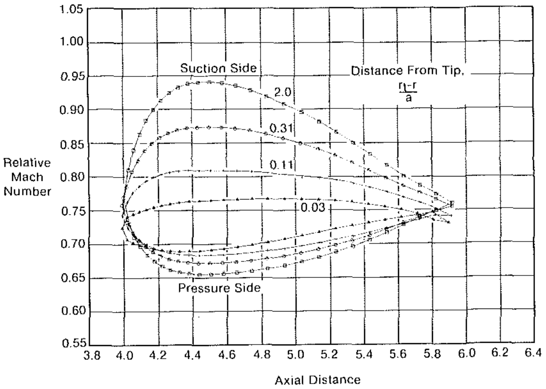

Fig. 23 Relative Mach number distributions from Euler analysis; aft blade row; example No. 2

6 The design approach employed takes into account automatically the first-order effects of sweep. However, near swept blade ends departure angle perturbations are required. It was shown that the conventional planform shape that employs back sweep at the tip and forward sweep at the hub causes reduced departure angles (angles of attack) at both blade ends.

Acknowledgments

The author wishes to thank J. S. Keith, R. D. Caney, I. K. Jennions, C. Shin, and G. G. Adkins for their consultations and executions of the numerical analysis, NASA for their support of the Purdue lifting surface analysis, and General Electric Company for permission to publish the paper.

References

1 Theodorsen, T., *Theory of Propellers*, McGraw-Hill, New York, 1948.

2 Smith, A. M. O., and Pierce, J., "Exact Solution of the Neumann Problem. Calculation of Non-circulatory Plane and Axially Symmetric Flows About or Within Arbitrary Boundaries," Douglas Aircraft Report No. ES 26988, 1958.

3 Hess, J. L., and Smith, A. M. O., "Calculation of Non-lifting Potential Flow About Arbitrary Three Dimensional Bodies," Douglas Aircraft Report No. ES 40622, 1962.

4 Smith, L. H., Jr., "The Radial-Equilibrium Equation of Turbomachinery," ASME JOURNAL OF ENGINEERING FOR POWER, Vol. 88, 1966, pp. 1-12.

5 Glauert, H., "Airplane Propellers," in: *Aerodynamic Theory*, W. F. Durand, ed., Vol. IV, Div. L., Chap. VII, Calif. Inst. of Tech., Jan. 1943.

6 Schouten, G., "Static Pressure in the Slipstream of a Propeller," *Journal of Aircraft Engineering Notes*, Vol. 19, No. 3, 1982, pp. 251-253.

7 Kaden, H,, "Aufwicklung einer unstabilen unstetigkeitsflache," *Ingenieur-Archiv 1*, 1931, Vol. II, No. 2, pp. 140-168.

8 Adkins, G. G., Jr., and Smith, L. H., Jr., "Spanwise Mixing in Axial-Flow Turbomachines," ASME JOURNAL OF ENGINEERING FOR POWER, Vol. 104, 1982, pp. 97, 100-110.

9 Smith, L. H., Jr., and Yeh, Hsuan, "Sweep and Dihedral Effects in Axial-Flow Turbomachinery," ASME *Journal of Basic Engineering*, Vol. 85, 1963, pp. 401-416.

10 Smith, L. H., Jr., "Secondary Flow in Axial-Flow Turbomachinery," *Transactions of the ASME*, Vol. 77, 1955, pp. 1065-1076.

11 McCormick, B. W., Eisenhuth, J. J., and Lynn, J. E., "A Study of Torpedo Propellers—Part I," Ordnance Research Laboratory, The Pennsylvania State University, Serial No. NOrd 16597-5, Mar. 30, 1956.

12 Eckhardt and Morgan, "A Propeller Design Method," Society of Naval Architects and Marine Engineers, 1955.

13 Crigler, J. L., "Application of Theodorsen's Theory to Propeller Design," NACA Report 924, Mar. 15, 1948.

14 Alsip, M. M., and Sullivan, J. P., "Numerical Methods Applied to the Design and Analysis of a Cascade of Wings," School of Aeronautics & Astronautics, Aerospace Sciences Laboratory, Purdue University, West Lafayette, IN, Dec. 1984.

15 Holmes, D. G., and Tong, S. S., "A Three-Dimensional Euler Solver for Turbomachinery Blade Rows," ASME JOURNAL OF ENGINEERING FOR GAS TURBINES AND POWER, Vol. 107, 1985, pp. 258-264.

16 Celestina, M. L., Mulac, R. A., and Adamczyk, J. J., "A Numerical Simulation of the Inviscid Flow Through a Counterrotating Propeller," ASME JOURNAL OF TURBOMACHINERY, Vol. 108, 1986, pp. 187-193.

C. M. Vaczy
Analytical Engineer,
Hamilton Standard,
Division of
United Technologies Corporation,
Windsor Locks, CT

D. C. McCormick
Associate Research Engineer,
United Technologies Research Center,
East Hartford, CT

A Study of the Leading Edge Vortex and Tip Vortex on Prop-Fan Blades

An oil flow visualization study was conducted on the blades of a counterrotating prop-fan model, the CRP-X1. A kink in the oil streaks was interpreted as an indication of the leading edge vortex reattachment line. The leading edge vortex was found to be on the lower surface for cases with negative leading edge loading and on the upper surface for cases with positive leading edge loading. For most cases, the leading edge vortex merged with a tip vortex. The results presented here represent the first systematic study of this phenomenon.

Introduction

Until the mid-1970s, propellers were designed with fairly light loading, straight blades, and thick airfoils. They were meant to operate at cruise Mach numbers below 0.6. These configurations were typically designed and analyzed successfully with lifting line analysis. With the advent of prop-fans, which have high loading, highly swept blades, and thin airfoils and are meant to operate at cruise Mach numbers between 0.7 and 0.8, more sophisticated methods such as lifting surface, full potential, and Euler methods were developed for the analysis. Hamilton Standard developed a vortex lattice method [1] which, with NASA funding, has since been extended to true lifting surface. For prop-fans the lifting surface method typically did well at the cruise design point, but overpredicted the power at high negative loading cases, such as windmill, and underpredicted the power at high positive loading cases, such as takeoff.

Although there had been a few explanations for this disagreement, none were convincing. Surface pressure measurements on the large-scale advanced prop-fan (LAP) [2] first gave an indication that prop-fans could be affected by leading edge vortex flow, as are wings which have high sweep, a low aspect ratio, and a sharp leading edge. In order to substantiate the existence of the leading edge vortex on prop-fan blades, and also to provide a data base to aid in computations accounting for both the leading and tip edge vortices, a flow visualization study was conducted on the blades of the CRP-X1, a counterrotating prop-fan model that was at the time being tested in the United Technologies Research Center (UTRC) acoustic research tunnel. The model is shown in Fig. 1. Reference [2] gave a preliminary result of the flow visualization, along with some noise implications. The current paper presents the detailed results of this flow visualization study, and shows that the leading edge and tip vortices at least partially explain the disagreement between test and theory.

Test Procedure

The flow visualization used was an oil/tracer method which yields surface flow patterns. For this technique a fluorescent paint pigment by Day-Glo was used as a tracer. The pigment was mixed with a heavyweight oil, 90 weight for the lower rpm cases and 120 weight for the higher rpm cases. The ratio by volume was approximately 1:1. After mixing the oil and tracer, the solution was allowed to settle for 30 min in order for the air bubbles to escape. A uniform coat of solution was applied to the entire blade surface. Two separate blades on each prop were used, one for the upper surface and one for the lower surface. The props were then run up to the desired speed (approximately 1 min to reach condition). This speed was held constant for 5 to 15 min depending on the rpm and the weight

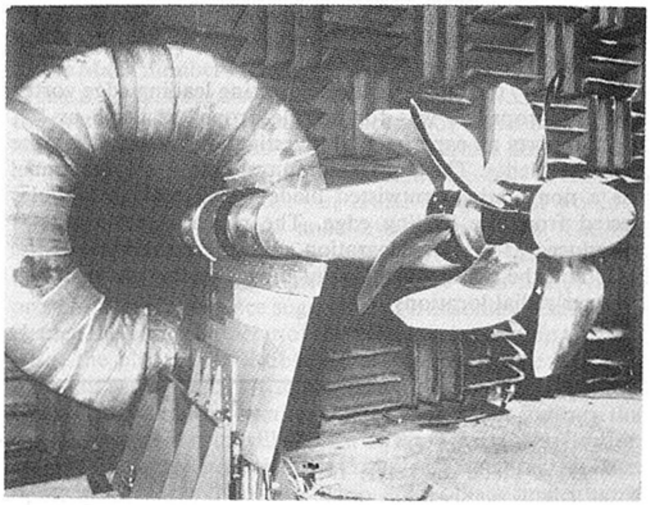

Fig. 1 CRP-X1 model in acoustic research tunnel

Contributed by the Gas Turbine Division of THE AMERICAN SOCIETY OF MECHANICAL ENGINEERS and presented at the 32nd International Gas Turbine Conference and Exhibit, Anaheim, California, May 31-June 4, 1987. Manuscript received at ASME Headquarters February 19, 1987. Paper No. 87-GT-234.

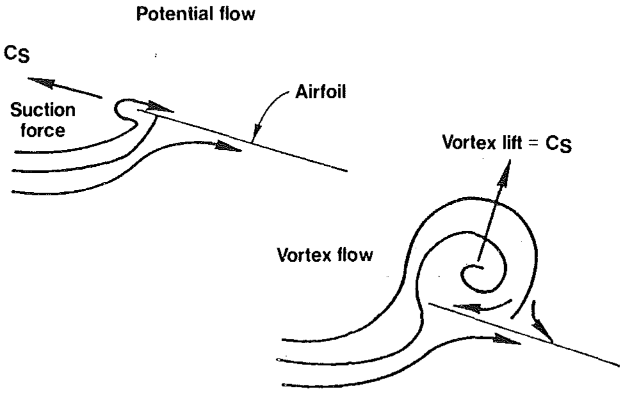

Fig. 2 Idealized view of leading edge flow conditions for two-dimensional flat plate airfoil

of the oil. The resulting patterns were essentially dry after this time so there was no influence on the patterns during the shutdown period. The patterns were photographed with a 4×5 in. view camera using Polaroid type 59 (ASA 80) and type 55 P/N (ASA 50) film. They were illuminated with two ultraviolet lamps (Magnaflux Model ZB lamp with Philips HPW 125 watt bulb) in order to stimulate the fluorescent nature of the pigment. A number 15 (orange) filter was used to filter any reflected ultraviolet light. The exposure times were generally 3 to 4 min with a high f/stop setting from 22–32 (high f/stops were necessary to obtain a large depth of field to accommodate the twisted blade).

Prop-Fan/Wing Oil Flow Pattern Comparison

The existence of the leading edge vortex on highly swept delta wings is well documented [3–6]. It has been shown that when the flow separates going around the leading edge, a vortex forms along the suction surface which causes lift that adds to the potential lift. This extra force is known in the wing literature as vortex lift or nonlinear lift. A simplified depiction of this is shown in Fig. 2. At cruise the angle of attack is sufficiently low to keep the flow attached, while at takeoff the angle of attack is sufficiently high to cause the flow to separate, roll up into a vortex, and reattach. Figure 3(*a*) (from [3]) shows the vortex sheets rolled up on a delta wing. The primary vortex is quite large, and underneath, a secondary vortex of opposite direction often exists. Figure 3(*b*) shows the typical oil-flow pattern resulting from this type of flow, while Fig. 3(*c*) shows the interpretation of the oil results. The streaks downstream of the attachment line are lined up with the external flow. Between the attachment line and the secondary separation line the streaks are s-shaped.

Until 1985, the only evidence indicating leading edge vortex flow for propellers was for marine propellers, such as [7], which reports an experimental investigation on swept marine propeller blades. The configuration tested in the water tunnel was a nonrotating, untwisted blade which had air bubbles ejected from the leading edge. The pattern that results is reproduced as Fig. 4. Separation starts near the knee of the blade and the reattachment point moves farther downstream at larger radial locations.

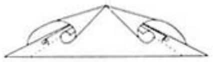

(a) Vortex sheets formed above the wing

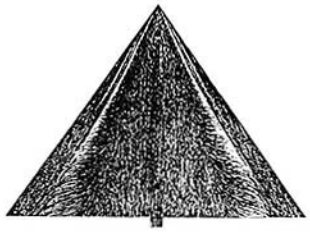

(b) 55° delta wing, flat upper surface. Oil-flow pattern at $\alpha = 10°$.

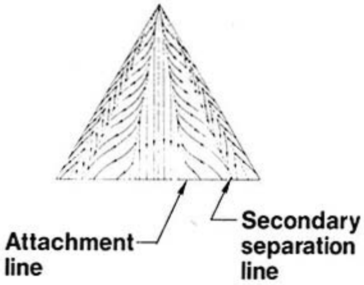

Surface flow pattern

(c) Typical flow over a delta wing at moderate incidence.

Fig. 3 Vortex flow on a delta wing ([3]; with permission)

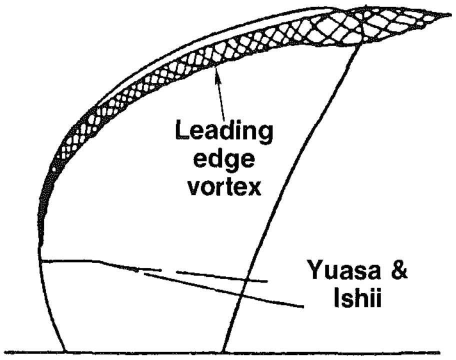

Fig. 4 Vortex flow visualization on a simulated marine propeller in a water tunnel ([7], with permission)

Figure 5 shows a typical result from the present study on the CRP-X1 front rotor for Mn = 0.25, $J = 1.05$, $\beta = 39.17$ deg. The approximate radial direction is shown with the arrow. In this figure the streaks are predominantly radial due to cen-

Nomenclature

Cp = power coefficient = $SHP/\rho n^3 D^5$
D = blade diameter, ft
J = advance ratio = V_∞/nD
Mn = flight Mach number
n = propeller speed, rps
N = propeller speed, rpm
V_∞ = flight speed, fps
x/c = nondimensional chordwise distance
β = blade angle at 3/4 radius
ΔCp = difference pressure coefficient
ρ = density, lb-s^2/ft^4

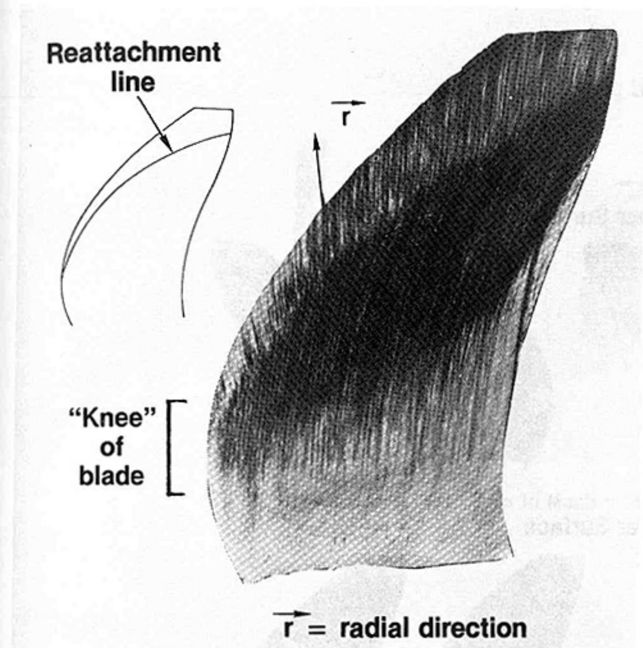

Fig. 5 Representative sample of flow visualization results; β = 39.78 deg, J = 1.05, Mn = 0.25, front blade, upper surface

Table 1 Test matrix for flow visualization on CRP-X1

	βF/ βR = 58.33°/55.68°	39.78°/37.13°	29.80°/31.42°
MN	J	J	J
.25	WINDMILL* 3.45,3.17 3.10,2.92 2.38,2.08	WINDMILL 1.82,1.67 1.20,1.05	WINDMILL 0.81
.13	WINDMILL 2.92	WINDMILL 1.20	
.08		WINDMILL 1.20	
.065		WINDMILL 1.20	
.03		WINDMILL 1.20	

* WINDMILL MEANS ZERO SHAFT POWER.

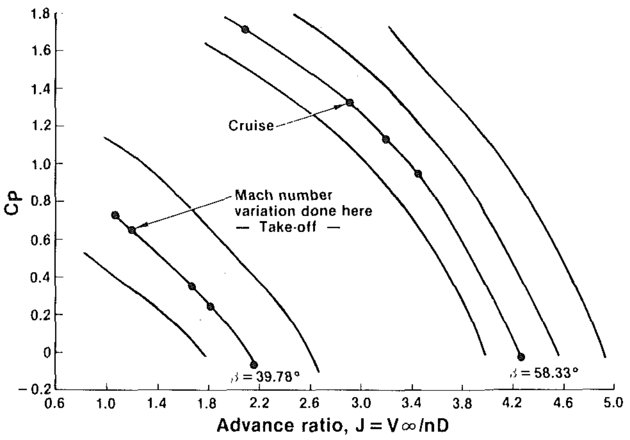

Fig. 6 Typical performance map at constant Mach number

trifugal effects. The streaks, however, undergo a distinct change in direction in a kink that runs from the knee of the blade to the tip. The kink is interpreted to be the reattachment line. Between the leading edge and the kink, a leading edge vortex exists which grows radially until it merges with the tip vortex. This pattern is very similar to that shown in Fig. 3(*b*) for the delta wing. Since the centrifugal force on the oil is on the order of 100 times (assuming on oil thickness of about 0.002 in.) larger than the boundary layer shear force, the pattern downstream of reattachment is mostly radial. In the region between the kink and the leading edge the streaks are s-shaped, qualitatively similar to those on the delta wing. In this region, if there had been no rotation, the vortex would have caused the oil streaks to be mainly lined up with the radial direction, as in Fig. 3(*c*) for the delta wing. Since the centrifugal force also acts in the radial direction, the s-shaped streaks are only modified, appearing to be stretched. As is shown in Fig. 3(*c*), there is also a secondary separation and reattachment on delta wings.

For some of the current visualization results, it appears that a secondary separation may be indicated, although it is not clear since the centrifugal effects obscure this. Therefore, the secondary separation and reattachment will not be discussed in this paper.

Prop-Fan Test Series

Table 1 shows the test matrix completed for the flow visualization study. The matrix covers a range of blade angles, advance ratios, and Mach numbers. Only the most pertinent of the cases tested will be presented here, and only the results on the front rotor. The rear rotor results are comparable to the front rotor results, and since there is no evidence of the front rotor vortex system affecting the rear rotor pattern, there is nothing extra to be learned about vortex flow from looking at the rear rotor results. Figure 6 illustrates the points that will be discussed in this paper on a performance map. On the map, power coefficient Cp is plotted versus advance ratio J for lines of constant blade angle at a constant Mach number. Since $J = V_\infty/nD$, an increase in rotor speed n with the Mach number held constant decreases J. As can be seen from Fig. 6, this increases the loading Cp from the windmill value (where windmill means no shaft power), which is slightly negative, to very high positive values. On this map three test series were run, and the flow visualization results for these three series will be presented. The first series is at a fixed β = 39.78 deg, Mn = 0.25. This represents the takeoff blade angle and Mach number. A series of five advance ratios, including the takeoff point of J = 1.2, was run. The second series run was again at β = 39.78 deg but at a fixed J = 1.2 as Mach number was varied from 0.25 to 0.03. This approximately maintains the air angles as the Reynolds number and Mach number are varied. This is equivalent to a wing operating at a fixed angle of attack as the Mach number is changed. The third series run was at the cruise β = 58.3 deg but at a Mach number of 0.25. Here, as in the first series, five different advance ratios were run, again increasing loading Cp, as J decreases. The cruise design point J of 2.92 was run. For an inflexible blade the only differences between this point and the true cruise design point would be the section Mach number and Reynolds numbers. The true cruise case would have transonic flow over a larger portion of the blade which the simulated cruise case does not even approach. Wing experience suggests that transonic effects do not change the basic character of the leading edge and tip vortices. Also, the blades are flexible. Since the true cruise is at J = 2.92 and Mn = 0.75, to achieve J = 2.92 at Mn = 0.25, the rpm must be reduced by about 1/3. Calculations indicate that this difference in rpm will cause a difference in the deflections between the simulated and true cruise cases. At the simulated cruise, the blade will be at a slightly higher blade angle than at the true cruise.

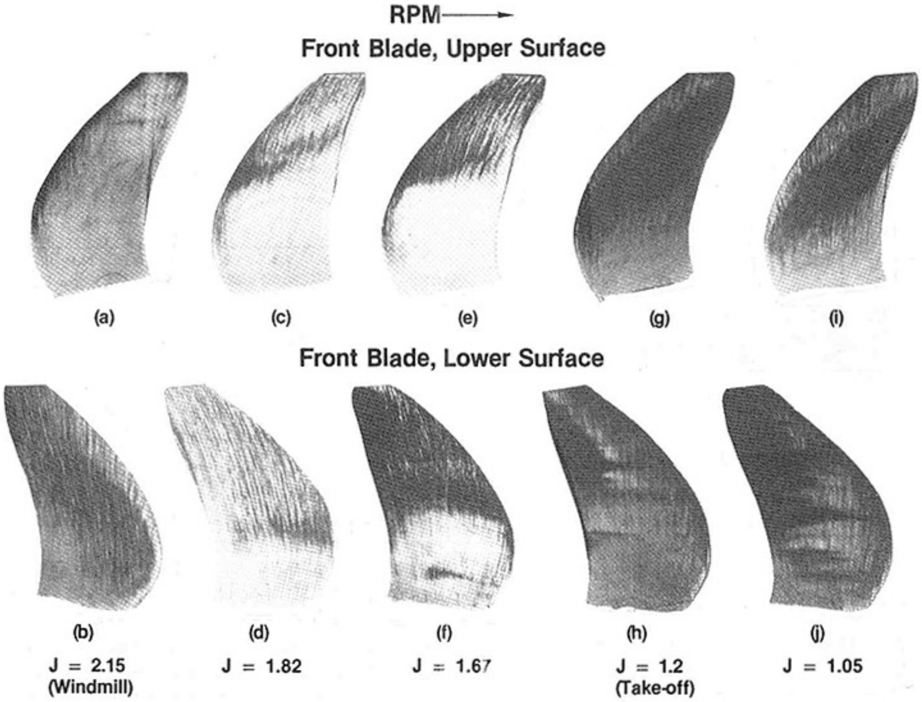

Fig. 7 Variations about takeoff condition, β = 39.78 deg, Mn = 0.25

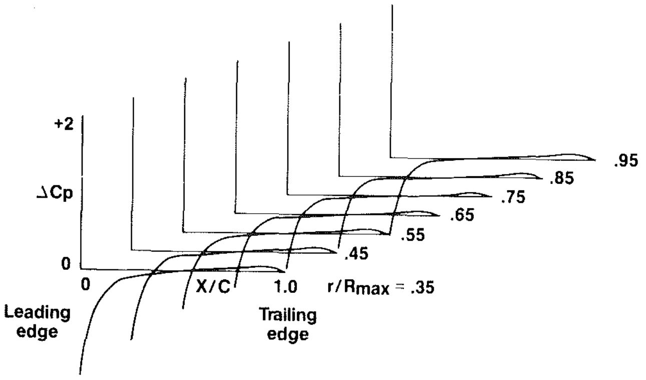

Fig. 8(a) Calculated results at windmill; Mn = 0.25, β = 39.78 deg, J = 2.15, CRP-X1 front blade

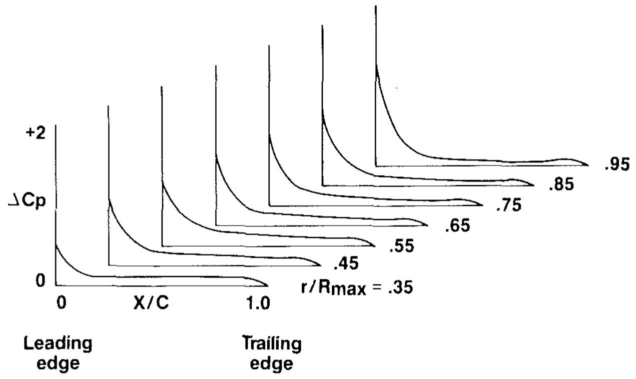

Fig. 8(b) Calculated results at takeoff; Mn = 0.25, β = 39.78 deg, J = 1.2, CRP-X1 front blade

Results at the Takeoff Blade Angle. Figures 7(*a–j*) show the flow visualization results at the takeoff blade angle. The top row shows the patterns on the upper side of the blade (camber or nominal suction), and the bottom row shows the patterns on the lower side of the blade (face or nominal pressure). From left to right the rpm, and therefore the loading, is increasing. The first upper/lower combination is the windmill case. The lifting surface analysis program was run for this case, and the results are presented in Fig. 8(*a*). In this figure the coefficient of lift pressure ΔCp is plotted versus x/c at seven radial stations. The leading edge loading is strongly negative. The stagnation point would then be on the upper surface, and the flow would go around the leading edge and separate, forming a vortex on the lower surface. The leading edge vortex is indicated by the kink on the lower side of the blade (Fig. 7*b*). There is no tip vortex apparent on the lower side; however, near the trailing edge on the upper surface (Fig. 7*a*), a small tip vortex is indicated. The lifting surface analysis (Fig. 8*a*) indicates positive loading over the last half of the chord near the tip, which would cause the flow to go from the lower side of the blade to the upper side. The flow, therefore, can be going from lower surface to upper surface over part of the blade, while going from upper surface to lower surface over other parts. This is the only case tested where the leading

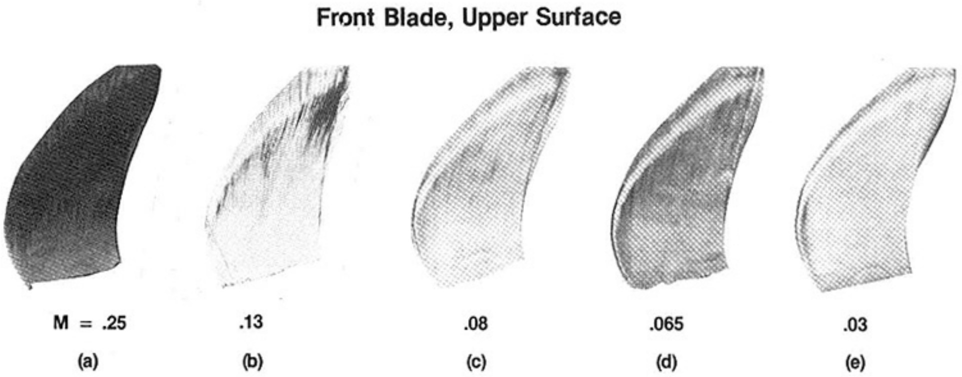

Fig. 9 Variations in Mach number at constant air angles, β = 39.78 deg, J = 1.2

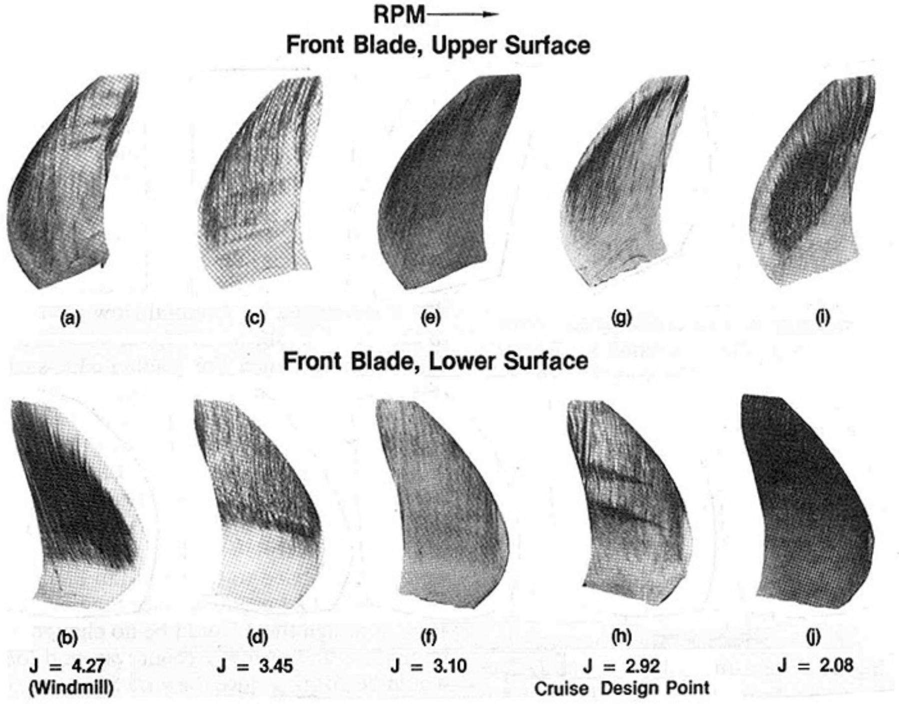

Fig. 10 Variations about simulated cruise, β = 58.33 deg, Mn = 0.25

edge and tip edge vortices did not appear as a system on the same side of the blade.

The second J combination (Figs. 7*c*, *d*) does not show a noticeable vortex on either side of the blade. The third combination (Figs. 7*e*, *f*) shows a small leading/tip edge vortex system on the upper side of the blade. The fourth combination (Figs. 7*g*, *h*), which represents the takeoff point, shows a fairly large leading/tip edge vortex on the upper side. For this case the lifting surface analysis program was run, and the results are presented in Fig. 8(*b*). The leading edge loading is very high, and the tip loading is positive over the entire chord. This is consistent with the large leading/tip edge vortex system indicated by the flow visualization. The fifth J combination (Figs. 7*i*, *j*) shows how the vortex grows as the rpm is increased beyond the takeoff value. Again the leading edge and tip edge vortex are merged on the upper side of the blade, and extend over a fairly large distance in the chordwise direction.

Mach Number Variation. Figures 9(*a*–*e*) show results at the takeoff β = 39.78 deg and a fixed J = 1.2 but with an excursion in Mach number from 0.25 to 0.03. Recall that holding β and J constant while Mn is varying maintains the flow angles (neglecting blade deflections). Note that this variation simultaneously changes the section Reynolds numbers.

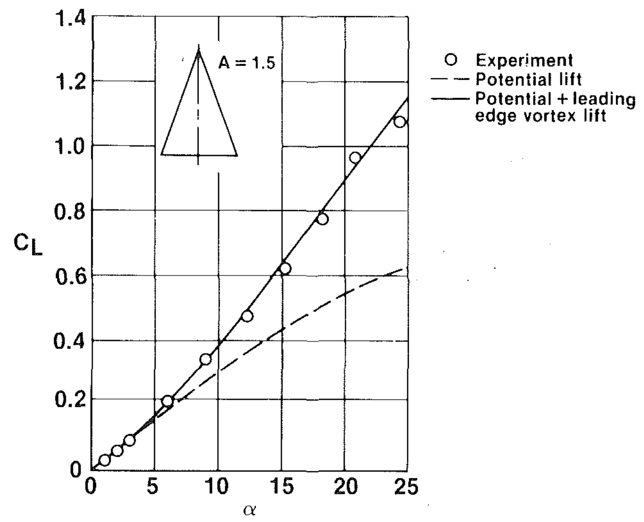

Fig. 11 Comparison theory and experimental data for sharp-edge delta wing [8]

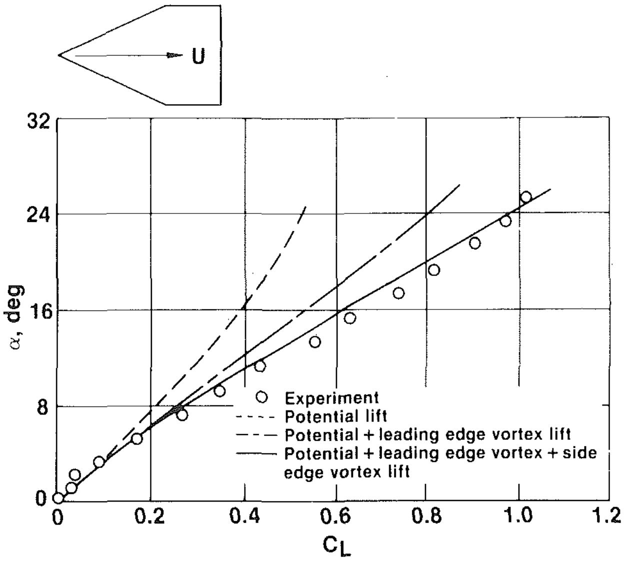

Fig. 12 Comparison of theory and experimental data for sharp-edge cropped delta wing [10]

Many of the details in Fig. 9 differ with Mach number, but the primary reattachment point is virtually unchanged with Mach number. This is consistent with wing experience.

Results at the Cruise Blade Angle. Figures 10(*a*–*j*) show the results of the flow visualization for the cruise blade angle. Again rpm is increasing from left to right. The first combination (Figs. 10*a*, *b*) is the windmill case. Again there is a large leading edge vortex on the lower surface, consistent with a negative leading edge loading which is always calculated at windmill. There is no apparent tip vortex on either side of the blade, and for this case the leading edge vortex extends further radially than it did for the takeoff blade angle. The second combination (Figs. 10*c*, *d*) is the "vortex free" case. This is at a higher *J* (lower rpm) than the simulated cruise design point. The third combination (Figs. *e*, *f*) shows a small leading/tip edge vortex system on the upper surface. The fourth combination (Figs. *g*, *h*), which is the simulated cruise design point, indicates a moderate leading/tip edge vortex system on the upper surface. The fifth combination (Figs. 10*i*, *j*) is an overpower condition showing an extremely large leading/tip edge vortex system which covers a large portion of the blade.

At the cruise design point it is desirable to avoid the leading edge vortex because of the loss of the leading edge thrust that accompanies the rotation of the thrust force to a lift force (recall Fig. 2). This series shows that the leading edge vortex can be avoided (Figs. 10*c*, *d*). The advance ratio where this occurs, however, is at a higher *J* than the cruise design *J*. The case which duplicates the cruise design *J* indicates a moderate leading/tip edge vortex system. Due to the differences in blade deflections between this case and the true cruise, as discussed previously, it is believed that the existence of the vortex at this condition is mostly due to the blade angle being higher than it would be at the true cruise rpm.

Additional Comments. There are other features in the oil patterns that are secondary and will be discussed briefly. The trailing edge streaks that are apparent for many of the cases (Figs. 7*c*, 7*e*, 10*e*, 10*g*, etc.) are not shocks since the Mach numbers are too low but may indicate either transition, separation, or a trailing edge vortex. This has not yet been resolved. The wedges (Figs. 7*a*, 7*f*, 10*h*, etc.) that appear frequently on the surface opposite the vortex are believed to be transition wedges because: (*a*) The Reynolds number is in the right range (between 100,000 and 1,000,000 based on chord) and (*b*) the streaks crossing the wedge always point more toward the trailing edge inside the wedge than the streaks on either side, which is consistent with a turbulent boundary layer having a higher shear than a laminar one. Although these two features are interesting, they may not be of practical importance as a full-size design will have a higher Reynolds number and therefore may not show these. The primary leading edge vortex, on the other hand, is known to be fairly insensitive to Reynolds number, and in full size should be quite similar to that found in the model.

For wings the effect of the leading edge and tip edge vortex has been successfully calculated. In 1966 Polhamus [8] presented a method that simply assumed that the leading edge thrust developed in potential flow would be oriented normal to the chord, as shown in Fig. 2, when the flow was separated. This method, called the leading-edge-suction analogy, gives results that are quite good when compared to test data for delta wings. An example of this is shown in Fig. 11. He later extended this work to account for the changes in drag due to the rotation of this force [9]. Lamar [10] expanded on this work by extending it to the side edge. For configurations such as cropped delta wings this bridged the gap between test and theory. An example of this is shown in Fig. 12. If the analogy were to be applied to the prop-fan blades, at windmill the extra lift would be negative since the vortex is on the lower surface, at design there would be no change since there should be no vortex, and at low *J* (high rpm and loading) the extra lift would be positive since the vortex is on the upper surface. This would increase the slope of the power coefficient with *J*, thus causing the agreement between test and theory to improve.

Summary and Conclusions

A flow visualization study was conducted on prop-fan blades at conditions representing takeoff and simulating cruise. It was found that oil flow visualization indicated a leading edge vortex that was substantial for some conditions, such as takeoff. The leading edge vortex appeared on the lower surface for cases with negative leading edge loading and on the upper surface for cases with highly positive leading edge loading. A vortex-free condition was found at each blade angle tested. At the takeoff blade angle of 39.78 deg this condition was achieved at a higher *J* than the takeoff *J*. For most cases tested the leading edge vortex merged with a tip vortex. A lifting surface analysis program indicated high leading edge loading when the flow visualization indicated a leading edge vortex. The test results presented here constitute the first systematic study of the phenomenon.

Acknowledgments

The authors would like to acknowledge Donald Hanson of Hamilton Standard for recognizing the existence of the leading edge vortex on prop-fan blades and initiating a program to study it and Greg Tillman of UTRC for helping to develop the oil/tracer technique for this application.

References

1 Hanson, D. B., "Compressible Helicoidal Surface Theory for Propeller Aerodynamics and Noise," *AIAA Journal*, Vol. 21, 1983, pp. 881–889.

2 Hanson, D. B., "Propeller Noise Caused by Blade Tip Radial Forces," AIAA Paper No. 86-1892, 1986.

3 Earnshaw, P. B., and Lawford, J. A., "Low-Speed Wind-Tunnel Experiments on a Series of Sharp-Edged Delta Wings," R.&M. No. 3424, Mar. 1964.

4 Kulfan, R. M., "Wing Geometry Effects on Leading Edge Vortices," AIAA Paper No. 79-1872, 1979.

5 Verhaagen, N. G., "An Experimental Investigation of the Vortex Flow Over Delta and Double-Delta Wings at Low Speed," AGARD Conference Proceedings No. 342, *Aerodynamics of Vortical Type Flows in Three Dimensions*, Reference 7, 1983.

6 Lambourne, N. C., and Bryer, D. W., "Bursting of Leading-Edge Vortices – Some Observations and Discussion of the Phenomenon," R.&M. No. 3282, Apr. 1961.

7 Yuasa, H., and Ishii, N., "Leading-Edge Separating Vortex and Pressure Distributions on Propeller Blades," *Proceedings of the Second International Symposium on Flow Visualization*, Bochum, West Germany, Sept. 1980, pp. 256–260; Hemisphere Publishing Corp., New York, 1982.

8 Polhamus, E. C., "A Concept of the Vortex Lift of Sharp-Edge Delta Wings Based on a Leading-Edge-Suction Analogy," NASA TN D-3767, Dec. 1966.

9 Polhamus, E. C., "Application of the Leading-Edge-Suction Analogy of Vortex Lift to the Drag Due to Lift of Sharp-Edge Delta Wings," NASA TN D-4739, Aug. 1968.

10 Lamar, J. E., "Extension of Leading-Edge-Suction Analogy to Wings With Separated Flow Around the Side Edges at Subsonic Speeds," NASA TR R-428, Oct. 1974.

M. Nallasamy
Sverdrup Technology, Inc.,
NASA Lewis Research Center,
Cleveland, OH 44135

B. J. Clark

J. F. Groeneweg

NASA Lewis Research Center,
Cleveland, OH 44135

Euler Analysis of the Three-Dimensional Flow Field of a High-Speed Propeller: Boundary Condition Effects

This paper presents the results of an investigation of the effects of far field boundary conditions on the solution of the three-dimensional Euler equations governing the flow field of a high-speed single rotation propeller. The results show that the solutions obtained with the nonreflecting boundary conditions are in good agreement with experimental data. The specification of nonreflecting boundary conditions is effective in reducing the dependence of the solution on the location of the far field boundary. Details of the flow field within the blade passage and the tip vortex are presented. The dependence of the computed power coefficient on the blade setting angle is examined.

Introduction

Advanced high-speed propellers with transonic helical tip Mach numbers are being developed for fuel efficient passenger aircraft to operate in the speed range of the current turbofan-powered aircraft. High-speed propellers incorporate many features which are quite different from low-speed ones. Advanced propellers employ eight or ten highly loaded, low aspect ratio, thin and highly swept blades (Fig. 1) to obtain high propulsive efficiency and to reduce noise radiation. To optimize the design of high-speed propellers in terms of the aerodynamic and aeroacoustic considerations, a knowledge of the complex flow field is essential. Experimental, analytical, and numerical approaches are being developed to define and analyze the flow field of an advanced high-speed propeller (Mikkelson et al., 1985).

The design procedure for advanced high-speed propellers employs the Goldstein type lifting line analysis modified to account for blade sweep, spanwise variation of blade loading, and blade-nacelle interaction (Rohrbach et al., 1982). For a detailed analysis and understanding of the high-speed propeller flow field, lifting surface analyses are used. The lifting surface analysis used in a full numerical approach to the understanding of the propeller flow field is either a potential flow analysis or an Euler analysis. The potential flow analysis solves the transonic potential equation and requires the specification of wake location. The potential flow solution has been extensively used in aerodynamic analysis. The assumption of potential flow is, however, not strictly correct when shock waves are present. A correct description of the inviscid transonic flow can be obtained by solving the three-dimensional Euler equations. These equations allow entropy rise through the shock waves while conserving mass, momentum, and energy. The Euler formulation provides for the treatment of rotational flows including vortices and strong shock effects. It has been reported that the solution of Euler equations has produced a reasonable description of leading edge vortex and vortex wake behavior (Rizzetta and Shang, 1986; Grinstein et al., 1986). The solutions of three-dimensional Euler equations have been found very useful in analyzing complex flows in turbomachines. Recently, they have also been employed to describe the flow fields of high-speed single-rotation (Barton et al., 1985; Clark and Scott, 1986) and counterrotation (Celestina et al., 1986) propellers.

The time-dependent Euler equations admit an infinite

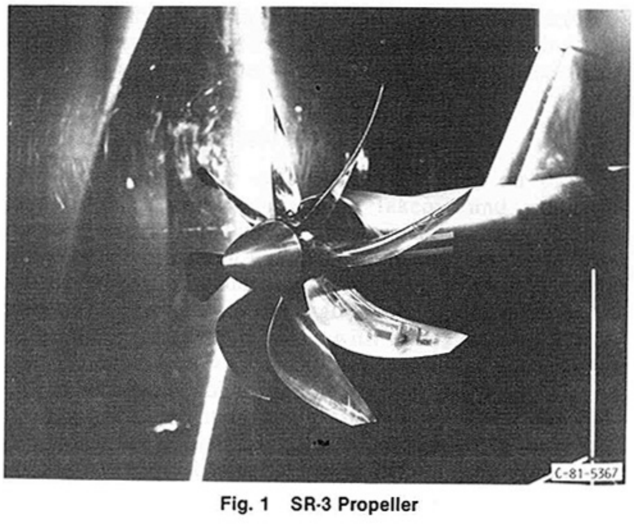

Fig. 1 SR-3 Propeller

Contributed by the Gas Turbine Division of The American Society of Mechanical Engineers and presented at the 32nd International Gas Turbine Conference and Exhibit, Anaheim, California, May 31–June 4, 1987. Manuscript received at ASME Headquarters February 24, 1987. Paper No. 87-GT-253.

number of solutions, each one defined by a set of initial and boundary conditions. Initial conditions remaining the same, any change in the boundary condition will produce a new solution. The specification of the boundary conditions for the time-dependent Euler equations governing the flow in an infinite domain, such as that of a propeller, needs careful consideration. The numerical solution of the differential equations governing the propeller flow field can be carried out in one of three ways:

1 Transform the infinite domain to a finite domain and specify the free-stream conditions at the far field boundary;

2 place the far field boundary at a distance sufficiently far away from the solid surface and specify the free-stream conditions on this boundary; or

3 place the boundary at a finite distance but relatively close to the region of interest, to keep the number of grid points and hence the computing time within limits. The boundary condition on this boundary then should be modified.

Option 3 is desirable in many respects particularly in terms of grid resolution and accuracy of the solution in the region of interest. However, boundary condition modification becomes complicated for three-dimensional flows. Simplified nonreflecting boundary conditions are often employed.

The aim of this paper is to study the sensitivity of the three-dimensional Euler predictions to far field boundary conditions. The present investigation considers the application of a simplified nonreflecting far field boundary condition and the effect of the location of the far field boundary in the Euler analysis of a propeller flow field. The solution obtained with the simplified far field boundary condition is found to be in good agreement with experimental data and published Euler analyses. The specification of a nonreflecting boundary condition is shown to be effective in reducing the dependence of the solution on the location of the far field boundary.

Numerical Treatment of Far Field Boundary Conditions

Several investigators have studied the effect of far field boundary conditions on the solution of Euler equations. The excellent study of boundary conditions for supersonic flows by Abbett (1973) clearly pointed out that the characteristic type schemes at boundaries tended to result in optimum accuracy. Approaches developed to reduce the influence of the location of the far field boundary and the boundary condition specified there on the solution of transonic flows include:

1 A far field boundary condition based on an expansion that is asymptotic in distance from an arbitrary origin, developed by Thomas and Salas (1986) and Bayliss and Turkel (1980).

2 Construction of a pseudo-differential operator which exactly annihilates the outgoing waves, developed by Engquist and Mazda (1981).

3 Rudi and Strikwerda's (1980) boundary condition in which the pressure at the outflow section is effectively relaxed to its correct value, using an arbitrary parameter.

4 Characteristic variable/Riemann invariant specification at the boundary developed by Morretti (1980), Jameson and Baker (1983), and others (for example, Celestina et al., 1986).

Kwak (1980) tested several of these boundary conditions on the time-dependent small disturbance equation for the flow over an airfoil and came to the conclusion that the characteristic condition is the most effective one in reducing the size of the computational domain and in accelerating convergence. The study of Berry (1984) on the effect of boundary conditions on the solution of two-dimensional Euler equations for the flow over an airfoil showed that the characteristic variable specification at the far field boundary produced the highest rate of convergence. An excellent description of the basis and the formulation of the characteristic boundary conditions for one-dimensional flow and extensions to multidimensional flows are given by Morretti (1980). To reduce the complexity and effort involved in the treatment of the far field boundary for three-dimensional flows, often it is treated by employing a local one-dimensional approximation and specifying characteristic variables at the boundary (Celestina et al., 1986; Jameson and Baker, 1983; Berry, 1984). Such a boundary condition is perfectly nonreflecting to waves in one dimension and to waves at normal incidence in two dimensions (Headstrom, 1979). The ideal boundary treatment should take into account all outgoing waves and assure transmission of all waves. Such a technique is described by Erdos et al. (1977). This technique is, however, too involved and time consuming and is not employed in practice. In this paper, we shall be concerned only with a local one-dimensional approximation technique (item 4 above).

Motivation

Clark and Scott (1986) employed Denton's (1980) time marching method, which is a finite-volume method developed for turbomachinery flow analysis, to solve the flow field of a high-speed propeller. They modified Denton's computer program to accommodate the far field boundary of the propeller flow field. They specified the far field boundary at a distance of two blade radii from the axis of the propeller and implemented the slip wall boundary conditions there. It has been argued that such a wall boundary specification for a propeller flow in an infinite domain could produce significant errors in

Nomenclature

$\bar{A}$ = area vector of face of element
C^+ = outgoing characteristic value
C^- = incoming characteristic value
C_p = power coefficient = $P/\rho_\infty \eta^3 D^5$
C_{Th} = thrust coefficient = $Th/\rho_\infty \eta^2 D^4$
c = sonic velocity
c_p = specific heat at constant pressure
D = blade (tip) diameter
dC_{Th}/dx = elemental thrust coefficient
dc_p/dx = elemental power coefficient
E = specific internal energy
H = specific stagnation enthalpy
$\bar{i}$ = unit vector
J = advance ratio
M = Mach number
n = rotational speed, revolutions per second
P = power
p = static pressure
R = gas constant
R_t = blade (tip) radius
T = static temperature
Th = thrust
t = time
$\bar{V}$ = velocity vector
Vol = volume of element
X = fractional radius
z, r, θ = cylindrical coordinates
$\beta_{3/4}$ = blade angle at 0.75 blade radius
γ = ratio of specific heats
$\Delta(\ )$ = change in a property in a time step
ρ = fluid density
Ω = rotational speed

Subscripts

e = extrapolated value
z, r, θ = in coordinate directions
∞ = at free-stream condition

the computed blade pressure distributions which are the input needed for acoustic computations. The importance of an accurate description of the blade pressure distributions has motivated the present study of the effect of far field boundary conditions on the Euler solution of the propeller flow field. In this paper we consider three different far field boundary conditions. They are the *free-stream condition*, *solid wall boundary condition*, and a *nonreflecting boundary condition*. These conditions are incorporated into the Denton computer program and the solutions are compared.

The experimental data on the high-speed propeller flow field are very limited. Use of the data is difficult because of the uncertainties in the dynamic blade shape. In this paper, the *sensitivity of the numerical solution to the blade-setting angle* is studied. In addition to the far field boundary condition, the study examines the effect of location of the far field boundary and nonreflecting boundary conditions at the inlet/exit sections.

Governing Equations. The governing equations describing the inviscid flow field of the propeller are the three-dimensional Euler equations, expressing the conservation of mass, momenta, and energy. It is convenient to work with absolute quantities, writing the equations in a coordinate frame rotating with the blade, so that centrifugal and Coriolis forces can be represented as body forces acting on each element. The equations are written in the form (Denton, 1980)

Continuity

$$\text{Vol}\,\Delta\rho=\Delta t\sum\rho\bar{V}\cdot\bar{A}+\Omega\frac{\partial\rho}{\partial\theta}\,\Delta t\,\text{Vol} \qquad (1)$$

Axial momentum

$$\text{Vol}\,\Delta(\rho V_Z)=\Delta t\sum(p\bar{i}_Z\cdot\bar{A}+\rho V_Z\bar{V}\cdot\bar{A})+\Omega\frac{\partial}{\partial\theta}(\rho V_Z)\,\Delta t\,\text{Vol} \qquad (2)$$

Radial momentum

$$\text{Vol}\,\Delta(\rho V_r)=\Delta t\sum(p\bar{i}_r\cdot\bar{A}+\rho V_r\bar{V}\cdot\bar{A})+\Omega\frac{\partial}{\partial\theta}(\rho V_r)\,\Delta t\,\text{Vol} \qquad (3)$$

Angular momentum

$$\text{Vol}\,\Delta(\rho rV_\theta)=\Delta t\sum(pr\bar{i}_\theta\cdot\bar{A}+\rho rV_\theta\bar{V}\cdot\bar{A})+\Omega\frac{\partial}{\partial\theta}(\rho rV_\theta)\,\Delta t\,\text{Vol} \qquad (4)$$

Energy

$$\text{Vol}\,\Delta(\rho E)=\Delta t\sum(\rho H\nabla\cdot\bar{A})+\Omega\frac{\partial}{\partial\theta}(\rho E)\,\Delta t\,\text{Vol} \qquad (5)$$

These equations are solved in conjunction with the perfect gas relationships

$$p=\rho RT \qquad (6)$$

$$H=C_pT+\frac{1}{2}V^2 \qquad (7)$$

$$\rho E=\frac{p}{\gamma-1}+\frac{1}{2}\rho V^2 \qquad (8)$$

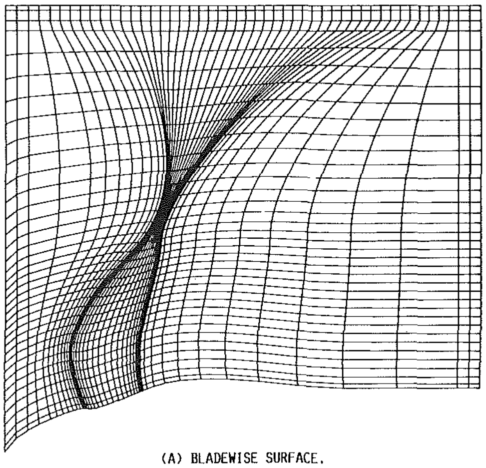

(A) BLADEWISE SURFACE.

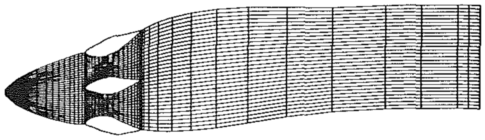

(B) STREAMWISE SURFACE.

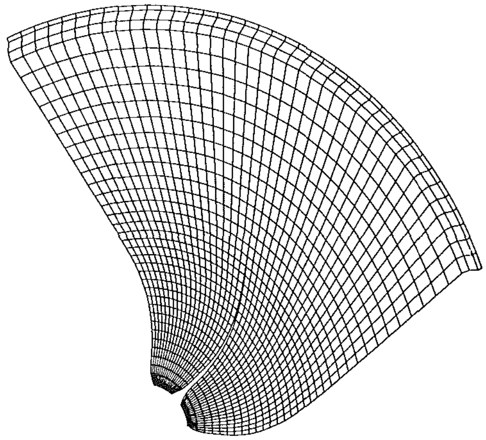

(C) SPANWISE SURFACE.

Fig. 2 Computational grid

Computational Grid. The governing equations are solved in the physical domain on a grid generated algebraically. The flow domain is discretized using three kinds of surfaces. The bladewise surfaces are evenly spaced and are limited by the suction side of one blade and pressure side of the adjacent one (Fig. 2*a*). In the figure the outer boundary is at a distance $2R_t$ from the axis of the spinner. The streamwise surfaces are variably spaced along the spanwise direction and are limited by the spinner/nacelle surface and the outer boundary (Fig. 2*b*). The spanwise (quasi-orthogonal) surfaces are variably spaced along the axial direction depending on the region, leading edge, trailing edge, blade surface, inlet or exit, and are limited by the inlet and exit planes. The computational nodes are located at the corners of each volume element defined by the streamwise, bladewise, and spanwise surfaces. The fluxes of mass, momenta, and energy through each face are calculated using the averages of the flow properties stored at the corners of that face.

Numerical Technique. Denton's explicit time marching method employs what is called an opposed difference scheme. The scheme uses upwind differences for fluxes of mass and momenta, and downwind differences for pressure, in the streamwise direction. The derivatives in the circumferential direction are evaluated using central differences. The time marching method uses a time step such that the Courant number is close to unity. The method itself ensures stability by solving the flow equations in the order of continuity – energy – momentum. The procedure is as follows:

1 For each time step and each control volume the continuity equation is used to find the new density associated with each grid point.

2 The energy equation is solved to yield new energy using the densities of the previous time step.

3 The new density is then used along with the velocities and energy from the previous time step to compute new pressures.

4 The velocities are then updated using the momentum equations with the new pressures and densities.

A variable time step appropriate for each volume element is used to accelerate convergence. The method is of first-order accuracy and is modified to achieve greater accuracy by adding a lagged correction factor to correct the upwind pressure to a value close to the true one. The scheme uses no explicit artificial viscosity. Only a smoothing is used after each time step to smooth out any waviness in the circumferential direction. The convergence is judged on the basis of mass conservation and the maximum change in the axial velocity component.

Initial and Boundary Conditions. The Euler equations governing the flow field of the propeller have to be solved in conjunction with appropriate initial and boundary conditions of the flow. Since the steady flow solution is of interest here, the initial conditions need be only approximate. The boundary conditions that need to be specified depend on the flow Mach number. The absolute flow entering and leaving the computational domain is assumed subsonic.

The effect of far field boundary condition on the blade pressure distribution is of main concern in the present study. The boundary conditions considered are:

1 Wall boundary conditions. The wall boundary condition requires that the mass flux through the surface be zero and the velocity normal to the surface be zero. The implementation of this condition is the same as that of Denton (1980) and Clark and Scott (1986). That is, the mass flux through the far field boundary is simply set to zero and the velocity components and density at this boundary are calculated using the changes in values at two points adjacent to the boundary. The pressure at the boundary is computed as for any inner field point.

2 Free-stream boundary condition. The free-stream static pressure, velocity components, and density are specified at the far field boundary.

3 A nonreflecting boundary condition based on a local one-dimensional flow approximation and specification of the characteristic variable normal to the boundary. Assuming a fixed incoming characteristic C^-

$$C^- = V_\infty - \frac{2C_\infty}{\gamma - 1} \tag{9a}$$

The outgoing characteristic C^+ is extrapolated from the interior of the computational domain

$$C^+ = V_e + \frac{2C_e}{\gamma - 1} \tag{9b}$$

From the Riemann invariants we can write

$$V_r = \frac{1}{2}(C^+ + C^-) \tag{10}$$

$$c = \frac{\gamma - 1}{4}(C^+ - C^-) \tag{11}$$

where V_r and c are the normal velocity and speed of sound to be specified at the far field boundary. The entropy is extrapolated (from points inside the computational domain adjacent to the boundary) or set equal to the free-stream value depending on the direction of the radial velocity. The density, energy, and pressure are calculated from the speed of sound and entropy. Depending on the direction of the radial velocity, the axial velocity at the boundary point is computed using either the axial velocity of the free stream or the axial velocity at the point adjacent to the boundary inside the computational domain. The tangential velocity component is extrapolated from the point adjacent to the boundary.

A periodicity condition is imposed ahead and downstream of the blade from hub to outer boundary and beyond the blade tip in the blade region. On the solid surfaces the mass flux through the surface is set to zero. At the inlet boundary the relative stagnation temperature, pressure, and flow angle are specified. The axial velocity is computed from the characteristic boundary condition. The upstream running characteristic C^- is extrapolated from the interior of the computational domain. Then using the specified total temperature and C^- the total inlet velocity is computed from isentropic relations. The individual velocity components are computed from geometric relations while density and pressure are calculated from isentropic relations. At the downstream boundary the static pressure is specified at the far field boundary. The radial variation of the static pressure satisfying the radial equilibrium is computed from

$$\frac{\partial p}{\partial r} = \frac{\rho V_\theta^2}{r} \tag{12}$$

Here V_θ and ρ are the extrapolated values from the interior of the domain. The downstream running characteristic C^+ is also extrapolated. The final density and speed of sound are calculated from isentropic relations. The exit axial velocity is computed from the extrapolated C^+ characteristic.

Results and Discussion

Solutions for the SR-3 propeller flow field have been obtained with three different far field boundary conditions, with the boundary located at twice the blade radius from the axis of the propeller. This boundary location was chosen primarily to assess the effects of wall boundary condition specified at the same location by Clark and Scott (1986). The computations have been carried out for the design conditions of the SR-3 propeller, $J = 3.06$, $M = 0.8$, and $\beta_{3/4} = 61.3$ deg. Results obtained with the three boundary conditions – wall boundary condition, free-stream boundary condition, and the nonreflecting boundary condition – are compared with each other and with experimental data where possible. The effect of location of the far field boundary and details of the propeller flow field are also examined. An accurate description of the pressures on the blade surfaces is essential as they are the input needed for acoustic computations. The effects of the far field boundary conditions are shown in the chordwise pressure distributions plotted in Fig. 3. The figure shows blade surface pressures at 21, 53, 84, and 100 percent span heights. First, it is observed that there exists an appreciable difference between the solutions obtained with the wall boundary condition and nonreflecting boundary condition. The large difference stems from the pressure rise introduced due to the confining wall boundary. The differences in pressures between nonreflecting and free-stream conditions are appreciable only at 84 and 100 percent locations. It is to be noted that only with the nonreflecting boundary condition are the computed solutions in good agreement with experimental data as discussed below.

Figure 4 shows the spanwise variation of the elemental power coefficient dc_p/dx obtained with the three boundary conditions. Also shown for comparison are the experimental data (Mikkelson et al., 1985) and the results of the lifting line analysis of the design condition (Rohrbach et al., 1982). The curve for the nonreflecting boundary condition shows good agreement with the experimental data. The variation of the

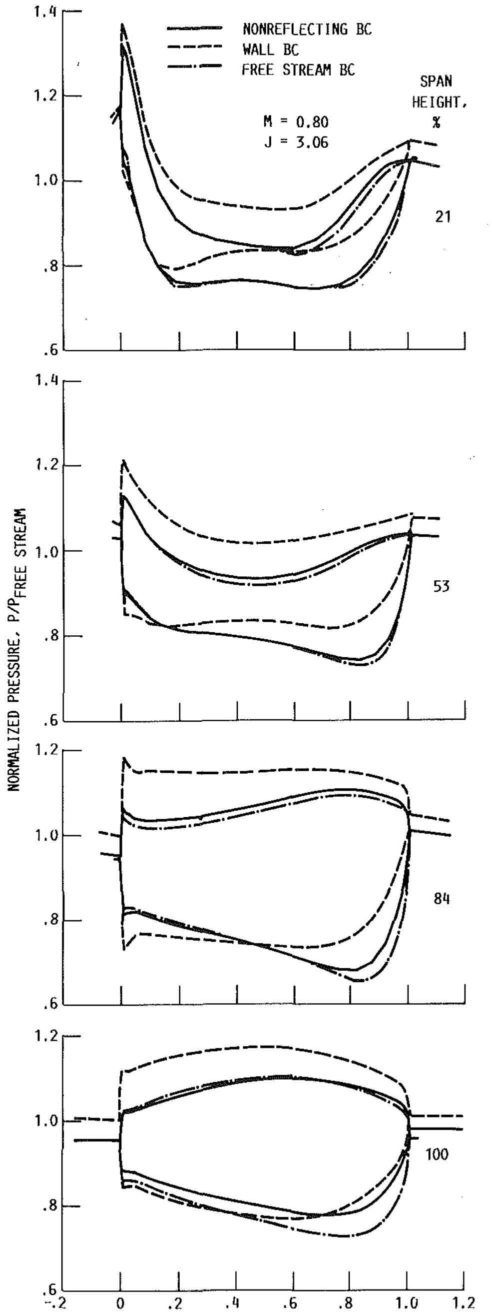

Fig. 3 Computed blade pressure distribution

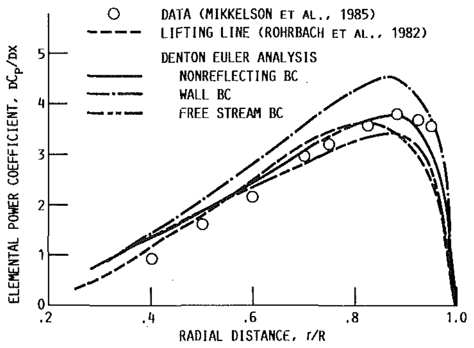

Fig. 4 Elemental power coefficient

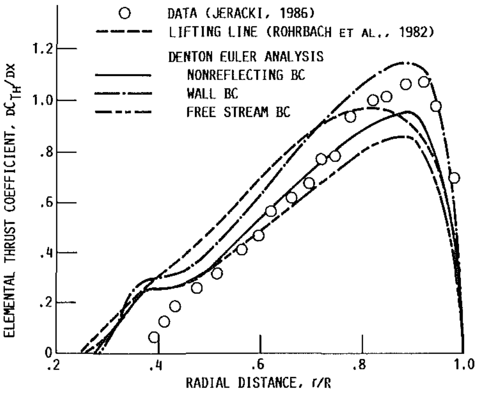

Fig. 5 Elemental thrust coefficient

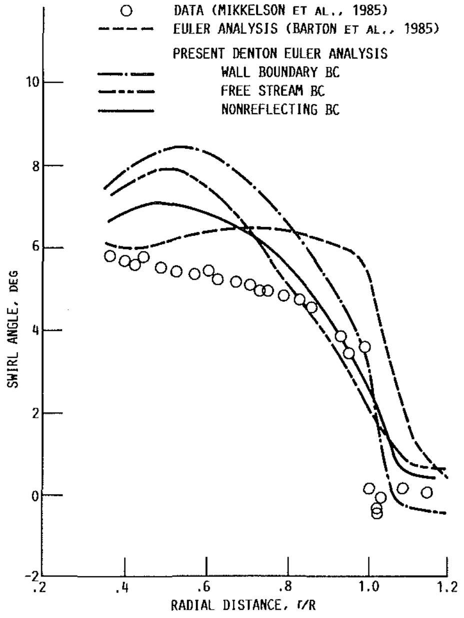

Fig. 6 Swirl angle comparisons at 0.21 diameter downstream

elemental power coefficient above 50 percent span height including the location of the peak power coefficient is well predicted. The Euler predictions near the blade root are poor in all cases. The lifting line analysis predicts well near the blade root but the prediction in the region of peak power coefficient is poor.

The spanwise variation of the elemental thrust coefficient dc_{TH}/dx is shown in Fig. 5. As before the curve for the nonreflecting boundary condition shows good overall agreement with experimental data (Jeracki, 1986). All of the three Euler predictions and the lifting line analysis significantly overpredict near the blade root region. The present results show a "transition" region in the predicted elemental thrust coefficient curve, which corresponds to the region of blade shape transition. The SR-3 propeller design incorporates airfoil sections of NACA series 16 from tip to 53 percent radius and NACA series 65 circular arc camber lines from 37 percent radius to the root with a transition fairing between. Detailed examination of projected areas of the blade elements gave no indication of a transition. Limited runs made with different grid densities did not alter the shape of the elemental thrust curve. Although the experimental data indicate a change in slope of the curve, they do not show a distinct transition region as in the predictions. It should be noted here that the measurement of the elemental thrust coefficient is not as direct as the power coefficient. The experimental data shown in Fig. 5 have been scaled to match the measured total thrust coefficient.

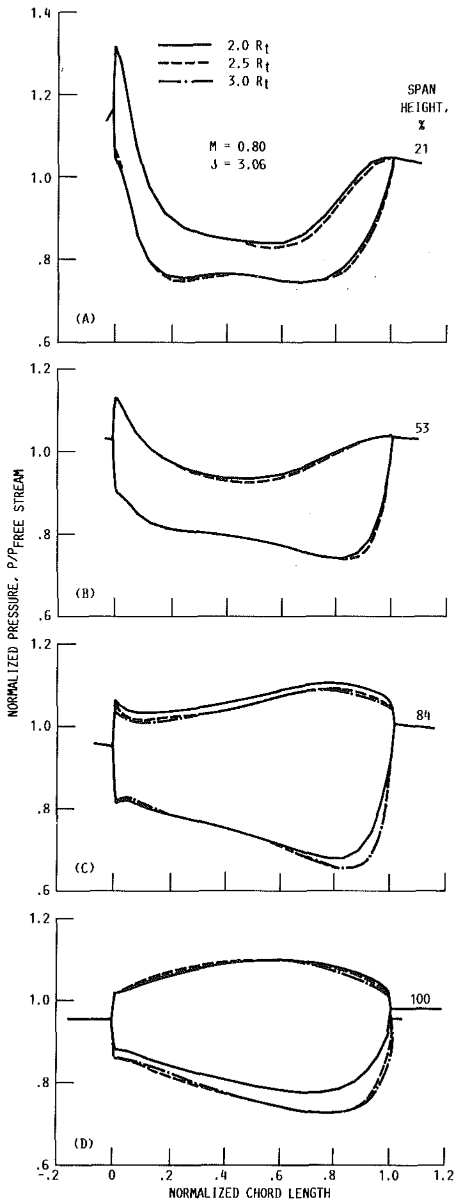

Fig. 7 Effect of location of far field boundary on computed blade pressure distribution

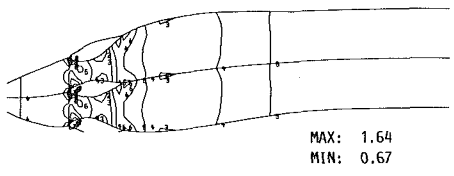

(A) HUB.

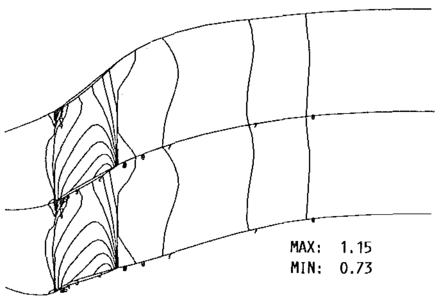

(B) MIDSPAN.

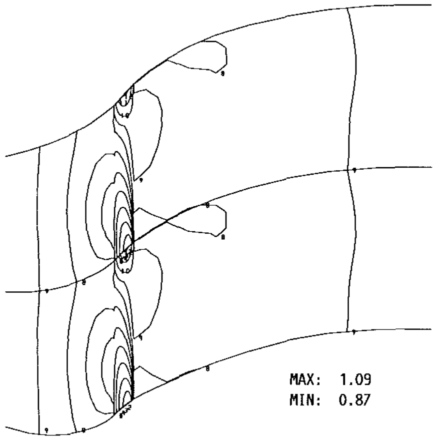

(C) TIP.

Fig. 8 Computed pressure distribution on streamwise surfaces, M = 0.8, J = 3.06

Another quantity of interest is the flow swirl angle downstream of the blade. Figure 6 shows the swirl angles predicted in the present study along with experimental data and predictions of Barton et al. (1985). (The Euler analysis of Barton et al., 1985, specifies free-stream conditions at the far field boundary located at nine radii from the axis of the propeller.) Use of the nonreflecting boundary condition tends to move the predicted swirl angles closer to the data.

The sensitivity to the choice of far field boundary location is small when the boundary is nonreflecting. Figure 7 shows pressure distributions for three boundary locations, namely, $2R_t$, $2.5R_t$, and $3R_t$. Results indicate that a noticeable difference in pressures obtained with the far field boundary located at 2 and $2.5R_t$ occurs at 84 percent span height and at the blade tip. However, the total power coefficient changes by only about 3 percent. The difference between the blade pressures obtained with the far field boundary at $2.5R_t$ and $3R_t$ is negligible indicating that $2.5R_t$ is sufficiently far when the nonreflecting boundary condition is used. Since the total power coefficient change in moving the far field boundary from $2R_t$ to $2.5R_t$ is small, comparisons with data are made with the boundary at $2R_t$ as in the paper of Clark and Scott. It may be noted here that the comparison has been carried out with the same number of grid points in the radial direction. After the implementation of the nonreflecting boundary condition at the far field, incorporation of the nonreflecting boundary conditions at the inlet/exit does not produce any noticeable difference in blade pressure distributions. For one- and two-dimensional flows, implementation of the nonreflecting far field boundary condition has been found to accelerate the convergence rate (Rudi and Strikwerda, 1980; Berry, 1984) of the solution to steady state. In the present computations only a 10 to 20 percent reduction in the number of iterations has been noted with the nonreflecting boundary conditions.

We have observed that the solution obtained with the nonreflecting boundary condition is in reasonably good agreement with experimental data. It is then instructive to examine the complete flow field provided by this solution. The contour plots of pressures in the blade passages are shown in Figs. 8 and 9. The figures show contour plots for two adjacent blade passages to aid understanding of the flow field. Figure 8 shows pressure contours at the blade root, midspan, and blade tip. The contours show the highly three-dimensional nature of the flow within blade passages. The blade-nacelle interaction effects are reflected in the contours at the blade root (Fig. 8*a*). The predicted flow is in qualitative agreement with other predictions and experiments summarized by Mikkelson et al.

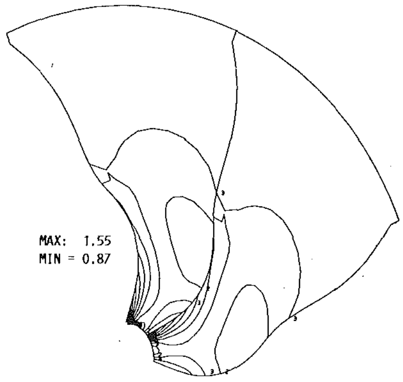

(A) LEADING EDGE.

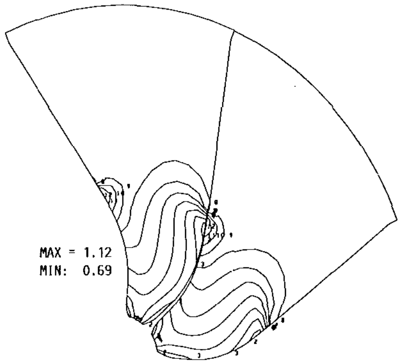

(B) MIDCHORD.

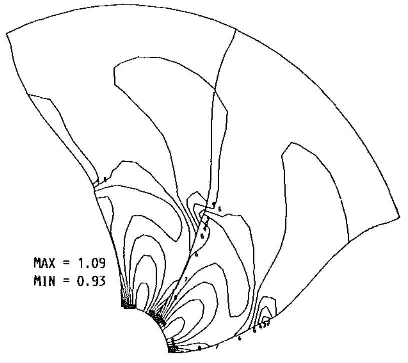

(C) TRAILING EDGE.

Fig. 9 Computed pressure distribution on spanwise surfaces, $M = 0.8$, $J = 3.06$

(1985). The pressure distributions at three axial stations, namely, leading edge, midchord, and trailing edge are shown in Fig. 9. The pressure contours at the trailing edge (Fig. 9*c*) indicate the propagation of pressure waves from the blade tip as pictured in color graphics by Adamczyk (1986). The midchord section contours show the nature of the pressure differential existing between the two sides of the blade.

Figure 10 shows the vorticity contours at two axial stations downstream of the trailing edge. Of particular interest are the vorticity contours in the tip region. One can observe the movement of the center of the vortex (marked by $\Delta\theta$ in Fig. 10*b*) in the direction of rotation of the blades. Such a displacement of the vortex from the blade wake has been observed in laser Doppler measurements of the high-speed propeller flow field (Neumann et al., 1983). It is attributed to the tip vortex rollup. One can also notice diffusion of vortex with axial distance, due to numerical diffusion. However, the fact that Euler solutions do provide a reasonable description of the vortex wake and leading edge vortex flows has been observed by many investigators (for example Rizzetta and Shang, 1986; Grinstein et al., 1986). Recently, Hanson (1986) estimated the noise produced by the radial forces associated with the tip vortex of a high-speed propeller.

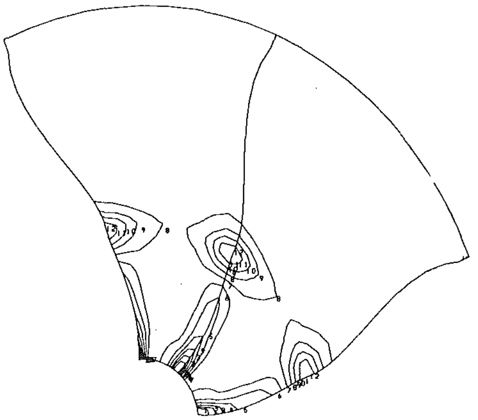

(A) $\omega_C = 2.25$.

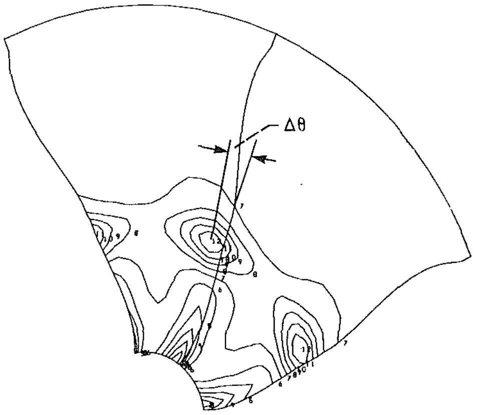

(B) $\omega_C = 1.82$.

Fig. 10 Computed vorticity distributions; ω_C = vorticity at the vortex center

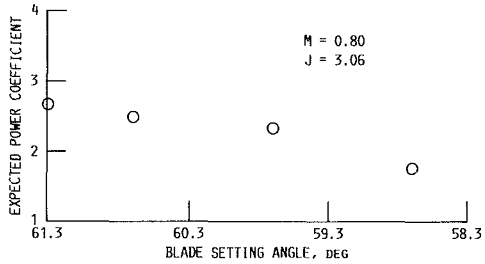

Fig. 11 Effect of blade setting angle

Experimental data on high-speed propellers indicate a strong dependence of the total power coefficient on the blade shape. It is difficult to determine precisely the dynamic blade shape. Here, the sensitivity of the numerical solution to the blade setting angle is examined. The design blade angle of the SR-3 propeller at 3/4 radius is 61.3 deg, which untwists to 58.7 deg, with centrifugal loading at design speed. The computations reported in this paper are with a blade angle of 58.7 deg, allowing for the dynamic untwist. The dependence of the computed power coefficient on the blade setting angle is shown in Fig. 11. It is seen that the power coefficient depends strongly on the blade setting angle (or the estimated untwist). Such a dependence has been observed in experiments (Rohrbach et al., 1982) and other Euler analysis (Barton et al., 1985).

Conclusions

The solution of the three-dimensional Euler equations governing the flow field of a high-speed propeller with nonreflecting boundary conditions yields results which are in fairly good agreement with experimental data. The solution obtained with the wall boundary condition at the far field overpredicts the blade loading in the region of the peak by as much as 20 percent. The resulting overprediction in the total power coefficient is about 14 percent. The study also shows that with the specification of the nonreflecting boundary condition, the far field boundary can be located as close as 2.5 blade radii from the axis of the propeller without affecting the computed solution.

Acknowledgments

The authors wish to acknowledge the helpful discussions with Messrs. M. Celestina and R. Jeracki and Drs. C. J. Miller, L. Bober, and J. Adamczyk during the present investigation.

References

Abbett, M. J., 1973, "Boundary Condition Calculation Procedures for Inviscid Supersonic Flow Fields," *Computational Fluid Dynamics Conference*, AIAA, New York, pp. 153–172.

Adamczyk, J. J., 1986, Private Communication.

Barton, J. M., Yamamoto, O., and Bober, L. J., 1985, "Inviscid Analysis of Advanced Turboprop Propeller Flow Fields," AIAA Paper No. 85-1263.

Bayliss, A., and Turkel, E., 1980, "Radiation Boundary Conditions for Wave Like Equations," *Communications in Pure and Applied Mathematics*, Vol. 33, pp. 707–725.

Berry, P. E., 1984, "Computation of Unsteady Flow in a Blade Passage," in: *Unsteady Aerodynamics of Turbomachines and Propellers*, D. S. Whitehead, ed., University of Cambridge, Cambridge, England, pp. 191–203.

Celestina, M. L., Mulac, R. A., and Adamzyck, J. J., 1986, "A Numerical Simulation of the Inviscid Flow Through a Counter-rotating Propeller," NASA TM-87200.

Clark, B. J., and Scott, J. R., 1986, "Coupled Aerodynamic and Acoustical Prediction of Turboprops," NASA TM-87094.

Denton, J. D., 1980, "Time Marching Methods for Turbomachinery Flow Calculations," in: *Numerical Methods in Applied Fluid Dynamics*, B. Hunt, ed., Academic Press, New York, pp. 473–493.

Engquist, B., and Mazda, A., 1981, "Numerical Radiation Boundary Conditions for Unsteady Transonic Flow," *Journal of Computational Physics*, Vol. 40, No. 1, pp. 91–103.

Erdos, J. I., Alzner, E., and Kalben, P., 1977, "Computation of Steady and Periodic Two-Dimensional Nonlinear Transonic Flows in Fan and Compressor Stages," in: *Transonic Flow Problems in Turbomachinery*, T. C. Adamson and M. F. Platzer, eds., Hemisphere Publishing Corp., Washington, pp. 95–111.

Grinstein, F. F., Oran, E. S., and Boris, J. P., 1986, "Numerical Simulations of Asymmetric Mixing in Planar Shear Flows," *Journal of Fluid Mechanics*, Vol. 165, pp. 201–220.

Hanson, D. B., 1986, "Propeller Noise Caused by Blade Tip Radial Forces," AIAA Paper No. 86-1892.

Headstrom, G. W., 1979, "Nonreflecting Boundary Conditions for Nonlinear Hyperbolic Systems," *Journal of Computational Physics*, Vol. 30, No. 2, pp. 222–237.

Jameson, A., and Baker, T. J., 1983, "Solution of the Euler Equations for Complex Configurations," AIAA Paper No. 83-1929.

Jeracki, R. J., 1986, unpublished data.

Kwak, D., 1980, "Nonreflecting Far Field Boundary Condition for Unsteady Transonic Flow Computation,'" AIAA Paper No. 80-1393.

Mikkelson, D. C., Mitchell, G. R., and Bober, L., 1985, "Summary of Recent NASA Propeller Research," *Aerodynamics and Acoustics of Propellers*, AGARD CP-366, AGARD, France, pp. 12.01-12.24.

Morretti, G., 1986, "A Physical Approach to the Numerical Treatment of Boundaries in Gas Dynamics," in: *Numerical Boundary Condition Procedures*, NASA CP-2201, pp. 73–95.

Neumann, H. E., Bober, L. J., Serafini, J. S., and Chang, L. K., 1983, "An Analytical and Experimental Comparison of the Flow Field of an Advanced Swept Turboprop," AIAA Paper No. 83-0189.

Rizzetta, D. P., and Shang, J. S., 1986, "Numerical Simulation of Leading-Edge Vortex Flows," *AIAA Journal*, Vol. 24, No. 2, pp. 237-245.

Rohrbach, C., Metzger, F. B., Black, D. M., and Ladden, R. M., 1982, "Evaluation of Wind Tunnel Performance Testings of an Advanced 45 Swept Eight Bladed Propeller at Mach Numbers from 0.45 to 0.85," NASA CR-3505.

Rudi, D. H., and Strikwerda, J. C., 1980, "A Nonreflecting Out Flow Boundary Condition for Subsonic Navier-Stokes Calculations," *Journal of Computational Physics*, Vol. 36, No. 1, pp. 55–70.

Thomas, J. L., and Salas, M. D., 1986, "Far-Field Boundary Conditions for Transonic Lifting Solutions to the Euler Equations," *AIAA Journal*, Vol. 24, No. 7, pp. 1074–1080.

R. B. Ginder

W. J. Calvert

RAE Pyestock,
Farnborough, Hants, United Kingdom

The Design of an Advanced Civil Fan Rotor

A recent ASME paper by the authors described a quasi-three-dimensional calculation system for transonic compressor blade rows. The system predicts both the internal flow field and the overall performance of the blade row. It therefore enables the compressor engineer to optimize the blade shapes in order to improve the design point efficiency. This is explored in the present paper. A new type of blade profile has been developed to allow sufficient freedom for the optimization. Application to the design of a high-efficiency, transonic civil fan rotor is discussed.

Introduction

A recent paper by the authors (Calvert and Ginder, 1985) described an S1–S2 calculation system for transonic compressor blade rows. This incorporates the S1BYL2 inviscid-viscous blade-to-blade method (Calvert, 1982) and an axisymmetric streamline curvature throughflow calculation method which has calculating stations within the blade row (Ginder, 1984). This system predicts both the internal flow field and the overall performance of a blade row. It was applied to a transonic fan rotor typical of a modern, civil aeroengine, and gave encouraging agreement with test data.

The detailed insight into the blade element aerodynamics given by the prediction methods provides a basis for optimizing blade shapes to improve the aerodynamics and hence efficiency of a design. The S1–S2 system provides a particularly suitable framework for blade profile development. Once a datum S1–S2 solution has been set up (based, for example, on a conventional design of the same duty) each of a chosen number of sections up the span can be developed more or less individually. The designer can check out each step of his optimization quickly and cheaply on the blade-to-blade code. The final design may need to be tuned using the full S1–S2 system, in case the blade element operating conditions and streamtube geometry are changed. However, unless a deliberate attempt has been made to alter the shock structure and/or the radial matching, these changes should be comparatively minor. This means that concentrating on the blade-to-blade aspects is valid, and this approach is adopted in the present paper.

The considerations involved in blade profile optimization, for the particular case of a transonic fan rotor, form the main subject matter of the paper. After briefly describing the blade-to-blade code (the accuracy of which is crucial to studies of this kind), the paper outlines a new type of blade profile which was specially developed for transonic fan rotors. It then discusses some of the main aerodynamic design aspects for such blade rows. These are: (*i*) precompression; (*ii*) incidence in supersonic inlet flow; and (*iii*) distribution of camber in the covered passage, including its effect on the blade boundary layer. Finally, an illustration of blade profile optimization is provided by examples taken from a design exercise on a civil transonic fan rotor. Sections at three stations along the span are considered, and the optimized profiles are compared with conventional profiles to illustrate the predicted improvements.

It should be noted that optimization at a single design point only is considered in the present paper. While it is realized that off-design requirements can also influence blade profile optimization, this does not negate the blading principles outlined.

Blade-to-Blade Calculation Method

The S1 method, which is described more fully elsewhere (Calvert, 1982) is an interactive inviscid-viscous treatment. The inviscid part consists of a time-marching Euler calculation, based on that of Denton (1982) so it can handle transonic flows, including the positions and strengths of shock waves. The calculation takes place on a specified axisymmetric stream surface, and it includes the effects of rotation and of varying radius and streamtube thickness in the axial direction. The viscous calculation is an integral technique consisting of three parts to estimate laminar boundary layer development, transition point, and turbulent boundary layer development, respectively. The inviscid-viscous matching procedure allows a valid solution to be obtained even when there are regions of separated flow on the suction surface due to shock wave–boundary layer interaction or to excessive diffusion. It is worth stressing that the modeling of such regions arises solely from the inviscid-viscous interaction, no separation or reattachment criteria being needed, and the only constraint applied is that the boundary layer must be turbulent throughout such critical regions. The viscous calculations continue in the wake downstream of the bladed region until the downstream boundary of the calculation domain. A compressible flow mixing calculation is carried out on the downstream boundary to determine the profile loss and overall exit conditions (Stewart, 1955). The shock loss is derived from the entropy

---

Contributed by the Gas Turbine Division of THE AMERICAN SOCIETY OF MECHANICAL ENGINEERS and presented at the 32nd International Gas Turbine *Conference and Exhibit*, Anaheim, California, May 31–June 4, 1987. Manuscript received at ASME Headquarters February 19, 1987. Paper No. 87-GT-218.

rise in the inviscid part of the calculation with a small correction for finite differencing errors.

For application to blade rows it is apparent that some consistent way of generating additional loss has to be incorporated in order to obtain realistic losses toward the blade ends (where three-dimensional effects not modeled in the S1–S2 treatment are of practical importance). Consequently the S1 calculation has provision to include a constant drag force within the blade row, whose magnitude can be chosen as required. However, its effects are relatively small in the examples to be considered in the current paper.

The method has been applied to a wide range of cascade test cases with encouraging results (Calvert, 1983), but the application to a transonic fan rotor (Calvert and Ginder, 1985) is of greater relevance here. The rotor is typical of a modern, high bypass ratio, civil aeroengine, having a bypass pressure ratio near 1.8 at a tip speed of 450 m/s. The hub/tip ratio is low and consequently there are large spanwise variations in blade profiles and flow conditions. For example inlet relative Mach number varies from ~ 0.8 to ~ 1.5. The S1 method, used as part of an S1–S2 calculating system, gave solutions which were in good agreement with the experimental results.

This validation provides confidence that the S1 and S2 methods are suitable for use as a design system in which the blade profiles are tailored solely on the basis of the predicted aerodynamics. However some limitations of the blade-to-blade method should be recognized. For example the boundary layer calculation, and in particular the modeling of transition, is by no means exact. Also the inviscid part of the calculation tends to produce longitudinal "smearing" of shocks, so that exact shock location may be in some doubt. (In an S1–S2 approach the accurate modeling of a real-life three-dimensional shock pattern is not guaranteed.) Limitations such as these are inevitable in the present "state of the art" of compressor flow calculations, and they must be taken into account in the design process by avoiding profiles whose performance is too critically dependent on the accuracy of the prediction methods.

A New Blade Profile Type for Transonic Compressors

The use of the blade-to-blade program described above enables blade shapes to be tailored for a given duty on the basis of the predicted internal aerodynamics. A "design-by-analysis" procedure is employed with a profile generator being used to produce blade section geometry from a parametric definition. This helps ensure that the section shapes considered are mechanically sensible and also means that a range of aerodynamic operating conditions can be considered as part of the design process if required.

A new type of blade profile has been developed which gives the designer sufficient freedom to produce optimized sections for the whole span of a transonic compressor blade row. The suction surface shape is considered to be of prime importance and it is specified by up to four circular arcs. These provide the flexibility to control separately the incidence and precompression ahead of the covered passage, and the amount and distribution of camber within the passage. A circular arc definition was chosen for simplicity, and the discontinuities of curvature at the arc junctions do not, from experience, seem to cause any predicted ill effects, perhaps due to their influence being swamped by the relatively large pressure gradients existing over much of any suction surface. The pressure surface is formed by two cubics joining at the maximum thickness point and having continuous slope and curvature at the junction. This allows the mechanical requirements of edge thicknesses, leading edge wedge angle, and position and magnitude of maximum thickness to be satisfied, while ensuring a reasonable aerodynamic shape.

Blade Profile Design Considerations

Some of the main aspects which influence the blade section design using the new profile type will now be discussed. When considering sections with supersonic inlet, the shock is assumed to be located near the passage entry at the design condition, as was the case for the transonic rotor discussed earlier.

"Precompression" With Supersonic Approach Flow. Viewed as a purely two-dimensional plane flow situation, supersonic flow when free from external interference expands along a convex surface and compresses along a concave one. It naturally then follows that appropriate shaping of the suction surface ahead of the covered passage can control the surface Mach number, and hence the level of mean preshock Mach number; for a tip section the latter may be reduced below the value in the approach flow, giving an amount of so-called "precompression."

Several extraneous influences change the situation from that of plane supersonic flow. They are: (*i*) varying radius, (*ii*) varying stream tube thickness, and (*iii*) the distributed total pressure loss incorporated to simulate blade "end" losses. For a tip section with a negative outer hade (reducing radius) and reducing streamtube thickness, given that flow angle is restrained by the presence of the blade, all three effects combine to reduce supersonic Mach number. Consequently precompression must be seen as the net diffusion ahead of the shock resulting from a combination of leading edge incidence, suction surface shape, and the extraneous effects just enumerated.

For a transonic fan rotor the benefits of precompression are potentially greatest near the tip of the blade where inlet Mach number is high. The extent to which it can be applied is constrained by two factors. First, the more the suction surface is decambered (or negatively cambered), the smaller the passage throat, the less its flow capacity, and the greater the likelihood of choking. Second, the flow has eventually to be turned to the required outlet angle and hence the overall suction surface camber is more or less decided a priori, so that if camber is removed from the uncovered part it must be added to the covered part, and, with the latter often being quite short, extra camber is liable to cause separation.

Further inboard, an increasing amount of overall camber is needed to achieve the desired duty, and precompression quickly becomes impracticable. However control of peak Mach number is still a requirement and this can be achieved by restraining camber in the uncovered region. Thus it becomes a matter of balancing peak Mach number against excess rear camber, while maintaining adequate choke margin.

A subsidiary benefit from reduced suction surface camber ahead of the covered passage, additional to that of lowering peak Mach number, deserves mention. With the shock located near the front of the covered passage, reduced camber in the uncovered region gives a more convergent passage at the shock–boundary layer interaction, thereby tending to lessen the chance of boundary layer separation at the interaction. It is thus obviously desirable, as a general principle, to delay the passage entry arc junction until aft of the foot of the shock (although other considerations sometimes militate against this).

Incidence With Supersonic Approach Flow. As is well known, when the flow entering the covered passage of a blade section is wholly supersonic (but with subsonic axial component), there is only one possible value of incidence for the particular approach Mach number. In the present designs the unique incidence condition is not reached until about 75 percent span; elsewhere the shock is slightly detached from the blade leading edge, so allowing a small amount of subsonic spill. Nevertheless, in order to explore variations of incidence resulting from modifications to suction surface front end shape, all at nominally fixed approach flow conditions, it is convenient to do so by running the S1 program with shock swallowed (i.e., in a unique incidence situation) and viscous effects omitted.

The term "capture wave" is used to denote the Mach wave emanating from the suction surface which strikes the leading edge of the adjacent blade. Levine (1957) indicates that, for a case of *two-dimensional* (i.e., plane) flow, and blades having zero leading edge thickness and uniform suction surface camber rate the whole way between the leading edge and the foot of the capture wave, and when operating at unique incidence, the incidence is close to (minus) one half of the suction surface camber between leading edge and capture wave foot. In other words, at the point on the suction surface about halfway to the capture wave foot the preceding camber and the incidence have canceled one another so that the surface slope equals the incoming flow angle. Results from the S1 time-marching program tend to support this thesis. For example, they show that, for a two-dimensional case with space/chord ratio and stagger typical of the transonic fan rotor tip region and an inlet Mach number of 1.5, incidence to the suction surface is zero with zero camber in the uncovered region (as expected), and increases to about +1½ deg with −5 deg camber.

The design situation differs from this simple concept in three ways:

(*i*) blades have finite leading edge thickness;
(*ii*) suction surface camber may not be uniform between leading edge and capture wave foot;
(*iii*) the flow field is not simply two-dimensional.

Considering point (*i*), S1 runs with realistic leading edge thickness introduced show an increase in incidence of typically just over ½ deg. Regarding point (*ii*), a comparison has been made for several cases, again at an inlet Mach number of 1.5, with varying suction surface shape ahead of the covered passage. These cases show that the incident flow direction tends to be such that the angle between it and the suction surface at a point about halfway between leading edge and capture wave foot remains constant. This suggests that, if the surface is to be divided into two arcs, so that the first arc can control incidence and the second control precompression, then this halfway point is likely to be a suitable junction.

These observations refer to a strictly two-dimensional (plane flow) situation. No simple scheme offers itself for relating incidence in two-dimensional flow to that in the quasi-three-dimensional situation, but it is thought that both should behave in a qualitatively similar manner. Thus the rule of thumb for dividing the uncovered suction surface into two arcs, with their separate functions, is adopted in this work (a minimum value of 10 percent chord being for convenience applied to the first arc). During the design process an upper limit on incidence is usually set, which may be dictated by off-design considerations, for example, and the suction surface first arc camber chosen to suit. Consequently, for sections toward the tip of the blade, designs of suction surface front end appear which are initially convex (camber positive) and then change to concave (camber negative), the net amount of precompression being limited by considerations already mentioned.

Rear End Camber Distribution. A blade with surfaces consisting of single circular arcs (the classic "DCA" blade) has the disadvantage that the diffusion rate in the passage near the trailing edge is fairly high and often sufficient to cause the suction surface boundary layer to separate, with consequent high profile loss. Hence there is an advantage in concentrating much of the camber in the forward part of the covered passage where that boundary layer is thinner and better able to sustain it. It may thus be possible to avoid separation completely and to reduce dramatically the losses. The high initial camber rate in the covered passage can also help in avoiding passage choking.

This philosophy is valid over much of the span for the case of the transonic fan rotor. However in the outer region, the shock near passage entry can become sufficiently strong to cause local separation of the boundary layer, and then a high camber rate immediately following could be dangerous. It could delay reattachment of the boundary layer and, for sections toward the tip which have only a short covered passage, separation could persist to the trailing edge. Here a more uniform distribution of rear end camber may be preferable.

Generally it is important to take close account of the predicted behavior of the boundary layer when seeking the correct balance of rear end camber distribution. Proximity to separation is the main concern and a convenient yardstick for this is the boundary layer parameter $\bar{H}$.[1] Experience with the present boundary layer calculation method suggests that separation in turbulent flow can be assumed if the predicted $\bar{H}$ reaches a value around 2.8. More important than the precise separation value, however, is the manner in which $\bar{H}$ behaves locally. Once it exceeds about 2.0, comparatively little further aggravation of the boundary layer is required to send the value shooting up. Furthermore, it is obviously desirable to maintain some margin of safety, for reasons both of the uncertain accuracy in prediction and of allowance for shifts of operating conditions in real life. While, therefore, one may with some confidence regard as separation-free a surface on which $\bar{H}$ is maintained below (say) 2.0, it is much more risky to choose a design giving sustained values around (say) 2.5. Rather than tolerate the latter it may be preferable to constrain $\bar{H}$ near the nominal value of 2.0 for as long as possible and then allow it to rise toward the rear of the blade. A small separated region could be tolerated near the trailing edge if necessary. This approach reduces the risk of early, and perhaps catastrophic, separation of the boundary layer occurring in practice owing to the uncertainties mentioned previously.

Blade Section Profiles

Blade-to-blade analyses of profiles at three stations along the span of a civil transonic fan rotor are now described. The first (*A*) is near the hub (subsonic inlet), the second (*B*) at part span (near-sonic inlet), and the third (*C*) toward the tip (supersonic inlet). In each case an optimized profile produced during a design exercise is compared with a conventional profile of the same duty and space/chord and thickness/chord ratios. The baseline profiles are of DCA type for the first two stations, while the profile at the third station has a low forward camber, giving nearly constant Mach number on the uncovered part of the suction surface.

The blade-to-blade analyses use streamtube geometries and blade operating conditions defined by a converged S1–S2 solution for each rotor. Leading parameters are given in the table.

Station A – Conventional Profile. The blade section shape is shown in Fig. 1, together with boundary layer displacement boundaries and contours of relative Mach number; the blade surface distributions of relative Mach number, and of boundary layer displacement and momentum thicknesses (δ^* and θ) and shape factor $\bar{H}$ are also shown. The duty at this station is not severe and the conventional profile (DCA type) is predicted to achieve it without severe problems. Following transition to turbulent flow at 5 percent chord, the boundary layer parameter $\bar{H}$ remains at a low value (1.5) until midchord, then rises through 2.0 near 85 percent chord, but following separation at 91 percent chord reaches a value of 5.6 at the

---

[1] $\bar{H}$ is effectively the shape factor (i.e., ratio of displacement and momentum thicknesses) of an equivalent incompressible boundary layer.

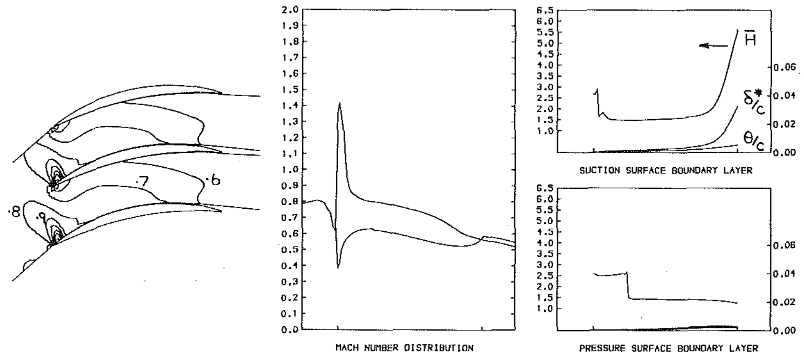

Fig. 1 Station A—conventional profile

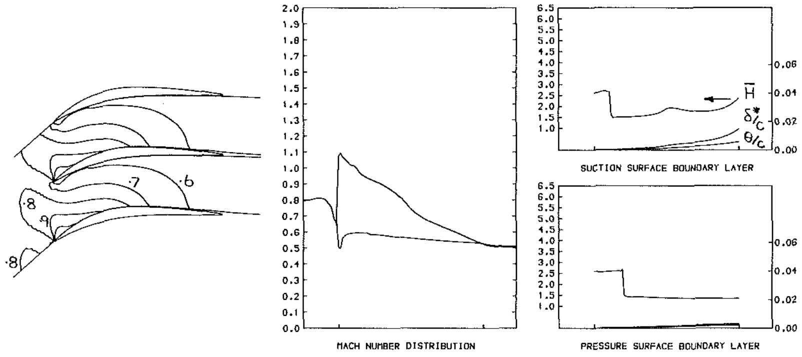

Fig. 2 Station A—optimized profile

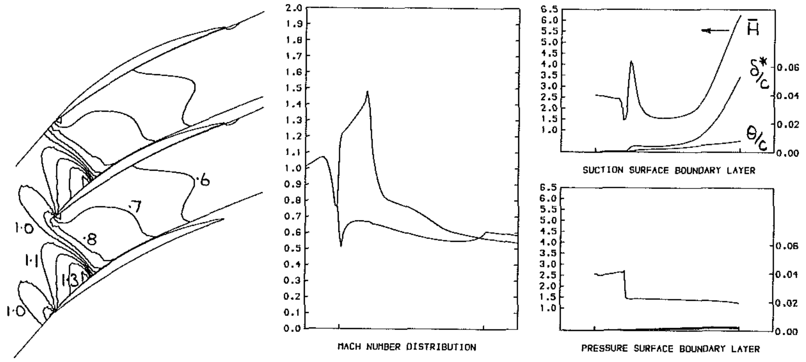

Fig. 3 Station B—conventional profile

trailing edge. The marked reduction in diffusion rate following separation can be seen clearly on Fig. 1. The predicted profile loss coefficient based on inlet relative dynamic head is 0.040.

A notable feature of the prediction is the large spike in Mach number near the leading edge. This is due to the high incidence at which this section is predicted to operate by the S1-S2 solution: suction surface incidence, $i_{ss} \simeq 3$ deg – about 1½ deg greater than anticipated when setting up the section using an S2 solution which did not have internal calculating stations. The blade-to-blade code does not predict any problems arising from the high incidence, but since it is known to be optimistic in this respect in other applications (Calvert, 1983), this indication may be misleading. For this section the high incidence has some advantages, because it helps avoid the passage choking problems which can be of concern with thick, low space/chord ratio blading.

Station A – Optimized Profile. The main geometric feature of the new profile is that nearly 80 percent of the suction surface camber is concentrated into the first half of the chord, resulting in a distinctly "flat-backed" profile. This can be seen in Fig. 2, together with the predicted aerodynamics. The high initial camber rate enables the blade to be set at a lower incidence ($i_{ss} = -1$ deg) without any choking (or passage reacceleration) problems, and with the peak Mach number remaining reasonably low, below 1.1. The low camber rate beyond midchord keeps the boundary layer under tight control and well clear of separation: $\bar{H}$ remains under 2.0 until 93 percent chord. The predicted profile loss is correspondingly low, the loss coefficient being 0.028.

Station B – Conventional Profile. The duty required of this section poses much greater difficulty. Several features all add their quota to the problem. Inlet Mach number is just over sonic and the pitch/chord ratio and stagger angle are that much higher. Overall the streamtube contraction is less than anywhere else due to the presence downstream of the splitter between core and bypass ducts, and the chordwise distribution of streamtube thickness is such that there is almost no contraction over the rear part of the blade; the latter feature in particular worsens the design difficulty. The required work level demands an amount of camber which is embarassingly large. As a result, with the DCA type section, there is significant supersonic acceleration on the uncovered part of the suction

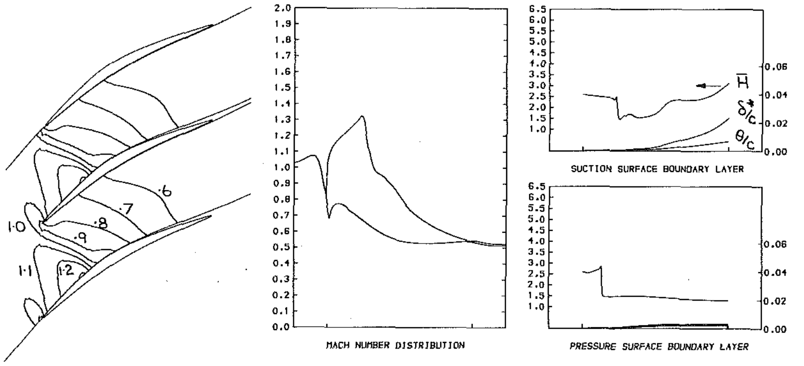

Fig. 4 Station B—optimized profile

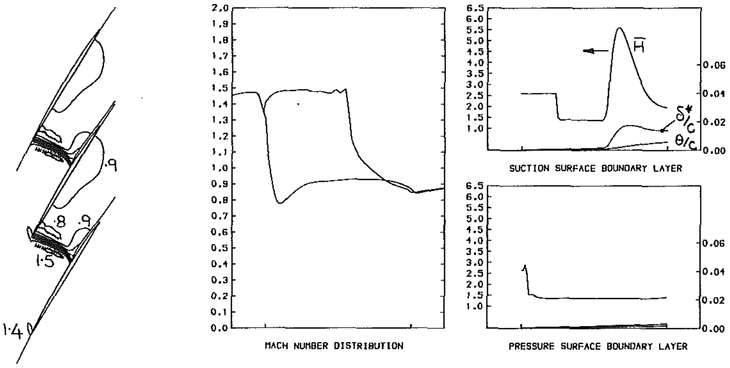

Fig. 5 Station C—conventional profile

surface, producing a shock with a peak entry Mach number approaching 1.5. As shown in Fig. 3, this is predicted to cause only a small boundary layer separation bubble since the preshock boundary layer is thin, due to the fact that transition occurs only just before the shock. However, the continued diffusion within the blade passage causes separation at about 82 percent chord and $\bar{H}$ exceeds 6 at the trailing edge. The predicted profile and shock loss coefficients are correspondingly high, being 0.034 and 0.038, respectively. The suction surface incidence is just over 2 deg, only a little lower than for Station A, but no leading edge incidence problems are apparent here.

Station B – Optimized Profile. As mentioned above the design of this section is quite challenging. The required camber is large, and the scope for distributing that camber is constrained by two opposing factors. High camber at the front adversely affects peak Mach number and hence the subsequent suction surface diffusion, which is in any case very large, since the outlet Mach number is down around 0.5 (similar to that at Station A). On the other hand, if peak Mach number is kept down then the camber has to go rearward, which upsets the boundary layer during the diffusion.

Some trials with various section designs suggest that there is benefit from having a very high camber rate immediately following the Mach number peak, with front and rear portions of the suction surface being almost flat. That arrangement gives a modest peak Mach number and allows the suction surface boundary layer to remain separation-free throughout the diffusion. Unfortunately, however, such very concentrated camber makes for high sensitivity to where the foot of the shock lies. As can be seen in Fig. 4, there is a tendency for the shock to be slanted across the passage, and the position of its foot in practice is a matter of some uncertainty. If the foot moves on to a region of such higher camber rate, there is immediate trouble. This type of camber distribution also tends to give rise to continuously high values of $\bar{H}$ (i.e., about 2.5) over a considerable portion of the covered passage, with the disadvantages enumerated earlier. Consequently this extreme type of camber distribution is not adopted.

Instead a compromise is reached (see Fig. 4): Peak Mach number is allowed to be rather higher (= 1.32, transition occurring at the peak, which is at 26 percent chord) and the rear part of the suction surface (from 60 percent chord) is made less nearly flat. As a result $\bar{H}$ rises from 1.6 to 2.2 in the high camber region, stays close to 2.3 as far as 80 percent chord, and reaches 3.1 (with separation) at the trailing edge. This is a case where, having once chosen the front end shape, the rest of the design is governed almost entirely by considerations of suction surface boundary layer behavior. Predicted profile loss coefficient is 0.020, and the shock loss is 0.017 – about 50 percent lower than the values for the conventional profile! Suction surface incidence is close to +1 deg.

Station C – Conventional Profile. For this station the deflection required is quite small (~ 5 deg) and the outlet Mach number quite high (~ 0.85) so, with a high inlet Mach number (1.46), Mach number control on the uncovered portion of the suction surface becomes of much greater concern than passage diffusion. The conventional profile for this station shown in Fig. 5 has a low camber suction surface, giving a near-constant Mach number close to 1.5 right up to the shock at passage entry. This preshock Mach number on the suction surface is similar to that for Station B, however the boundary layer is predicted to be much thicker in this case because of the significant length available for growth after transition near 30 percent chord. This causes the boundary layer to separate severely at the shock ($\bar{H}$ approaching 6 locally), and it only just re-attaches before the end of the short covered passage. The profile and shock loss coefficients are 0.025 and 0.054, respectively. The suction surface incidence is +1 deg; this is the "unique" incidence for this section, which operates with a swallowed shock.

Station C – Optimized Profile. The new profile at this station, shown in Fig. 6, uses negative camber on the uncovered

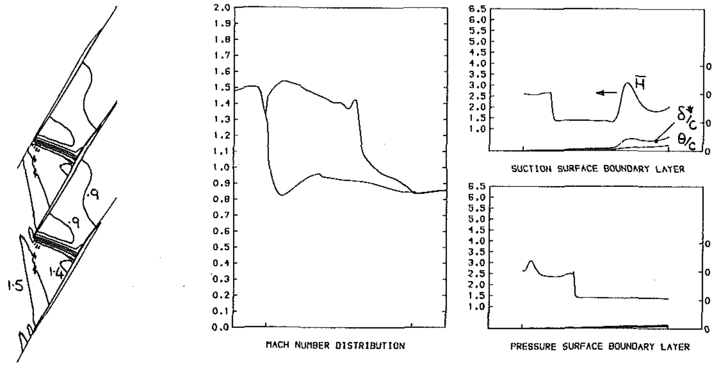

Fig. 6 Station C—optimized profile

Table 1 Design parameters

STATION	LEADING EDGE RADIUS*	TRAILING EDGE RADIUS*	INLET MACH NO	INLET FLOW ANGLE	STREAMTUBE CONTRACTION	PRESSURE RATIO	SPACE-CHORD RATIO	THICKNESS-CHORD RATIO	EDGE-MAX THICKNESS RATIO
A	0.37	0.43	0.82	39½°	0.86	1.55	0.35	0.06	0.10
B	0.55	0.58	1.04	48½°	0.93	1.75	0.49	0.05	0.11
C	0.92	0.91	1.47	62°	0.86	1.88	0.76	0.03	0.17

*Non-dimensionalised by the leading edge tip radius.

part of the suction surface to reduce the preshock Mach number to 1.4 (ignoring the preshock spike). The benefits of this in reducing shock loss are plain; what is perhaps more surprising is the large reduction in predicted shock wave-boundary layer interaction compared with the conventional profile. The boundary layer is predicted only to separate momentarily near the shock foot and then to recover almost immediately, with $\bar{H}$ remaining near 2.0 over much of the covered passage. The whole passage is only about 35 percent chord in length, including the interaction region, so that not much camber can be applied and fortunately not much deflection is needed (5 deg only). Only a single arc is used within the covered region.

The success of this profile is closely tied to the accuracy of the boundary layer prediction. If in reality the postshock boundary layer is not as thin as predicted, quite severe choking problems could ensue (the Mach number at the passage throat is near 0.9). However, this sensitivity could be reduced by using less precompression.

The predicted profile loss for the section is low, being 0.018 compared with 0.025 for the conventional section. A precise comparison of shock loss is made difficult by the fact that predicted values of this are very sensitive to shock position. However, the optimized section certainly gives a significant reduction, and the result shown corresponds to a shock loss coefficient of 0.040 compared with 0.054 for the conventional profile. Finally the suction surface incidence is near + 1½ deg, being constrained to this predetermined limit by the use of a short initial arc of positive camber.

Note on Profile Definition. Each of the three blade profiles described uses only three of the four available suction surface arcs. However, they are used differently: Two arcs are used in the covered region for Stations A and B whereas two are used in the uncovered region for Station C. As might be inferred, some stations on the blade intermediate between B and C can profitably employ two arcs in each region, making full use of the freedom available with the new type of profile.

Concluding Remarks

The considerations involved in the design of advanced blade profiles for a transonic civil fan rotor have been discussed. Predicted blade-to-blade aerodynamics for three blade profiles taken at different heights from such a rotor are used to illustrate the points made. These profiles were designed using an inviscid-viscous blade-to-blade code and a new type of blade profile generator as the main tools. The predicted performance levels of these sections have been compared with those for conventional profiles, and significant loss reductions predicted.

Acknowledgments

The authors wish to acknowledge the valuable contribution made by Dr. M. V. Herbert to the work described in this paper.

References

Calvert, W. J., 1982, "An Inviscid-Viscous Interaction Treatment to Predict the Blade-to-Blade Performance of Axial Compressors With Leading Edge Normal Shock Waves," ASME Paper No. 82-GT-135.

Calvert, W. J., 1983, "Application of an Inviscid-Viscous Interaction Method to Transonic Compressor Cascades," in: *Viscous Effects in Turbomachines*, AGARD-CP-351, pp. 2.1-2.13.

Calvert, W. J., and Ginder, R. B., 1985, "A Quasi-Three-Dimensional Calculation System for the Flow Within Transonic Compressor Blade Rows," ASME Paper No. 85-GT-22.

Denton, J. D., 1983, "An Improved Time-Marching Method for Turbomachinery Flow Calculation." ASME JOURNAL OF ENGINEERING FOR POWER, Vol. 105, pp. 514-524.

Ginder, R. B., 1984, "A Streamline Curvature Throughflow Calculation for Transonic Axial-Flow Compressors Including Stations Within the Blade Row," *Computational Methods in Turbomachinery*, I Mech E Conference Publication 1984-3, pp. 25-32.

Levine, P., 1957, "Two-Dimensional Inflow Conditions for a Supersonic Compressor With Curved Blades," ASME *Journal of Applied Mechanics*, Vol. 24, pp. 165-169.

Stewart, W. L., 1955, "Analysis of Two Dimensional Compressible Flow Loss Characteristics Downstream of Turbomachine Blade Rows in Terms of Basic Boundary Layer Characteristics," NACA TN 3515.

An Accurate and Efficient Euler Solver for Three-Dimensional Turbomachinery Flows

C. F. Shieh

R. A. Delaney

Allison Gas Turbine Division,
General Motors Corporation,
Indianapolis, IN 46206

Accurate and efficient Euler equation numerical solution techniques are presented for analysis of three-dimensional turbomachinery flows. These techniques include an efficient explicit hopscotch numerical scheme for solution of the three-dimensional time-dependent Euler equations and an O-type body-conforming grid system. The hopscotch scheme is applied to the conservative form of the Euler equations written in general curvilinear coordinates. The grid is constructed by stacking from hub to shroud two-dimensional O-type grids on equally spaced surfaces of revolution. Numerical solution results for two turbine cascades are presented and compared with experimental data to demonstrate the accuracy of the analysis method.

Introduction

Over the past decade, considerable progress has been made in the development of three-dimensional flow analyses for turbomachinery blade rows. These analyses are needed to assess effectively three-dimensional flow effects resulting from leaning, bowing, and sweeping of blades, as well as endwall contouring. Such features cannot be accurately treated with conventional quasi-three-dimensional analyses, which invoke limiting streamsurface geometry assumptions.

The three-dimensional analysis methods that have been the most highly developed and have afforded the greatest advancements in turbomachinery analysis capability are the time-dependent Euler solvers. They provide a single unified approach for simulating subsonic, transonic, and supersonic flows and, for the most part, afford automatic shock-capturing capability. Also, because they are based on primitive variable formulations, complex turbomachinery boundary conditions are readily treated. Furthermore, unlike methods based on potential flow formulations, time-dependent Euler solvers can simulate rotational flows resulting from nonuniform inlet total pressure distributions or embedded shock waves. This feature is important for analysis of high-Mach-number turbines and compressors in which there are significant regions of rotational flow due to curved shock waves.

The history of the development of three-dimensional Euler solvers for turbomachines began about 10 years ago with the pioneering work of Denton [1, 2]. Since then Denton [3] has made improvements to his original technique, and others [4, 5] have explored similar methods for the same application. As a result of these developments, robust and efficient three-dimensional Euler solvers are now used routinely in the turbomachinery design process throughout the aircraft gas turbine industry.

In parallel with the Euler solver developments over the past five years, there has been substantial development of new grid generation concepts that hold considerable promise for improving the accuracy of turbomachinery flow calculations. New techniques for constructing O- and C-type grids have been developed [6, 7] and used for two-dimensional cascade calculations [8–10]. These new grids have been demonstrated to provide significantly improved solution accuracy when compared with the conventional H-type grids employed by Denton and others [1–5]. For the most part, this increased accuracy is the result of better leading-edge resolution with the O- and C-type grids. Accurate simulation of the leading-edge flow is particularly important with Euler solvers because any errors incurred at the leading edge are convected downstream and adversely affect the solution accuracy over the entire airfoil surface. Inaccurate leading-edge modeling, inherent with H-type grids, leads to the generation of artificial total pressure losses. One approach to minimizing these losses [11] is to invoke the isentropic relation along the airfoil surface. This approach, however, generally leads to a violation of one or more of the conservation equations.

This paper describes an accurate three-dimensional turbomachinery flow analysis method that combines an efficient hopscotch time-dependent Euler solver with an O-type body-conforming grid system. The method is based on the two-dimensional cascade analysis method developed by Delaney [8]. Included in the paper are descriptions of the governing equations, the grid generation scheme, and the numerical solution techniques. Finally, numerical solution results for two three-dimensional turbine cascade flows are presented and compared with experimental data to demonstrate the accurate predictive capability of the analysis method.

Contributed by the Gas Turbine Division of The American Society of Mechanical Engineers and presented at the 31st International Gas Turbine Conference and Exhibit, Düsseldorf, Federal Republic of Germany, June 8–12, 1986. Manuscript received at ASME Headquarters March 13, 1987. Paper No. 86-GT-200.

Governing Equations

For turbomachinery flow calculations it is convenient to write the three-dimensional unsteady Euler equations in a cylindrical polar coordinate system. In the relative system, attached to a rotating or stationary blade row, the equations can be expressed in conservation form as

$$\frac{\partial Q}{\partial t}+\frac{\partial E}{\partial z}+\frac{\partial F}{\partial \theta}+\frac{\partial G}{\partial r}=H \tag{1}$$

where

$$Q=r\begin{bmatrix}\rho\\ \rho u\\ \rho v\\ \rho w\\ \rho e_0\end{bmatrix} \qquad E=r\begin{bmatrix}\rho u\\ \rho u^2+p\\ \rho uv\\ \rho uw\\ \rho ue_0+pu\end{bmatrix}$$

$$F=\begin{bmatrix}\rho(v-r\Omega)\\ \rho(v-r\Omega)u\\ \rho(v-r\Omega)v+p\\ \rho(v-r\Omega)w\\ \rho(v-r\Omega)e_0+pv\end{bmatrix} \qquad G=r\begin{bmatrix}\rho w\\ \rho uw\\ \rho vw\\ \rho w^2+p\\ \rho we_0+pw\end{bmatrix}$$

$$H=\begin{bmatrix}0\\ 0\\ -\rho vw\\ \rho v^2+p\\ 0\end{bmatrix}$$

and where ρ is the density; p, the pressure, u, v, and w, the absolute velocity components in the z, θ, and r directions, respectively; Ω, the rotational speed of the blade row; and e_0, the total internal energy given by the relation

$$e_0=\frac{1}{(\gamma-1)}\frac{P}{\rho}+\frac{1}{2}[u^2+v^2+w^2] \tag{2}$$

Equations (1) and (2) comprise a system of six equations for the six dependent variables u, v, w, p, ρ, and e_0.

To solve the system of equations numerically on a body-conforming grid system, it is desirable to first transform the system to an arbitrary curvilinear coordinate system. If the transformation equations are written

$$\xi=\xi(z,\theta,r)$$
$$\eta=\eta(z,\theta,r)$$
$$\zeta=\zeta(z,\theta,r)$$

then, using the chain rule for differentiation, equation (1) can be expressed as

$$\frac{\partial Q'}{\partial t}+\frac{\partial E'}{\partial \xi}+\frac{\partial F'}{\partial \eta}+\frac{\partial G'}{\partial \zeta}=H' \tag{3}$$

where

$$Q'=Q/\mathrm{J}=r\mathrm{J}^{-1}\begin{bmatrix}\rho\\ \rho u\\ \rho v\\ \rho w\\ \rho e_0\end{bmatrix}$$

$$E'=\xi_zE+\xi_\theta F+\xi_rG=r\mathrm{J}^{-1}\begin{bmatrix}\rho U\\ \rho uU+\xi_zp\\ \rho vU+\xi_\theta/rp\\ \rho wU+\xi_rp\\ (\rho e_0+p)U+\xi_\theta/r(r\Omega)p\end{bmatrix}$$

$$F'=\eta_zE+\eta_\theta F+\eta_rG=r\mathrm{J}^{-1}\begin{bmatrix}\rho V\\ \rho uV+\eta_zp\\ \rho vV+\eta_\theta/rp\\ \rho wV+\eta_rp\\ (\rho e_0+p)V+\eta_\theta/r(r\Omega)p\end{bmatrix}$$

$$G'=\zeta_zE+\zeta_\theta F+\zeta_rG=r\mathrm{J}^{-1}\begin{bmatrix}\rho W\\ \rho uW+\zeta_zp\\ \rho vW+\zeta_\theta/rp\\ \rho wW+\zeta_rp\\ (\rho e_0+p)W+\zeta_\theta/r(r\Omega)p\end{bmatrix}$$

$$H'=H/\mathrm{J}=\mathrm{J}^{-1}\begin{bmatrix}0\\ 0\\ -\rho vw\\ \rho v^2+p\\ 0\end{bmatrix}$$

and where U, V, and W are the contravariant velocity components in the ξ, η, and ζ directions, respectively, given by the relations

$$U=\xi_zu+\xi_\theta/r(v-r\Omega)+\xi_rw \tag{4}$$

$$V=\eta_zu+\eta_\theta/r(v-r\Omega)+\eta_rw \tag{5}$$

$$W=\zeta_zu+\zeta_\theta/r(v-r\Omega)+\zeta_rw \tag{6}$$

The inverse Jacobian of the transformation, J^{-1}, is defined as

$$\mathrm{J}^{-1}=\begin{vmatrix}z_\xi & z_\eta & z_\zeta\\ \theta_\xi & \theta_\eta & \theta_\zeta\\ r_\xi & r_\eta & r_\zeta\end{vmatrix}$$

and the metrics ξ_z, ξ_θ, ξ_r, etc., are given by the equations

Nomenclature

C_x = airfoil axial chord
e_0 = total internal energy
i, j, k, n = grid-point indices in ξ, η, ζ, and t coordinates, respectively
J = Jacobian of coordinate transformation
M = Mach number
p = static pressure
p_0 = total pressure
t = time
U, V, W = contravariant velocity components in ξ, η, and ζ directions, respectively
u, v, w = velocity components in z, θ, and r directions, respectively
V_{cr} = critical velocity
z, θ, r = cylindrical polar coordinates
$\alpha_\xi, \alpha_\eta, \alpha_\zeta$ = damping coefficients in ξ, η, and ζ directions, respectively
γ = ratio of specific heats
ξ, η, ζ = general curvilinear coordinates
ρ = density
ρ_0 = total density
Ω = rotational speed of rotor

Subscripts

z, θ, r = differentiation in z, θ, and r directions, respectively
ξ, η, ζ = differentiation in ξ, η, and ζ directions, respectively
1 = uniform upstream condition
2 = uniform downstream condition

Superscripts

$'$ = nondimensional variable

Abbreviations

CFL = Courant-Friedrichs-Lewy
CPU = central processor unit

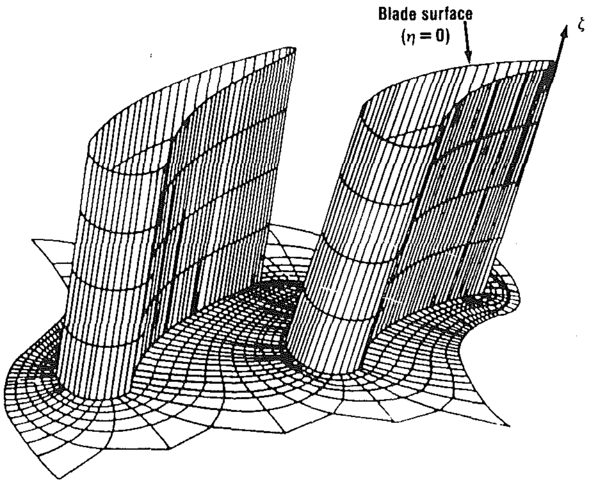

Fig. 1 Three-dimensional body-conforming grid system

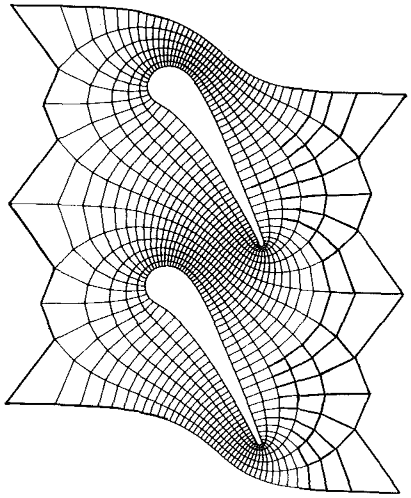

Fig. 2 Two-dimensional O-type grid system

$$
\begin{aligned}
\xi_z &= (\theta_\eta r_\zeta - r_\eta \theta_\zeta)/\mathrm{J}^{-1}\\
\xi_\theta &= (z_\zeta r_\eta - r_\eta r_\zeta)/\mathrm{J}^{-1}\\
\xi_r &= (z_\eta \theta_\zeta - z_\zeta \theta_\eta)/\mathrm{J}^{-1}\\
\eta_z &= (r_\xi \theta_\zeta - \theta_\xi r_\zeta)/\mathrm{J}^{-1}\\
\eta_\theta &= (z_\xi r_\zeta - z_\zeta r_\xi)/\mathrm{J}^{-1}\\
\eta_r &= (z_\zeta \theta_\xi - z_\xi \theta_\zeta)/\mathrm{J}^{-1}\\
\zeta_z &= (\theta_\xi r_\eta - \theta_\eta r_\xi)/\mathrm{J}^{-1}\\
\zeta_\theta &= (z_\eta r_\xi - z_\xi r_\eta)/\mathrm{J}^{-1}\\
\zeta_r &= (z_\xi \theta_\eta - z_\eta \theta_\xi)/\mathrm{J}^{-1}
\end{aligned}
\tag{7}
$$

These transformation equations are applicable to any curvilinear coordinate system for which the Jacobian is nonsingular.

Nondimensional dependent variables are used in the actual numerical calculations. The choice of reference conditions is arbitrary but it is convenient to use inlet total conditions and to write the variables in nondimensional form as follows:

$$
\begin{aligned}
\rho' &= \rho/\rho_{01}\\
p' &= p/p_{01}\\
u' &= u/(p_{01}/\rho_{01})^{1/2}\\
v' &= v/(p_{01}/\rho_{01})^{1/2}\\
w' &= w/(p_{01}/\rho_{01})^{1/2}
\end{aligned}
$$

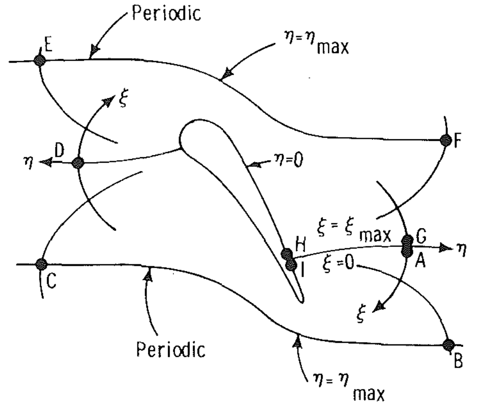

a. Physical plane

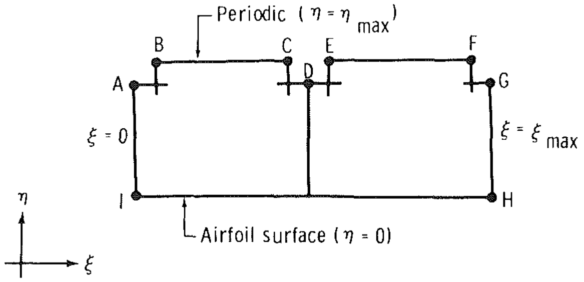

b. Computational plane

Fig. 3 Schematic of mapping from the physical plane to the computational plane for the O-type grid

where p_{01} and ρ_{01} are the inlet total pressure and density, respectively. If nonuniform inlet total conditions are prescribed, the reference inlet total conditions are taken as those on the hub surface.

Coordinate System

The coordinate system for the three-dimensional cascade analysis is an O-type body-conforming system. Shown in Fig. 1, this system is constructed by stacking (in the radial direction) two-dimensional O-type grids on equally spaced surfaces of revolution (ζ = const). Each O grid, shown in Fig. 2, is constructed using the Adamczyk scheme [6] modified as described subsequently for coordinate generation on arbitrary surfaces of revolution. This type of grid is particularly attractive because it affords high resolution of the leading- and trailing-edge regions. It is also periodic for ease of enforcement of the cascade periodic flow condition.

The Adamczyk grid generation scheme combines a singularities technique for determining the grid point distribution on the airfoil surface and an elliptic partial differential equation generation procedure for establishing the interior point coordinates. The singularities technique is based on an electrostatic analog that describes the potential field around an infinite cascade. Once the airfoil surface mesh points are established, the elliptic procedure is employed to solve a set of Laplace equations for the interior point coordinates. The equations are solved in the rectangular computational plane, shown in Fig. 3, using standard successive overrelaxation (SOR) techniques.

The Adamczyk scheme is limited to planar two-dimensional cascades and, therefore, cannot be used directly to construct grids on arbitrary surfaces of revolution as needed for the three-dimensional grid generation procedure. This limitation results from a requirement of constant airfoil spacing through the blade row. A modification, suggested by Adamczyk, to treat cascades with variable spacing is to solve the grid generation problem on an m, θ coordinate system, where m is the meridional coordinate on the surface and θ is the polar angle. In this system the airfoil spacing, $\Delta\theta_s$, is constant. This approach does work. However, scaling the physical circumferential coordinate $r\theta$ by the radius severely distorts and thins the airfoil which, in turn, leads to grids that are nonorthogonal and sparse in the leading- and trailing-edge regions.

A better approach to O grid construction, the one incorporated in the three-dimensional grid generation procedure, is to first multiply the airfoil circumferential coordinates $r\theta$ by the radius ratio r_m/r, where r is the local radius and r_m is the average of the stream surface radii at the leading and trailing edges. This amounts to projecting the airfoil sections onto a circular cylinder with radius r_m. Next, the O grids are generated on these mean surfaces using the Adamczyk procedure and are then projected back onto the original surfaces of revolution by multiplying the grid circumferential coordinates by the inverse radius ratio r/r_m. This procedure has been found to produce acceptable grids for a wide variety of blade and flow path geometries.

Information on the particular coordinate system employed in the numerical solution of equation (3) is provided through the metrics. The metrics z_ξ, z_η, z_ζ, etc., in equation (7) are evaluated by simply taking finite differences of the known grid coordinates z, θ, r in the three-dimensional rectangular computational space. However, as noted by Steger [12] and Hindman [13], the grid conservation law must be satisfied when forming the derivatives to avoid serious numerical errors. This law states that the differencing scheme (backward, forward, or central) used to calculate the metrics must be identical to the scheme used to approximate the spatial derivatives in the governing system of equations. If the grid conservation law is not satisfied, the numerical solution scheme will not reproduce uniform flow conditions. An additional obvious constraint on the difference approximations used to form the metrics is they must be good representations of the exact derivatives.

Numerical Solution Algorithm

A modified version of the hopscotch-Lax scheme originally developed by Gourlay and Morris [14] is used to solve the system of Euler equations (3). This modified scheme was successfully used by Delaney [8] to solve the two-dimensional Euler equations on an O-type cascade coordinate system.

The hopscotch algorithm is a two-sweep scheme employing central differences for the spatial derivatives and forward and backward differences for the time derivatives on alternate sweeps. Applied to the system of Euler equations (3) (with prime notation omitted), the algorithm is expressed as (first sweep, $i + j + k + n$ even)

$$Q^{n+1}_{i,j,k} = Q^n_{i,j,k} - \Delta t(\partial_\xi E^n + \partial_\eta F^n + \partial_\zeta G^n) + \Delta t H^n_{i,j,k} + \alpha_\xi \delta_\xi Q^n + \alpha_\eta \delta_\eta Q^n + \alpha_\zeta \delta_\zeta Q^n \tag{8}$$

(second sweep, $i + j + k + n$ odd)

$$Q^{n+1}_{i,j,k} = Q^n_{i,j,k} - \Delta t(\partial_\xi E^{n+1} + \partial_\eta F^{n+1} + \partial_\zeta G^{n+1}) + \Delta t H^n_{i,j,k} + \alpha_\xi \delta_\xi Q^{n+1} + \alpha_\eta \delta_\eta Q^{n+1} + \alpha_\zeta \delta_\zeta Q^{n+1} \tag{9}$$

where i, j, k, and n are the point indices in the ξ, η, ζ, and t coordinate directions, respectively, and ∂ and δ are the central difference operators for the first and second derivatives, respectively, at the point i, j, k. The last three terms in equations (8) and (9) are added damping terms needed to stabilize the solution in regions of large gradients. Consistent with the grid conservation law, the metrics used in the formation of the E, F, and G flux vectors are evaluated using central differences. Note that during the second sweep, the flux vectors E, F, and G at neighboring points resulting from the central spatial differencing at the $n+1$ time level have been previously determined during the first sweep. Also, note that $Q^{n+1}_{i,j,k}$ on the right-hand side of equation (9) resulting from the central-difference approximations to the second derivatives can be moved to the left-hand side and, therefore, the second sweep scheme is explicit.

If the nonhomogeneous terms $H^n_{i,j,k}$, and the damping coefficients α_ξ, α_η, and α_ζ in equations (8) and (9) are treated as constants, then it can be shown that the first sweep scheme is equivalent to a simple linear extrapolation in time of the dependent variables, i.e.,

$$Q^{n+1}_{i,j,k} = 2Q^n_{i,j,k} - Q^{n-1}_{i,j,k} \tag{10}$$

This modified scheme with first sweep extrapolation has been determined to be stable and nearly twice as fast at the original scheme. Note that the three-time-level process indicated in equation (10) requires only two-time-level storage because $Q^{n-1}_{i,j,k}$ can be overwritten with $Q^{n+1}_{i,j,k}$.

The hopscotch algorithm is stable for all positive values of the damping coefficients ($\alpha_\xi \geq 0$, $\alpha_\eta \geq 0$, $\alpha_\zeta \geq 0$) for all Δt satisfying the CFL stability criterion

$$\Delta t \leq (U + V + W + \mathrm{J}Aa)^{-1} \tag{11}$$

where

$$A = (\xi_z^2 + \xi_\theta^2/r^2 + \xi_r^2)^{1/2} + (\eta_z^2 + \eta_\theta^2/r^2 + \eta_r^2)^{1/2} + (\zeta_z^2 + \zeta_\theta^2/r^2 + \zeta_r^2)^{1/2}$$

and where a is the local acoustic speed. The independence of the damping coefficients and the time increment permits an arbitrary variation in the amount of damping introduced during the computation without further restricting the allowable time increment.

The damping coefficients, α_ξ, α_η, α_ζ, in equations (8) and (9) are the same as those employed by Delaney [8] in two dimensions. They yield second- and product fourth-order damping terms and are expressed as

$$\alpha_\xi = \alpha'_\xi + 0.5\,|\delta_\xi p^n|/p^n_{i,j,k} \tag{12}$$

$$\alpha_\eta = \alpha'_\eta + 0.5\,|\delta_\eta p^n|/p^n_{i,j,k} \tag{13}$$

$$\alpha_\zeta = \alpha'_\zeta + 0.5\,|\delta_\zeta p^n|/p^n_{i,j,k} \tag{14}$$

where α'_ξ, α'_η, and α'_ζ are constants that are at most of the order of the mesh spacing in each of the coordinate directions to ensure second-order spatial accuracy. The coefficients involving second derivatives of pressure in equations (12), (13), and (14) yield product fourth-order damping terms in equations (8) and (9). Generally, the product fourth-order terms have a significant impact on the solution only in the trailing-edge region where strong gradients occur and where large truncation errors alone adversely affect the solution accuracy. Local reduced accuracy in the trailing-edge region has been shown to have no adverse effect on the rest of the solution.

Boundary Conditions

The boundary conditions for the three-dimensional cascade analysis are imposed along the hub and shroud endwalls, $\zeta = 0$ and $\zeta = \zeta_{\max}$; the blade surface, $\eta = 0$; and at the inlet and exit boundary points A, B, C, D, E, F, and G in Fig. 3.

The points along the periodic boundaries B-C, E-F, A-I, and G-H in Fig. 3 are regular interior points and require no special solution procedures.

At the solid boundaries, a special adaptation of the full two-sweep scheme (no extrapolation in the first sweep) is used. Central differences in the direction normal to the surface are replaced by two-point one-sided differences and the damping terms in that direction are omitted. After the equations are

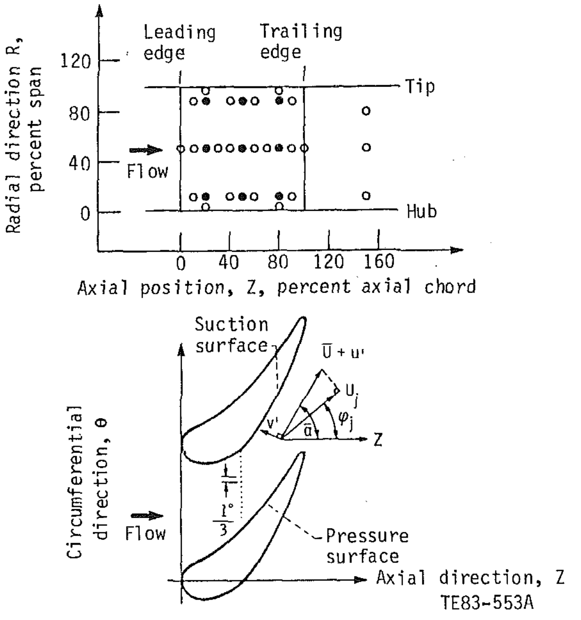

Fig. 4 Airfoil geometry and flow path for the annular turbine vane cascade [16]

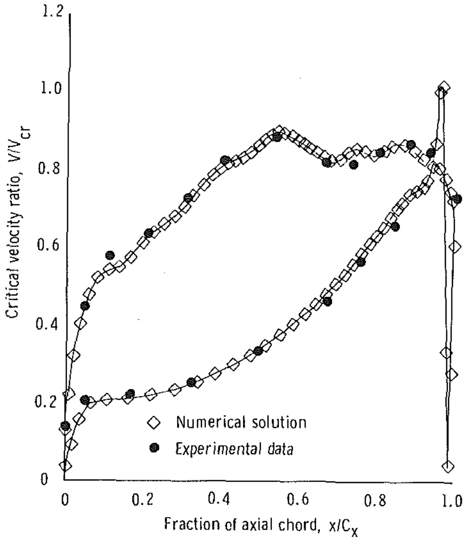

Fig. 5 Calculated and experimental midspan velocity distributions for the annular turbine vane cascade (experimental data from [16])

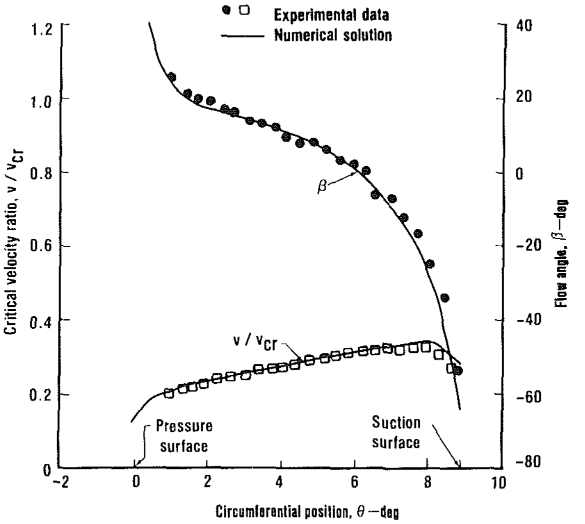

Fig. 6 Comparison of measured and calculated blade-to-blade velocity and flow angle distributions for the annular turbine vane cascade at 50 percent span and 1.3 percent axial chord (experimental data from [16])

solved, the velocity components are recalculated to ensure that there is no flow normal to the surface. This is accomplished by solving equations (4)–(6) for u, v, and w with the contravariant velocity component normal to the surface set equal to zero. This procedure is invoked at all surface points after each sweep.

At the inlet and exit boundaries, the boundary conditions are imposed using a reference plane method of characteristics. This method was employed because it ensures correct specification of boundary conditions and is more accurate than other techniques based on standard finite difference procedures. The development of the characteristic direction and compatibility relations follows that employed by Delaney [8] for two-dimensional cascade flows and given by Cline [15]. The derivation of the characteristic relations for three-dimensional flows is straightforward but lengthy and, therefore, is not presented.

The boundary conditions at the inlet are the radial and circumferential velocity components or flow angles and the total pressure and temperature. Nonuniform radial distributions of any of these properties can be imposed. At the exit boundary points, the static pressure is set on the hub surface and the radial pressure distribution is determined from the simple radial equilibrium equation

$$\frac{\partial p}{\partial r}=\frac{\rho v^2}{r}$$

This equation is integrated at each time step following the solution of the characteristic compatibility relations for ρ, u, v, and w. The calculated pressure distribution is then imposed as a boundary condition at the next time step.

Results and Discussions

Numerical solution results for two turbine cascades are presented and compared with experimental data. The solutions were started from stagnation conditions ($u' = 0$, $v' = 0$, $w' = 0$, $p' = 1.0$, $\rho' = 1.0$) with the inlet and exit conditions set to the steady-state values. The second-order damping coefficients, α_ξ', α_η', α_ζ', were set equal to 0.025. To increase the convergence rate to the steady solution, the time increment at each point was set equal to the maximum allowable value under the CFL stability criterion. The solutions were assumed to be converged when the maximum relative change in static pressure between time steps

$$|p^{n+1}_{i,j,k}-p^{n}_{i,j,k}|/p^{n}_{i,j,k}$$

was less than 10^{-5}.

Annular Turbine Vane Cascade. The first example solution is for an annular turbine vane cascade tested by Goldman and Seasholtz [16]. The cascade, shown in Fig. 4, is comprised of constant-section vanes mounted between cylindrical endwalls. The data, taken for the design exit critical velocity ratio, $V/V_{cr} = 0.78$, include laser anemometer (LA) velocity measurements at about 600 points within the test section and vane surface static pressure measurements. Midspan blade-to-blade LA surveys were made at 11 axial planes (every 10 percent axial chord) within the vane passage. Additional LA surveys were made at several axial stations near the hub and shroud.

The computations were performed on a 91 × 7 × 5 grid (91 normals and 7 contours on 5 equally spaced surfaces of revolution), shown in Fig. 1. The solution converged after approximately 1000 time steps and required abut 10 CPU min on an IBM 3081 computer.

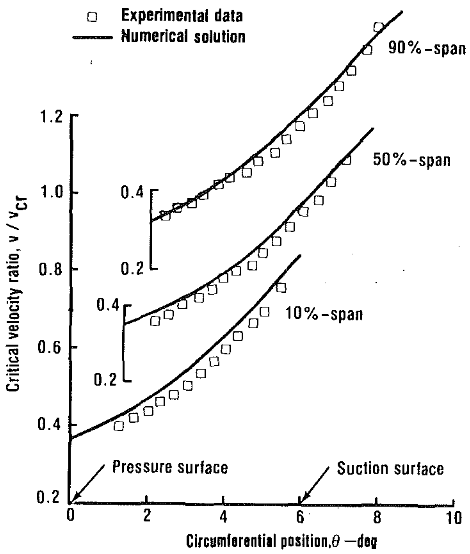

Fig. 7 Comparison of measured and calculated blade-to-blade velocity distributions for the annular turbine vane cascade at 50 percent axial chord (experimental data from [16])

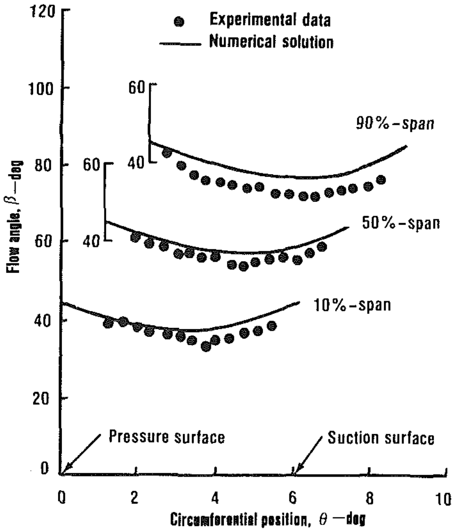

Fig. 8 Comparison of measured and calculated flow angle distributions for the annular turbine vane cascade at 50 percent axial chord (experimental data from [16])

Figure 5 presents a comparison of the calculated and experimentally derived midspan vane surface velocity distributions. Excellent agreement between the two data sets is shown over the entire airfoil surface. It is also clear from Fig. 5 that the analysis method accurately resolved the leading edge flow.

Comparisons of midspan experimental and predicted blade-to-blade flow angle and velocity distributions near the leading edge are given in Fig. 6. Clearly, the analysis accurately predicted all of the flow details in this high gradient region. This is the region where other methods based on more conventional H-type grids show poor predictive capability.

Finally, comparisons of the predicted and experimental blade-to-blade flow angle and velocity distributions at 50 percent axial chord and 10, 50, and 90 percent span are given in Figs. 7 and 8. Again, good correlation is shown at all locations.

Flared Endwall Rectilinear Turbine Blade Cascade. The second example solution is for a flared endwall rectilinear turbine blade cascade tested by Camus et al. [17]. This six-bladed cascade, shown in Fig. 9, was run solely for the purpose of acquiring data to test the accuracy of three-dimensional analyses. To establish a three-dimensional flow, one endwall was flared inward at 22.3 deg. The two central blades were heavily instrumented with static pressure taps on opposing pressure and suction surfaces along a line parallel to the flared endwall. These two blades were mounted on sliding bars and moved across the flow path to map the entire blade surface pressure distribution. The test conditions covered the range of exit Mach numbers from 0.7 to 1.2 and incidence angles from -10 deg to $+5$ deg.

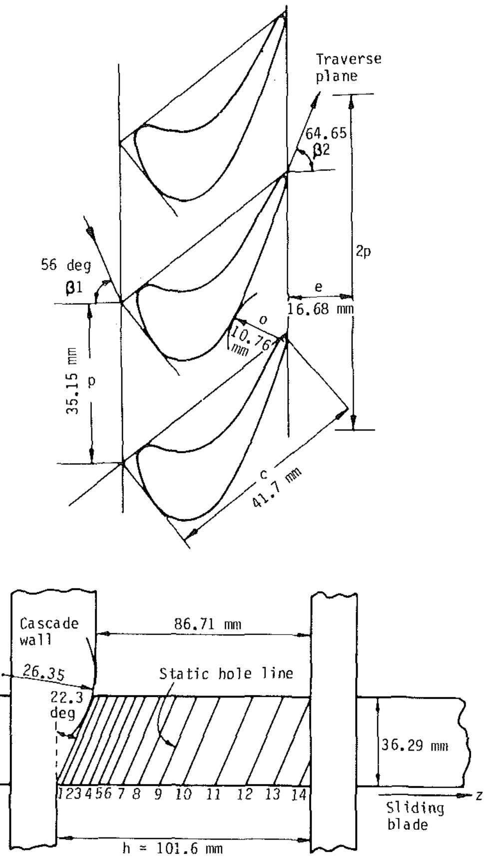

Fig. 9 Airfoil geometry and flow path for the flared endwall rectilinear turbine blade cascade [17]

Calculations were performed on a $91 \times 7 \times 6$ grid over the entire range of reported conditions. All solutions required approximately 1000 time steps and 12 CPU min to converge. Results are presented for incidence angles of 0 deg and -10 deg with exit Mach number $M_I = 1.2$.

Predicted and experimental blade surface Mach number distributions at 8.28 and 48.9 percent span (percent span is measured from the flared endwall) are shown in Figs. 10 and 11, respectively, for incidence angle $i = 0$ deg and in Figs. 12 and 13, respectively, for incidence angle $i = -10$ deg. Results near the flat endwall are not presented because the flow near that surface was dominated by viscous effects resulting from a thick inlet boundary layer [18]. These effects are not modeled with the inviscid Euler solver.

The predictions in Figs. 10-13 show the same high level of agreement with the experimental measurements as that achieved for the annular cascade presented previously. Again, the figures show excellent resolution of the strong leading-edge gradients. The fact that the predictions at the off-design incidence condition in Figs. 12 and 13 are as accurate as those at nominal incidence is of particular interest because Euler solvers based on H-type grids generally yield reduced accuracy at off-design incidence conditions. All of the figures show

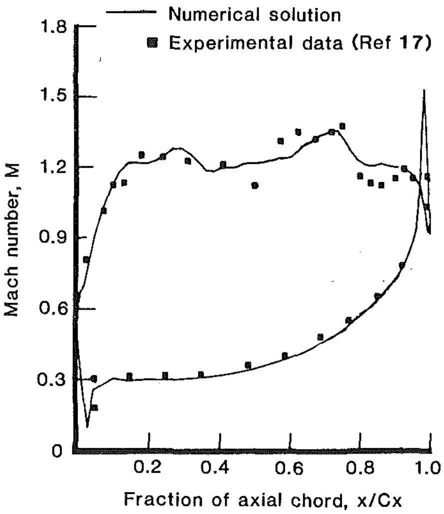

Fig. 10 Calculated and experimental blade surface Mach number distributions for the flared endwall cascade at 8.2 percent span; M_2 = 1.2, i = +0 deg

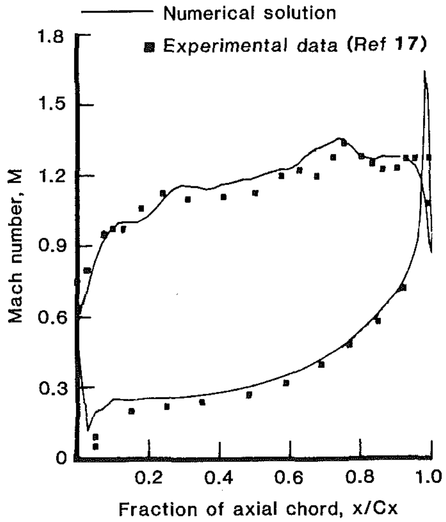

Fig. 11 Calculated and experimental blade surface Mach number distributions for the flared endwall cascade at 48.9 percent span; M_1 = 1.2, i = 0 deg

good correlation between the numerical and experimental Mach number distributions on the uncovered portion of the suction surface downstream of the throat (x/C_x = 0.7), another area where H-grid Euler solvers have shown reduced accuracy due to airfoil trailing-edge geometry approximations.

Conclusions

An accurate and efficient three-dimensional turbomachinery flow analysis method has been presented. The method combines a hopscotch numerical scheme for solution of the three-dimensional time-dependent Euler equations and an O-type body-conforming grid system. The hopscotch scheme has been shown to be computationally efficient and to possess optimal pseudoviscosity damping characteristics. The numerical techniques have been generalized to arbitrary curvilinear coordinates for application to the O-type grid system. The grid is constructed by stacking two-dimensional O-type grids on equally spaced surfaces of revolution. Numerical solution results for two three-dimensional turbine cascade flows have been presented and compared with experimental data to demonstrate the accuracy and computational efficiency of the analysis method.

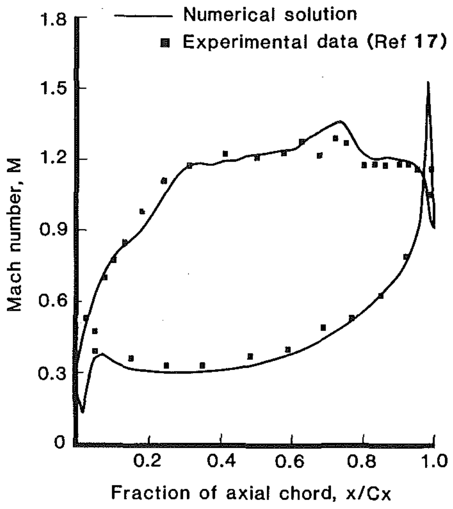

Fig. 12 Calculated and experimental blade surface Mach number distributions for the flared endwall cascade at 8.28 percent span; M_2 = 1.2, i = −10 deg

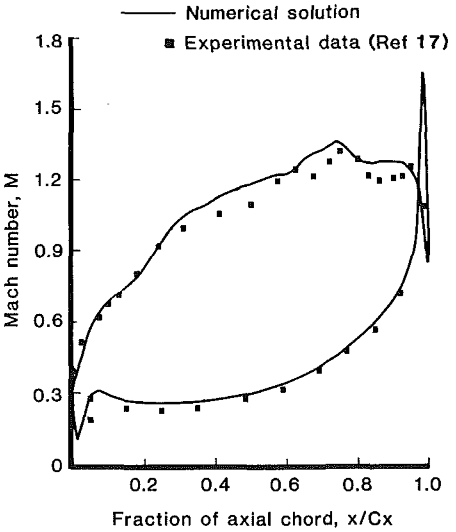

Fig. 13 Calculated and experimental blade surface Mach number distributions for the flared endwall cascade at 48.9 percent span; M_2 = 1.2, i = −10 deg

Although the computations were performed on a scalar computer, the explicit hopscotch scheme is readily modified for efficient operation on vector machines. Future work will involve vectorizing the code for operation on the General Motors Cray X-MP computer. At least an order of magnitude increase in computational speed is expected on this machine.

References

1 Denton, J. D., "A Time-Marching Method for Two-Dimensional and Three-Dimensional Blade-to-Blade Flows," ARC R&M 3775, 1974.

2 Denton, J. D., "Extension of the Finite-Area Time-Marching Method to Three-Dimensions," in: *Transonic Flows in Axial Turbomachinery*, VKI LS 84, 1976.

3 Denton, J. D., "An Improved Time-Marching Method for Turbomachinery Flow Calculation," ASME Paper No. 82-GT-236. 1982.

4 Van Hove, W., "Calculation of Three-Dimensional, Inviscid, Rotational Flow in Axial Turbine Blade Rows," ASME JOURNAL OF ENGINEERING FOR GAS TURBINES AND POWER, Vol. 106, 1984, pp. 430–436.

5 Arts, T., "Calculation of the Three-Dimensional, Steady, Inviscid Flow in a Transonic Axial Turbine Stage," ASME JOURNAL OF ENGINEERING FOR GAS TURBINES AND POWER, Vol. 107, 1985, pp. 286-292.

6 Adamczyk, J. J., "An Electrostatic Analog for Generating Cascade Grids," in: *Numerical Grid Generation Techniques*, NASA Conference Publication 2166, Oct. 1980, pp. 129-142.

7 Dulikravich, D. S., "Fast Generation of Body Conforming Grids for 3-D Axial Turbomachinery Flow Calculations," in: *Numerical Grid Generation Techniques*, NASA Conference Publication 2166, Oct. 1980, pp. 241-252.

8 Delaney, R. A., "Time Marching Analysis of Steady Transonic Flow in Turbomachinery Cascades Using the Hopscotch Method," ASME JOURNAL OF ENGINEERING FOR POWER, Vol. 104, No. 2, Apr. 1983, pp. 272-279.

9 Chima, R. V., "Analysis of Inviscid and Viscous Flows in Cascades With an Explicit Multiple-Grid Algorithm," AIAA Paper No. 84-1663, June 1984.

10 Subramanian S. V., and Bozzola, R., "Application of Runge-Kutta Time Marching Scheme for the Computation of Transonic Flows in Turbomachines," AIAA No. Paper 85-1332, July 1985.

11 Denton, J. D., and Xu, L., "A New Approach to the Calculation of Transonic Flow Through Two-Dimensional Turbomachine Blade Rows," ASME Paper No. 85-GT-5, 1985.

12 Steger, J. L., "Implicit Finite-Difference Simulation of Flow About Arbitrary Two-Dimensional Geometries," *AIAA Journal*, Vol. 16, No. 4, 1978, pp. 679-686.

13 Hindman, R. G., "Geometrically Induced Errors and Relationships to the Form of the Governing Equations and the Treatment of Generalized Mappings," AIAA Paper No. 81-1008, June 1981.

14 Gourlay, A. R., and Morris, J. L., "Hopscotch Difference Methods for Nonlinear Hyperbolic Systems," *IBM Journal of Research and Development*, Vol. 16, No. 4, July 1972, pp. 349-353.

15 Cline, M. C., "NAP: A Computer Program for the Computation of Two-Dimensional, Time-Dependent, Inviscid Nozzle Flow," Los Alamos National Laboratory Report LA-5894, Jan. 1977.

16 Goldman, L. J., and Seasholtz, R. G., "Laser Anemometer Measurements in an Annular Turbine Cascade of Core Turbine Vanes and Comparison With Theory," NASA TP 2018, 1982.

17 Camus, J. J., Denton, J. D., Soulis, J. V., and Scrivener, C. T. J., "An Experimental and Computational Study of Transonic Three-Dimensional Flow in a Turbine Cascade," ASME JOURNAL OF ENGINEERING FOR GAS TURBINES AND POWER, Vol. 106, 1984, pp. 414-420.

18 Camus, J. J., Private Communication, Nov. 1984.

Three-Dimensional Flows and Loss Reduction in Axial Compressors

Y. Dong
S. J. Gallimore
H. P. Hodson

Whittle Laboratory,
Cambridge University,
Cambridge, United Kingdom

Measurements have been performed in a low-speed high-reaction single-stage axial compressor. Data obtained within and downstream of the rotor, when correlated with the results of other investigations, provide a link between the existence of suction surface-hub corner separations, their associated loss mechanisms, and blade loading. Within the stator, it has been shown that introducing a small clearance between the stator blade and the stationary hub increases the efficiency of the stator compared to the case with no clearance. Oil flow visualizaton indicated that the leakage reduced the extensive suction surface-hub corner separation that would otherwise exist. A tracer gas experiment showed that the large radial shifts of the surface streamlines indicated by the oil flow technique were only present close to the blade. The investigation demonstrates the possible advantages of including hub clearance in axial flow compressor stator blade rows.

Introduction

The flow through a multistage axial compressor is very complex, being three dimensional, unsteady, and viscous. As the apparent trend toward higher blade loadings and lower aspect ratios continues, these phenomena will have an even greater effect upon the overall performance of a machine. Present design methods are barely adequate in this context and it is important to improve our understanding of the basic mechanisms of fluid flow in such machines if this situation is to change. This paper is concerned with the character of the three-dimensional flows within a single-stage axial compressor. Particular attention is given to that flow which occurs near the junctions of the blades with the hub and with the casing.

An example of the three dimensionality of the rotor flow field is provided by Dring et al. [1]. At the outlet of an isolated rotor, they observed two regions of high loss, one near each endwall. At the hub, the high loss was associated with the separation of the blade and endwall surface boundary layers near the ends of the suction surface. At the tip, the leakage flow was thought to be responsible. A reduction in the flow coefficient caused the loss region near the hub to extend spanwise across the whole annulus while thinning in the circumferential direction. Simultaneously, the loss region near the tip grew until it occupied most of the pitch. On the rotors of a two-stage machine [2], similar features have been noted. In that study, the flow visualizations revealed large areas of separated flow on the blade surfaces near the hub and significant radial flows.

Joslyn et al. [3] made a similar study of a second-stage stator. A "stalled" region of high loss fluid was observed in the suction surface hub endwall corner which extended up to 75 percent near stall. A small casing corner "stall" also existed, but this diminished in size as the flow coefficient was reduced.

In a two-dimensional cascade, Dean [4] and Lakshminarayana and Horlock [5] have also observed suction surface endwall corner separations. These investigations were concerned with the effects of tip clearance. In both studies, it was found that the extent of the corner separation was reduced when a small amount of tip leakage was present. In all of the tests, a minimum value of total pressure loss occurred when the gap reached approximately 4 percent of the chord. However, it was only when the secondary flows were significant that this minimum loss was less than the zero-clearance value.

Clearly, the three-dimensional flow which exists within an axial compressor requires further investigation. Significantly perhaps, Cumpsty [6], while questioning the relevance of the above compressors to current designs, noted that extensive regions of separated flow appeared on both the rotor [1, 2] and stator [3] blades even at design conditions. Accordingly, the present experimental investigation was undertaken to determine the nature of the flow and the loss mechanisms in a single-stage low-speed axial compressor which is typical of a modern high-pressure stage.

Experimental Facility

All of the experiments were performed in the No. 2 rotating cascade wind tunnel of the Whittle Laboratory. Figure 1 shows the configuration of the single-stage axial compressor. The compressor was a high-reaction free vortex design with blade loadings which are similar to those of modern high-pressure aero-engine compressors. The stage consisted of 51 rotor blades and 36 stators with a hub-to-tip ratio of 0.7. The twisted C4 profiles, fitted to circular arc camber lines, were radially stacked about the center of gravity of the sections. Further details of the blading can be found in Table 1 and [7].

The flow at inlet to the stage was known to be uniform (see below and [7]). The flow coefficient, therefore, was deter-

---

Contributed by the Gas Turbine Division of THE AMERICAN SOCIETY OF MECHANICAL ENGINEERS and presented at the 31st International Gas Turbine Conference and Exhibit, Düsseldorf, Federal Republic of Germany, June 8–12, 1986. Manuscript received at ASME Headquarters February 11, 1986. Paper No. 86-GT-193.

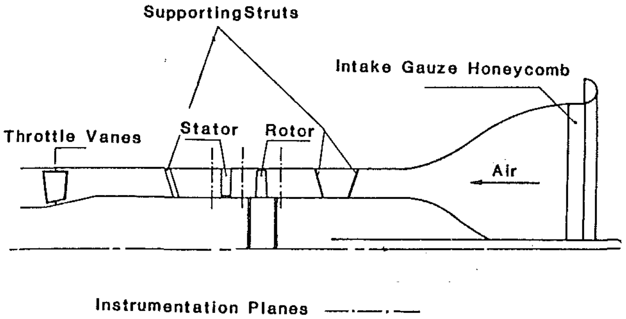

Fig. 1 Single-stage axial flow compressor

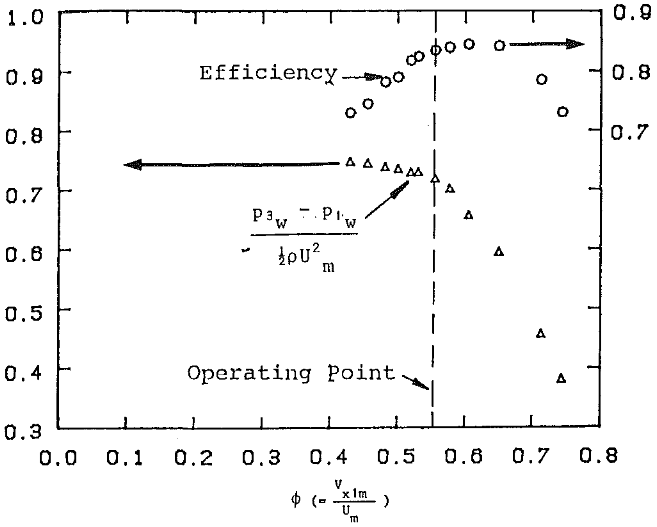

Fig. 2 Compressor overall performance

mined using measurements of the midheight velocity (18.6 m/s) 3.6 blade chords upstream of the rotor. All of the tests were carried out at a rotational speed of 500 rpm, giving a nominal flow coefficient, based upon the mean blade speed, of 0.545 and a Reynolds number of 3.0×10^5 based upon rotor chord and relative inlet velocity. The measured characteristics of this compressor (Fig. 2) show that the chosen flow coefficient was close to that of maximum efficiency. Table 2 provides further information.

Low-blockage (3 mm max dia) pneumatic probes were traversed upstream of the rotor, between the blade rows and downstream of the stage. The location of the traverse planes is shown in Fig. 1. All the pressures were measured using a scanning system connected to a minicomputer. Measurements were only taken when the instantaneous rotor speed was within 1 rpm of the nominal 500 rpm. The random variation of total pressure caused by such variations in the wheel speed was thus equal to 0.4 percent of the relative inlet dynamic head.

A part of the investigation was concerned with a measurement of the radial movement of fluid near the suction surface endwall region of the stator blades using a tracer gas technique, based upon that of Usui and Denton [8]. A small but continuous stream of ethylene was isokinetically injected into the flow through a probe made from 0.5-mm-dia steel tube of a shape which previous tests [9] had shown produced the least amount of interference to the flow. The air, contaminated with ethylene, was sampled at a constant rate through the center hole of a three-hole cobra probe aligned with the flow direction. Concentrations of the order of a few parts-per-million could be detected. The arrangement of the test and the trajectory of the ethylene are shown in Fig. 3.

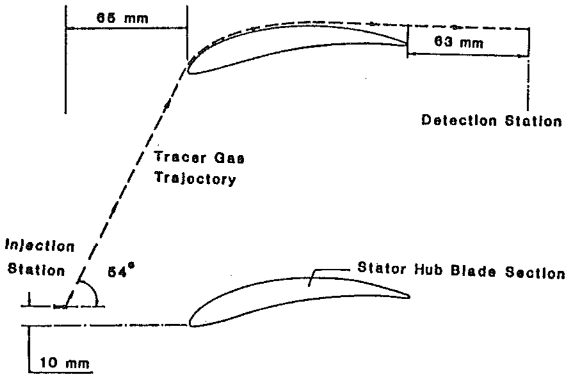

Fig. 3 Tracer gas path line

Table 1 Blade geometry

	Radius ratio	Inlet angle	Exit angle	Solidity	Deviation [11]	Diffusion factor
Rotor						
	0.70	56.6 deg	15.6 deg	1.74	8.9 deg	0.56
	0.85	58.6 deg	36.8 deg	1.43	6.1 deg	0.50
	1.00	61.9 deg	48.8 deg	1.22	4.5 deg	0.43
Stator						
	0.70	37.7 deg	−10.2 deg	1.23	11.6 deg	0.45
	0.85	32.3 deg	−13.2 deg	1.01	11.6 deg	0.43
	1.00	28.1 deg	−15.0 deg	0.86	11.5 deg	0.42

Table 2 Rig geometry and test conditions

	Rotor	Stator
Chord, mm	114.	114.
Aspect ratio	2.0	2.0
Tip diameter, m	1.524	1.524
Clearance-chord ratio	0.017	0.000/0.017
Inlet axial velocity, m/s	18.6	
Rotational speed, rpm	500.	
Flow coefficient, ϕ	0.545	
Reynolds number	3.0×10^5	

Results and Discussion

Rotor. An oil and dye flow visualization mixture was applied to the rotor hub. Because the hub was cylindrical, the oil flow patterns were not affected by the centrifugal force (149*g*) which acts in a direction normal to the surface of the hub.

The results of the visualization are presented in Fig. 4. It

Nomenclature

c = blade chord
D = $(1 - V_2/V_1) + \Delta V_{\theta 12}/2\sigma V_1$
= diffusion factor
p = static pressure
P_0 = total pressure
t = tip (hub) clearance

U = blade speed
V = velocity
ρ = density
σ = solidity (chord/pitch)
ϕ = flow coefficient
ψ = static pressure rise coefficient

Subscripts

m = blade midspan height
w = conditions at casing wall
x = axial direction
θ = tangential direction
1 = upstream of rotor
2 = downstream of rotor
3 = downstream of stator

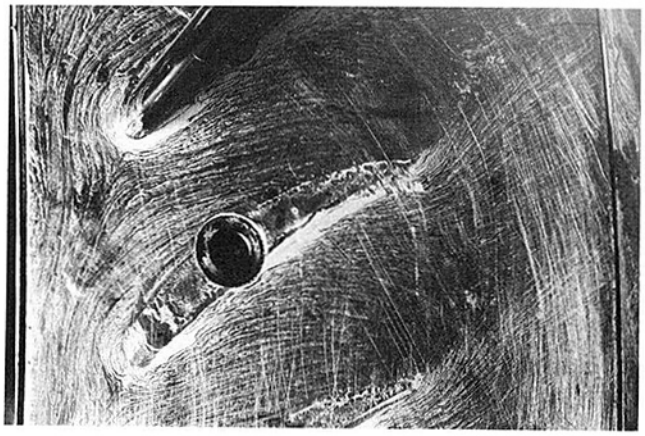

Fig. 4 Rotor hub flow visualizaton

shows that the inlet skew which arises as a result of the relative motion of the hub and the inlet boundary layer is reduced by the action of viscous forces within the boundary layer as the flow develops along the hub. Where the hub boundary layer meets the leading edge of the blades, the oil flow pattern indicates that a horseshoe vortex is formed. The saddle point and separation lines associated with his vortex are clearly visible. Within the blade passage, the oil flow is overturned as a result of the transverse pressure gradient. Consequently, the suction side leg of the horseshoe vortex moves onto the suction surface near the midchord position. The trace of the separation line of pressure side leg of the vortex is only just visible. It appears to leave the passage near midpitch, after which it mixes with the wake. The deviation of the streamlines downstream of the blade row is less than the value indicated by a stationary frame traverse.

The existence of significant overturning within the rotor passage is probably related to the extent of the rotating hub upstream of the rotor blades where the inlet skew is attenuated. In the current compressor, this extension is more typical of machines with cantilevered stators. In the case of shrouded stators, the extension will be less and the skew reduction will not extend as far into the free stream. Thus, since the endwall flow is turned by the free-stream pressure field, the net overturning will be reduced. However, it is the diffusion and loading which dominate the features of the flow near the hub with which this discussion is primarily concerned.

The results of the present flow visualization must be compared with those in [1, 2], both of which revealed significant regions of suction surface–endwall corner separation, albeit only in the suction surface patterns. The hub flow patterns of [1, 2] are inadequate in this context. Although the state of the blade surface boundary layers of the present compressor is not known, the flow visualization on the hub does imply that no such separation exists. This is because, as the stator flow visualization patterns show, a corner separation would have been revealed had it existed.

Figure 5(*a*) shows the axial velocity profile at rotor inlet, measured using the cobra probe. The boundary layers on the hub and the casing are similar in size and shape, both with a thickness of about 10 percent of the span and displacement and momentum thicknesses of 1.4 and 0.9 percent of the span, respectively.

The flow properties downstream of the rotor were also obtained from a radial traverse using the cobra probe. The possibility of circumferential variations being caused by the presence of the stators was examined by making several circumferential traverses at different radial locations. This variation was found to be negligible so that the results of the radial traverse shown in Figs. 5(*b*–*d*) represent the axisymmetric

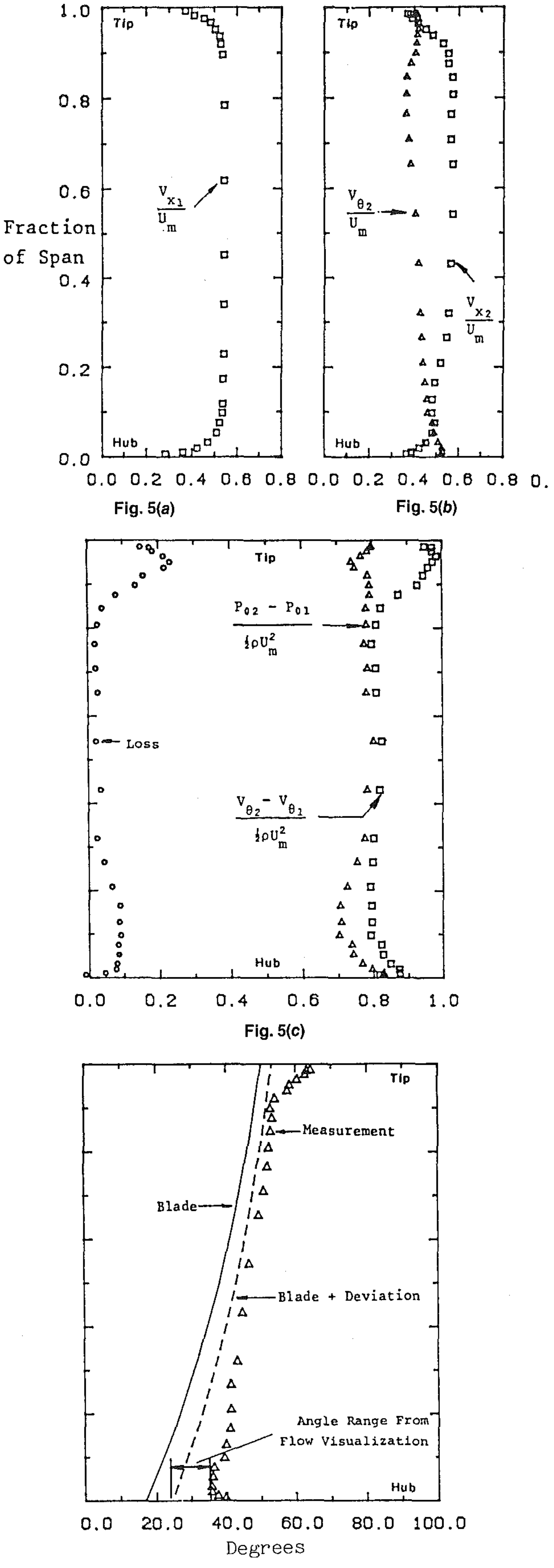

Fig. 5(*a*)

Fig. 5(*b*)

Fig. 5(*c*)

Fig. 5(*d*)

Fig. 5 Velocity distributions: (*a*) rotor inlet, (*b*) rotor exit; (*c*) rotor Euler work input, total pressure rise, and loss distribtion; (*d*) rotor exit angle distribution time-averaged flow downstream of the rotors. In interpreting these results it must be remembered that the traversing position was 96 percent C downstream of the rotor trailing edge and 76 percent C upstream of the stators.

Figure 5(*b*) shows the axial and tangential velocity profiles downstream of the rotor. The thickening of the viscous region close to the casing is readily apparent. Near the hub, a similar thickening occurs. There is also an increase in the blockage. As a result of these effects, the ratio of the midspan axial velocity to the mean blade speed increases from 0.545 upstream of the rotor to 0.570 downstream, which will tend to unload the stator near midspan.

Figure 5(*c*) shows that near the rotor tip at about 95 percent span, the total pressure rise drops below that obtained at midheight. However, it then increases as the outer casing is approached until it again reaches the midspan value very close to the wall. In contrast, the specific work input (calculated using Euler's work equation) increases between about 86 and 96 percent span before decreasing as the wall is approached. The rotor therefore performs extra work within the endwall boundary layer but this process is less efficient near the casing and as a consequence, the deviation increases (see Fig. 5*d*). The variations of total pressure rise and input work coefficients follow similar trends toward hub but the loss of efficiency, which is represented by the difference between them, becomes smaller very near the wall. This is thought to be due to the flow redistribution caused by the three-dimensional flows as well as additional work input by the viscous force as the flow passes through the rotor.

In the region of the midspan, the efficiency reaches a maximum of 97 percent and the profile loss coefficient, based on the rotor relative inlet velocity, is equal to 0.018. This value is comparable with that obtained for blades with similar loadings [10], where the blades were operating near to the condition of minimum loss. By integrating over the entire span, the total-to-total efficiency of the rotor is found to be 93 percent.

Figure 5(*d*) shows the spanwise variation of the rotor-relative exit flow angle derived from the cobra probe measurements. Also shown are the predicted values obtained using the deviation rule [11] together with the range of values indicated by the flow visualization. Near the tip, the clearance results in an increased deviation. Between 30 and 90 percent of the span however, there is reasonable agreement between the measurements and predictions. This, together with the measured small loss in this region (Fig. 5*c*), suggests that there is very little three-dimensional flow in this region. At the hub the deviation is much greater than predicted, a result which is thought to be due to the presence of the rotating hub. The resulting skew at the hub does not however remove the relative under and overturning which suggests that a passage vortex exists near 10 percent of the span. The relatively high loss, blockage, and increased deviation between the hub and 25 percent span may be a consequence of this secondary flow, but it is also possible that a blade suction surface separation has occurred. It is also apparent that, from the results of the radial traverses (Fig. 5), there is no evidence of the excessive loss which might be associated with a large area of corner stall, thus reinforcing the conclusion drawn from the flow visualization experiment that no such phenomenon exists.

It has been demonstrated that the major difference observed of flow features in the rotor of present work and those of previous investigations [1, 2] is the behavior of the flow in the vicinity of the hub. An estimation of blade loading using blade angles and predicted deviation [11] suggests that the designed diffusion factors along the span of the isolated rotor of [1] are well beyond the conventional limit of 0.6, the value which is often taken as an indication of the onset of stall or separation. Near the hub, the diffusion factor should reach a value of about 0.96. In practice, however, the above-mentioned hub section operates at approximately 10 deg of negative incidence [2] so the diffusion factors based upon the actual inlet angle and predicted exit angle are smaller, ranging from 0.63 at the tip to 0.57 at midspan and 0.63 at the hub. The diffusion factor of the present rotor is equal to 0.43 at the tip, increasing to 0.50 at midspan and 0.56 at the hub. Of course, using the diffusion factor to assess the loading is probably not justified near the endwall regions where viscous and three-dimensional effects play an important role. Nevertheless, in the rotors of [2] the high turning of the blade close to hub with a moderate value of solidity must be the cause of the separation. The blockage formed by the separated flow will reduce the diffusion and therefore pressure gradient across the passage. This may contribute to the absence of signs of secondary flow. In the case of the second rotor of the two-stage machine [2] the diffusion factor is estimated to be equal to 0.51 at midspan, approaching 0.61 near the hub where a corner separation was also observed, and the loss is much smaller than that of the isolated rotor [1]. Comparing the diffusion factors, etc., and the magnitude of the corner separations of the rotors of [1, 2] with those of the current rotor leads to the conclusion that the substantial separation and therefore high loss was a result of the excessive diffusion chosen for the design.

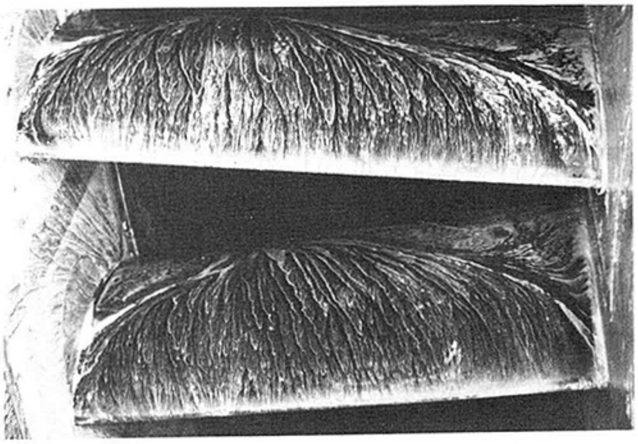

Fig. 6 Stator suction surface flow visualization (hub clearance sealed)

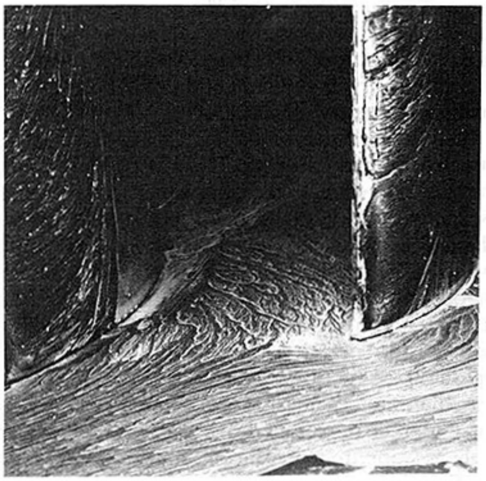

Fig. 7 Stator hub flow visualization (hub clearance sealed)

Stator With Sealed Hub. A surface oil flow visualization experiment was also performed in the stator row. The results are shown in Figs. 6 and 7. Care must be taken when examining

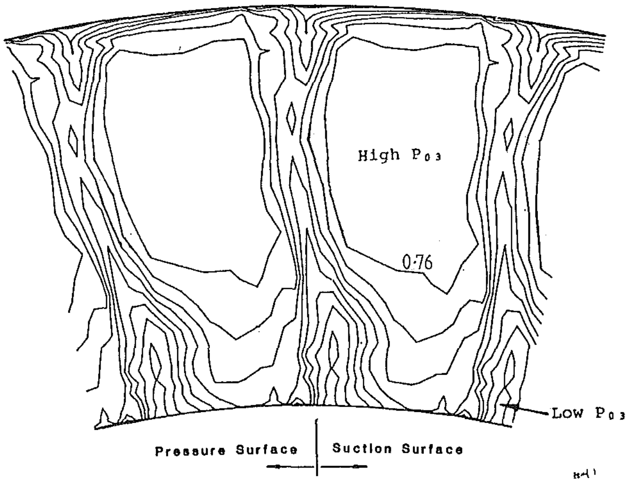

Fig. 8 Stator exit total pressure contours—contour interval (hub clearance sealed) $C_{pt_3} = (P_{03} - P_{01_m})/(\frac{1}{2}\rho U_m^2) = 0.04$

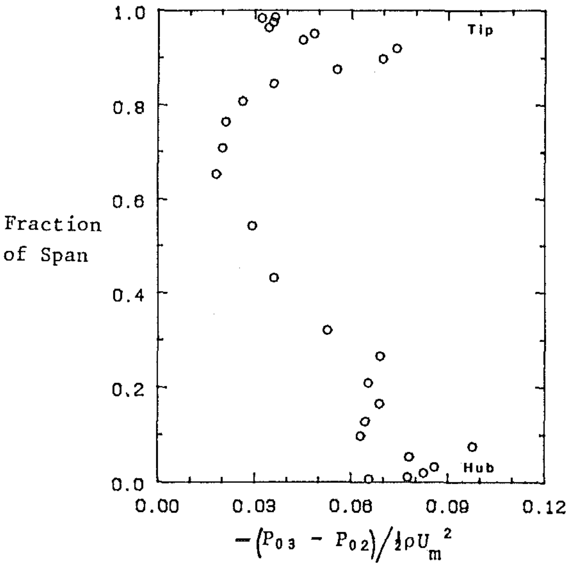

Fig. 9 Circumferentially averaged total pressure loss across stator (hub clearance sealed)

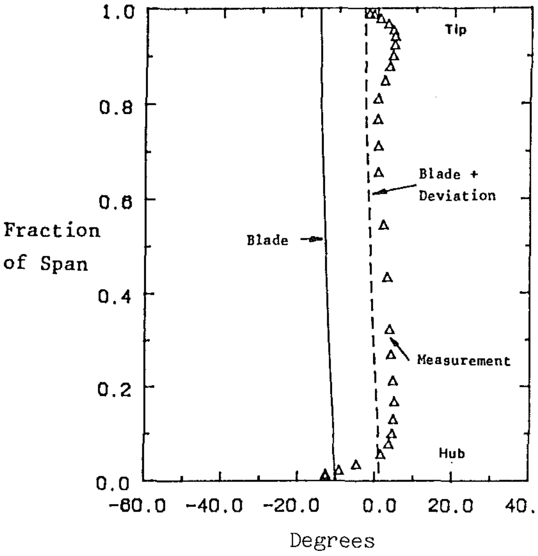

Fig. 10 Stator exit angles

these values since gravity was found to affect the oil flow. The direction of gravity is indicated. Only those surfaces which were horizontal are discussed.

The suction surfaces of the stator blades, viewed from upstream, are shown in Fig. 6. The most striking features are the two regions of separated flow which originate near the hub and casing endwalls. The separation near the hub begins close to the leading edge and has extended to beyond midspan near the trailing edge. There appears to be a large amount of radial outflow on the blade surface both within and outside of the separation area. A region of backflow, very similar to that seen on the rotor of [1], is also visible within the separated flow region on the suction surface near to the hub. The separation near the outer casing has the same characteristics but is somewhat smaller in extent, starting nearer the trailing edge. Although not apparent in the photograph, this test showed that the flow is separated across the entire span near to the trailing edge of the suction surface.

In contrast to the situation on the suction surface, the visualization showed that the flow was essentially two dimensional on the pressure surface.

On the hub endwall (Fig. 7), it can be seen that the stagnant flow region extends to some 20 percent of the pitch away from the suction surface. Outside this area the endwall flow is overturned by the cross passage pressure gradient, the effect of inlet skew being apparently negligible. On the outer casing, the flow visualization pattern revealed similar characteristics.

The results of the flow visualization of Joslyn et al. [3] on a second-stage stator of similar diffusion characteristics to the present stator also revealed the presence of hub and tip corner separations on the suction surface even at the design condition. Similarly, the flow on the pressure surface was essentially two dimensional. However, the behavior of the flow on the hub differs in that the present results show significant cross passage secondary flows outside the stagnant flow regions while the results of [3] showed no such large effects. As in the case of the present rotor, the reduction in skew may be responsible for this observation, although differences in the flow visualization techniques may also contribute.

Measurements of the stator outlet flow were obtained using a Kiel probe which was aligned with the nominal flow direction. Contours of the stator exit stagnation pressure are shown in Fig. 8. Regions of relatively low stagnation pressure exist near the corners of the blade suction surface and the hub and tip endwalls. Similar regions have been found by Joslyn et al. [3] in the second stator of a two-stage machine but in the present discussion, these features will not be referred to as "corner stall." As Fig. 8 shows, the high loss region near the tip is smaller than that near the hub. It is also confined close to the blade suction surface. The high loss region near the hub is larger both in the spanwise and pitchwise directions, although its core again lies adjacent to the suction side of the passage. Between the high loss region near the hub and the wake of the adjacent blade, the free-stream stagnation pressure is not constant, a result which is mainly due to the radial profile of stagnation pressure (Fig. 5*c*) which exists at stator inlet. The fact that the contours in the above-mentioned region are not circumferential indicates that some redistribution of the Bernoulli surfaces has occurred.

The spanwise distribution of the total pressure loss has been calculated using a mass-weighted average. Since the majority of the measurements were made using the Kiel probe, it has been necessary to use the static pressure and yaw angle data obtained using the cobra probe during a radial traverse at midpitch in order to reduce the Kiel probe data. The traverse plane was located 0.55 chord lengths downstream of the stator. Therefore, the inaccuracies inherent in this method of data reduction are considered to be insignificant. The pitchwise-averaged results are shown in Fig. 9. High loss regions appear

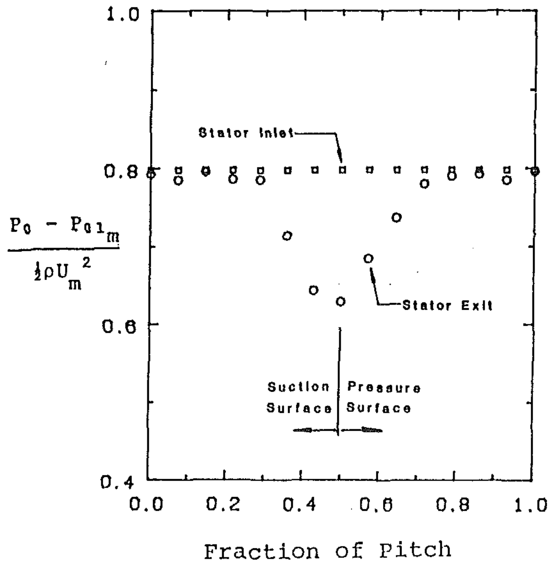

Fig. 11 Circumferential distributions of total pressure near midspan of stator

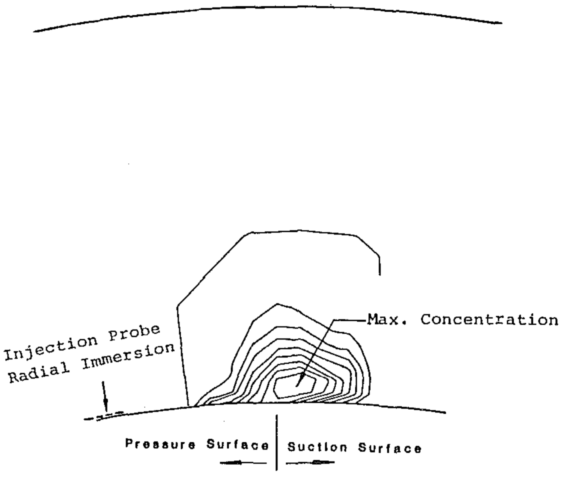

Fig. 12 Traced gas concentration contours

near the endwalls, with that nearer the hub being greater both in spanwise extent and in loss. The flow is also overturned in these regions, particularly near the hub (Fig. 10).

The circumferential variation of the total pressure coefficient at the midspan of the stator is plotted in Fig. 11. To produce this result, the inlet total pressure profile was assumed to be axisymmetric. It is found that there is a small reduction in the free-stream total pressure, that is, between the wakes. Whether this is due to a radial movement of the stream tubes or further mixing of the upstream rotor wakes is unclear. Significantly, perhaps, its magnitude (15 percent of the total) is such that doubt must be cast upon the generality of the results published in [12], where it was observed that approximately one third of the average total pressure loss across the stator midspan was due to a change in the free-stream total pressure which could not be accounted for using conventional theories.

In the present work, the flow visualization indicated that there were large radial movements within the stator suction surface hub endwall corner whereas the probe traverses only revealed a region of high loss which was confined near the suction side of the passage. The authors of [3] also suggest that radial redistribution is significant and that it is caused by the blockage associated with the corner separation and the radial flow within that region. Therefore it was decided to determine, using a tracer gas, the extent to which the radial flows indicated in the surface flow visualization caused a radial redistribution of the flow. The use of a tracer gas to follow the streamlines in turbomachinery flows is a well-established technique (e.g., [8]). Wagner et al. [13] used carbon dioxide to investigate the radial distortions of the stream surfaces as they passed through a compressor rotor row. Ths study has particular relevance to the present work because the experiments were conducted on the same rotor for which substantial areas of separation, and hence large radial flows, were found on the suction surface [2]. However, the carbon dioxide contours downstream of the rotor did not seem to show as much radial distortion as one might have expected if these radial flows were as significant as they appeared from the flow visualization on the blades.

Only one test was conducted to investigate the flow over the stator suction surface after preliminary tests had ensured that the bulk of the ethylene appeared in the high loss region measured downstream of the stator near the hub. The equispaced concentration contours obtained by making an area traverse downstream of the stator trailing edge are shown in Fig. 12. The height of the injection probe (0.8 percent span) is also indicated. Close to the hub the contours have been swept across the passage toward the suction surface by the overturning of the flow at stator exit (Figs. 6 and 7). The position of the maximum concentration has remained close to the endwall as the flow passed through the passage, indicating that there is little net radial flow. Indeed, the shape of the contours also indicates a lack of radial flow since the contours exhibit shapes which can only be associated with a uniform spreading of the ethylene. Although it cannot be certain that some of the ethylene passed along the suction surface of the blade and so experienced the relatively large radial displacements indicated by the flow visualization, the fact that the region of peak concentration is coincident with the area of peak loss (Fig. 8) would imply that this was the case. This result therefore implies that the large radial movements toward the casing observed in the flow visualization on the suction surface do not extend very far from that surface. Indeed, the tangential extension of the low-energy fluid near the hub is little different from that of the wake near midspan. Similar but more extensive work [9] on the stator of similar design in a four-stage compressor confirms this view. The work of Wagner et al. [13] also showed that radial distortions of the stream surfaces were localized near the blade surface. Thus, the radial redistribution of the stream surfaces which was noted in Fig. 8 must be a consequence both of the secondary flows and the blockage which are known to exist. This further suggests that while most of the high loss fluid which is found near the suction side of the wake close to the hub undoubtedly comes from the region of separated flow, the source of the remainder lies elsewhere.

The flow visualization on the hub (Figs. 6 and 7) indicated a significant movement of low energy fluid away from the pressure surface toward the suction surface. Results obtained using the cobra probe at midpitch (Fig. 10) indicate that this overturning also occurs at some distance from the surface. Therefore, it is suggested that a significant portion of the high loss fluid originates in the endwall boundary which is then swept across the blade passage by the secondary flow. Because the region of high loss is not due entirely to the separation of the boundary layers, these regions have not been referred to as "corner stall." A similar conclusion may be drawn about the high loss region near the stator tip, even though it is much less significant.

Stator With Clearance Gap at the Hub. It has been reported in the open literature that a small tip clearance may have a beneficial effect upon blade row performance [4, 5]. Therefore, given the extensive suction surface–endwall separations and significant secondary flows, it was decided to in-

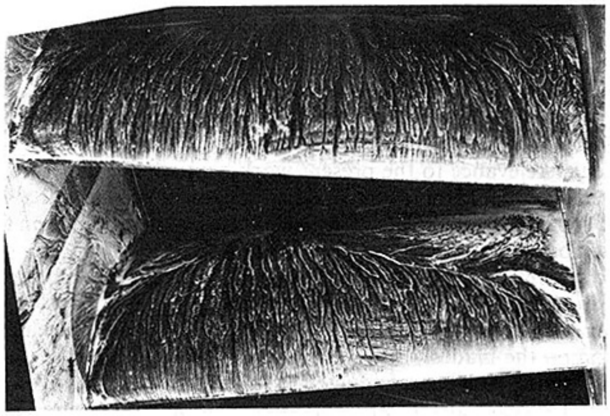

Fig. 13 Stator suction surface flow visualization (hub clearance unsealed and sealed)

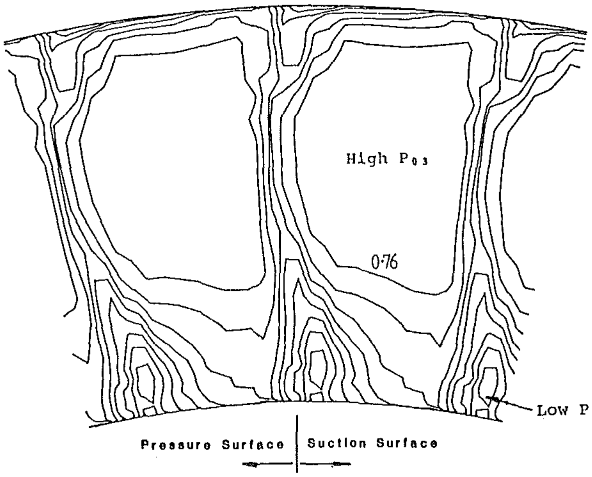

Fig. 14 Stator exit total pressure contours—contour interval (hub clearance unsealed) $C_{pt_3} = (P_{03} - P_{01_m})/(\frac{1}{2}\rho U_m^2) = 0.04$

vestigate the possibility of incorporating a clearance into the present design. A clearance of 1.7 percent chord was provided between the stator blade and the stationary hub. The hub rather than the tip was provided with the clearance because the separation was greatest there. It is also more practical.

The surface flow patterns on a stator both with and without this clearance are shown in the composite photograph of Fig. 13. The flow patterns on the two blades were obtained during two separate experiments. The difference is self-evident. Providing a hub clearance significantly reduces the extent of the suction surface separation. It begins much later and occupies far less of the span. This effect is thought to be caused by the leakage flow through the gap from the pressure to the suction side. It is driven by the pressure difference across the end of the blade, which energizes the low-momentum fluid in the suction surface endwall corner and thus delays blade separation.

In order to assess any improvement in performance the stator inlet and exit flows were traversed using pneumatic probes. The distribution of total pressure, measured using the Kiel probe at stator exit, is shown in Fig. 14. The high loss regions near the suction surface-endwall corner, observed with the sealed stator, are again apparent. A comparison between this result and that obtained with a sealed root shows that the extent of this low-energy fluid is reduced. This confirms the result suggested by the flow visualization. It is also apparent that the wake loss is smaller in the case with clearance. The fact that the region of highest loss occurs further away from the suction surface and that the peak is more diffuse when the gap is present reinforces the suggestion that the secondary flow indicated in the endwall flow visualizations involve the movement of low-energy fluid in this region.

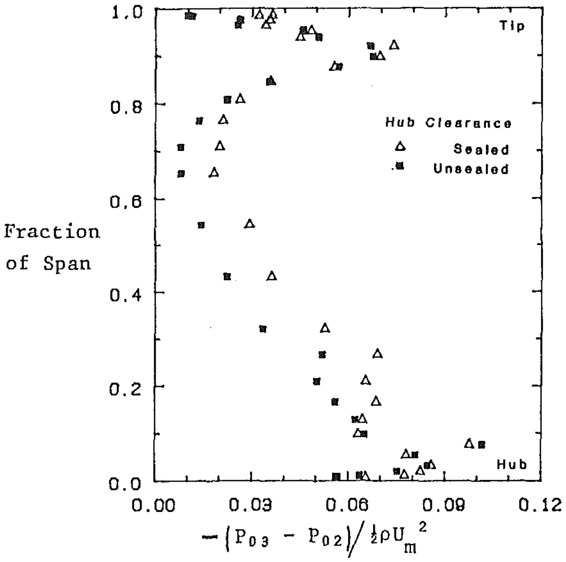

Fig. 15 Circumferentially averaged total pressure loss across stator

Figure 15 shows the spanwise variation of the circumferentially integrated total pressure at exit from the stator with a clearance at the hub together with the result for the sealed case. This clearly shows the improvement in stator performance when the gap is introduced. Much of this improvement is to be found between 10 and 80 percent span which indicates that the improved performance particularly results from a reduction in the severity of the separation on the blade surface but also from a suppression of the secondary flows by the hub leakage. Previous experimental investigations [4, 5] have shown that if, in the presence of a stationary endwall, the secondary flow is small, then a clearance does not reduce the overall loss despite a reduction in the size of the suction surface separation. This is presumably due to the relative magnitudes of any reduction and the newly introduced hub leakage loss. This is also suggested by the results of Fig. 15.

The stator of [3] has a loading which is similar to the present design. In that case also, a significant region of high loss fluid was found near the hub endwall. Thus, it is possible that such a situation exists in all machines of modern design. A spanwise integration reveals that the state efficiency is increased from 88.5 to 89.7 percent as the stator total pressure loss coefficient reduces from 0.041 to 0.031. Therefore, it appears that a certain amount of hub leakage between a stationary hub and a stator blade may be beneficial in such machines.

Conclusions

Experiments have been performed in a low-speed high-reaction single-stage axial flow compressor operating near the point of maximum efficiency. Comparisons with the results of other investigations indicate that excessive diffusion appears to result in substantial regions of separated flow near the junctions of the blade suction surfaces and the endwalls. As a consequence, an unnecessary deterioration in performance can be expected.

On the hub of the present rotor, where the diffusion factor is equal to 0.56, significant secondary flows were observed. There was, however, no evidence of the suction surface-endwall separation mentioned above and observed in other compressors.

At both ends of the stator, these suction surface-endwall corner separations did exist, that at the hub being greatest. The surface flow visualization suggested the existence of large radial movements of the surface flow within and outside these regions. A tracer gas experiment showed that the radial flows observed must only occur very close to the suction surface. The separations in the suction surface-endwall corners and the secondary flows were responsible for the high loss found downstream.

The introduction of a clearance between the stator blade and stationary hub significantly reduced the extent of the suction surface-hub separation with a simultaneous decrease in the loss. Comparisons with other investigations suggest that such a clearance might be beneficial in all modern machines similar to that investigated.

Acknowledgments

The authors are indebted to Dr. N. A. Cumpsty whose comments first suggested the work described here and with whom the authors had many welcome discussions. Thanks must also go to Mr. A. D. Jackson who provided much of the information necessary to operate the experimental facility. The compressor blades were originally supplied by Rolls-Royce P.L.C.

References

1 Dring, R. P., Joslyn, H. D., and Hardin, L. W., "An Investigation of Compressor Rotor Aerodynamics," ASME Journal of Engineering for Power, Vol. 104, 1982, pp 84–96.

2 Dring, R. P., Joslyn, H. D., and Wagner, J. H., "Compressor Rotor Aerodynamics," AGARD-CP-351, Copenhagen, 1983.

3 Joslyn, H. D., and Dring, R. P., "Axial Compressor Stator Aerodynamics," ASME Journal of Engineering for Gas Turbines and Power, Vol. 107, 1985, pp. 485–493.

4 Dean, R. C., Jr., "The Influence of Tip Clearance on Boundary Layer Flow in a Rectilinear Cascade," MIT Report No. 27-3, 1954.

5 Lakshminarayana, B., and Horlock, J. H., "Leakage and Secondary Flows in Compressor Cascades," A.R.C. R & M 3483, 1967.

6 Cumpsty, N. A., see discussion of [3].

7 Jackson, A. D., "Stall Inception in Axial Compressors," M.Sc. Thesis, Cambridge Univ. Eng. Dept., 1985.

8 Denton, J. D., and Usui, S., "Use of a Tracer-Gas Technique to Study Mixing in a Low Speed Turbine," ASME Paper No. 81-GT-86.

9 Gallimore, S. J., "Spanwise Mixing in Axial Flow Compressors,"' Ph.D. Thesis, Cambridge Univ. Eng. Dept., to be submitted.

10 "Aerodynamic Design of Axial Flow Compressors," NASA SP-36, 1965, p. 205.

11 McKenzie, A., "The Design of Axial Compressor Blading Based on Tests of a Low Speed Compressor," *I. Mech. E. Proc.*, Vol. 194, No. 6, 1980.

12 Okiishi, T. H., Hathaway, M. D., and Hansen, J. L., "A Note on Blade Wake Interaction Influence on Compressor Stator Row Aerodynamic Performance," ASME Journal of Engineering for Power, Vol. 107, 1985, p. 549.

13 Wagner, J. H., Dring, R. P., and Joslyn, H. D., "Inlet Boundary Layer Effects in an Axial Compressor Rotor: Part II—Throughflow Effects," ASME Journal of Engineering for Gas Turbines and Power, Vol. 107, 1985, pp. 381–386.

corner separations did exist, that at the hub being greatest. The surface flow visualization suggested the existence of large radial movements of the surface flow within and outside these regions. A tracer gas experiment showed that the radial flows observed must only occur very close to the suction surface. The separations in the suction surface–endwall corners and the secondary flows were responsible for the high loss found downstream.

The introduction of a clearance between the stator blade and stationary hub significantly reduced the extent of the suction surface–hub separation with a simultaneous decrease in the loss. Comparisons with other investigations suggest that such a clearance might be beneficial in all modern machines similar to that investigated.

Acknowledgments

The authors are indebted to Dr. N. A. Cumpsty whose comments first suggested the work described here and with whom the authors had many welcome discussions. Thanks must also go to Mr. A. D. Jackson who provided much of the information necessary to operate the experimental facility. The compressor blades were originally supplied by Rolls-Royce P.L.C.

References

1 Dring, R. P., Joslyn, H. D., and Hardin, L. W., "An Investigation of Compressor Rotor Aerodynamics," ASME Journal of Engineering for Power, Vol. 104, 1982, pp 84–96.

2 Dring, R. P., Joslyn, H. D., and Wagner, J. H., "Compressor Rotor Aerodynamics," AGARD-CP-351, Copenhagen, 1983.

3 Joslyn, H. D., and Dring, R. P., "Axial Compressor Stator Aerodynamics," ASME Journal of Engineering for Gas Turbines and Power, Vol. 107, 1985, pp. 485–493.

4 Dean, R. C., Jr., "The Influence of Tip Clearance on Boundary Layer Flow in a Rectilinear Cascade," MIT Report No. 27-3, 1954.

5 Lakshminarayana, B., and Horlock, J. H., "Leakage and Secondary Flows in Compressor Cascades," A.R.C. R & M 3483, 1967.

6 Cumpsty, N. A., see discussion of [3].

7 Jackson, A. D., "Stall Inception in Axial Compressors," M.Sc. Thesis, Cambridge Univ. Eng. Dept., 1985.

8 Denton, J. D., and Usui, S., "Use of a Tracer-Gas Technique to Study Mixing in a Low Speed Turbine," ASME Paper No. 81-GT-86.

9 Gallimore, S. J., "Spanwise Mixing in Axial Flow Compressors,"' Ph.D. Thesis, Cambridge Univ. Eng. Dept., to be submitted.

10 "Aerodynamic Design of Axial Flow Compressors," NASA SP-36, 1965, p. 205.

11 McKenzie, A., "The Design of Axial Compressor Blading Based on Tests of a Low Speed Compressor," *I. Mech. E. Proc.*, Vol. 194, No. 6, 1980.

12 Okiishi, T. H., Hathaway, M. D., and Hansen, J. L., "A Note on Blade Wake Interaction Influence on Compressor Stator Row Aerodynamic Performance," ASME Journal of Engineering for Power, Vol. 107, 1985, p. 549.

13 Wagner, J. H., Dring, R. P., and Joslyn, H. D., "Inlet Boundary Layer Effects in an Axial Compressor Rotor: Part II—Throughflow Effects," ASME Journal of Engineering for Gas Turbines and Power, Vol. 107, 1985, pp. 381–386.

DISCUSSION

R. P. Dring[1]

The authors have presented some very welcome and interesting results on the occurrence and impact of corner separation in an axial compressor stage which is "typical of a modern high-pressure stage." However, in comparing their results with those of [1–3, 13] some additional observations can be made.

The authors state that corner separation is probably not present at their rotor hub since it can not be seen in their endwall flow visualization (Fig. 4). However, the flow visualization results of [2] (Figs. 2 and 3) show that corner separation can definitely be present on an airfoil without any strong evidence of its presence in the endwall flow visualization.

The authors suggest that the relatively high loss, deviation, and blockage at the hub of their rotor (Fig. 5) may be a consequence of secondary flow and/or blade suction surface separation and that they are probably not associated with corner separation since the loss is not "excessive." However, the loss distributions in [2] (Figs. 7 and 8) show that rotors with corner separation can have loss distributions which are similar to those reported by Dong et al. (Fig. 5*c*).

The authors conclude that the corner separation on the rotors of [1, 2] is due to "excessive diffusion." In fact, however, the diffusion factors calculated in both the pretest design analysis and those calculated from the measured inlet and exit flow data were well within conventional limits for both of the rotors in [1–3]. These diffusion factors ranged from 0.5 to 0.6 at the hub to 0.45 in the core flow region. These values are very close to the values quoted by Dong et al. for their rotor (Table 1).

To summarize, the rotor flow described by Dong et al. is very similar in many respects to those of [1, 2]. The arguments that their rotor did not have corner separation are not convincing. It is regrettable that blade surface flow visualization results are not available for their rotor.

The stator investigated by Dong et al. had diffusion factors in the range of 0.42 to 0.45. The stator of [3] at its nominal design flow coefficient had diffusion factors from 0.45 to 0.55. In spite of these relatively modest levels both stators had massive corner separation, even at nominal design conditions.

For rotors and stators corner separation can result from "excessive diffusion"; however, the occurrence of corner separation does not necessarily imply a diffusion factor which is "beyond the conventional limit of 0.6." None of the airfoils in this discussion were beyond this limit. This fact can also be seen in the work of Cyrus [14] and in the work of Gallus and Hoenen [15]. The question remains open as to the occurrence and importance of corner separation in typical modern compressor designs. Additional input to the literature from other researchers would be of considerable value.

References

14 Cyrus, V., "Experimental Study of the Three-Dimensional Flow in an Axial Compressor Stage," ASME Paper No. 86-GT-118, 1986.

15 Gallus, H. E., and Hoenen, H., "Experimental Investigations of Airfoil and Endwall Boundary Layers in a Subsonic Compressor Stage," ASME Paper No. 86-GT-143, 1986.

---

[1] Manager, Gas Turbine Technology, United Technologies Research Center, East Hartford, CT 06108.

Through-Flow Models for Mass and Momentum-Averaged Variables

C. Hirsch
Vrije Universiteit Brussel,
1050 Brussels, Belgium

R. P. Dring
United Technologies Research Center,
East Hartford, CT 06108

The turbomachinery through-flow equations are reformulated for mass and momentum-averaged quantities. The background of this analysis is the need for an improved assessment of the accuracy of through-flow computations. Traditional through-flow analyses are based on density-weighted averaged quantities reducing to an area average in incompressible flows. On the other hand, experimental data are usually evaluated under the form of mass-averaged quantities, particularly with regard to the overall energy balance and efficiency estimations. The transition between these two sets of quantities is usually taken into account by introducing an averaged aerodynamic blockage factor in addition to the blade blockage factor resulting from the density-averaged quantities. The present analysis provides a rigorous derivation for the momentum-averaged flow quantities and shows that some strong assumptions on the nature of the nonaxisymmetric flow components are necessary in order to justify the current practice of introducing aerodynamic blockage. The recent availability of detailed flow data in single and two-stage axial compressors allows a partial validation of these assumptions, by the comparison of the various nonaxisymmetric components.

Introduction

Classical through-flow analysis models, as applied in aerodynamic design systems of turbomachinery, are generally based on density-weighted averaged quantities (reducing to area averages in incompressible flows) [1-4]. This formulation leads to the introduction of additional "interaction" terms, having the same structure as the turbulent Reynolds stress, but arising from the nonaxisymmetry of the flow and contributing to the averaged radial equilibrium. These interaction terms have to be evaluated explicitly in quasi-three-dimensional modifications of turbomachinery flows whereby iterative computations of through-flows (S2 surfaces) and axisymmetric blade-to-blade (S1 surfaces) flows are performed, with appropriate data being transmitted from one family to the other family of surfaces [3, 5].

An alternative to the explicit evaluation of the interaction terms, as describing the effects of the nonaxisymmetry on the averaged flow, is to introduce instead an aerodynamic blockage factor, based on mass flow considerations, in addition to the blade blockage resulting from the density-weighted averaging. This approach is followed by Calvert and Ginder [6] in order to define a consistent quasi-three-dimensional interactive procedure. These authors rightly point out that their aerodynamic blockage factor should contain the same information on the nonaxisymmetry of the flow as the interaction terms, and that its use in the continuity equation replaces the interaction terms in the radial equilibrium momentum equation. As a consequence of this, Calvert and Ginder define a mass-averaged through-flow instead of the density-weighted area-averaged flow considered by the previously mentioned authors.

Earlier, both the present authors had separately stressed the importance of the introduction of an aerodynamic blockage in through-flow evaluation methods [7, 8]. More particularly, this last reference proposes a quantitative definition of blockage as the ratio between the axial velocity component based on mass-averaged quantities and the area-averaged axial velocity component. Based on the extensive data base for single and multistage axial compressors obtained in the last years by the second author and his co-workers [9-14], quantitative evaluations of the blockage factor were made possible, showing its importance particularly near the end walls. This has been confirmed more recently by Dring and Joslyn [15-17], who showed that both the level and spanwise distribution of aerodynamic blockage are important and have a strong impact on the computed flow field at the outlet of blade rows. In these latter analyses the computed quantities were also considered as mass-averaged quantities.

The debate between the two families of averaged quantities is central to the validation of through-flow models. On one hand, coherent through-flow models can be defined for density-area-averaged quantities, but on the other hand, physical arguments and the strong connection between mass-averaged quantities, like stagnation pressure, total energy, and machine efficiency, are essential to the correct estimation of the energy exchange within the turbomachinery blade row.

Contributed by the Gas Turbine Division of THE AMERICAN SOCIETY OF MECHANICAL ENGINEERS and presented at the 32nd International Gas Turbine Conference and Exhibit, Anaheim, California, May 31-June 4, 1987. Manuscript received at ASME Headquarters February 4, 1987. Paper No. 87-GT-52.

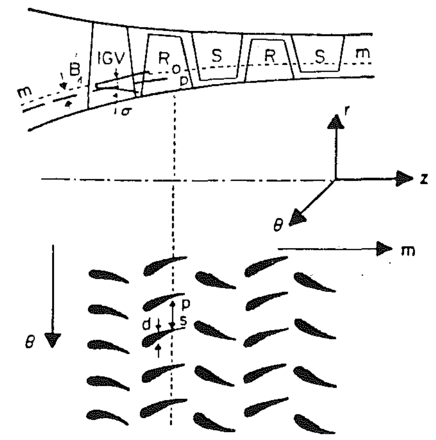

Fig. 1 Through-flow modeling—meridional and blade-to-blade planes

The present report aims at the derivation of a consistent through-flow model for mass, or more precisely, momentum-averaged flow variables. A consistent model can be obtained, at the cost of six different blockage coefficients, depending on which components of the momentum flux are to be considered.

As will be shown, if the strong assumption is made of the equality of all the blockage coefficients, then a simplified model is obtained, which entirely justifies the semi-intuitive approaches followed by Calvert and Ginder [6] and Dring and Joslyn [15]. Comparison with experimental data allows an evaluation of the limits of validity of this assumption.

1 Definition of Passage-Averaged Flow Equations

All flow equations are averaged over the blade passage, defined as the region between the suction surface $\theta = \theta_s$ and the pressure surface of the next blade, $\theta = \theta_p$ (Fig. 1). The area average of an arbitrary quantity is defined as

$$\bar{A} = \frac{1}{\theta_s - \theta_p} \int_{\theta_p}^{\theta_s} A \, d\theta \tag{1.1}$$

With the introduction of the blade thickness d in the tangential direction, and the blade pitch s, one can write $\bar{A}$ as

$$\bar{A} = \frac{1}{2\pi b/N} \int_p^s A \, d\theta \tag{1.2}$$

where

$$b = 1 - \frac{d}{s} \tag{1.3}$$

and N is the number of blades.

This averaging procedure is applied to all the conservation equations (mass, momentum, and energy) and in order to handle compressibility effects a density-weighted passage average is defined [3] by

$$\bar{\rho}\tilde{A} = \overline{\rho A} = \frac{1}{2\pi b/N} \int_p^s \rho A \, d\theta \tag{1.4}$$

The deviations from axisymmetry are defined by A' and A'' according to

$$A = \bar{A} + A' = \tilde{A} + A'' \tag{1.5}$$

with

$$\overline{A'} = \overline{\rho A''} = 0 \tag{1.6}$$

In the following we will use the notation $A^{(a)}$ instead of $\tilde{A}$, in order to distinguish those quantities from corresponding mass-averaged values $A^{(m)}$.

1.1 Turbomachinery Flow Model. It is important, in an attempt to assess the validity of different assumptions on through-flow quantities, to keep in mind the approximations at the basis of the flow models generally used in turbomachinery.

The essential approximation is expressed by a distributed loss model [18], in which the shear stresses are replaced by a loss (entropy)-generating friction force $\mathbf{F}_f$, considered as a distributed force, defined by the total pressure loss coefficients. Similarly, the energy and entropy equations are simplified by the assumption that the shear stress work is exactly balanced by the heat conduction effects, leading to the following set of equations, written in the relative system.

$$\frac{\partial \rho}{\partial t} + \nabla \cdot (\rho \mathbf{w}) = 0$$

$$\frac{\partial (\rho \mathbf{w})}{\partial t} + \nabla \cdot (\rho \mathbf{w} \cdot \mathbf{w}) = -\nabla p - 2\rho(\omega \times \mathbf{w}) + \rho\omega^2 \mathbf{r} + \rho \mathbf{F}_f$$

$$\frac{\partial (\rho I)}{\partial t} + \nabla \cdot (\rho \mathbf{w} I) = \frac{\partial p}{\partial t}$$

$$\frac{\partial}{\partial t}(\rho s) + \nabla \cdot (\rho \mathbf{w} s) = \frac{w}{T} \rho F_f \tag{1.7}$$

Nomenclature

b = airfoil tangential blockage
d = airfoil tangential thickness
f_B = body force
F_f = friction force
H = total enthalpy
h = static enthalpy
I = rothalpy
K_{ij} = blockage factor
m = meridional distance
M_0^* = rotary Mach number, equation (2.27)
N = number of airfoils
n = normal distance
p = static pressure
r = gas constant
$\mathbf{r}$ = position vector
r = radial distance
R_m = radius of curvature, equation (2.18)
S = airfoil pitch
s = entropy
T = static temperature
t = time
u = wheel speed
v = absolute velocity
w = relative velocity
z = axial distance
γ = specific heat ratio
θ = circumferential coordinate
ρ = density
σ = stream surface flow angle (Fig. 2)
ω = rotation rate

Subscripts

m = meridional component
n = normal component
0 = total
p = pressure surface
r = radial component
s = suction surface
z = axial component
θ = tangential component

Superscripts

$\bar{\ }$ = area average
$\sim, (a)$ = density-weighted average
$'$ = deviation from area average
$''$ = deviation from density-weighted average
$'''$ = deviation from mass-flux-weighted average
(m) = mass average
$=(\ )$ = momentum average
$\hat{\ }$ = see equations (1.21) and (2.7)
$*$ = rotary

In these equations, written in conservative form, $\mathbf{w}$ is the relative velocity related to the absolute velocity $\mathbf{v}$ by

$$\mathbf{v}=\mathbf{w}+\mathbf{u}=\mathbf{w}+\omega\times\mathbf{r} \tag{1.8}$$

for a steady rotation of angular velocity ω.

The rothalpy I is defined by

$$I=h+\frac{\mathbf{w}^2}{2}-\frac{\mathbf{u}^2}{2}=H-\mathbf{u}\bullet\mathbf{v} \tag{1.9}$$

where the stagnation enthalpy H is

$$H=h+\frac{\mathbf{v}^2}{2} \tag{1.10}$$

These equations are considered as Reynolds averaged for the turbulence fluctuations, and we will assume that they are also averaged for the unsteady effects, leaving us with a steady flow in the relative system.

An interesting discussion of the interrelation between different averaging scales in time can be found in Adamczyk [19].

1.2 Passage-Averaged Equations. The stationary forms of the system of equations (1.7) are passage averaged, following the definition (1.2). A detailed derivation can be found in Hirsch [20]. As is well known, the averaging procedure introduces a blockage factor b and a body force $\mathbf{f}_B$ as a consequence of the three dimensionality of the flow. The following system is obtained:

Continuity equation

$$\nabla\bullet(\overline{\rho\mathbf{w}b})=0 \tag{1.11}$$

Momentum equation

$$\begin{aligned}\nabla\bullet(\overline{\rho\mathbf{w}\bullet\mathbf{w}})b=&-b\nabla\bar{p}+\bar{\rho}\omega^2\mathbf{r}b-2\overline{\rho(\omega\times\mathbf{w})}b\\&+\overline{\rho\mathbf{F}_f}b+\bar{\rho}\mathbf{f}_Bb\end{aligned} \tag{1.12}$$

Energy equation

$$\nabla\bullet(\overline{\rho\mathbf{w}Ib})=0 \tag{1.13}$$

The blockage factor b is defined by equation (1.3) and the blade force is obtained from the pressure differences along the airfoil surfaces.

Expansion of equations (1.11)–(1.13) in cylindrical coordinates leads to:

Continuity equation

$$\frac{\partial}{\partial r}(\overline{\rho w_r br})+\frac{\partial}{\partial z}(\overline{\rho w_z br})=0 \tag{1.14}$$

Momentum equations

$$\frac{1}{br}\frac{\partial}{\partial r}(\overline{\rho w_r w_r br})+\frac{1}{br}\frac{\partial}{\partial z}(\overline{\rho w_r w_z br})-\frac{\overline{\rho w_\theta w_\theta}}{r}$$

$$=-\frac{\partial\bar{p}}{\partial r}+\bar{\rho}\ \omega r^2+2\overline{\rho w_\theta}\omega+\bar{\rho}(F_{fr}+f_{Br})\frac{1}{br}\frac{\partial}{\partial r}(\overline{\rho w_r w_z br})$$

$$+\frac{1}{br}\frac{\partial}{\partial z}(\overline{\rho w_z w_z br})=-\frac{\partial\bar{p}}{\partial z}+\bar{\rho}(F_{fz}+f_{Bz})$$

$$\frac{1}{br}\frac{\partial}{\partial r}(\overline{\rho w_r w_\theta br})+\frac{1}{br}\frac{\partial}{\partial z}(\overline{\rho w_z w_\theta br})+\frac{\overline{\rho w_\theta w_r}}{r}$$

$$=-2\overline{\rho w_r}\omega+\bar{\rho}(F_{f\theta}+f_{B\theta}) \tag{1.15}$$

Energy equation

$$\frac{\partial}{\partial r}(\overline{\rho w_r Ibr})+\frac{\partial}{\partial z}(\overline{\rho w_z Ibr})=0 \tag{1.16}$$

No decision has yet been made with regard to the choice of the most suitable method of averaging the variables for use in computation. Currently the most preferred averaging method is the density-weighted area average as defined in equation (1.4) [3,4]. Writing the density-weighted, area-averaged quantities with a superscript (a), instead of the tilde in equation (1.4), one obtains the following consistent through-flow model:

$$\begin{gathered}\frac{\partial}{\partial r}(\bar{\rho}brw_r^{(a)})+\frac{\partial}{\partial z}(\bar{\rho}brw_z^{(a)})=0\\ \nabla\bullet(\overline{\rho\mathbf{w}}\bullet\mathbf{w}^{(a)}br)=-b\nabla\bar{p}+\bar{\rho}b\bar{\mathbf{F}}+\nabla\bullet(\bar{\bar{\tau}}^{(s)}b)\\ \nabla\bullet(\overline{\rho\mathbf{w}}I^{(a)}b)=-\nabla\bullet(\overline{\rho\mathbf{w}''I''b})\end{gathered} \tag{1.17}$$

In equations (1.17), the term $\bar{\mathbf{F}}$ is the sum of all the forces

$$\bar{\mathbf{F}}=\omega^2\mathbf{r}-2\bar{\rho}(\omega\times\mathbf{w}^{(a)})+\mathbf{F}_f+\mathbf{f}_B \tag{1.18}$$

and the additional stress term $\bar{\bar{\tau}}^{(s)}$ represents the sum of the "interaction" terms expressed as the gradient of a "secondary" stress tensor

$$\bar{\bar{\tau}}^{(s)}=-\overline{\rho\mathbf{w}''\bullet\mathbf{w}''} \tag{1.19}$$

The energy equation shows that the averaged total energy $I^{(a)}$ given by

$$I^{(a)}=h^{(a)}+\frac{\mathbf{w}^{2(a)}}{2}-\frac{\mathbf{u}^2}{2} \tag{1.20}$$

is not constant along a density-area-averaged streamline. This has important consequences on the consistency of through-flow models and will be discussed in more detail in section 2. The averaged total energy differs from the total energy of the density-weighted averaged flow $\hat{I}^{(a)}$

$$\hat{I}^{(a)}=h^{(a)}+\frac{{\mathbf{w}^{(a)}}^2}{2}-\frac{\mathbf{u}^2}{2}=I^{(a)}-\frac{\overline{\rho\mathbf{w}''\mathbf{w}''}}{2\bar{\rho}}\equiv I^{(a)}-k^{(a)} \tag{1.21}$$

The quantity $I^{(a)}$ is the density-weighted, area-averaged total energy of the flow, while $\hat{I}^{(a)}$ is the total energy of the averaged flow. These two quantities differ by the average of the kinetic energy of the fluctuations $\mathbf{w}''$.

2 Averaged Energy Equation

The total energy I (or H) plays an essential role in all the through-flow models, since the through-flow computations have to rely on the energy relation along the meridional streamlines. In most, if not all, of the through-flow programs based on axisymmetric models, the constancy of the rothalpy is applied in order to relate quantities in two consecutive calculation stations. When dealing with the influence of the nonaxisymmetric effects it is essential to be able to estimate their influence on the energy transport and exchange.

From the third of equation (1.17), one can see that neither the density-averaged total energy $I^{(a)}$, which satisfies

$$\bar{\rho}w_m^{(a)}\frac{\partial}{\partial m}I^{(a)}=-\frac{1}{b}\ \nabla\bullet(\overline{\rho\mathbf{w}''I''b}) \tag{2.1}$$

nor the total energy of the average flow $\hat{I}^{(a)}$, which obeys the equation

$$\bar{\rho}w_m^{(a)}\frac{\partial}{\partial m}\ \hat{I}^{(a)}=-\frac{1}{b}\ \nabla\bullet(\overline{\rho\mathbf{w}''I''b})-\bar{\rho}w_m^{(a)}\frac{\partial}{\partial m}\ k^{(a)} \tag{2.2}$$

are conserved along a streamline $w_m^{(a)}$. On the other hand, if *the streamsurfaces are assumed to be axisymmetric*, a unique mass-averaged total energy can be defined by

$$\overline{\rho\mathbf{w}I}\equiv\bar{\rho}\mathbf{w}^{(a)}I^{(m)}=\frac{1}{b}\int_p^s(\rho\mathbf{w}I)d\theta \tag{2.3}$$

from equation (1.13)

$$\nabla\bullet(\bar{\rho}\mathbf{w}^{(a)}I^{(m)}b)=0 \tag{2.4}$$

or taking into account the continuity equation (1.15)

$$\bar{\rho}(\mathbf{w}^{(a)}\bullet\nabla)I^{(m)}=0 \tag{2.5}$$

This shows that the mass-averaged enthalpy is conserved along a streamline defined by the density-weighted, area-averaged flow (which actually is the mass-flow conserving average). Indeed, equation (2.5) can be written as

$$\bar{\rho} w_m^{(a)} \frac{\partial}{\partial m} I^{(m)} = 0 \tag{2.6}$$

The total energy of the mass-averaged flow ($\hat{I}^{(m)}$) is defined by

$$\begin{aligned} I^{(m)} &= h^{(m)} + \frac{\mathbf{w}^{2(m)}}{2} - \frac{\mathbf{u}^2}{2} \\ &= h^{(m)} + \frac{1}{2}(\mathbf{w}^{(m)})^2 - \frac{\mathbf{u}^2}{2} + \frac{\overline{\rho w_m \mathbf{w}''' \bullet \mathbf{w}'''}}{2\bar{\rho} w_m^{(a)}} \\ &\equiv \hat{I}^{(m)} + k^{(m)} \end{aligned} \tag{2.7}$$

where the mass-averaged velocity vector is defined by

$$\mathbf{w}^{(m)} \equiv \frac{\overline{\rho w_m \mathbf{w}}}{\bar{\rho} w_m^{(a)}} \tag{2.8}$$

and the fluctuations $\mathbf{w}''$ are determined by

$$\mathbf{w} = \mathbf{w}^{(m)} + \mathbf{w}''' \tag{2.9}$$

with

$$\overline{\rho w_m \mathbf{w}'''} = 0 \tag{2.10}$$

Inserting (2.7) into (2.6), one obtains

$$\bar{\rho} w_m^{(a)} \frac{\partial}{\partial m} \hat{I}^{(m)} = -\bar{\rho} w_m^{(a)} \frac{\partial}{\partial m} k^{(m)} \tag{2.11}$$

showing that $\hat{I}^{(m)}$, the total energy of the mass-averaged flow, is not rigorously conserved along a density-area-averaged streamline, even for axisymmetric stream surfaces.

According to Jennions and Stow [5], the contribution of the kinetic energy of the fluctuations can be as high as 30 percent of the total energy of the averaged mean flow.

2.1 Nonaxisymmetric Streamsurfaces – Radial Mixing Effects.

If the blade-to-blade streamsurfaces are not close to an axisymmetric shape, as a consequence of secondary flows, the assumption (2.3) ceases to be strictly valid.

Instead, the mean values appearing in equation (1.16) are evaluated as follows, writing (Fig. 2)

$$\begin{aligned} w_r &= w_m \sin \sigma = w_m \sin (\bar{\sigma} + \sigma') \\ w_z &= w_m \cos \sigma = w_m \cos (\bar{\sigma} + \sigma') \end{aligned} \tag{2.12}$$

introducing hereby the averaged streamsurface slope angle $\bar{\sigma}$, and the "twist" angle σ' defined as the difference between the actual angle σ and the mean (axisymmetric) value $\bar{\sigma}$

$$\sigma(r,\ \theta,\ z) = \bar{\sigma}(r,\ z) + \sigma'(r,\ \theta,\ z) \tag{2.13}$$

Decomposing equation (2.12) and assuming that

$$\overline{\cos\ \sigma'} = 1 \text{ and } \overline{\sin\ \sigma'} = 0$$

one can estimate the averaged products as follows. For the first term, one would have

$$\overline{\rho w_m I \sin (\bar{\sigma} + \sigma')} \cong \overline{\rho w_m I} \sin \bar{\sigma} + \overline{\rho w_m I \sin \sigma'} \bullet \cos \bar{\sigma} \tag{2.14a}$$

and for the second term

$$\overline{\rho w_m I \cos (\bar{\sigma} + \sigma')} \cong \overline{\rho w_m I} \cos \bar{\sigma} - \overline{\rho w_m I \sin \sigma'} \bullet \sin \bar{\sigma} \tag{2.14b}$$

These expressions are introduced in the energy equation (1.16). The first terms of (2.14) give the axisymmetric contribution of the left-hand side of equation (2.4).

A mass-averaged rothalpy $I^{(m)}$ is defined by

$$\overline{\rho w_m I} = \bar{\rho} w_m^{(a)} I^{(m)} \tag{2.15}$$

Note that the definition (2.15) of $I^{(m)}$ is identical to the definition (2.3) in the case of axisymmetry.

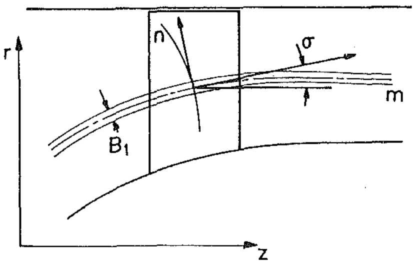

Fig. 2 Trace of axisymmetric streamsurface in a meridional plane section

The energy fluctuations I''' are defined by:

$$I = I^{(m)} + I''' \tag{2.16}$$

Introducing the derivatives in the direction normal to the axisymmetric (averaged) streamsurface $\partial/\partial n$ by

$$\frac{\partial}{\partial n} = \cos\ \bar{\sigma} \frac{\partial}{\partial r} - \sin\ \bar{\sigma} \frac{\partial}{\partial z} \tag{2.17}$$

and the radius of curvature (Fig. 2) by

$$\frac{1}{R_m} = -\frac{\partial \bar{\sigma}}{\partial m} \tag{2.18}$$

leads to the following equation (see also [21]):

$$\bar{\rho} b r w_m^{(a)} \frac{\partial I^{(m)}}{\partial m} = \frac{\partial}{\partial n}(br\overline{\rho' w_r' I'''}) \tag{2.19}$$

In equation (2.19), only the gradient terms have been retained because the gradients of the nonaxisymmetric terms are more significant than the amplitudes of the terms. Equation (2.19) is the nonaxisymmetric form of the energy equation, in effect generalizing equation (2.6). Note that the right-hand side of equation (2.19) represents a source term originating from the radial component of the secondary velocity field and describes therefore a *radial mixing* of the total energy.

If a gradient model is assumed (such as in [22]) for the large-scale nonaxisymmetric fluctuations, one could write

$$\overline{\rho' w_r' I'''} \equiv \epsilon \frac{\partial I^{(m)}}{\partial r} \tag{2.20}$$

or

$$\overline{\rho' w_r' I'''} \equiv \hat{\epsilon} \frac{\partial I^{(m)}}{\partial n} \tag{2.21}$$

giving rise to a diffusion type equation for the energy redistribution due to the nonaxisymmetric flow field.

When the energy equation is written for the total energy of the averaged flow $\hat{I}^{(m)}$, the radial mixing term has to be added to the right-hand side of equation (2.11), which becomes

$$w_m^{(a)} \frac{\partial}{\partial M} \hat{I}^{(m)} = \frac{1}{br\bar{\rho}} \frac{\partial}{\partial n}(br\overline{\rho' w_r' I'''}) - w_m^{(a)} \frac{\partial}{\partial m} k^{(m)} \tag{2.22}$$

The nonconstancy of the total energy of the averaged flow, $\hat{I}^{(a)}$ or $\hat{I}^{(m)}$, poses a fundamental problem in through-flow computations where the application of some form of total energy conservation has to be applied. As mentioned above, the calculations performed by Jennions and Stow [5] in the case of gas turbine nozzle vanes indicates that the kinetic energy terms in equations (2.2) or (2.11) are not negligible. This can also be seen in Fig. 5. One might wonder, therefore, what influence this might have on the evaluation of the right-hand side terms in the radial equilibrium equation when written, for instance, under Crocco's form.

The following argument tends to support the statement that the entropy variations, or more precisely the rotary stagnation pressure gradients, are more important than the enthalpy variations, at least for low-speed flows.

From the isentropic relations between static and absolute or relative stagnation conditions, one has

$$T_0 ds = dH - \frac{d_{p_0}}{\rho_0} \tag{2.23}$$

where the subscript 0 indicates absolute stagnation conditions. For rotary, relative conditions, whereby

$$T_0^* = T + \frac{\mathbf{w}^2}{2c_p} - \frac{\mathbf{u}^2}{2c_p} \tag{2.24}$$

$$p_0^* = p\left(\frac{T_0^*}{T}\right)^{\gamma/\gamma-1}$$

one has

$$T_0^* ds = dI - \frac{dp_0^*}{\rho_0^*} \tag{2.25}$$

Hence

$$\begin{aligned} Tds - dI &= \frac{T}{T_0^*}\, dI - \frac{T}{\rho_0^* T_0^*}\, dp_0^* - dI \\ &= \left(\frac{T}{T_0^*} - 1\right) dI - \frac{rT}{p_0^*}\, dp_0^* \\ &= \left(\frac{T}{T_0^*} - 1\right) dI - \frac{p}{\rho p_0^*}\, dp_0^* \end{aligned} \tag{2.26}$$

Introducing a rotary Mach number M_0^*

$$\mathrm{M}_0^{*2} = \frac{\mathbf{w}^2 - \mathbf{u}^2}{\gamma r T} \tag{2.27}$$

the coefficients in equation (2.26) become

$$\frac{T_0^* - T}{T_0^*} = 1 - \frac{1}{1 + \frac{\gamma - 1}{2}\mathrm{M}_0^{*2}} = \frac{\frac{\gamma-1}{2}\mathrm{M}_0^{*2}}{1 + \frac{\gamma - 1}{2}\mathrm{M}_0^{*2}} \tag{2.28}$$

$$\frac{p}{p_0^*} = \left(\frac{1}{1 + \frac{\gamma - 1}{2}\mathrm{M}_0^{*2}}\right)^{\gamma/\gamma-1} \tag{2.29}$$

The terms $(T\nabla s - \nabla I)$ in the right-hand side of Crocco's momentum equation become, independently of the type of averaged quantity considered

$$T\nabla s - \nabla I = \frac{\frac{\gamma-1}{2}\mathrm{M}_0^{*2}}{1 + \frac{\gamma - 1}{2}\mathrm{M}_0^{*2}} \nabla I$$

$$- \frac{1}{\rho} \frac{1}{\left(1 + \frac{\gamma - 1}{2}\mathrm{M}_0^{*2}\right)^{\gamma/\gamma-1}} \nabla p_0^* \tag{2.30}$$

In low-speed compressors the blade exit rotary Mach number equation (2.27) should be small. When this is the case, as in the sample compressor data discussed in the next section, the stagnation pressure variation should be the dominating influence on the through-flow and the momentum exchange. It can be expected that small errors in the evaluation of the enthalpy transport will not significantly affect the radial equilibrium of the flow.

3 Momentum and Mass-Averaged Through-Flow Equations

With density-weighted, area-averaged variables one can clearly define a consistent through-flow model where, in addition to the blade blockage factor b, interaction terms due to the nonaxisymmetric secondary stresses $\bar{\bar{\tau}}^{(a)}$ describe the three-dimensional effects on the average flow.

As mentioned in the introduction, mass-averaged variables such as stagnation pressure and total enthalpy are more representative of the physical energy exchange than the corresponding area-averaged variables. In an attempt to formulate a coherent through-flow model for mass-averaged variables we reconsider the passage-averaged equations (1.14) to (1.16), where for simplicity the momentum equations are considered in the absolute frame of reference.

The mass conservation equation and the energy equation have already been discussed, with the following outcome.

Mass Conservation. The natural averaged quantities are the density-weighted, area-averaged velocities which lead to the first equation (1.17), reproduced here

$$\frac{\partial}{\partial r}(\bar{\rho} b r v_r^{(a)}) + \frac{\partial}{\partial z}(\bar{\rho} b r v_z^{(a)}) = 0 \tag{3.1}$$

or in vector form

$$\nabla \bullet (\bar{\rho} b r \mathbf{v}^{(a)}) = 0 \tag{3.2}$$

3.1 Momentum Equations – Momentum-Averaged Velocity Components.

Considering equations (1.15) in the absolute system, *it appears that it is not possible to define a unique momentum-averaged velocity component, since different momentum flux components appear in the projections of the equation of motion.* For instance, in the radial component, the averaged flux components $\overline{\rho v_r v_r}$, $\overline{\rho v_r v_z}$, and $\overline{\rho v_\theta v_\theta}$ occur, while in the axial projection one encounters the components $\overline{\rho v_z v_r}$ and $\overline{\rho v_z v_z}$. This leads to the definition of *momentum-averaged* velocity components such as

$$\overline{\rho v_r v_r} = \overline{\rho v_r} \bullet \bar{\bar{v}}_r^{(r)} = \bar{\rho}\, \bar{\bar{v}}_r^{(r)} v_r^{(a)} \tag{3.3}$$

$$\overline{\rho v_r v_r} = \frac{1}{b}\int_p^s \rho v_r v_r d\theta \tag{3.4}$$

and

$$\overline{\rho v_r v_z} = \overline{\rho v_r}\, \bar{\bar{v}}_z^{(r)} = \bar{\rho} v_r^{(a)} \bar{\bar{v}}_z^{(r)} \tag{3.5}$$

$$\overline{\rho v_r v_z} = \frac{1}{b}\int_p^s \rho v_r v_z d\theta \tag{3.6}$$

One finds also

$$\overline{\rho v_r v_z} = \bar{\rho} v_z^{(a)} \bar{\bar{v}}_r^{(z)} \tag{3.7}$$

The averaged velocity component $\bar{\bar{v}}_r^{(r)}$ represents the average of v_r weighted by the radial momentum ρv_r. Similarly, from equations (3.6) and (3.7), one can define another averaged radial velocity component $\bar{\bar{v}}_r^{(z)}$, representing an average v_r, weighted this time by the axial momentum ρv_z. A priori there is no reason to consider these two components as equal. From the definition of the velocity fluctuations $\mathbf{v}''$, following equation (1.5), one can write for instance for $\overline{\rho v_r v_z}$

$$\overline{\rho v_r v_z} = \bar{\rho} v_r^{(a)} v_z^{(a)} + \overline{\rho v_r'' v_z''} \tag{3.8}$$

where $\overline{\rho v_r'' v_z''}$ are the components of the secondary stress tensor $\bar{\bar{\tau}}^{(S)}$ considered in the absolute system.

We define now six different blockage coefficients K_{ij}, where i and j represent the components (r, θ, z) by

$$K_{ij}^{-1} = \frac{\overline{\rho v_i v_j}}{\bar{\rho} v_i^{(a)} v_j^{(a)}} = \frac{\bar{\bar{v}}_j^{(i)}}{v_j^{(a)}} \tag{3.9}$$

Hence K_{ij}^{-1} is the ratio between the averaged velocity component v_j weighted with the momentum ρv_i divided by the corresponding density-weighted, area-averaged velocity component $v_j^{(a)}$.

From the symmetry between i and j, best seen in equation (3.9), one finds also

$$K_{ij}^{-1} = \frac{\bar{\bar{v}}_i^{(j)}}{v_i^{(a)}} = K_{ji}^{-1} \tag{3.10}$$

or

$$K_{ij} \bar{\bar{v}}_i^{(j)} = v_i^{(a)} \tag{3.11}$$

This definition of a blockage coefficient with respect to a selected momentum component generalizes the definition of the aerodynamic blockage coefficient introduced in [8] and discussed in more detail in [15]. In these references, the averaged velocity $\bar{v}_z^{(m)}$ is determined from the mass-averaged dynamic pressure and mass-averaged flow angles.

From equation (3.9) one can also write

$$K_{ij}^{-1} = 1 + \frac{\overline{\rho v_i'' v_j''}}{\bar{\rho} v_i^{(a)} v_a^{(j)}} \tag{3.12}$$

Introducing the $\bar{\bar{v}}_i^{(j)}$ component in equations (1.15) leads to the following formulation for the radial component:

$$\frac{1}{br}\frac{\partial}{\partial r}\,(\bar{\rho} v_r^{(a)} \bar{\bar{v}}_r^{(r)} br) + \frac{1}{br}\frac{\partial}{\partial z}\,(\bar{\rho} v_z^{(a)} \bar{\bar{v}}_r^{(z)} br)$$
$$- \frac{\bar{\rho} v_\theta^{(a)} \bar{\bar{v}}_\theta^{(\theta)}}{r} = -\frac{\partial \bar{p}}{\partial r} + \bar{\rho}(F_{fr} + f_{Br}) \tag{3.13}$$

or as a function of the K_{ij} coefficients, eliminating the density-area-averaged component

$$\frac{1}{br}\frac{\partial}{\partial r}(\bar{\rho} K_{rr} \bar{\bar{v}}_r^{(r)} \bar{\bar{v}}_r^{(r)} br)$$
$$+ \frac{1}{br}\frac{\partial}{\partial z}(\bar{\rho} K_{rz} \bar{\bar{v}}_r^{(z)} \bar{\bar{v}}_z^{(r)} br)$$
$$- \frac{\bar{\rho} K_{\theta r} \bar{\bar{v}}_\theta^{(r)} \bar{\bar{v}}_\theta^{(\theta)}}{r} = -\frac{\partial \bar{p}}{\partial r} + \bar{\rho}(F_{fr} + f_{Br}) \tag{3.14}$$

An alternative formulation is obtained as a function of the density-weighted velocity components $v_i^{(a)}$. Equation (3.13) becomes by eliminating the variables $\bar{\bar{v}}_i^{(j)}$

$$\frac{1}{br}\frac{\partial}{\partial r}(\bar{\rho} v_r^{(a)} v_r^{(a)} br K_{rr}^{-1})$$
$$+ \frac{1}{br}\frac{\partial}{\partial z}(\bar{\rho} v_z^{(a)} v_r^{(a)} br K_{rz}^{-1}) - \frac{\rho v_\theta^{(a)} v_\theta^{(a)}}{r} K_{\theta\theta}^{-1}$$
$$= -\frac{\partial \bar{p}}{\partial r} + \bar{\rho}(F_{fr} + f_{Br}) \tag{3.15}$$

Equation (3.15) is to be compared to the projections of equation (1.15); for instance the radial component gives in the absolute system

$$\frac{1}{br}\frac{\partial}{\partial r}(\bar{\rho} v_r^{(a)} v_r^{(a)} br) + \frac{1}{br}\frac{\partial}{\partial z}(\bar{\rho} v_z^{(a)} v_r^{(a)} br)$$
$$- \frac{\rho v_\theta^{(a)} v_\theta^{(a)}}{r} = -\frac{\partial \bar{p}}{\partial r} + \bar{\rho}(F_{fr} + f_{Br}) - \frac{1}{br}\frac{\partial}{\partial r}(\overline{\rho v_r'' v_r'' br})$$
$$- \frac{1}{br}\frac{\partial}{\partial z}(\overline{\rho v_r'' v_z'' br}) + \frac{\overline{\rho v_\theta'' v_\theta''}}{r} \tag{3.16}$$

It can be seen from the relation (3.12) that both formulations are identical and that the coefficients K_{ij}^{-1} do contain the same information as the secondary stress $\bar{\bar{\tau}}^{(s)}$. Hence the interaction terms do not appear in equation (3.15), since the whole influence of the nonaxisymmetry is contained in the K_{ij} coefficients. The other components of the momentum equation can be treated in a similar way; see Hirsch and Dring [23] for more details.

Continuity Equation. In a similar way, the continuity equation can be rewritten as a function of the momentum-averaged velocity components, in different ways, according to the choice of the K_{ij} coefficients. From equations (3.1) and (3.11) one can write, with the absolute velocity components

$$\frac{\partial}{\partial r}(\bar{\rho} \bar{\bar{v}}_r^{(r)} K_{rr} br) + \frac{\partial}{\partial z}(\bar{\rho} \bar{\bar{v}}_z^{(r)} K_{zr} br) = 0 \tag{3.17}$$

A difficulty appears when the equations have to be derived in other forms, for instance in the nonconservative form or Crocco's form. One cannot introduce the continuity equation in the conservative form of the averaged momentum equation as a consequence of the nonequality of velocity components such as $\bar{\bar{v}}_r^{(r)} \neq \bar{\bar{v}}_r^{(z)}$.

Indeed, the left-hand side of equation (3.13) can be worked out, leading to

$$\bar{\rho} v_r^{(a)} \frac{\partial}{\partial r} \bar{\bar{v}}_r^{(r)} + \bar{\rho} v_z^{(a)} \frac{\partial}{\partial z}\ \bar{\bar{v}}_r^{(z)}$$
$$+ \frac{1}{br}\left[\bar{\bar{v}}_r^{(r)} \frac{\partial}{\partial r}(\bar{\rho} v_r^{(a)} br) + \bar{\bar{v}}_r^{(z)} \frac{\partial}{\partial z}(\bar{\rho} v_z^{(a)} br) \right]$$
$$- \frac{\bar{\rho} v^{(a)} \bar{\bar{v}}_\theta^{(\theta)}}{r} = -\frac{\partial \bar{p}}{\partial r} + \bar{\rho}(F_{fr} + f_{Br}) \tag{3.18}$$

If $\bar{\bar{v}}_r^{(r)} = \bar{\bar{v}}_r^{(z)}$ one could factor out this velocity component, and the term in brackets would vanish due to mass conservation. Otherwise, one could not obtain Crocco's form in a consistent way, without the simultaneous appearance of different components $\bar{\bar{v}}_r^{(z)}$, $\bar{\bar{v}}_r^{(r)}$.

3.2 Simplifying Assumptions – Unique Blockage Coefficients. The assumption is made of a *unique* ratio between density and momentum-averaged quantities. This corresponds to the assumption that

$$\begin{aligned}
\bar{\bar{v}}_r^{(z)} &= \bar{\bar{v}}_r^{(r)} = \bar{\bar{v}}_r^{(\theta)} \equiv v_r^{(m)} \\
\bar{\bar{v}}_z^{(z)} &= \bar{\bar{v}}_z^{(r)} = \bar{\bar{v}}_z^{(\theta)} \equiv v_z^{(m)} \\
\bar{\bar{v}}_\theta^{(z)} &= \bar{\bar{v}}_\theta^{(r)} = \bar{\bar{v}}_\theta^{(\theta)} \equiv v_\theta^{(m)}
\end{aligned} \tag{3.19}$$

implying that all the K_{ij} coefficients are equal. Hence, if this is satisfied, there is a unique definition of *mass-averaged* velocities, since for the axial component for instance

$$v_z^{(m)} = \frac{\overline{\rho v_z v_z}}{\rho \bar{v}_z^{(a)}} = \frac{\overline{\rho v_z v_m}}{\overline{\rho v_m^{(a)}}} = K^{-1} v_z^{(a)} \tag{3.20}$$

and similarly for the other components.

With this assumption, the continuity equation (3.17) becomes

$$\frac{\partial}{\partial r}(\bar{\rho} v_r^{(m)} Kbr) + \frac{\partial}{\partial z}(\bar{\rho} v_z^{(m)}\ Kbr) = 0 \tag{3.21}$$

This equation is similar to the density-weighted formulation (1.17) where the replacement by mass-averaged velocities has led to the introduction of a global blockage coefficient, $B = Kb$. This coefficient is a product of the total blade blockage and of an aerodynamic blockage K due to the nonaxisymmetry of the flow.

The momentum equations can be reduced as follows, considering first the radial component (3.14), and introducing Crocco's form.

With the continuity equation (3.21) one obtains, with the assumptions that the thermodynamic variables $T^{(a)}$ and $h^{(a)}$ relate to their mass-averaged values in the same way as the velocity components [23]

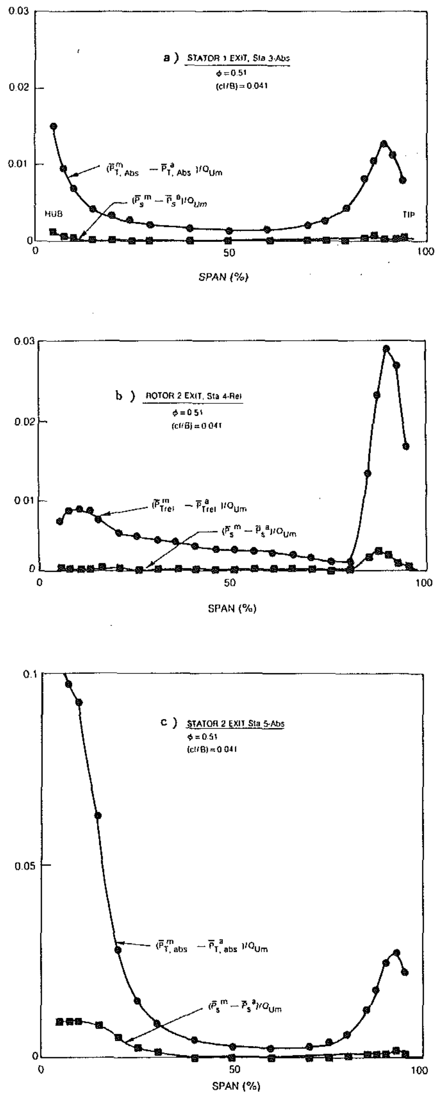

Fig. 3 Distribution of the difference between mass-averaged and area-averaged static and total pressures

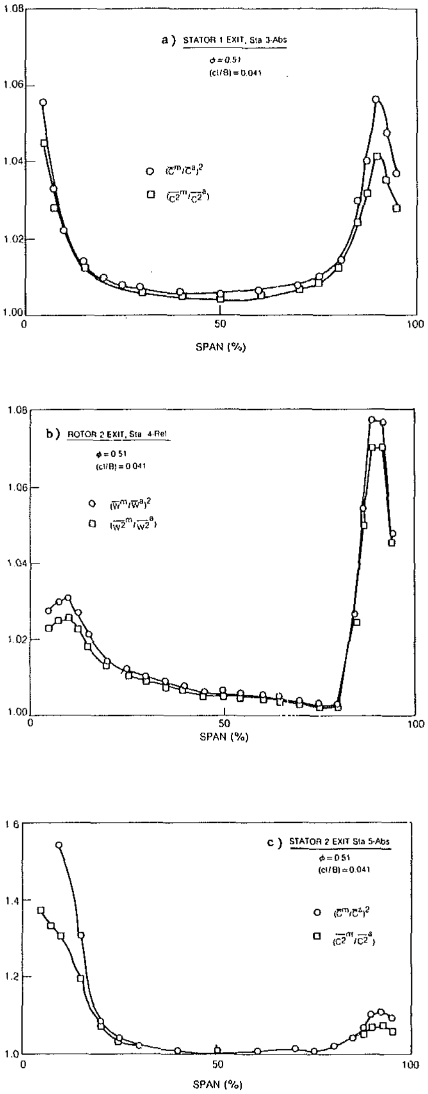

Fig. 4 Ratio of mass-averaged and area-averaged velocities

$$h^{(m)} = K^{-1} h^{(a)}$$

$$T^{(m)} = K^{-1} T^{(a)} \tag{3.22}$$

$$v_z^{(m)} \left[\frac{\partial}{\partial z} v_r^{(m)} - \frac{\partial}{\partial r} v_z^{(m)} \right] - \frac{v_\theta^{(m)}}{r} \frac{\partial}{\partial r} (r v_\theta^{(m)})$$

$$= T^{(m)} \frac{\partial s}{\partial r} - \frac{\partial}{\partial r} \hat{H}^{(m)} + (F_{fr} + f_{Br})/K \tag{3.23}$$

where $\hat{H}^{(m)}$ is derived from $\hat{I}^{(m)}$ by setting the wheel speed to zero.

Within the above simplifying assumptions, the throughflow equations can be interpreted as *functions of the mass-averaged flow variables*. The influence of the "interaction" terms in equation (1.17) is taken up by the K coefficients. In the continuity equation the geometric blockage factor $b = 1 - d/s$ is to be multiplied by K, leading to an overall blockage coefficient

$$B = bk \tag{3.24}$$

which has to be taken into account also in the axial regions between adjacent blade rows, e.g., where $b = 1$, but $K \neq 1$.

Equations (3.21) and (3.22) are consistent with the radial equilibrium treatments of Calvert and Ginder [6] as well as Dring and Joslyn [15-17], in terms of mass-averaged quantities and a simple aerodynamic blockage coefficient replacing the interaction terms in the density-weighted formulation.

The energy equation follows from (2.22) for a nonrotating blade row

$$v_m^{(m)} \frac{\partial}{\partial m} \hat{H}^{(m)} = -v_m^{(m)} \frac{\partial}{\partial m} k^{(m)} + \frac{1}{\bar{\rho} b r} \frac{\partial}{\partial r} (b r \overline{\rho' v_r' H'''}) \tag{3.25}$$

showing that $\hat{H}^{(m)}$ as appearing in equation (3.23) is not conserved, even in a nonrotating blade row. However, as discussed in section 2, in combination with the entropy term, the dominating effects will most probably come from the stagnation pressure variations.

3.3 Comparison With Data. From the data base collected in the last years [8-15], the K_{ij} coefficients can be evaluated at different stations of both single and two-stage axial compressors at design and off-design conditions. All of the data presented in the following paragraphs were acquired using pneumatic (slow response) instrumentation with the compressors operating at design conditions.

Figure 3 shows the difference between mass-averaged and area-averaged static and absolute and relative stagnation pressures at the exits of stator 1, rotor 2, and stator 2 of the two-stage compressor reported by Dring et al. [10, 11].

The common observation is the nearly axisymmetric behavior of the static pressure, while the stagnation pressures

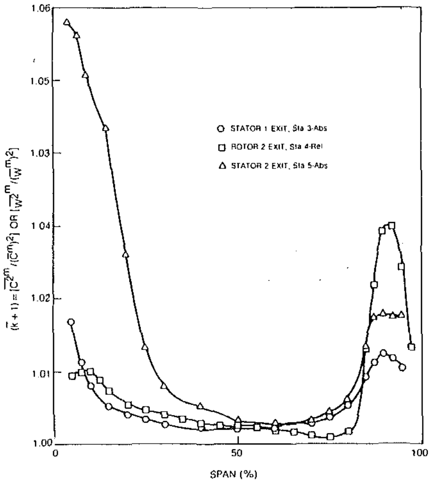

Fig. 5 Comparison of ratio of mass-averaged and area-averaged velocity at stator 1, rotor 2, and stator 2 exists

show large nonaxisymmetric effects in the end-wall regions. This observation is based on the differences between the mass and area averages of the pressures.

Figure 4 shows the corresponding ratios of mass to area-averaged absolute or relative velocities squared, as well as the ratios of the averaged kinetic energies. The curves follow very closely the stagnation pressure variations, as expected since static pressure is nearly constant. In addition, the difference between the two curves is a measure of the influence of the kinetic energy of the fluctuations $k^{(m)}$. This influence is mostly sensible in the end-wall regions as can be seen from Fig. 5, where the quantity $1 + k^{(m)}$ is plotted as a function of span. Figure 6 displays the K_{ij} coefficients at the same three locations.

The validity of the uniformity assumption (3.19) can be estimated on the basis of these results. For the components not involving the radial velocity, the assumption of equality of the K_{ij} is satisfied with an acceptable accuracy even in the end-wall regions.

The results of the coefficients involving the radial velocity components are more puzzling. It should be noticed however that due to the small magnitude of the radial component of velocity, a large error is connected to the determination of the K_{ri} coefficients, and more data would be required from turbomachines having larger average radial velocities.

Conclusions

A detailed analysis of the momentum-averaged formulation has shown that a simplified model can be obtained, in the line of more intuitive considerations, if a simple blockage coefficient can be assumed.

This coefficient is then defined as the ratio between the density-weighted, area-averaged velocity and the mass-averaged velocity. It contains full information on the influence of the nonaxisymmetry of the real flow on its averaged through-flow.

The present analysis therefore confirms the importance of the aerodynamic blockage as a major parameter to be introduced to the through-flow design systems, instead of the interaction terms based on the secondary stresses.

Acknowledgments

The work presented here was carried out under Naval Air Systems Command funding (Contract No. N62271-85-M-0990) under the direction of Dr. Raymond Shreeve.

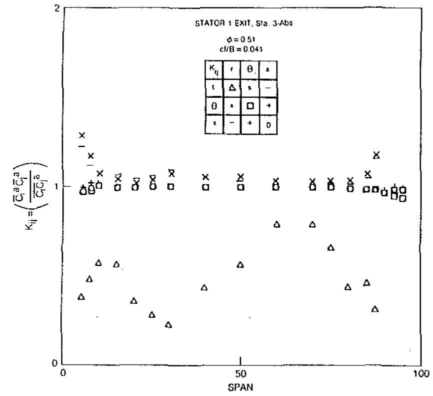

Fig. 6(a) Distribution of K_{ij} coefficients at stator 1 exit

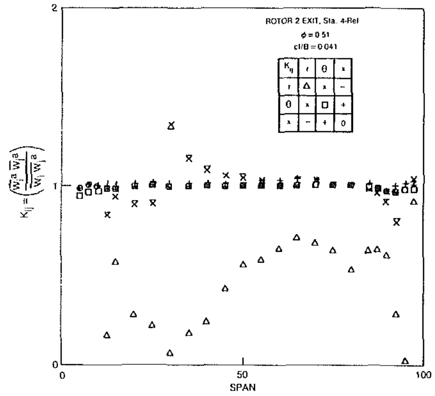

Fig. 6(b) Distribution of K_{ij} coefficients at rotor 2 exit

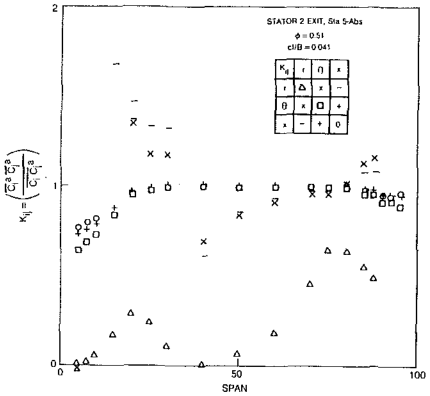

Fig. 6(c) Distribution of K_{ij} coefficients at stator 2 exit

References

1 Smith, L. H., "The Radial Equilibrium Equation of Turbomachinery," ASME JOURNAL OF ENGINEERING FOR POWER, Vol. 88, No. 1, 1966, pp. 1-12.

2 Hirsch, Ch., and Warzee, G., "A Finite Element Method for Through-Flow Calculations in Turbomachines," ASME *Journal of Fluids Engineering*, Vol. 98, 1976, pp. 403-421.

3 Hirsch, Ch., and Warzee, G., "An Integrated Quasi-3D Finite Element Calculation Program for Turbomachinery Flows," ASME JOURNAL OF ENGINEERING FOR POWER, Vol. 101, 1979, pp. 141-148.

4 Jennions, I. K., and Stow, P., "A Quasi Three Dimensional Turbomachinery Blade Design System: Part I—Through-Flow Analysis; Part II—Computerized System," ASME JOURNAL OF ENGINEERING FOR GAS TURBINES AND POWER, Vol. 107, 1985, pp. 301-316.

5 Jennions, I. K., and Stow, P., "The Importance of Circumferential Non-uniformities in a Particle Averaged Quasi-Three Dimensional Turbomachine Design System," ASME JOURNAL OF ENGINEERING FOR GAS TURBINES AND POWER, Vol. 108, 1986, pp. 240-245.

6 Calvert, W. J., and Ginder, R. B., "A Quasi-Three Dimensional System

for the Flow Within Transonic Compressor Blade Rows," ASME Paper No. 85-GT-22, 1985.

7 Hirsch, Ch., and Denton, I., eds., "Through-Flow Calculations in Axial Turbomachines," AGARD AR175, Report of WG12, 1981.

8 Dring, R. P., "Blockage in Axial Compressors," ASME JOURNAL OF ENGINEERING FOR GAS TURBINES AND POWER, Vol. 106, 1984, pp. 712–714.

9 Dring, R. P, Joslyn, H. D., and Hardin, L. W., "Experimental Investigation of Compressor Rotor Wakes," AFAPL-TR-79-2107, Air Force Aero Propulsion Laboratory, Technology Branch, Turbine Engine Division (TBX), Wright-Patterson AFB, OH, 1979.

10 Dring, R. P., Joslyn, H. D., and Hardin, L. W., "An Investigation of Compressor Rotor Aerodynamics," ASME JOURNAL OF ENGINEERING FOR POWER, Vol. 104, 1982, pp. 84–96.

11 Dring, R. P., Joslyn, H. D, and Wagner, J. H., "Compressor Rotor Aerodynamics," in: *Viscous Effects in Turbomachines*, AGARD-CP-351, Copenhagen, Denmark, June 1-3, 1983, Paper No. 24.

12 Wagner, J. H., Dring, R. P., and Joslyn, H. D., "Axial Compressor Middle Stage Secondary Flow Study," NASA CR-3701, 1983.

13 Wagner, J. H., Dring, R. P., and Joslyn, H. D., "Inlet Boundary Layer Effects in an Axial Compressor Rotor, Part I: Blade-to-Blade Effects," ASME JOURNAL OF ENGINEERING FOR GAS TURBINES AND POWER, Vol. 107, 1985, pp. 374–380.

14 Wagner, J. H., Dring, R. P., and Joslyn, H. D., "Inlet Boundary Layer Effects in an Axial Compressor Rotor, Part II: Through-Flow Effects," ASME JOURNAL OF ENGINEERING FOR GAS TURBINES AND POWER, Vol. 107, 1985, pp. 381–386.

15 Dring, R. P., and Joslyn, H. D., "Through-Flow Modeling of Axial Turbomachinery," ASME JOURNAL OF ENGINEERING FOR GAS TURBINES AND POWER, Vol. 108, 1986, pp. 246–253.

16 Dring, R. P., and Joslyn, H. D., "Through-Flow Analysis of a Multistage Compressor. Part I – Aerodynamic Input," ASME JOURNAL OF TURBOMACHINERY, Vol. 108, 1986, pp. 17–22.

17 Dring, R. P., ande Joslyn, H. D., "Through-Flow Analysis of a Multistage Compressor. Part II – Analytical-Experimental Comparisons," ASME JOURNAL OF TURBOMACHINERY, Vol. 108, 1986, pp. 23–31.

18 Hirsch, Ch., "An Analysis of Flow Models From Navier-Stokes to Potential Flow Equations," AGARD lecture series LS140, 1985.

19 Adamczyk, J. J., "Model Equation for Simulating Flows in Multistage Turbomachinery," NASA TM 86869, Nov. 1984.

20 Hirsch, Ch., "Computational Models for Turbomachinery Flows," Report NPS-67-84-022, Naval Postgraduate School, Dept. Aeronautics, Monterey, CA 93943-5100, 1984.

21 Stow, P., "Modeling Viscous Flows in Turbomachinery," in: *Thermodynamics and Fluid Mechanics of Turbomachinery*, Proceedings of the NATO Advanced Study Institute, Ucer, Stow, and Hirsch, eds., Vol. 1, 1985, p. 37.

22 Adkins, G. G., and Smith, L. H., "Spanwise Mixing in Axial Turbomachines," ASME JOURNAL OF ENGINEERING FOR POWER, Vol. 104, 1982, p. 97.

23 Hirsch, Ch., and Dring, R. P., "Through-Flow Models for Mass and Momentum Averaged Variables," Report NPS67-85-012CR, Naval Postgraduate School, Monterey, CA 93943-5100, 1985.

T. P. Hynes

E. M. Greitzer[1]

Whittle Laboratory,
Engineering Department,
Cambridge University,
Cambridge CB3 0EL, England

A Method for Assessing Effects of Circumferential Flow Distortion on Compressor Stability

This paper describes the development of a new analysis to predict the onset of flow instability for an axial compressor operating in a circumferentially distorted inlet flow. A relatively simple model is used to examine the influence of various distortions in setting this instability point. It is found that the model reproduces known experimental trends for the loss of stability margin with increasing distortion amplitude and with changes in reduced frequency. In particular, there is a recognizable "critical sector angle" which characterizes loss of stability margin. To the authors' knowledge, this is the first time the effects described herein have been theoretically demonstrated as the direct result of a fluid dynamic stability calculation.

Introduction

Perhaps the most important problem associated with circumferential inlet flow distortion in axial compressors is that it usually degrades compressor stability margin. For this reason, a large amount of work has been done on this topic and, as a result, various correlative/predictive approaches have been developed. These enable engine manufacturers to assess, from a series of base tests, what the response to inlet distortion will be in other given situations; see for example [1-3].

In spite of the large amount of work, however, there still does not appear to be any "first-principles" approach to predicting the decrease in stall margin. The most notable of the previous theoretical investigations of this problem have been based around various time marching methods. The first of these was by Adamczyk [4] for an isolated rotor, followed by related studies by Pandolfi et al. [5]. Unsteady versions of parallel compressor models have also been used to address this topic [6-8]. These (especially [6]) have been very useful in providing insight into some of the important fluid dynamic effects associated with inlet distortion. However, the difficulties inherent in deciding upon the origin of the instability, whether fluid dynamic or numeric, together with the amount of computation required, make these methods somewhat unwieldy tools for assessing compressor stability.

In addition to the work on inlet distortion, there have been many *small perturbation* theories used to investigate the stability of compressors (and compression systems) operating with a *uniform* (undistorted) *inlet flow*. These have provided valuable insight into many aspects of the uniform inlet flow situation. A recent example is to be found in [9], where the effect of coupling between the two spools of a gas turbine engine is addressed. It is our assessment that there is no comparable analytic framework for the distorted flow situation, even on a rudimentary basis. The present effort is an attempt to provide such an analysis.

The problem addressed is the stability (to small amplitude traveling perturbations) of the circumferentially nonuniform flow field in an axial compressor. The approach taken differs from previous attempts at this problem in several respects. First, previous analyses have been limited to single stages or isolated rotors, whereas our interest is in multistage compressors. Second, and perhaps more important, we are concerned only with stability prediction, and the analysis that is developed takes advantage of this fact. As a result, a simple flow description emerges, which one can use to rapidly survey the effects on stability of different compressor parameters.

Basic Assumptions and Concepts

It is useful at the outset to state two basic concepts that are embodied in this model. The first, which should be evident but which does not appear to have been recognized always in the past, is that to analyze the distorted flow situation, the steady flow nonuniformity must come into the problem in a *nonlinear* manner. If this is not so, there is no interaction between a small-amplitude steady flow distortion and a small-amplitude propagating perturbation, so that a linear treatment of this problem is *fundamentally unable* to describe any of the relevant fluid mechanic coupling.

The second point is that the most important aspect of this nonlinearity appears to be the manner in which the steady and unsteady velocity and pressure nonuniformities are coupled by the compressor (or, in point of fact, by the matching conditions across the compressor). More explicitly, any model of this problem involves some description of the flow fields upstream and downstream of the compressor and of the compressor performance. This latter essentially enters as a set of matching conditions relating the upstream and downstream

---

[1] Present address: Department of Aeronautics and Astronautics, Massachusetts Institute of Technology, Cambridge, MA 02139; Fellow ASME.

Contributed by the Gas Turbine Division for publication in the JOURNAL OF TURBOMACHINERY. Manuscript received by the Gas Turbine Division September 13, 1985.

flows. One can envisage a hierarchy of models of the problem starting with completely linear, then including only the nonlinearity associated with the compressor pressure–velocity relationship, and finally taking account of the nonlinear effects in the flow field.

The first level of these models is irrelevant for the problem of present interest. As suggested by Marble, however, a major part of the "physics" of the problem is obtained by going to the second level [10]. The central argument is that, for velocity nonuniformities associated with typical distortions of interest, the quadratic terms in the (upstream and downstream) flow fields are generally much smaller than the first-order terms. Hence, their neglect has little effect on the flow field. This should be particularly true for multistage compressors where the pressure-flow characteristics are quite steep. We will briefly consider this on an *a posteriori* basis and show that it is a good approximation in the cases examined, but we can also note that there exists other supporting evidence for this treatment in [6, 11–13]. In the first two references, which treated the steady flow distortion problem, a linear flow field analysis was used for the upstream and downstream flows (coupled to a nonlinear compressor model). This gave very good agreement between theory and experiment, even for total pressure distortions of large amplitude. In the latter two, this specific point was examined numerically and shown to be valid for the situations studied.

It is true that *locally* the second-order effects can be significant. For example, the total pressure in a steady distorted flow will be convected along streamlines which are slightly different than those associated with the mean flow, i.e., the total pressure distribution at the compressor will be somewhat different than that far upstream. Thus, at locations near high total pressure gradients, the velocity computed at a given circumferential location could be different in a linear and a nonlinear flow field. If we were crucially interested in distortions of small extent, or in the local flow, this could be a drawback of the present approach. It is, however, distortions of large circumferential extent that are most important as far as stability is concerned and, as will be shown below explicitly, the localized flow field variations that we have mentioned affect this to a small extent only. Hence, the assumption will be valid in precisely those parameter regimes which are of most interest.

This discussion pertains to the flow field only. The situation as regards the *compressor behavior* is quite different. The regimes of operation in which we are interested are near the peak of the compressor characteristic. Even for small nonuniformities in axial velocity, the local slope of the compressor characteristic can change sign. Thus, as one looks around the compressor annulus, some parts of the compressor (which are on negatively sloped portions of the characteristic) will be operating in a regime that one might regard as favorable to stability, while others (on positively sloped portions) might have a deleterious effect on stability. It is vital to include this nonlinearity in the problem, and the present treatment does this.

Stability Assessment

Whether or not the flow through a compressor with a given level of inlet distortion is stable is examined as follows. First of all, a *steady* solution to the distortion transfer problem for the given (finite) distortion level is found. It will be seen that, because of the algorithm used, this can be done whether or not the unsteady behavior of such a flow would exhibit instability in practice. The stability of this steady nonuniform flow is then decided by a conventional fluid dynamic stability analysis, i.e., a general, small-amplitude, unsteady perturbation (which, in the present situation, is *not* strictly sinusoidal) is imposed, and stability is determined by whether such perturbations grow or decay in time. The advantage of this approach is that both steps are essentially analytic ones, and there is no danger of confusing numeric and fluid dynamic instability.

Compressor Dynamics

The compressor is regarded as being of sufficiently high hub-to-tip ratio that the flow through it can be considered two dimensional. Compressor pressure rise, as well as the relevant Mach numbers, are taken to be low enough so that com-

Nomenclature

a = speed of sound
a_n = Fourier coefficients of axial velocity perturbation at compressor face
A = flow-through area
b = blade chord
b_x = axial chord
B = nondimensional stability parameter = $(U/2a)\sqrt{V_{\text{plenum}}/A_2L_{\text{tot}}}$
c_n = Fourier coefficient of compressor characteristic slope
C = absolute velocity
C_x = axial velocity
$\text{DC}(\theta_{\text{crit}})$ = distortion parameter
F_i = ith stage pressure rise in axisymmetric flow
l_c = nondimensional effective length = L_{tot}/R
L_0 = length of ducting upstream of compressor
L_1 = length of ducting downstream of compressor
L_{tot} = overall effective length of compressor ducting
n = harmonic number
N = number of stages
p = static pressure
p_t = total pressure
Δp = stage pressure rise
$\Delta p|_{\text{uns}}$ = pressure rise due to local accelerations
r = mean radius
t = time
T = nondimensional throttle parameter
U = wheel speed
W = relative velocity
x = axial coordinate
γ = stagger angle
$\delta(\ )$ = perturbation quantity
θ = nondimensional circumferential coordinate
θ_{crit} = "critical angle" of distortion
λ = unsteady blade response parameter; defined in equation (5)
μ = unsteady blade response parameter; defined in equation (5)
ρ = density
τ = blade row unsteady parameter
τ_R = rotor unsteady parameter
τ_S = stator unsteady parameter
ϕ = axial flow coefficient = C_x/U
ψ = nondimensional compressor pressure rise in axisymmetric flow = $(p_{\text{exit}} - p_{t_{\text{inlet}}})/\rho U^2$
ω = radian frequency of perturbation
$\tilde{\omega}$ = nondimensional radian frequency = $\omega r/U$

Subscripts and Superscripts

exit = compressor exit
inlet = compressor inlet
0 = inlet to compressor duct
2 = compressor inlet
3 = compressor exit
4 = plenum inlet (compressor duct)
5 = throttle outlet
$(\bar{\ })$ = time and annulus-averaged quantity

pressibility effects can be neglected. It is further assumed that the compressor pressure rise in unsteady flow can be found from the axisymmetric flow performance together with a correction to account for flow unsteadiness. The nature of this correction is in itself a topic for substantial research. We will adopt a rudimentary model, following that developed by Moore [14], who has had reasonable success in applying it to predictions of rotating stall behavior. Although there is no bar to adopting more sophisticated models (for the correction) it should be noted that the inclusion of a conventional unsteady loss model, e.g. [6], can also be cast into this form. This type of approach thus appears to be of wide generality and suffices to show, in a simple manner, the overall methodology, as well as to illustrate some of the central conclusions that can be drawn.

The basic idea stems from regarding the unsteady correction to the pressure rise across each blade as balancing the acceleration of the fluid in the blade row. Thus, across a blade row, there is a local unsteady pressure rise given by

$$\Delta p\,|_{\rm uns} = -\rho b\,\frac{\partial C}{\partial t} \tag{1}$$

for a stator and

$$\Delta p\,|_{\rm uns} = -\rho b\left(\frac{\partial W}{\partial t} + \frac{U}{r}\,\frac{\partial W}{\partial \theta}\right)$$

for a rotor. In this equation, θ denotes the angle around the compressor annulus.

If the contributions for the rotor and stator are added and circumferential flow redistribution between blade rows is neglected, the static pressure rise for the ith stage can be written

$$\left\{\frac{\Delta p}{\rho U^2}\right\}_i = F_i(\phi) - \tau_{R_i}\left(\frac{\partial \phi}{\partial t} + \frac{U}{r}\,\frac{\partial \phi}{\partial \theta}\right) - \tau_{S_i}\,\frac{\partial \phi}{\partial t} \tag{2}$$

F_i is the pressure rise produced by this stage in axisymmetric flow, and is a function of flow coefficient $\phi = C_x/U$. τ_R and τ_S are given by

$$\tau = \frac{b_x}{U\cos^2\gamma}$$

for the rotor and stator, respectively.

For the compressor inlet guide vanes, it is necessary to take account of the flow angle variations at inlet to the blade row. (For blade rows internal to the compressor, these are accounted for by the steady-state performance $F_i(\phi)$.) If the unsteady flow through the IGV's is modeled by lossless turning at the leading edge followed by unsteady channel flow then

$$\left.\frac{p_{\rm exit} - p_{t_{\rm inlet}}}{\rho U^2}\right|_{\rm IGV} = F_{\rm IGV}(\phi) - \tau_{\rm IGV}\,\frac{\partial \phi}{\partial t} \tag{3}$$

which is just a special case of equation (2).

The performance of the compressor as a whole is given by

$$\frac{p_{\rm exit} - p_{t_{\rm inlet}}}{\rho U^2} = \psi(\phi) - \lambda\,\frac{\partial \phi}{\partial \theta} - \frac{r\mu}{U}\,\frac{\partial \phi}{\partial t} \tag{4}$$

where $\psi(\phi)$ is the inlet total-to-exit static pressure rise coefficient in axisymmetric flow.

The quantities λ and μ are associated with the unsteady effects and are defined as

$$\lambda = \sum_{i=1}^{N}\left(\tau_{R_i}\right)\frac{U}{r} \quad \text{and} \quad \mu = \left[\sum_{i=1}^{N}\left(\tau_{R_i} + \tau_{S_i}\right) + \tau_{\rm IGV}\right]\frac{U}{r} \tag{5}$$

The form for $\psi(\phi)$ that will be used in the rest of this study is shown in Fig. 1. The portion of the curve with negative slope is based upon the performance of an existing three-stage low-speed machine. The portion to the left of the peak pressure rise has been chosen somewhat arbitrarily based on models of axisymmetric stalled characteristics developed in [15]. The influence of the compressor performance in this region upon the results obtained will be a subject of a further study, but it can be stated that the calculations carried out so far imply that the central conclusions appear not to be affected by the precise shape of the curve.

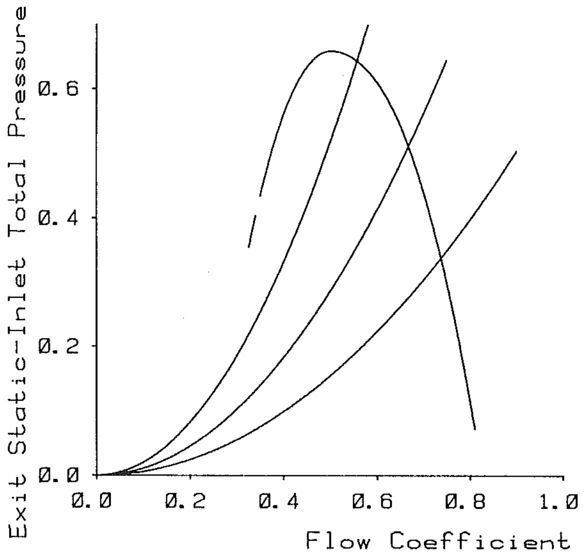

Fig. 1 Compressor characteristic used in numerical examples

As stated, this model of the unsteady flow through a compressor was developed by Moore [14] to study rotating stall. Moore suggests that each τ should be modified by a multiplicative constant to allow for the fluid in the interblade row gaps and for unsteady viscous effects. We will not pursue this point further here except to note that the conclusions, which are based on the relative response to different distortions, should not be critically dependent on the exact form of the model used.

For the steady distorted flow through the compressor, equation (4) reduces to

$$\frac{p_{\rm exit} - p_{t_{\rm inlet}}}{\rho U^2} = \psi(\phi) - \lambda\,\frac{\partial \phi}{\partial \theta} \tag{6}$$

From (4) and (6) it is found that unsteady small perturbations to this flow are described by the linearized equation

$$\frac{\delta p_{\rm exit} - \delta p_{t_{\rm inlet}}}{\rho U^2} = \frac{d\psi}{d\phi}\,\delta\phi - \lambda\,\frac{\partial \delta\phi}{\partial \theta} - \frac{r\mu}{U}\,\frac{\partial \delta\phi}{\partial t} \tag{7}$$

To summarize this section: Equation (6) determines how the flow field at compressor entry must rematch as a function of θ to satisfy the compressor pressure rise equation. Having found that match, the solution of equation (7) (together with the upstream and downstream flow fields) determines whether or not such a flow is stable.

We can compare the form of equation (7) with the case of no distortion. The major modification is that, for distorted flow, $d\psi/d\phi$ is no longer a constant but is *a strong function of* θ, with the precise shape depending on the particular characteristic used. One expects that those parts of the annulus where $d\psi/d\phi$ is positive will be locally destabilizing, while those where $d\psi/d\phi$ is negative will be (locally) stabilizing. At the point of instability, these positive and negative slope regions will thus be in some sort of balance.

Compression System

In analyzing this problem, we must address the compressor as part of a compression system. This is true for two reasons. First, the annulus-averaged performance of the compressor is affected by the presence of inlet distortion and it is relevant to

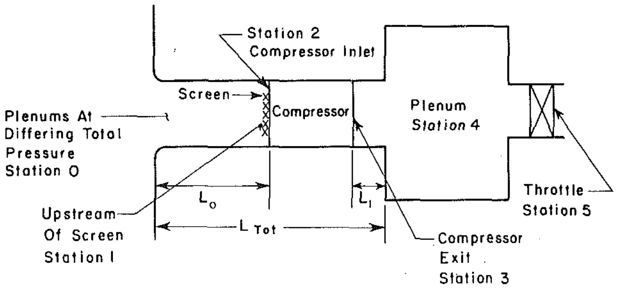

Fig. 2 Compression system and station nomenclature

make comparisons at fixed throttle setting. Secondly, because the steady mean flow is a function of θ, the small, unsteady perturbations will *no longer be purely sinusoidal in* θ. In particular, they will result in *changes in the annulus averaged flow* through the compressor. It is thus necessary to take account of the system response to these flow changes. The system considered is shown in Fig. 2.

A further aspect of the description of the overall system is that, in practice, compressor testing with inlet distortion is usually carried out using screens which block part of the annulus. Thus, the distortion intensity, as we have defined it, will vary over the flow range as the inlet dynamic pressure varies. In addition, the coupling between the distortion generating screen and the compressor can change as the compressor operating point changes.

We have (so far) not tried to address the various permutations of screen geometry and spacing, but rather have looked at two limiting cases which bound the cases of interest. These are: (1) distortion created by a screen placed at the compressor inlet, and (2) distortion created far upstream, say by supplying the compressor from large plenums at differing total pressures. These simplifications are made in the interests of clarity and it is to be emphasized that they do not represent any limitation in the capability of the analysis.

Compressor Inlet Flow Field

As stated, there are two cases to be considered. In the first, the total pressure distortion is specified far upstream. The assumption that the flow field upstream of the compressor can be treated in a linearized manner greatly simplifies the analysis because, in the steady, distorted flow, the total pressure is convected along streamlines of the undistorted flow. Thus

$$p_{t0}(\theta) = p_{t2}(\theta) \tag{8}$$

For the situation in which a distortion generating screen exists at the compressor inlet, we have for the steady flow

$$p_{t1} = p_{t0} = \text{const} \tag{9}$$

and the upstream flow is irrotational. The pressure drop through the screen is

$$\frac{p_{t1} - p_{t2}}{\rho U^2} = \frac{S(\theta)}{2}\left(\frac{C_x(\theta)}{U}\right)^2 \tag{10}$$

Here $S(\theta)$ is a specified *local* screen loss parameter and the C_x/U that occurs in equation (10) is the local value. For the type of screens that are commonly used, $S(\theta)$ would be essentially a square wave with a finite value over part of the annulus and zero over the rest.

Whichever set of conditions is imposed, the unsteady perturbations upstream of the compressor will be of potential type. This is clearly the case if the distortion is generated at the compressor inlet. Even if the distortion is generated far upstream, however, the linearization that has been adopted implies that the unsteady perturbations do not interact with the vortical disturbances present in the steady distorted flow field.

For the unsteady perturbations, a general small amplitude disturbance can be taken to have time dependence $\exp(i\omega t)$, with ω being determined from the stability analysis. If ω has a negative imaginary part, growth of the disturbance is implied and the flow is unstable. The most general form of a small (unsteady) axial velocity perturbation at the compressor face is

$$\frac{\delta C_{x2}}{U} = \sum_{n=-\infty}^{\infty} a_n e^{in\theta + i\omega t} \tag{11}$$

(Note that $C_{x1} = C_{x2}$.)

In the upstream region, the axial momentum equation can be written as

$$\frac{\partial \delta C_x}{\partial t} + \frac{\partial \delta p_t}{\partial x} = 0 \tag{12}$$

Equation (12) can be integrated once in x since the unsteady velocity perturbations are potential. Doing this and invoking the boundary condition of time independent total pressure at the upstream plenum ($\partial \delta p_{t0}/\partial t = 0$) implies that the unsteady perturbations in total pressure are of the form

$$\frac{\delta p_{t2}}{\rho U^2} = -\sum_{\substack{n=-\infty \\ n\neq 0}}^{\infty} \frac{i}{|n|}\,\frac{\omega r}{U}\, a_n e^{in\theta + i\omega t} - \frac{i\omega L_0}{U}\, a_0 e^{i\omega t} \tag{13}$$

Compressor Outlet Flow Field

It will be assumed that the compressor under study has axial outlet flow through a row of high solidity stators. In such circumstances, provided there is no downstream compressor, diffuser, struts, etc. within several mean annulus radii, the static pressure will be circumferentially uniform in the steady distorted flow, and will be the same as the plenum pressure

$$p_4 = p_3. \tag{14}$$

Using continuity of compressor inlet and outlet axial velocity, and employing the high solidity exit condition, the downstream perturbations can be shown to satisfy

$$\frac{\delta p_4}{\rho U^2} - \frac{\delta p_3}{\rho U^2} = -\sum_{\substack{n=-\infty \\ n\neq 0}}^{\infty} \frac{i}{|n|}\,\frac{\omega r}{U}\, a_n e^{in\theta + i\omega t} - \frac{i\omega L_1}{U}\, a_0 e^{i\omega t} \tag{15}$$

and

$$\frac{\delta C_{x3}}{U} = +\sum_{n=-\infty}^{\infty} a_n e^{in\theta + i\omega t}. \tag{16}$$

Plenum Dynamics

In steady flow, the static pressure in the plenum is determined by the throttle setting

$$\frac{p_4 - p_5}{\rho U^2} = \frac{1}{2}\left(\frac{\bar{C}_{x5}}{U^2}\right)^2 = \frac{T}{2}\left(\frac{\bar{C}_{x3}}{U}\right)^2 \tag{17}$$

To complete the description of the unsteady flow in the plenum, we take the flow through the throttle to be quasi-steady. In addition, we assume pressure and density changes in the plenum can be related by an isentropic relationship [16]. Using these assumptions in the continuity equation for the plenum, we obtain

$$\left(4\,B^2\,\frac{L_{\text{tot}}}{r}\cdot\frac{i\omega r}{U} + \frac{1}{\bar{\phi}_3 T}\right)\frac{\delta p_4}{\rho U^2} = \frac{\delta \bar{C}_{x3}}{U} \tag{18}$$

The quantity L_{tot} is equal to $L_0 + L_1 + \mu r$ and is the "effective length" of the compressor as defined in [16]. The nondimensional parameter B is given by

$$B = \frac{U}{2a}\sqrt{\frac{\text{Volume of plenum}}{A_2 L_{\text{tot}}}} \tag{19}$$

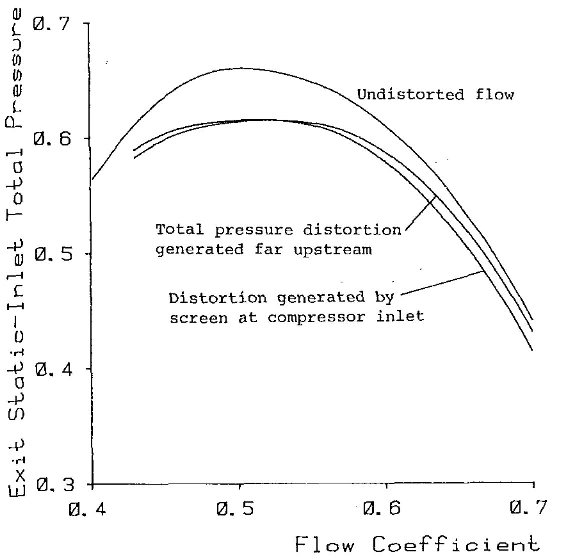

Fig. 3 Undistorted and distorted flow compressor characteristics

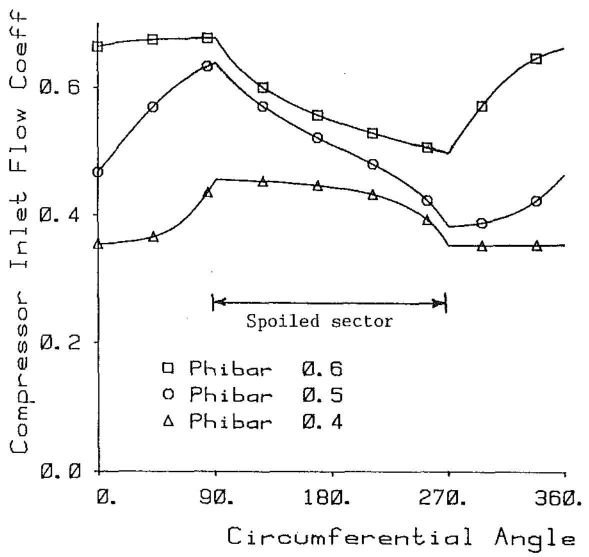

Fig. 4 Axial velocity profiles for steady 180 deg inlet distortion; square wave, $p_{t_{max}} - p_{t_{min}} = 0.2\,\rho U^2$

Its crucial role in system stability considerations is discussed in [17].

Steady Distorted Flow: Solution Procedure and Numerical Example

Once the inlet distortion is specified, the equations determining the steady flow, (6), (8), (14), and (17), can be combined to obtain equations that describe the way in which the flow at compressor entry must adjust to satisfy the condition of uniform exit pressure, namely

$$\frac{p_3 - p_{t2}(\theta)}{\rho U^2} = \psi(\phi_2) - \lambda \frac{d\phi_2}{d\theta} \tag{20}$$

and

$$\frac{p_3 - p_5}{\rho U^2} = \frac{T}{2}(\bar{\phi}_2)^2. \tag{21}$$

The first equation is a first-order differential equation for ϕ_2 and can be solved in a variety of ways. The approach adopted here is to use a pseudospectral (Fourier transform) method [18] to solve equations (20) and (21). In this method, the flow variables are transformed into Fourier space with respect to θ, and derivatives (or other operators) with respect to θ are algebraic in the transformed variable. Evaluating the equations at discrete points around the annulus (collocation points) then yields a set of coupled nonlinear algebraic equations for the Fourier coefficients a_n.

There are several advantages of using this type of method. First, it is computationally efficient, in that excellent computer routines to find and invert discrete Fourier transforms are universally available (although it is to be stressed that we have not at all attempted to optimize the algorithm for the overall solution procedure). Second, the same approach can be used for the unsteady problem. A further important aspect is that because one develops the solution in terms of the eigenfunctions of the configuration (here a rectangular domain in x and θ), spectral methods offer the possibility of increased insight into the physics of the problem.

The specific approach used here was straightforward and involved collocation and iteration on the Fourier transform of ϕ_2. Using this method, equation (20) can be solved over the whole range of throttle settings. Figures 3 and 4 demonstrate results obtained for a 180 deg "square wave" distortion, with the largest amplitude distortion examined. It should be noted that, at the conditions of interest, i.e., near an average value of $\phi \sim 0.5$, the value of distortion chosen is approximately 1.6 times the inlet dynamic pressure based on the mean velocity. In other words, it is to be emphasized that this is *not* a small distortion.

Figure 3 shows the compressor characteristics for uniform flow and with inlet distortion. Distorted flow characteristics are shown in the figure for the two limiting cases described previously; one for a total pressure distortion, $\Delta p_t/\rho U^2 = 0.2$, imposed far upstream, and one for a total pressure distortion generated by a screen at the compressor inlet. In the latter situation, the screen porosity has been chosen so that the distortions in the two cases have the same magnitude at $\bar{\phi} = 0.5$, this being the region of greatest interest. This implies that the screen-generated total pressure distortion is larger than that generated far upstream for higher values of $\bar{\phi}$ and lower for lower values of $\bar{\phi}$ and this appears to be reflected in the relative positions of the performance curves. As is well known, the effect of distortion is to decrease the peak pressure level attained, and the distorted flow characteristics illustrate the magnitude of this effect in the situations investigated. Only a portion of the computed performance curves are shown, but it is to be emphasized that this steady-state part of the calculation can be carried out over the whole flow range of interest.

In Fig. 4, the axial velocity at the compressor inlet is plotted versus circumferential angle for the case of total pressure distortion generated far upstream. The shapes of these axial velocity profiles can be understood qualitatively with reference to basic parallel compressor theory. The upper curve is roughly similar to the total pressure distortion, with low pressure rise and high velocity in the region of high total pressure. The lowest curve, which is essentially 180 deg out of phase with the total pressure distortion, reflects the fact that the compressor slope is positive so that low velocity is associated with high pressure rise.

The center curve is roughly in quadrature with the inlet total pressure profile. This is because the velocities shown imply local compressor operation on both sides of the peak of the characteristic. In addition, the slopes encountered are smaller so that it is the unsteady effects that are important in this regime [6]. This phase shift of the axial velocity, relative to the total pressure, will be shown to have important consequences for the disturbance mode shapes.

The results of Fig. 4 can also be used to estimate the effect of the neglect of the nonlinear terms (in the field equations) for the steady flow calculation. From Fig. 4, for the midflow case which is the region of most interest, the value of the ratio of nonlinear to linear terms is approximately 0.25 (based on amplitude). Hence, even for the case of this very large inlet distortion, the nonlinear terms are small. For the other cases examined, and for many cases of practical interest, the approximation is considerably better.

As regards flow instability, the solution corresponding to the high flow case is expected to be stable, since the flow coefficient is everywhere greater than the value (0.5) for instability of the undistorted flow. The midflow case could be stable or unstable. The low flow situation would be expected to be unstable, with the flow coefficient always being less than 0.5. These solutions demonstrate that numerical instability is not present in the steady-state calculation.

Stability Calculation

The stability of any steady flow generated by the procedure outlined in the previous section is determined by examining the growth of small unsteady disturbances. Because a general perturbation is most easily represented as a Fourier series, as in equation (12),

$$\frac{\delta C_{x1}}{U}=\frac{\delta C_{x2}}{U}=\frac{\delta C_{x3}}{U}=\sum_{n=-\infty}^{\infty} a_n e^{in\theta+i\omega t} \tag{12}$$

it is convenient to represent the function $d\psi/d\phi$ also in this form

$$\frac{d\psi}{d\phi}=\sum_{n=-\infty}^{\infty} c_n e^{in\theta} \tag{22}$$

The term $d\psi/d\phi$ is the slope of the compressor characteristic evaluated at the *local* (distorted) flow coefficient. Note that, in the overall total-to-static case of the screen at compressor inlet, the overall total-to-static pressure rise will include the pressure difference across the screen. Thus, $d\psi/d\phi$ must also include the local slope of the screen pressure drop curve, $-S\phi$, where S and ϕ are functions of θ (from equation (10)).

This local compressor characteristic slope defines the environment in which small perturbations must propagate and is *the key element* in the stability issue. The equations describing the unsteady perturbations in the various parts of the system (equations (7), (11)–(13), (15), (16), (18)) can be combined to form a set of equations for the spatial form that any perturbations may take and for the growth rate ω. Doing this, one obtains, for $n\neq 0$

$$\left(\left(\frac{2}{|n|}+\mu\right)\tilde{\omega}+\lambda n+ic_0\right)a_n=-i\sum_{\substack{s=-\infty\\ s\neq 0}}^{\infty} c_{n-s}a_s \tag{23}$$

and for $n=0$

$$\left(l_c\tilde{\omega}+ic_0-\frac{i}{4B^2 l_c i\omega+\dfrac{1}{\bar{\phi}_3 T}}\right)a_0=-i\sum_{\substack{s=-\infty\\ s\neq 0}}^{\infty} c_{-s}a_s \tag{24}$$

where $\tilde{\omega}=\omega r/U$ and $l_c=(L_0+L_1)/r+\mu=L_{\text{tot}}/r$.[2]

If $d\psi/d\phi$ were independent of θ (no distortion), the only nonzero c_n would be c_0. Equation (23) would then reduce to the undistorted compressor flow stability criterion. Each harmonic in the perturbation would become independent, and for $n\neq 0$

$$\tilde{\omega}=-\frac{ic_0+\lambda n}{\dfrac{2}{|n|}+\mu} \tag{25}$$

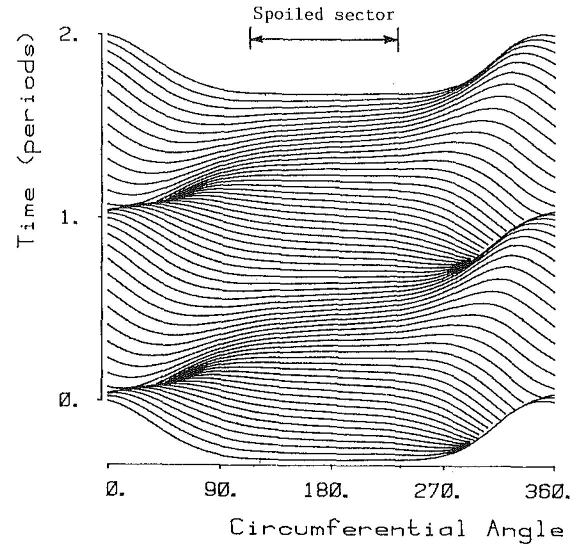

Fig. 5 Axial velocity perturbation at instability point; 120 deg distortion, B = 0.82, l_c = 4.0, λ = 1.0, μ = 2.0

Thus, the nonzero harmonics become unstable when the slope of the compressor characteristic c_0 becomes zero. For the $n=0$ mode, on the other hand, there are two possible solutions for $\tilde{\omega}$, which satisfy

$$4B^2 l_c^2\tilde{\omega}^2+i\left(4B^2 l_c c_0-\frac{l_c}{\bar{\phi}T}\right)\tilde{\omega}+\frac{c_0}{\bar{\phi}T}-1=0 \tag{26}$$

$\tilde{\omega}$ as given by (26) can have a negative imaginary part (implying instability) when either $c_0 > \bar{\phi}T$ (corresponding to *the compressor characteristic slope exceeding that of the throttle*), or when $c_0 > 1/4B^2\bar{\phi}T$, when the system is dynamically unstable.

With circumferential distortion, since $d\psi/d\phi$ is a function of θ, different harmonics of the perturbations are coupled. A standard eigenvalue routine is thus used to solve equations (23) and (24) for the eigenvalues $\tilde{\omega}$. If any of the solutions for $\tilde{\omega}$ have a negative imaginary part, the flow is unstable. Calculation of the instability point for a given inlet distortion consists of carrying out computations at decreasing values of throttle setting until an operating point is found at which the imaginary part of any of the possible $\tilde{\omega}$ (i.e., any eigenvalue) first becomes negative.

A rough rule of thumb that has emerged from the calculations that have been done *so far* is that instability will occur approximately where the annulus average compressor characteristic slope, $(1/2\pi)\int_0^{2\pi}(d\psi/d\phi)\,d\theta$, is zero. This occurs near the peak of the *distorted flow* characteristic, and the latter might thus be tentatively regarded as an operational criterion for onset of instability in distorted flow. Since the same equations govern the axial velocity perturbations whether or not the compressor inlet screen is present, this statement is valid for both the situations that we consider, provided that, in the case of the screen at inlet (as stated previously), $d\psi/d\phi$ includes the appropriate (local) pressure change across the screen.

The modal structure of the perturbations is complex, and we will not discuss it here in any sort of generality. However, it is perhaps instructive to examine one of the eigensolutions at the neutral stability point. The example chosen is based on a far upstream total pressure distortion of 120 deg extent. The mode examined is that with the first harmonic the strongest, since the rotating stall disturbances encountered in practice are of this type.

Figure 5 shows the waveforms of the normalized axial velocity perturbation (for this mode) at the compressor versus circumferential position. The different curves correspond to

---

[2] Note that this is not the form in which the equations are actually set up to be solved. Equation (24) is rather written as two first-degree (in $\tilde{\omega}$) equations, so the system defined by (23) and (24) constitutes a standard eigenvalue problem for $\tilde{\omega}$.

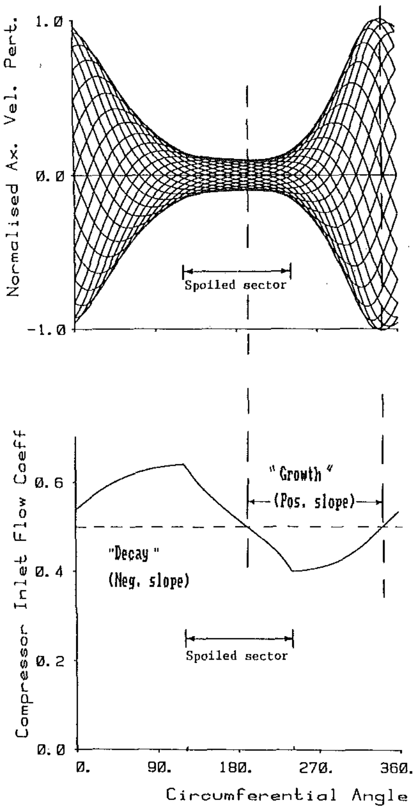

Fig. 6 Top: envelope of axial velocity perturbation at instability; bottom: steady axial velocity profile showing regions of growth and decay

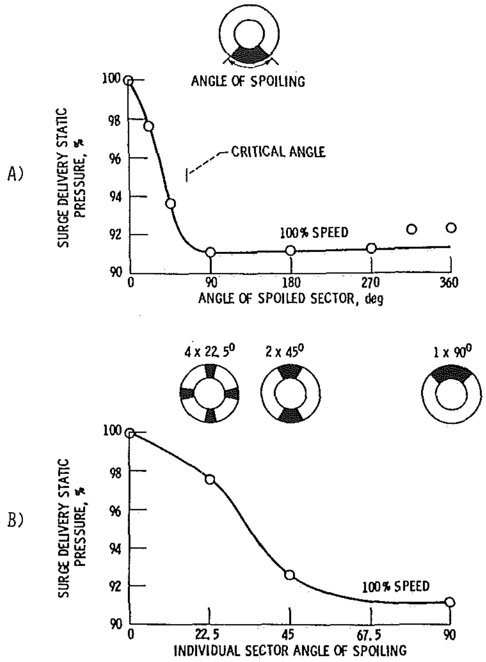

Fig. 7 Reid's experimental results (taken from [2]): (*a*) loss in stability margin versus spoiled sector size; (*b*) loss in stability margin versus number of sectors

different times, and two complete periods of the wave are plotted. The extent of the distortion is indicated in the figure, and the specific parameters used are given in the caption.

Several features can be seen in the figure. First, the wave changes shape as well as (peak to peak) "amplitude" as it travels around the annulus. The velocity of travel of the peaks (the group velocity) also varies around the annulus. Third, the mode comprises both the traveling wave type of perturbation and the one-dimensional type of perturbation that one associates with a system transient, since the mean level of the perturbation moves up and down. One can thus perhaps regard the system type perturbations as being "driven" by the propagating disturbances. Finally, we see that the degree of fluctuation, i.e., the fluctuation that a hot wire, say, would see, also differs considerably around the annulus.

The last of these points is illustrated in the upper part of Fig. 6. This shows the axial velocity waves at different times plotted on the same axes, to illustrate the *wave envelope*. The circumferential extent of the distortion is also indicated. Note that calculations show that this envelope shape is very similar for other modes as well. Thus, no matter which mode actually becomes unstable, the envelope of axial velocity fluctuations is found to have approximately the same θ dependence.

The manner in which the peak-to-peak fluctuations vary with circumferential position can be at least qualitatively understood by considering the variation in local compressor operating point. If local operation on the positively sloped part of the characteristic is a situation in which small unsteady perturbations are (locally) amplified and operation on the negatively sloped part of the characteristic is a situation in which these perturbations decay, it follows that the regions of largest fluctuation should occur at the end of the region of operation on the positive slope. Conversely, the lowest amplitude fluctuations should occur at the end of the region of operation on the negative slope.

The compressor characteristic used in the calculations, which was shown in Fig. 1, has its peak at $\phi = 0.5$. Positive slopes thus occur for values of ϕ below this and negative slopes occur for values above. Examination of the steady axial velocity profile thus gives an indication of the regimes of local amplification (positive slope) and decay (negative slope) of the unsteady perturbation.

The steady axial velocity profile is shown in the lower part of Fig. 6, which has the same abscissa as the upper part. If we compare the regions of positive and negative slope indicated in the lower part of the figure with the growth and decay shown in the wave envelope in the upper part, we see that the correspondence is quite good. It thus appears that this type of local stability argument does explain the trends seen in the mode shapes, but clearly the topic deserves further study.

Numerical Calculations of Distortion Effects on Stability

1 Loss of Stability Margin. The basic experiments of Reid [19] illustrate some of the fundamental concepts associated with the effects of inlet distortion on compressor stability margin. These are summarized in Figs. 7(*a*) and 7(*b*) (taken from [2]). In Fig. 7(*a*), the compressor delivery pressure at the instability point is plotted versus the extent of the spoiled sector (it is actually the extent of the gauze used to create the flow distortion, but the two values are not greatly different). It can be seen that increasing the angle of the spoiled sector steadily degrades stability until a "critical sector angle" is reached.

To examine this point, a set of calculations was carried out following this procedure. The example compressor was subjected to "square wave" total pressure distortions of increasing sector angle. In the calculations, the values of B, l_c, λ, and μ were kept constant at 0.82, 4.0, 1.0, and 2.0, respectively, and the distortion was taken to be generated far upstream.

The calculated effect on compressor (inlet total to exit static) pressure rise at instability is shown in Fig. 8, which

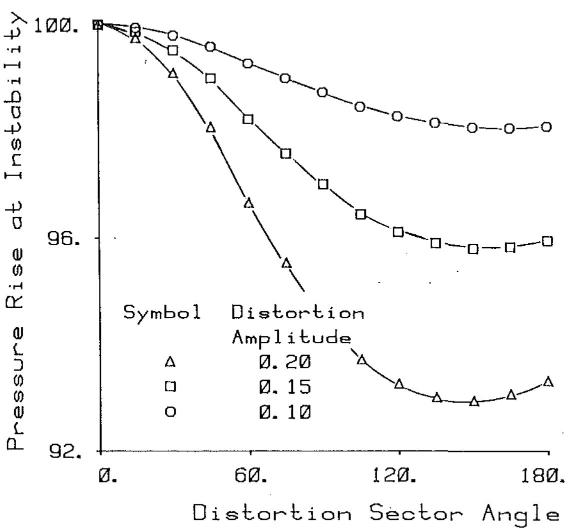

Fig. 8 Loss in stability margin versus spoiled sector size

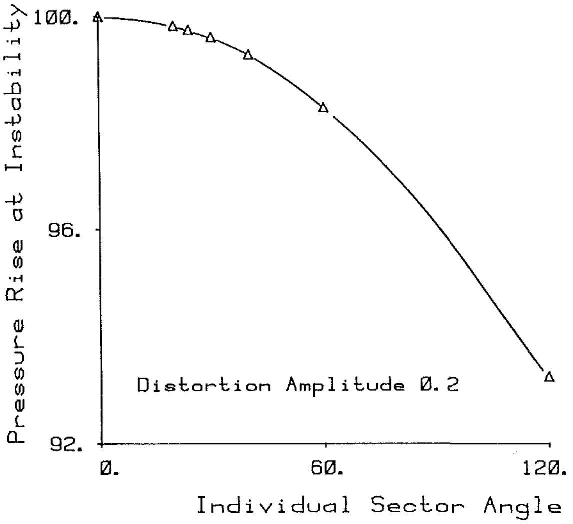

Fig. 9 Loss in stability margin versus number of sectors

gives the percent loss in peak pressure rise at instability, versus sector angle, for three different amplitudes of total pressure distortion: 0.1, 0.15, and 0.2. As stated before, to convert these to units of dynamic pressure based on the mean inlet velocity, they should be multiplied by roughly a factor of eight. Although this manner of showing the decrease in compressor stability with inlet distortion is somewhat crude, we have done it to compare with the trends shown in [19]. From the calculations, the "critical sector angle" for the example compressor (using the definition of Reid) appears to be of the order of 120 deg. Presumably this will be compressor geometry dependent; however, we have not yet carried out enough parametric studies to infer any generalizations about the relation between compressor parameters and critical angle.

A second set of calculations is presented in Fig. 9. These address the effect shown in Fig. 7(*b*), i.e., the effect of keeping the total spoiled sector angle constant, but splitting it into smaller and smaller segments. The trend found by Reid was that, as the number of segments (and hence the blade reduced frequency) increased, there was a significantly smaller effect on compressor stability. The same trend is shown in the calculations presented in Fig. 9, which were done for a total spoiled sector of 120. To the authors' knowledge, this is the first time that such trends have been shown based on direct fluid dynamic stability calculations.

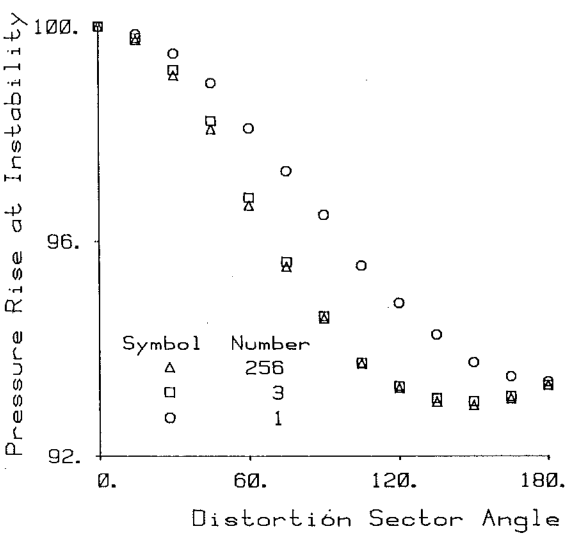

Fig. 10 Effect of number of harmonics in distortion description on instability prediction; square wave total pressure distortion

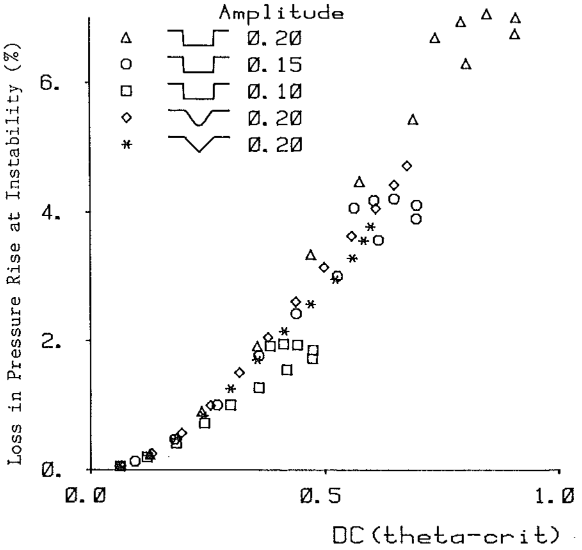

Fig. 11 Loss in stability margin versus DC(θ_{crit})

2 Effect of Harmonic Content of Distortion on Stability. One of the questions it is useful to ask concerning circumferential distortion is how accurately one has to simulate the distortions that are observed in practice, i.e., how many of the Fourier components that describe the distortion are, in fact, important. In order to examine this, we have carried out calculations with representations of the inlet distortions composed of various numbers of terms. Figure 10 shows the results for Fourier series representations consisting of 1, 3, and 256 harmonics, the last being the number that all other calculations were done with.

It can be seen that one harmonic (i.e., representing the distortion as a sine wave) is not enough, but three harmonics does appear to do a reasonable job. This has two implications. First, when one simulates inlet distortions, it is only the lower harmonics that matter. Second, although the flow field linearization adopted here may be incorrect locally in regions of high velocity gradients, Fig. 10 shows that a description of these regions (which involves the higher harmonics of the distortion) does not appear to be necessary for an adequate description of the overall stability of the flow. As stated previously, this implies that the approximation is valid in the range of parameters which are most important in determining the instability point.

3 Correlation of Pressure Loss at Stall With DC(θ_{crit}). There are now well-established procedures, developed by the engine manufacturers, which correlate results for complex distortion patterns with those obtained by testing with simple gauzes and with those obtained by the use of relatively simple parallel compressor models. Several of these are built around the use of distortion indices based on some sort of weighted average over a critical sector. A description of one of these, the so-called DC(θ_{crit}) method, is given in [1, 3].

In order to make the connection between the present analysis and these types of correlation, calculations have been carried out for a range of distortion patterns. Those examined are square wave (with which most testing is actually done), triangular, and a much smoother shape based on a quartic curve. The shapes are indicated on Fig. 11, which shows loss in stall pressure rise versus DC(θ_{crit}). θ_{crit} for this purpose was estimated from Fig. 8 and taken as 125 deg. The correlation might be improved for a slightly different choice, but even with this rough estimate for θ_{crit}, it can be seen that there appears to be a strong correspondence between the analytical results and the semi-empirical methods used in practice to predict the effects of inlet distortion on compressor stall.

Summary and Conclusions

A new analysis has been presented for assessing the impact of inlet distortion on compressor stability margin. The limited calculations that have been carried out using this analysis show that:

1 The current method correctly predicts widely observed trends in compressor behavior.

2 The method is largely analytic and defines the operating point delineating stable from unstable operation to an arbitrary precision. There is no doubt that the origin of the instability is fluid dynamic.

3 Being largely analytic, the assumptions made in formulating the model are clearly stated and can be easily scrutinized.

4 All possible two-dimensional disturbances are considered. There are no extra considerations, from which another stability criterion might arise.

5 We believe that the model includes a proper fluid dynamic interaction between the spoiled and unspoiled sectors of the compressor.

6 The model is capable of considerable extension. It can be used to explore the nature of the disturbances which are responsible for instability, and to determine the major factors influencing stability margin loss.

Acknowledgments

T. P. Hynes would like to thank Rolls-Royce Limited for support during the course of this work and, in particular, Mr. D. D. Williams for helpful comments and encouragement. The support of the Royal Society and the Science and Engineering Research Council for E. M. Greitzer is gratefully acknowledged, as are the efforts of N. A. Cumpsty, Sir William Hawthorne, and D. S. Whitehead in arranging his stay in Cambridge. The hospitality shown the junior author by the staff and students of the Whittle Laboratory is very much appreciated. Partial support for the work from NASA Lewis Research Center under Grant NSG-3208 is also acknowledged with thanks.

References

1 Hercock, R., and Williams, D. D., "Aerodynamic Response," in: *Distortion Induced Engine Instability*, AGARD Lecture Series LS72, 1974.

2 Bowditch, D. N., and Coltrin, R. E., "A Survey of Inlet Engine Distortion Compatibility," NASA TM 83421, 1983.

3 Williams, D. D., "Inlet-Engine Compatibility," Workshop on Engine-Airframe Integration, Bangalore, India, 1984.

4 Adamczyk, J. J., "Unsteady Fluid Dynamic Response of an Isolated Rotor With Distorted Inflow," AIAA Paper No. 74-49, 1974.

5 Pandolfi, M., and Colasurdo, "Numerical Investigation on the Generation and Development of Rotating Stall," ASME Paper No. 78-WA/GI-5.

6 Mazzawy, R. S., "Multiple Segment Parallel Compressor Model for Circumferential Flow Distortion," ASME JOURNAL OF ENGINEERING FOR POWER, Vol. 99, Apr. 1977, pp. 228–246.

7 Steenken, W. G., "Modeling Compressor Component Stability Characteristics—Effects of Inlet Distortion and Fan Bypass Duct Disturbances," in: *Engine Handling*, AGARD CP-324, Oct. 1982.

8 Baghdadi, S., and Lucke, J. E., "Compressor Stability Analysis," ASME Paper No. 81-WA/FE-18.

9 Ham, C. J., and Williams, D. D., "Some Applications of Actuator and Semi-Actuator Disk Theory to the Problem of Intake/Engine Compatibility," JSME International Gas Turbine Conference, Tokyo, Paper No. 83-Tokyo-IGTC-50, 1983.

10 Marble, F. E., personal communication, 1981.

11 Greitzer, E. M., Mazzawy, R. S., and Fulkerson, D. A., "Flow Field Coupling Between Compression System Components in Asymmetric Flow," ASME JOURNAL OF ENGINEERING FOR POWER, Vol. 100, Jan. 1978, pp. 66–72.

12 Takata, H., and Nagano, S., "Nonlinear Analysis of Rotating Stall," ASME JOURNAL OF ENGINEERING FOR POWER, Vol. 95, Oct. 1973.

13 Adamczyk, J. J., personal communication, 1984.

14 Moore, F. K., "A Theory of Rotating Stall of Multistage Compressors, Parts I-III," ASME JOURNAL OF ENGINEERING FOR GAS TURBINES AND POWER, Vol. 106, 1984, pp. 313–336.

15 Koff, S. G., and Greitzer, E. M., "Stalled Flow Performance for Axial Compressors—I: Axisymmetric Characteristic," ASME Paper No. 84-GT-93.

16 Greitzer, E. M., "Surge and Rotating Stall in Axial Flow Compressors," ASME JOURNAL OF ENGINEERING FOR POWER, Vol. 98, Apr. 1976, pp. 190–217.

17 Greitzer, E. M., "The Stability of Pumping Systems—The 1980 Freeman Scholar Lecture," ASME *J. Fluids Eng.*, Vol. 103, June 1981, pp. 193–242.

18 Peyret, R., and Taylor, T. D., *Computational Methods for Fluid Flow*, Springer-Verlag, New York, 1983.

19 Reid, C., "The Response of Axial Flow Compressors to Intake Flow Distortion," ASME Paper No. 69-GT-29.

Effects of Slotted Hub and Casing Treatments on Compressor Endwall Flow Fields

M. C. Johnson[1]

E. M. Greitzer

Department of Aeronautics and Astronautics,
Massachusetts Institute of Technology,
Cambridge, MA 02139

An experimental investigation was carried out to examine the influence of a rotating slotted hub treatment on a compressor stator passage endwall. Detailed mapping of the three-dimensional unsteady velocity field near the hub was done for a smooth hub and a hub having axial skewed slots. With the smooth wall, the velocity measurements indicate that a large region of blockage occurs near the rear of the blade passage. This blockage is seen to be associated with the hub endwall rather than either the suction surface or the pressure surface of the blade. With axial skewed slots, the blockage is markedly decreased, the stalling flow coefficient is reduced, and the peak pressure rise greatly increased. Due to the axial (rear-to-front) flow in the slots, there is a region of fluid removal (from the endwall) near the rear of the passage and a strong fluid injection, or jet, near the front. The data appear to show that this flow removal is an important part of the effect on stall margin found with hub and casing treatment. Furthermore, the data indicate that it is the (dissipation of the) high velocities in the jet that is the prime source of the efficiency reduction associated with this treatment.

Introduction

Background. It is well known that the application of grooves or slots over the tips of compressor rotor blades can have a marked effect on the compressor stall margin. Recent examples of this (with many supplementary references to the phenomenon) are discussed in [1–5]. Although the mechanism of operation of casing treatment is still not well understood, the measurements that have been carried out show clearly that the treatment reduces the boundary layer blockage associated with the endwall and retards the onset of rotating stall.

It has also recently been shown that a slotted "hub treatment" rotating beneath a cantilevered stator can lead to a substantial stall margin increase [6]. As with the casing treatment, there was a strong suppression of endwall blockage when treatment was applied.

An important result, which applies to both hub and casing treatment, is that one can often make a distinction between two modes of compressor stall [1, 2, 5, 6]. One of these, termed "blade stall," is a basically two-dimensional type of stall where a significant portion of the blade span has a separation on the suction surface. The other, termed "wall stall," occurs when a separation occurs on the endwall. The data in [1, 2, 5, 6] show that casing treatment, or hub treatment, is only effective when the type of stall is wall stall.

Approach and Scope of the Paper. To try to clarify the mechanism of casing treatment operation, we have undertaken an investigation of a particularly effective treatment, the axial skewed slot. This treatment has given very large improvements in stall margin although with some efficiency penalty. A deliberate choice, however, was made to use the axial skewed configuration in order to maximize the effects under investigation.[2]

As discussed subsequently, although there are some differences between the flow in the hub of a cantilevered stator and that over the tip of a rotor, there is a great deal of similarity between the two. This implies that similar mechanisms of operation occur for hub and for casing treatment. As well as being of engineering interest itself, this is an extremely useful result from another aspect, because it enables examination of the mechanism of (tip) casing treatment without the need for rotating instrumentation. This is the approach taken in the present investigation; further justification is presented below.

In the past, substantial attention has been focused on a particular feature associated with the axial skewed slots, namely the strong flow injection, or jet, which occurs near the leading edge of the slots as a result of the overall rear-to-front throughflow. One reason for this is that the jet is a very evident feature and changes in jet velocity have been seen to be associated with changes in stall margin.

This latter point is seen in the data of [3], which also includ-

---

[1] Present address: Department of Mechanical Engineering, Texas A&M University.

Contributed by the Gas Turbine Division of THE AMERICAN SOCIETY OF MECHANICAL ENGINEERS and presented at the 31st International Gas Turbine Conference and Exhibit, Düsseldorf, Federal Republic of Germany, June 8–12, 1986. Manuscript received at ASME Headquarters February 21, 1986. Paper No. 86-GT-247.

[2] The loss in efficiency can be substantially decreased using baffles at the midslot axial location, e.g., [4, 7], although with some decrease in stall margin. This also was not done for the reason discussed above.

ed a careful parametric investigation of casing treatments and some initial results for stator hub treatment. Of the treatments used, an axial slot, skewed so that the slot faced the blade pressure surface, gave the greatest improvement in stall margin compared to a smooth wall. On the other hand, an axial slot, skewed so that the slot faced the suction surface, actually decreased the stall margin compared to a smooth wall. Further, the former had a high-velocity (comparable to the mean axial velocity) jet from the front of the slot, whereas in the latter, the jet was much weaker (on the order of one-third the mean axial velocity or less) [3].

The jet, however, is not the only way in which the presence of the slot changes the flow in the endwall. Associated with the jet from the front part of the slots there must be, from continuity, suction, or removal of flow, at the rear of the slots. There are thus two processes which could affect the flow in the endwall layer: the injection of a high-velocity jet at the front of the blade passage and the removal of low-velocity (high blockage) fluid at the rear due to the net slot throughflow. Situations in which the jet is weak are also those in which there is little flow removal, so that both effects go together.

A basic issue regarding the mechanism of casing treatment operation is which of these is important in affecting the stall point, and in [1], it was in fact speculated that it was the removal. The experiments described below show that this removal of the low-velocity fluid near the rear of the passage does appear to be an important effect in creating the improvement in stall margin. This, in turn, has important consequences as regards design optimization of casing and hub treatments.

It is recognized that considerable further work needs to be carried out to settle the above issue and to define completely the fluid dynamic features of casing and hub treatment, and the present short paper by no means presents a complete picture. Nevertheless, we believe that the structure of the flow revealed by these experiments is both new and of sufficient phenomenological content to be of interest in itself.

Experimental Facility

Experimental Design and Critical Features. The experiment was carried out in a single-stage, low-speed, axial compressor. In the conceptual design of the experiment, there are two objectives that are crucial: namely, that the stator hub be stall limiting and that the type of stall be wall stall. To achieve this, several specific features were incorporated in the experimental design:

1 The relative stagger of rotor and stator is set so that the rotor is lightly loaded relative to the stator. The rotor (and inlet guide vane) thus act merely as a swirl flow generator for the stator.

2 The low twist rotor blading used created a small pressure rise across the rotor hub relative to the rotor tip. The resulting total pressure profile at stator inlet was thus severely skewed (i.e., "hub weak") with a difference of almost one-half the mean dynamic pressure existing between the flow just outside the endwall boundary layers at tip and hub, respectively. In effect, the stator is presented with a hub distortion, in much the same spirit that tip distortions are often used in casing treatment tests.

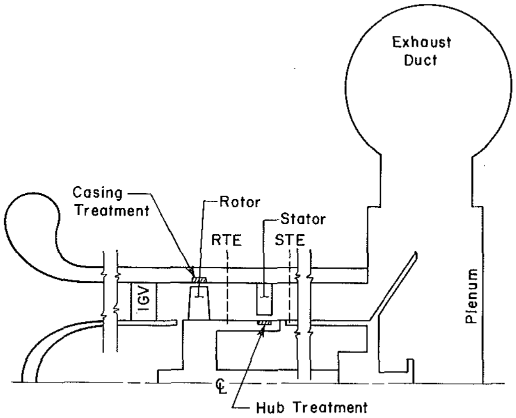

Fig. 1 Compressor schematic showing hub treatment location

3 To decouple the rotor and stator, as well as to allow ample room for rotor wakes to mix out, a large axial distance (roughly 1.1 span) was left between rotor and stator. As shown in [6], to the limits of the experimental accuracy there was thus no difference in rotor output (i.e., no "back pressuring" of the rotor) so that *the stator inlet conditions were the same with the hub treatment and with the smooth wall.* Note that, in connection with the subject of inlet conditions, the presence of a rotating (rather than stationary) hub is also necessary as part of the simulation of a rotor tip flow.

4 Stator tip clearance and stagger were selected to ensure endwall stall, based on the criteria presented in [8]. The stall limit was rotating stall, as seen by hot wires in and downstream of the passage.

5 Analysis of pneumatic and hot-wire data indicated that the stall did indeed originate at the hub [6, 9, 11]. The values of $\Delta P/q$ varied (roughly linearly) from 0.2 at 90 percent span (near the tip) to 0.38 at the 15 percent span (near hub) location. Stator D-factors, while not overly high near the hub (0.4 at the 15 percent span location), as is to be expected with a wall stall situation, also showed that the hub sections had the heaviest loadings. Furthermore, the hot-wire data showed the highest activity near the hub with greatly decreased activity as the probe was moved outward.

A cross-sectional schematic of the compressor showing blading and treatment locations is given in Fig. 1. Both rotor

Nomenclature

C_r = radial velocity component
C_x = axial velocity component
$\bar{C}_x$ = annulus-averaged axial velocity
C_θ = circumferential velocity component
P = static pressure
P_t = total pressure
ΔP = static pressure rise across blade row
ΔP_t = total pressure rise across blade row measured in absolute reference frame
δP_t = total pressure change across blade row measured in blade reference frame
U = mean rotor velocity
U_H = hub velocity
W = work done by hub, per unit overall mass flow
W_{jet} = jet velocity measured relative to moving hub
W_θ = circumferential velocity component measured relative to moving hub
η = efficiency
η_d = diffuser efficiency
ρ = density

Subscripts

1 = blade row inlet
2 = blade row exit
sm = with smooth wall
tr = with slotted (treated) wall
LE = leading edge
TE = trailing edge

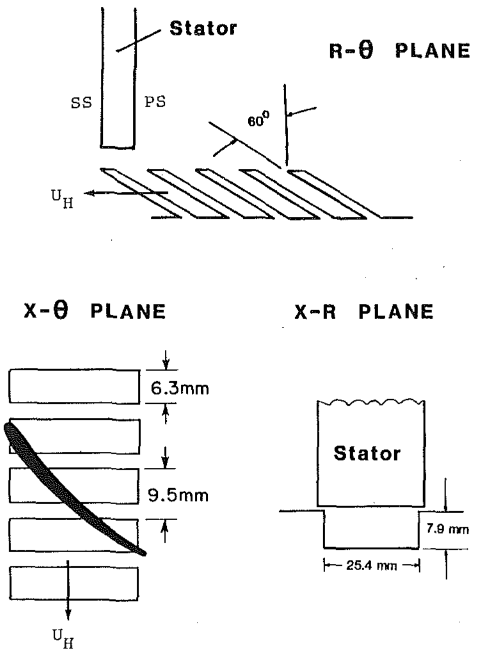

Fig. 2 Hub treatment geometry; PS and SS denote pressure side and suction side of blade. Hub treatment moves with velocity U_H.

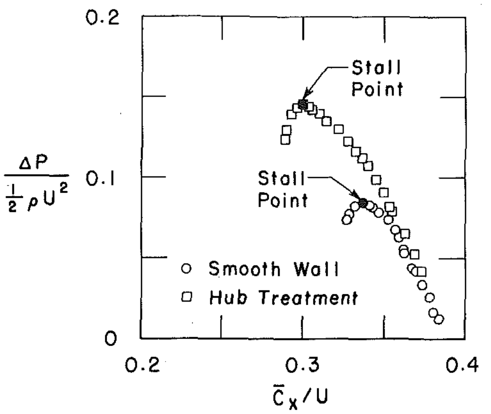

Fig. 3 Stator performance map; solid points are onset of rotating stall

and stator have a constant chord of 38 mm, solidity at midspan of 1.0, and (constant) camber of 30 deg. Stator stagger at midspan is 42.5 deg from axial with a total twist of 5 deg. Stator aspect ratio is 1.9. The hub/tip radius ratio is 0.75, the outer diameter is 0.59 m, and the blade aspect ratio is 1.9. Tip clearance is 7 percent of staggered spacing, somewhat higher than the "nominal value" of 5.5 percent used in [8]; again, this was deliberately done to ensure hub wall stall.

Experiments were run with both smooth wall and treated (slotted) rotating hubs. All of the measurements were taken at 2600 rpm, corresponding to a rotor tip Mach number of 0.24 and a stator midspan blade chord Reynolds number of 10^5 at the stall point. Because of the rather low value of this latter quantity, Reynolds number effects on the compressor characterisic had been previously examined [6] and shown to be at least an order of magnitude less than the solid wall/hub treatment differences that are of interest here.

As stated previously, the hub treatment slot geometry is one that has been used successfully as a rotor casing treatment. It consists of axial slots skewed at a 60 deg angle to the radial direction, as shown in Fig. 2. The slots are skewed such that they face toward the pressure surface, and extend axially over the middle 90 percent of the stator passage at the hub.

The data to be presented below are given in nondimensional form. For the overall performance characteristics, mass flow is presented as $\bar{C}_x/U$ (where U is mean rotor blade speed), and pressure differences are nondimensionalized by $\frac{1}{2}\rho U^2$. For these measurements, the relative uncertainties are estimated at approximately 1 percent or less. For the detailed measurements, velocities are referenced to $\bar{C}_x$, the annulus-averaged axial velocity; this is seen as being more directly relevant for characterizing the passage velocity field than the wheel speed.

Hot-Wire Technique. Acquisition of time-resolved velocity data was by hot-wire anemometry, using a modification of the technique presented by Wagner and Okiishi [10]. A single hot wire was immersed in the flow and rotated about its axis, with the output measured at three different angular locations. The three measurements, plus calibrations relating probe output to pitch angle, yaw angle, and speed, allow one to derive a three-dimensional velocity vector [11]. Both the time-*averaged* flow field and the time-*resolved* flow field were obtained. The time-averaged flow fields were obtained by averaging the hot-wire measurements over 13.2 rotor revolutions, which corresponds to 2200 slot passings (580 rotor blade passings).

To obtain time-resolved data, a phase lock system was used in conjunction with an ensemble-averaging technique (250 traces). Comparison of instantaneous and ensemble-averaged time-resolved measurements was also made throughout the data acquisition to ensure that no important features of the former were lost by the averaging process [11].

Overall Effects of Hub Treatment on Stator Performance and Stall Limits

Constant speed compressor characteristics for the smooth and treated wall builds (essentially those given in [6]) are presented in Fig. 3. The axes are nondimensional outer wall static pressure rise across the stator, $\Delta P/\frac{1}{2}\rho U^2$, versus $\bar{C}_x/U$. It is apparent from the figure that the application of hub treatment resulted in a considerable change in the overall stator row performance.

At the flow coefficient at which the detailed data were obtained, $\phi = 0.35$, the static pressure rise is 20 percent higher with the hub treatment than with the solid wall. As described in some detail in [6], this can be directly associated with the substantially decreased blockage in the stator hub endwall, and hence the increased area ratio across the blade row.

Time-Averaged Velocity Field in Passage Endwall

Velocity fields for both the smooth and treated (slotted) builds were obtained at a "near stall" flow coefficient of 0.350. This corresponds respectively to 4 percent and 16 percent in $\bar{C}_x/U$ from the stall value for smooth and treated builds.

In any presentation of a three-dimensional data field there is some question of the most useful manner of presentation. We have chosen here to present velocity vector plots, as these seem to show clearly the quantitative as well as qualitative flow features. The velocity vectors are presented from three different "views": *radial*, which presents the vectors projected onto a θ-x surface at constant radius; *chordwise*, which presents the vector projected onto a surface parallel to the blade stagger; and *axial*, which presents the vectors projected onto a plane normal to the axial (x) direction. In each case, the origin (tail) of the vector is the location where the measurement was made. In addition, a symbol is printed at the origin which indicates the direction of the flow normal to the view. A zero (0) indicates flow out of the paper and an X indicates flow into the paper. As stated, the vectors are scaled to $\bar{C}_x$, the annulus-averaged axial velocity, and this is shown in each figure for reference.

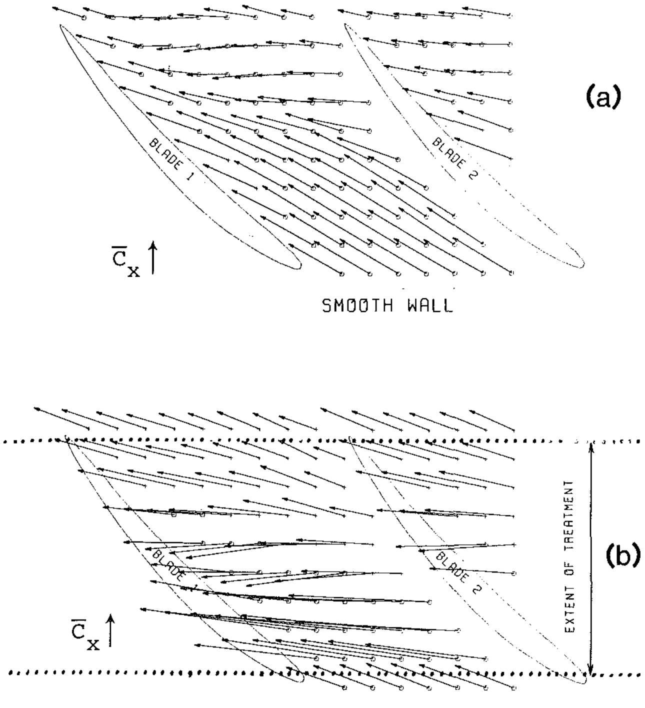

Fig. 4 Radial views at 2 percent span from hub

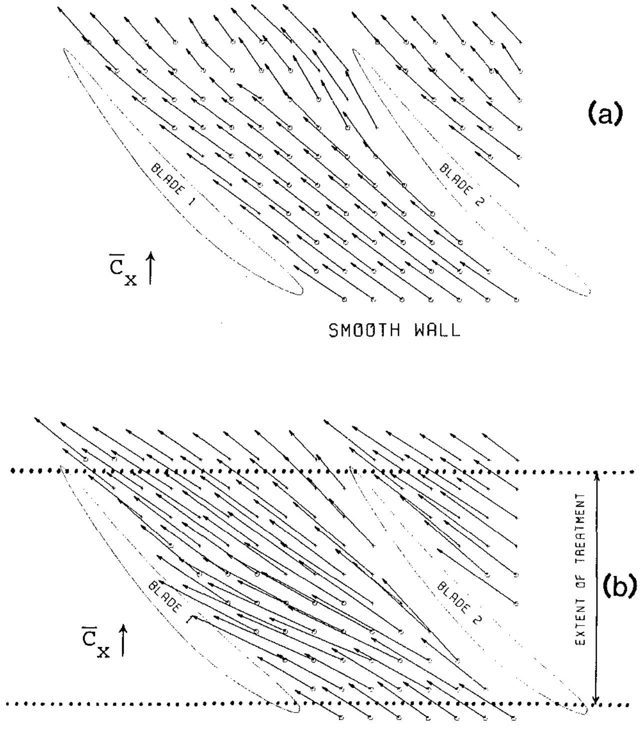

Fig. 5 Radial views at 6 percent span from hub

The views of time-averaged velocity vectors are shown in pairs, with one view for smooth wall and one for treated build. The radial views will first be presented and discussed to provide detailed information about axial and tangential velocity components. To discuss the radial velocity component, chordwise and axial views will then be shown.

Radial Views of Time-Averaged Velocity Vectors. Figures 4 and 5 present radial views at two radial locations near the hub. In these and succeeding figures, the radial location is described in terms of percent span, i.e., radial distance from the hub divided by the hub-to-casing radial distance. (Radial clearance between stator tip and the hub is 2.7 percent span.) The axial extent of the treatment is also indicated on the figures.

Figure 4, at 2 percent span, corresponds to a location in the clearance below the bottom of the blade. For the smooth wall, Fig. 4(*a*), there is a large region of high-tangential, low-throughflow velocity (and consequently high blockage) which covers the rear of the passage over nearly the entire pitch. This region is much less pronounced in the smooth wall data at 6 percent span, Fig. 5(*a*) (although it can be seen in the chordwise view to be discussed below). Note, however, that in Fig. 5(*a*) the vectors near the suction surface are following the surface (the flow is not separated) as would be expected, based on the stator D-factors [9]. Because of the absence of separation at 6 percent and higher locations, the implication is thus that it is not large-scale radial migration of the stator suction side boundary layer that is appearing in the endwall. The high blockage occurring with the smooth wall is rather due to the fluid in the endwall layer, most likely from the hub clearance flow [1].

The treated flow field displayed in Figs. 4 and 5 shows a much different flow structure. Comparing Figs. 4(*a*) and 4(*b*), the most evident difference is seen near the leading edge where, in the latter, the velocity is extremely high (about four times $\bar{C}_x$), and almost tangenital in direction. This is due to the injection from the slots into the mean flow. In a time-averaged sense, the jet due to this flow injection is present across the entire pitch, from the leading edge to about 40 percent axial chord, although its magnitude decreases with distance from the leading edge. The jet moves across the passage to impact the blade pressure surface which diverts it downstream. A point to note is that near the leading edge, the flow is moving with a very low axial velocity, and the incoming flow must thus divert radially over the jet (note the 0's at the vector origins).

A perhaps less striking, but also important, characteristic of the treated wall flow field is the flow *removal* which takes place near the trailing edge. This can be seen in both Figs. 4(*b*) and 5(*b*) (note the X's at the origin of the vectors). When compared to the smooth wall views of these figures, the region of flow removal in the treated flow field (X's at the vector origins) can be seen to correspond closely with the region that gives rise to the high-flow blockage in the smooth wall flow field (0's at the vector origins).

Chordwise Views of Time-Averaged Velocity Vectors. The chordwise views of the flow can also be examined to show quantitative information about the radial flows. Figures 6 and 7 display these for two pitch locations, one near the pressure surface (8 percent away) and the other (at 38 percent) representative of conditions in the central pitchwise locations. (In the figures, the extent of the blade passages is also indicated.) In Fig. 7(*a*), the smooth wall data indicate large blockage near the rear of the passage, especially near the mid-pitch plane. Although not shown, this region of high blockage extends a considerable distance across the passage; for example, the data at 68 percent pitch look similar to those at 38 percent [11]. With the treated wall (Fig. 7*b*) however, this blockage is eliminated. Furthermore, regions of strong flow removal with the hub treatment are regions of high blockage with the smooth wall. Very clearly, the low-momentum fluid has been sucked into the slots and reinjected near the leading edge in the form of a high-velocity, high-total-pressure jet.

The jet from the leading edge region is also visible in Figs. 6(*b*) and 7(*b*), due to its large radial velocity component. Furthermore, in Fig. 6(*b*), the path the jet follows after it impacts the pressure surface is quite evident. The jet proceeds diagonally along the pressure surface so the regions of the

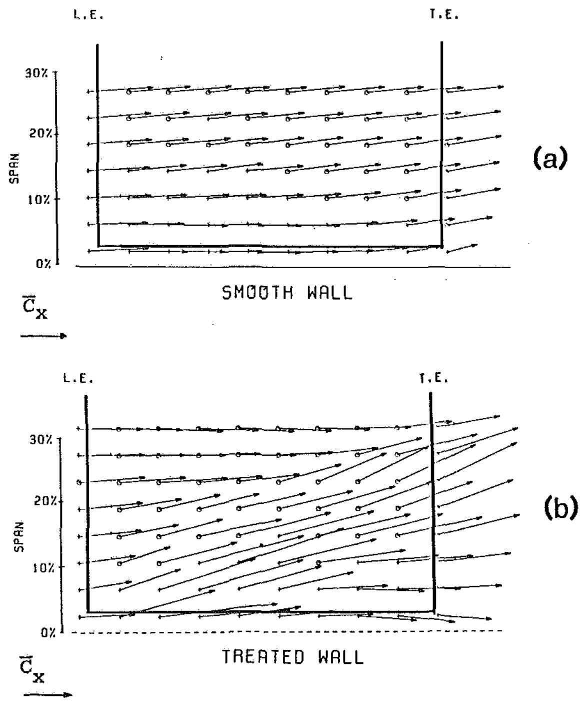

Fig. 6 Chordwise planes at 8 percent pitch from pressure surface

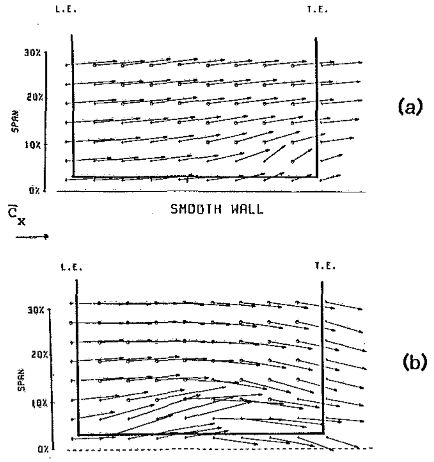

Fig. 7 Chordwise planes at 38 percent pitch from pressure surface

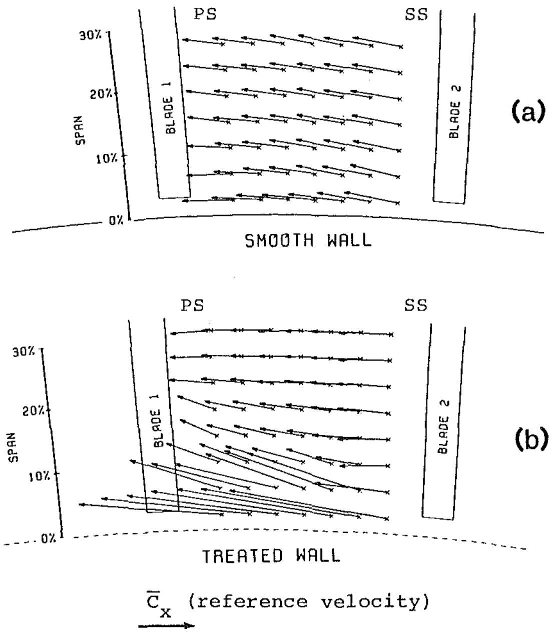

Fig. 8 Axial planes at 20 percent axial chord

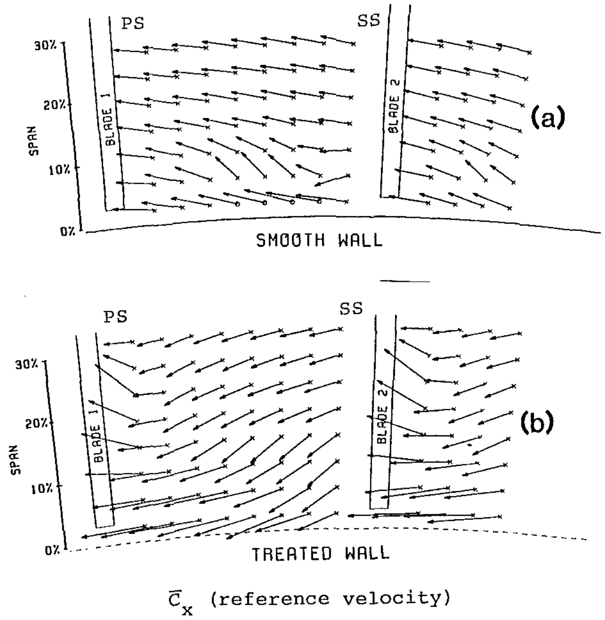

Fig. 9 Axial planes at 78 percent axial chord

highest velocities at the exit of the passage are between (roughly) 20 to 30 percent span, which is consistent with the exit traverse measurements in [6].

From Figs. 4(*b*) and 6(*b*), then, the jet travels across the passage to impact the pressure surface, proceeds across the blade in a combined radial-chordwise direction, and exits the passage at between 20 and 30 percent span. The important point is that the jet is nowhere near the center of the passage in the aft part, which is the region where (in the smooth wall build) the main blockage occurs. It might be argued that the decrease in blockage could be primarily due to either boundary layer jet interaction near the front of the passage (since it is known, for example, that a jet in a crossflow will lead to the production of streamwise vorticity and hence enhanced mixing), or to direct momentum injection. The picture presented by the time-resolved measurements (described below), however, indicates that this is less likely.

Axial Views of Velocity Vectors. The axial views of the stator endwall flow field are presented in Figs. 8 and 9. Figure 8, for 20 percent axial chord, shows the features associated with the leading edge region. With the smooth wall (Fig. 8*a*), the flow has only a slight upward bias. This is to be expected since the major blockage increase occurs further downstream. With the treated wall (Fig. 8*b*), the jet can be clearly seen moving across the passage toward the pressure surface.

The views of Fig. 9, which are at 78 percent axial chord, show typical features of the aft region of the passage. With the smooth wall (Fig. 9*a*), the region of high blockage is again very apparent on the endwall in the middle of the passage. In the treated build data of Fig. 9(*b*), the blockage is absent, with a substantial flow moving downward into the slots, implying a direct causal relationship between this removal and the decrease in blockage.

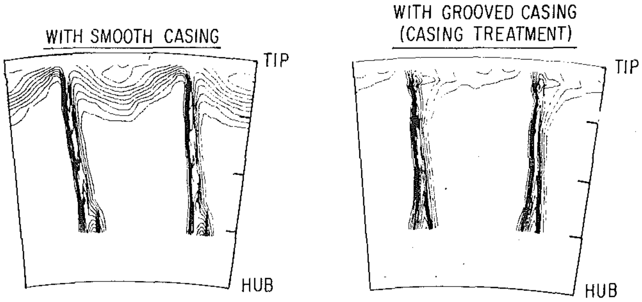

Fig. 10 Relative total pressure contours at rotor exit

Comparison of Rotor and Stator Endwall Stall Behaviors. It seems useful here to discuss the connection between the present results for hub treatment and those which exist for casing treatment. It is to be stressed that the situation in which the blockage is mainly due to the flow in the endwall region (rather than the blade) and is seen in the middle of the passage is not particular to a stator hub (or to this rig), but has been reported before with casing treatment applied to a rotor tip [1, 2, 5].

These references presented contours of relative total pressure [2] and relative dynamic pressure [1, 5] at the rotor exit at a near stall condition. Figure 10 from [2] is reproduced here. It is evident that with the solid wall a large region of low-velocity flow occurs on the rotor tip endwall similar to the situation at the hub endwall in the present experiment. This same type of behavior is also evident in the data in [1, 5].

In addition to these detailed results, one can also consider the overall pressure rise/flow curves for blade stall and wall stall *rotors*, with solid wall and with casing treatment. These show very much the same behavior as those for blade stall and wall stall *stators* with and without hub treatment (compare Fig. 7 of [2] and Figs. 3 and 4 of [6]).

These data imply to us that the hub treatment configuration shows behavior which is similar, on both a *local* and a *global* basis, to that obtained with casing treatment. As suggested previously, therefore, the treated stator provides a very useful arena to study the mechanism of operation of the latter.

Time-Resolved Unsteady Velocity Field. Time-resolved velocity fields were also measured for both treated and smooth builds, and a detailed account of the high response data acquisition technique is given in [11]. The result was ensemble-averaged, time-resolved traces of the three velocity components at each position in the data acquisition grid. The time traces cover a period of time equal to 1.5 rotor blade passings or 5 slot passings.

Although not examined in detail, the measurements showed that the level of unsteadiness in the blade passage is low, except for regions directly in the path of the jet. Even here, however, the mixing on a slot-to-slot basis is rapid enough so that the unsteadiness in the radial component is nearly gone at the 10 percent radius location. This rapid mixing out of the jets was also referred to in [3].

Although there are a number of ways of displaying the unsteady effects, straightforward examination of the time history of the velocity components suffices for the purposes here. These contain all of the information available at a given location. Smooth wall results are not shown, because the main unsteadiness comes from upstream and, as expected based on the experimental design, it is weak. The actual magnitude of the unsteadiness varies depending on where in the passage one measures but, over most of the passage, unsteady velocities in the smooth wall situation are considerably less than 5 percent of the average absolute velocity.

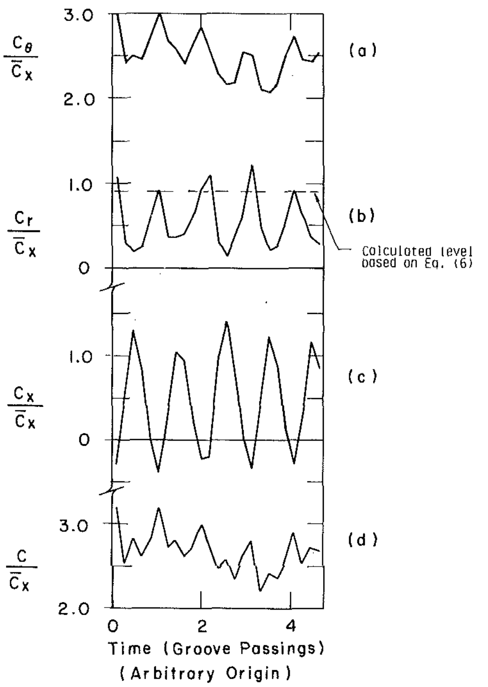

Fig. 11 Unsteady velocity components at 2 percent span (midpassage near leading edge of slots)

Unlike the smooth build, the treated build has regions of very strong unsteadiness. These can be seen in Fig. 11, which shows the time-resolved velocity components C_r, C_θ, and C_x. The data are for a location slightly downstream of the slot leading edge, in the middle of the passage, at 2 percent radial span. All velocities are normalized by the annulus-averaged axial velocity $\bar{C}_x$.

In each of the components graphed in Fig. 11, the slot passings are visible, but the effect of the jets is most striking for the axial component. The axial velocity is seen to vary from levels near $\bar{C}_x$ to substantial *negative* values, as the jet from the slot sweeps by. Furthermore, the tangential and radial velocity components are 90 deg out of phase with the axial velocity component, i.e., when the axial velocity is low, corresponding to a jet passing by, the radial velocity is high. The jets are thus associated with a reversal in the axial component and a strong outward radial velocity so that the momentum flux imparted to the endwall boundary layer at this location is such as to decrease the axial momentum (there is however an influx of streamwise momentum). Thus, in our opinion it is not direct momentum injection that is responsible for the decrease in endwall blockage, although the measurements are not really conclusive on this point.

Efficiency Penalty and Slot-Endwall Interaction

Efficiency Loss and Hub Treatment Work. The results presented point to the existence of the region of flow removal (of the high-blockage fluid) at the rear of the blade passage as an important feature of the slotted treatment. In these sections some comments are presented relating to the effect of the slots on efficiency and the magnitude of the flow through the slots.

We look first at the former. The "diffuser efficiency" [12] for the stator blade row can be written in terms of the work W per unit overall mass flow rate, done by the moving hub on the fluid in the endwall region, the total pressure change across the blade row δP_t, and the static pressure rise across the blade row ΔP,[3] as

---

[3] Note that $\delta P_t = P_{t1} - P_{t2}$ and $\Delta P = P_2 - P_1$, i.e., the former is inlet minus exit and the latter is exit minus inlet.

$$\eta_d = \frac{1}{1 + \dfrac{\left(\dfrac{\delta P_t}{\rho} + W\right)}{\Delta P/\rho}} \tag{1}$$

The ratio of the diffuser efficiencies for treated and smooth walls is thus

$$\frac{\eta_{d_{\mathrm{tr}}}}{\eta_{d_{\mathrm{sm}}}} = \frac{1 + \left(\dfrac{(\delta P_t + \rho W)}{\Delta P}\right)_{\mathrm{sm}}}{1 + \left(\dfrac{(\delta P_t + \rho W)}{\Delta P}\right)_{\mathrm{tr}}} \tag{2}$$

If we make the approximation that the work done by the moving hub (or casing) is small in the smooth wall situation (since the boundary layer is in an adverse pressure gradient and the skin friction thus likely to be low) we have

$$\frac{\eta_{d_{\mathrm{tr}}}}{\eta_{d_{\mathrm{sm}}}} \simeq \frac{1 + [\delta P_t/\Delta P]_{\mathrm{sm}}}{1 + \left(\dfrac{(\delta P_t + W\rho)}{\Delta P}\right)_{\mathrm{tr}}} \tag{3}$$

with all the quantities defined in the blade reference frame.

To calculate the change of efficiency, it can be seen that there are two quantities that must be known, the change in total pressure and the work done by the slotted hub. The data show that there is a large amount of work done on the fluid that recirculates through the slots. The fluid enters the slots with an absolute tangential velocity of 0.4–0.5 of the hub velocity and emerges with a tangential velocity of 1.2–1.3 of the hub velocity. Thus, the work done per unit mass flow rate through the slots (work put in by the hub) is $W \simeq 0.8\ U_H^2$, much of which winds up as excess kinetic energy in the jet. Using the measured time-averaged mass flow through the slots (4 percent of the overall mass flow obtained by integrating the radial velocities), and the measured total pressure changes and work done ($[\delta P_t/(\Delta P)]_{\mathrm{sm}} \simeq 0.37$, $[\delta P_t/(\Delta P)]_{\mathrm{tr}} \simeq 0.0$ from the data in Fig. 8 of [6], $[\rho W/(\Delta P)]_{\mathrm{tr}} \simeq 0.46$), the ratio of diffuser efficiencies for the stator row is

$$\frac{\eta_{d_{\mathrm{tr}}}}{\eta_{d_{\mathrm{sm}}}} \simeq 0.94 \tag{4}$$

Although diffuser efficiency may be a more basic measure of the flow processes in the passage, a more common measure of efficiency is the adiabatic efficiency. Within the above framework, the ratio of adiabatic efficiencies for a smooth wall and a treated hub (or casing) can be written as

$$\frac{\eta_{\mathrm{tr}}}{\eta_{\mathrm{sm}}} = \frac{1 + \left(\dfrac{(\delta P_t)_{\mathrm{rel}}}{\Delta P_t}\right)_{\mathrm{sm}}}{1 + \left(\dfrac{(\delta P_t)_{\mathrm{rel}} + \rho W}{\Delta P_t}\right)_{\mathrm{tr}}} \tag{5}$$

where ΔP_t is the total pressure *rise* across the blade row as measured in the absolute system, and again $\delta P_{t\mathrm{rel}} = (P_{t1} - P_{t2})$ in the relative system.

To recap, the efficiency of a treated compressor stage is determined by the efficiency with which the work done by the treated hub (or casing) is converted into useful total pressure rise. Since the overall efficiency drops considerably when treatment is applied, it is clear that the configurations used are not making good use of this work which, as stated, is to a large extent dissipated as the jets mix out.

To improve stage efficiency, two things are needed. First, to reduce the potential for efficiency loss, the slots should be designed to do work as possible, consistent with their effective operation. Second, in order to decrease the stagnation pressure rise for a given amount of work, the jets can be reinjected more smoothly into the flow, thus reducing the losses due to mixing.

Throughflow in the Slots. A main point of the paper is the connection between the improvement in stability and the flow removal at the rear of the passage. To understand this, it is necessary to examine the quantitative relationship between flow removal, flow injection, and stability, and this is an important area to address. While this is beyond the scope of the present paper, a key part of any analysis of this relationship will involve a description of the flow through the slots, and it is this aspect that we briefly consider here.

From the above data, as well as those in [1, 5], and from potential flow estimates that we have made, it appears that the flow in the slots can be usefully approximated as steady, driven by the time-averaged front-to-rear pressure difference. For example, the relative jet velocity at the slot leading edge can be given approximately in terms of the relative velocity at inlet to the slots, $W_{\theta_{\mathrm{TE}}}$, and the pressure rise across the blade row as

$$W_{\mathrm{jet}} = \left[\frac{2(P_{\mathrm{TE}} - P_{\mathrm{LE}})}{\rho} + W_{\theta_{\mathrm{TE}}}^2\right]^{1/2} \tag{6}$$

In this, we have neglected the small differences between the axial velocity at slot inlet and exit.

Inserting the numbers we find that $W_{\mathrm{jet}} = 1.8\ \bar{C}_x$. If the jet is taken to exit at the slot angle, this implies that the radial velocity near the leading edge of the slots is $0.9\ \bar{C}_x$ and, as indicated in Fig. 11, this can be seen to be in agreement with the measurements. The absolute value of jet velocity computed in this manner is $3.7\ \bar{C}_x$, which also compares well with the values in Figs. 4 and 11, although this is a less sensitive comparison than that of the radial velocity because a major part of W_{jet} is the hub velocity.

An important assumption for the type of slots considered was that there seems to be little total pressure loss as the fluid enters the slots. This might be expected, based on the geometry, which is such as to provide a relatively smooth entrance. It will not be the case, however, for slots such as radial, or reversed skewed slots, and these would be expected to have significantly less mass flow through them. The parametric dependence of the mass flow on slot angle is a subject now under investigation.

Some Comments on an Additional Mechanism for Casing Treatment Operation

As a result of the measurements presented we have seen that suction of the high-blockage fluid at the rear of the passage is also important. There is, however, another view of the mechanism of casing treatment operation that can also be commented on. This has to do with the effect of tip clearance. It is well known that tip clearance has a marked effect on compressor stability [8, 13]; see also [14–16].

An additional mechanism for operation of the slotted hub might therefore be that the jet somehow suppresses the tip leakage flow that occurs with the solid wall. There are few data to argue either for or against this. The hot-wire measurements presented above, however, as well as the computations of [17], indicate that much of the tip leakage flow is aft of the region where the jet impacts on the pressure side of the blades, but the evidence is not conclusive. It thus appears that a way to make the ideas much more conclusive is through an experiment in which one can provide separately a jet at the front of the passage and a suction at the rear. This key experiment is currently being planned, using a slotted hub that is open to an inner plenum chamber which can be pressurized or aspirated.

Summary and Conclusions

An investigation of the flow phenomena associated with compressor wall treatment has been carried out using a rotating hub under a cantilevered stator row. Application of the hub treatment resulted in a large increase in stable flow range and peak pressure rise compared to operation with a smooth wall. In addition, the flow features encountered with stator hub treatment were similar to those found with rotor casing treatment.

The three-dimensional unsteady and time-averaged velocity field has also been examined via hot-wire anemometry for smooth and treated wall hubs. Results with the smooth hub showed that (near stall) a region of high blockage is located at the rear of the passage on the endwall, not near the blades, and that wall stall occurred. With the treated build, there are two strong effects: a high-velocity jet near the leading edge, and a region of fluid removal near the trailing edge. This flow removal acts directly on the region of high blockage. The main path of the jet at the leading edge, on the other hand, never approaches this region.

Since it is the blockage that leads to rotating stall, it is the blockage *removal* at the rear of the passage that can also be important for the effectiveness of the slots in improving stall margin.

With the treatment, measurements of the unsteady velocity field showed that unsteadiness was small except near the hub where the individual jets exit from their respective slots. In this region, the *axial* component of velocity varied from values near $\bar{C}_x$ to substantially negative values. The time average was less than for the smooth wall at this radius and at some locations actually negative. However, this does not rule out the possibility that injection of streamwise momentum is also involved in the mechanism of treatment operation.

A brief discussion concerning the connection between the jet and compressor efficiency has also been presented, showing the relation between efficiency loss and work done by the slots.

Acknowledgments

The authors would like to acknowledge the helpful comments of Professor W. Cheng, Drs. N. A. Cumpsty, C. S. Tan, V. Modi, and D. C. Wisler, and the assistance with the experiment of Mr. Hu Zong-An, Dr. H-W Shin, and Mr. W. Cook. The discussions during the review process with Mr. C. C. Koch are also appreciated. Support for this project was provided by the Air Force Office of Scientific Research through the Air Force Research on Aero Propulsion Technology Program and AFOSR Contract F49620-85-C-0018, Dr. J. D. Wilson, Program Manager.

References

1 Smith, G. D. J., and Cumpsty, N. A., "Flow Phenomena in Compressor Casing Treatment," ASME Journal of Engineering for Gas Turbines and Power, Vol. 106, 1984, pp. 532-541.

2 Greitzer, E. M., Nikkanen, J. P., Haddad, D. E., Mazzawy, R. S., and Joslyn, H. D., "A Fundamental Criterion for the Application of Rotor Casing Treatment," ASME *J. Fluids Engineering*, Vol. 101, 1979, pp. 237-243.

3 Takata, H., and Tsukuda, Y., "Stall Margin Improvement by Casing Treatment – Its Mechanism and Effectiveness," ASME Journal of Engineering for Power, Vol. 99, 1977, pp. 121-133.

4 Fujita, H., and Takata, H., "A Study on Configurations of Casing Treatment for Axial Flow Compressors," *Bulletin of the JSME*, Vol. 27, No. 230, 1984, pp. 1675-1681.

5 Smith, G. D. J., "Casing Treatment in Axial Compressors," Ph.D. Thesis, Engineering Department, University of Cambridge, Apr. 1980.

6 Cheng, P., Prell, M. E., Greitzer, E. M., and Tan, C. S., "Effects of Compressor Hub Treatment on Stator Stall Margin and Performance," *J. Aircraft*, Vol. 21, No. 7, 1984, pp. 469-475.

7 Prince, D. C., Wisler, D. C., and Hilners, D. E., "Study of Casing Treatment Stall Margin Improvement Phenomena," ASME Paper No. 75-GT-60.

8 Koch, C. C., "Stalling Pressure Rise Capability of Axial Flow Compressor Stages," ASME Journal of Engineering for Power, Vol. 103, 1981, pp. 645-656.

9 Cheng, P., "Effects of Compressor Hub Treatment on Stator Stall and Pressure Rise," MIT Gas Turbine Laboratory Report No. 167, Sept. 1982.

10 Wagner, J. H., and Okiishi, T. H., "Analysis of Multistage, Axial Flow Turbomachine Wake Production, Transport, and Interaction," Department of Mechanical Engineering, Iowa State University, ISU-ERI-AMES-78173, Dec. 1977.

11 Johnson, M. C., "The Effects of Hub Treatment on Compressor Endwall Flowfields," M.S. Thesis, Department of Aeronautics and Astronautics, MIT, Jan. 1985.

12 Dixon, S. L., *Fluid Mechanics, Thermodynamics of Turbomachinery*, 3rd ed., Pergamon Press, New York, 1985, chap. 2.

13 Hunter, I. H., and Cumpsty, N. A., "Casing Wall Boundary-Layer Development Through an Isolated Compressor Rotor," ASME Journal of Engineering for Power, Vol. 104, 1982, pp. 805-818.

14 Freeman, C., "Effect of Tip Clearance on Compressor Stability and Engine Performance," in: *von Karman Institute Lecture Series*, "Tip Clearance Effects in Axial Turbomachines," von Karman Institute, 1985.

15 Wisler, D. C., "Aerodynamic Effects of Tip Clearance, Shrouds, Leakage Flow, Casing Treatment and Trenching in Compressor Design," in: *von Karman Lecture Series*, "Tip Clearance Effects in Axial Turbomachines," von Karman Institute, 1985.

16 Inoue, M., Kuroumaru, M., and Fukuhara, M., "Behavior of Tip Leakage Flow Behind an Axial Compressor Rotor," ASME Journal of Engineering for Gas Turbines and Power, Vol. 108, 1986, pp. 7-14.

17 Hah, C., "A Numerical Modelling of Endwall on Tip Clearance Flow of an Isolated Compressor Rotor," ASME Journal of Engineering for Gas Turbines and Power, Vol. 108, 1986, pp. 15-21.

Some Experiments With a Supersonic Axial Compressor Stage

A. J. Wennerstrom
Aero Propulsion Laboratory,
Air Force Wright Aeronautical Laboratories,
Wright-Patterson Air Force Base, OH

Between 1970 and 1974, ten variants of a supersonic axial compressor stage were designed and tested. These included two rotor configurations, three rotor tip clearances, addition of boundary-layer control consisting of vortex generators on both the outer casing and the rotor, and the introduction of slots in the stator vanes. Design performance objectives were a stage total pressure ratio of 3.0 with an isentropic efficiency of 0.82 at a tip speed of 1600 ft/s (488 m/s). The first configuration passed only 70 percent of design flow at design speed, achieving a stage pressure ratio of 2.25 at a peak stage isentropic efficiency of 0.61. The rotor was grossly separated. The tenth variant passed 91.4 percent of design flow at design speed, producing a stage pressure ratio of 3.03 with an isentropic efficiency of 0.75. The rotor achieved a pressure ratio of 3.59 at an efficiency of 0.87 under the same conditions. Major conclusions were that design tools available today would undoubtedly permit the original goals to be met or exceeded. However, the application for such a design is currently questionable because efficiency goals considered acceptable for most current programs have risen considerably from the level considered acceptable at the inception of this effort. Splitter vanes placed in the rotor permitted very high diffusion levels to be achieved without stalling. However, viscous effects causing three-dimensional flows violating the assumption of flow confined to concentric stream tubes were so strong that a geometry optimization does not appear practical without a three-dimensional, viscous analysis. Passive boundary-layer control in the form of vortex generators and slots does appear to offer some benefit under certain circumstances.

Introduction

From the 1940s through the early 1970s, a variety of efforts were underway dealing with research and development on supersonic axial compressor stages. They have long held an attraction for turbine engine designers because of their potential for very high stage pressure ratios, theoretically, at competitive efficiencies. At a constant level of diffusion factor, the capacity for work done by a compressor stage increases nearly with the second power of wheel speed, and increased wheel speed is usually accompanied by increased Mach number. Much of the early work is well summarized by Erwin (1964), Ferri (1964), Klapproth (1961), and Wilcox et al. (1959). In 1973, J. Fabri of ONERA produced a bibliography of over 170 references pertaining to work in this area giving a good indication of the level of effort which had been applied over a 30-year period. In the 1960s, the United States Air Force was particularly active in supporting a number of contract efforts involving supersonic compressors aimed at direct lift and engines requiring extremely high thrust-to-weight ratios. Both two-stage counterrotating compressors with a single stage on each spool, and more conventional layouts were attempted, but none with notable success. At the time, an isentropic efficiency in the low 80 percent bracket would have been considered competitive. This paper describes the results of a related in-house effort conducted between 1970 and 1974 by the United States Air Force Aerospace Research Laboratories (disestablished July 1975) at Wright-Patterson Air Force Base. One of the principal motives of this effort was to evaluate to what extent passive boundary-layer control might help to solve the severe separation problems often encountered with such stages.

A supersonic stage, according to the generally accepted definition, is one in which the Mach number relative to the rotor leading edge is supersonic over the full span at design speed. The stage described in this paper was not designed for a specific application. It was designed with the objective of evaluating several design concepts and the potential of passive boundary-layer control in an appropriate environment of Mach number and level of diffusion. The program consisted of a baseline design, a rotor variant containing splitter vanes, and then a series of tests involving rotor tip clearance changes and boundary-layer control devices. Boundary-layer control devices examined included vortex generators on the outer casing upstream of the rotor, on the rotor itself, and the introduction of slots in the stator. The original performance objectives

---

Contributed by the Gas Turbine Division for publication in the JOURNAL OF TURBOMACHINERY. Manuscript received by the Gas Turbine Division May 6, 1986.

were not achieved within the life of this program. However, a number of interesting results were obtained which may prove of value to future investigators.

Baseline Design

The baseline design, and the methods used to accomplish it, are fully described by Wennerstrom and Hearsey (1971). The description provided in this paper is deliberately brief with the principal objective of putting the experiments in the proper context. The design-point characteristics of the stage included an inlet hub/tip radius ratio of 0.75, a corrected tip speed of 1600 ft/s (488 m/s), a design total pressure ratio of 3.0, and an isentropic efficiency objective of 82 percent. The rotor inlet diameter was 18 in. (457 mm), and the design corrected flow rate was 30 lb/s (13.6 kg/s). There were no inlet guide vanes or bleeds and there was no variable geometry. The rotor contained 30 blades and was unshrouded. The stator contained 49 blades and was shrouded at both end walls; i.e., there were no end wall gaps.

The design was accomplished using an axisymmetric computational code of the streamline curvature type. The computation, which included four computing stations within each blade row as well as at blade-row edges and in free spaces, solved the "full" radial equilibrium equation with the exception that equivalent blade force terms, such as discussed by Wennerstrom (1974), were not included in the momentum equation. Overall losses across each blade row were considered to be the sum of diffusion losses plus shock losses. The diffusion losses were obtained from Lieblein's correlation of Loss Parameter versus Diffusion Factor (Johnson et al., 1965) with the exceptions that the extra losses Lieblein showed for the rotor tip region were not employed and the data were extrapolated to higher diffusion factors. Shock losses were calculated on the basis of a normal shock with an upstream Mach number arbitrarily reduced by one third of the excess above Mach 1.0 of the mean inlet Mach number. (The mean inlet Mach number is the average of the relative inlet value and the value on the suction surface where a normal shock would impinge.) This Mach number reduction was based upon the presumption that approximately that level of precompression could be obtained on the suction surface through the effects of annulus contraction. Within each blade row, from leading to trailing edge, the total loss was linearly distributed. This simple distribution was selected because firm justification for a more complex distribution was lacking, and also because the meridional distribution of loss has a relatively weak influence on the results.

The rotor blade camber lines were defined by a polynomial which had zero curvature at the leading edge. Maximum thickness was placed at 70 percent chord. Maximum camber occurred in the same region. The stator employed double-circular-arc streamsurface sections. Deviation angle was calculated by Carter's rule, without modification, for the stator sections. Carter's rule was also used to predict rotor deviation angles, except that a new curve, which corresponded to a point of maximum camber further aft, was assumed for the constant *m* as a function of stagger angle. A common curve was assumed to describe the variation of deviation inside blade rows from the first internal computing station to the trailing edge in terms of the ratio of local deviation to the trailing edge value predicted by Carter's rule. An airfoil optimization goal was established which was based upon the concept that the meridional distribution of circumferentially averaged static pressure through a blade row should rise in a smooth manner with minimum slope and then decline near the trailing edge to satisfy the Kutta condition. Incidence angles, the rotor hub contour, and the stator hub and tip contours were adjusted until this goal was satisfied to the maximum practical extent within the region of both blade rows.

End-Wall Boundary Layer

Blockage was calculated according to Jansen's method (Jansen, 1967), and the hub and tip streamlines were displaced by the amount predicted. Blockage was assumed to change linearly across each blade row. The predicted total blockage, in terms of annulus area, amounted to approximately 1 percent at the rotor inlet, 2 percent at the rotor exit, and 5 percent at the stator exit. The maximum thickness of the rotor varied from 5 percent chord at the hub to 3 percent chord at the tip. The rotor leading edge thickness was constant at 0.010 in. (0.25 mm). Rotor sections were stacked approximately on their centroids. Stator maximum thickness was constant at 4 percent chord, and its edge thickness was also 0.010 in. (0.25 mm). Stator sections were stacked on their trailing edge.

Rotor solidity varied from 2.17 at the hub to 1.86 at the tip. The predicted inlet relative Mach number varied from 1.23 to 1.58, and the corresponding variation in diffusion factor was from approximately 0.5 to 0.7. Stator solidity varied from 2.39 at the hub to a minimum of 1.80 at midspan and rose to 2.14 at the outer casing. This variation was the result of an approximately parabolic leading edge contour which was swept upstream toward both end walls. The predicted stator inlet Mach number was approximately 1.02 at both end walls and peaked about 1.06 near midspan. Diffusion factors for the stator were predicted to be approximately the inverse of the rotor, i.e., 0.7 at the hub and 0.5 at the tip. A meridional cross section of the stage is shown in Fig. 1. Blading characteristics are presented in Table 1.

Baseline Performance

It was not anticipated that the baseline design would meet its performance goals. However, it missed them by a margin considerably larger than expected. At design-corrected speed, corrected flow was approximately 30 percent low, rotor efficiency was 14 points low, and stage efficiency was 21 points low. Rotor total pressure ratio was 2.63 versus a design value of approximately 3.3, and stage total pressure ratio was 2.25 versus 3.0. The largest single reason for this substantial shortfall appeared to be the behavior of the rotor deviation angle as a function of incidence angle. Figure 2 illustrates this for a rotor midradius section. Deviation angle increased approximately 3 deg for every degree increase in incidence angle throughout the part speed regime. Lacking bleeds or variable geometry, the rotor was forced to operate at very high incidence at part speed. The corresponding increase in deviation and losses caused such a reduction in rotor work that it was never able to approach its design conditions. Complete test results are reported by Wennerstrom et al. (1974).

A cascade test of a rotor blade section corresponding to approximately 62 percent span was reported by Holtman et al. (1972). In the cascade test the turning was achieved. In fact, the deviation angle was approximately 3 deg less than predicted. However, losses were about 24 percent higher than estimated for design purposes due, primarily, to the optimistic shock loss model used. Also, the cascade spilled at a static pressure ratio just over 2.0, whereas the design static pressure ratio was about 2.3. Static pressures measured on the cascade suction surface just prior to the spill point showed no expansion or precompression at the shock impingement point. A more realistic shock loss would be that corresponding to a normal shock at the relative inlet Mach number. The loss predicted in this manner, including diffusion losses predicted by the Lieblein correlation (Johnson et al., 1965), fell within about 1.0 percent of the experimental value achieved just prior to spill.

Addition of Splitter Vanes

The next step in the program was designed to limit excur-

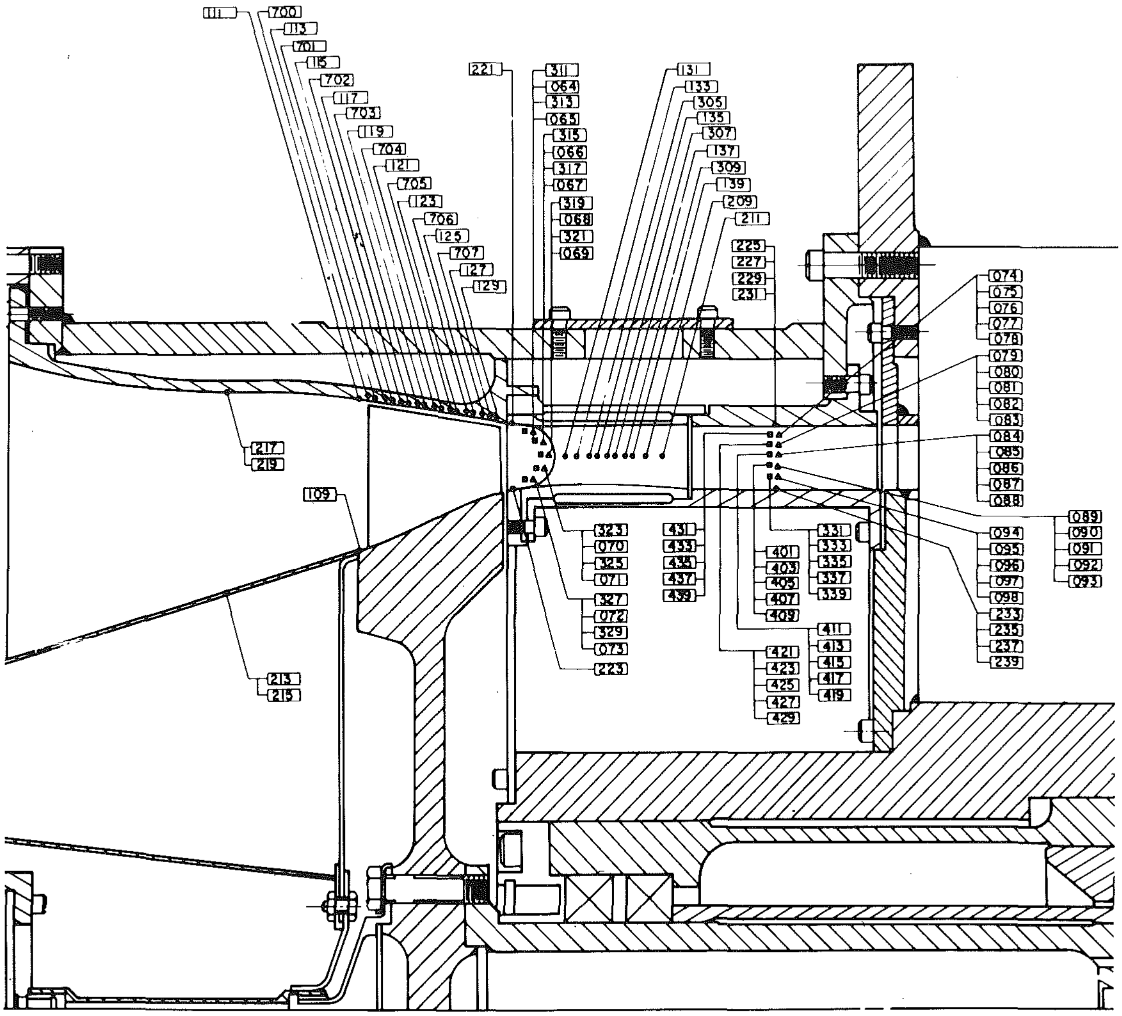

Fig. 1 Compressor stage cross section

Table 1 Stage blading characteristics

Streamline No.	Rotor Camber Deg	Rotor Stagger Deg	Rotor Chord in	Rotor Chord mm	Stator Camber Deg	Stator Stagger Deg	Stator Chord in	Stator Chord mm
Hub	*49.1*	*48.3*	*3.00*	*76.2*	*54.4*	*18.7*	2.35	59.7
3	46.4	49.2	3.05	77.5	54.8	18.4	2.14	54.4
5	43.9	50.1	3.11	79.0	55.3	18.2	1.99	50.5
7	42.3	51.0	3.17	80.5	55.9	18.0	1.89	48.1
9	41.3	51.9	3.23	82.1	56.4	18.1	1.87	47.5
11	40.6	52.7	3.29	83.6	57.0	18.3	1.92	48.8
13	40.1	53.4	3.34	84.9	58.4	19.0	2.07	52.6
Case	40.4	54.0	3.39	86.1	62.4	20.7	2.37	60.1

sions in rotor deviation angle at severe off-design conditions. This consisted of the introduction of splitter vanes in the downstream portion of the rotor as depicted in Fig. 3. The design of this rotor is fully described by Wennerstrom and Frost (1974). It followed the same procedure as described for the baseline, and design values of loss and deviation were not revised. The rotor hub contour was adjusted to compensate for the additional metal blockage introduced by the splitter. The splitter camber line duplicated the camber line of the principal blades and was indexed one half of the circumferential spacing between principal blades. The same number of full rotor blades (30) was employed resulting also in 30 splitter vanes. A chordwise thickness distribution corresponding to a double-circular-arc section of equal camber was distributed symmetrically about the splitter-vane camber line. Maximum thickness varied from 8 percent splitter chord at the hub to 4 percent at the tip. The splitter vanes extended full span and their leading edge was placed exactly halfway between inlet and exit planes of the rotor, as viewed in the meridional pro-

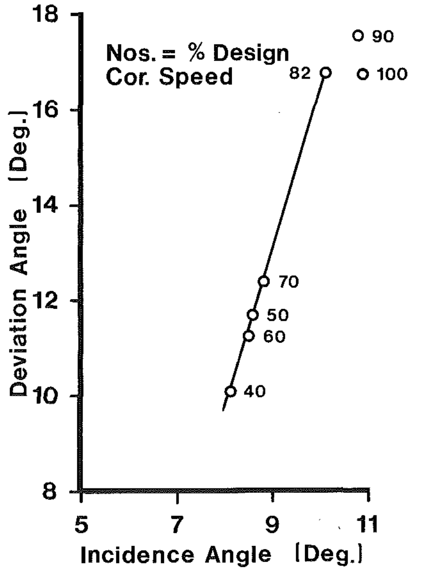

Fig. 2 Rotor midradius deviation versus incidence

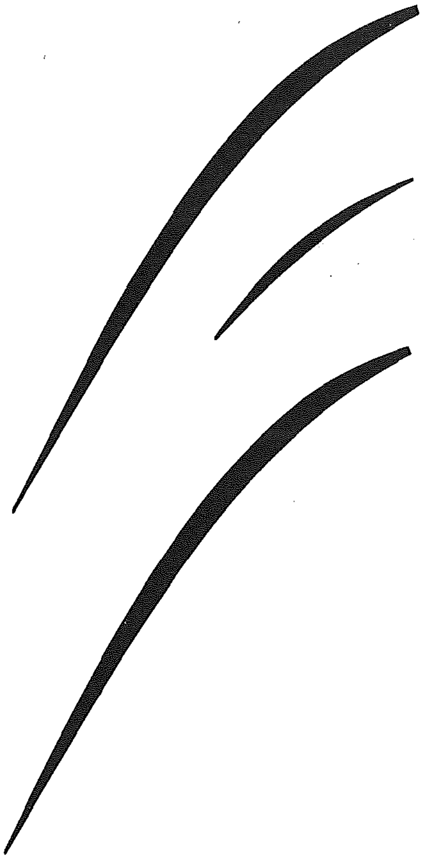

Fig. 3 Rotor cascade with splitter vanes

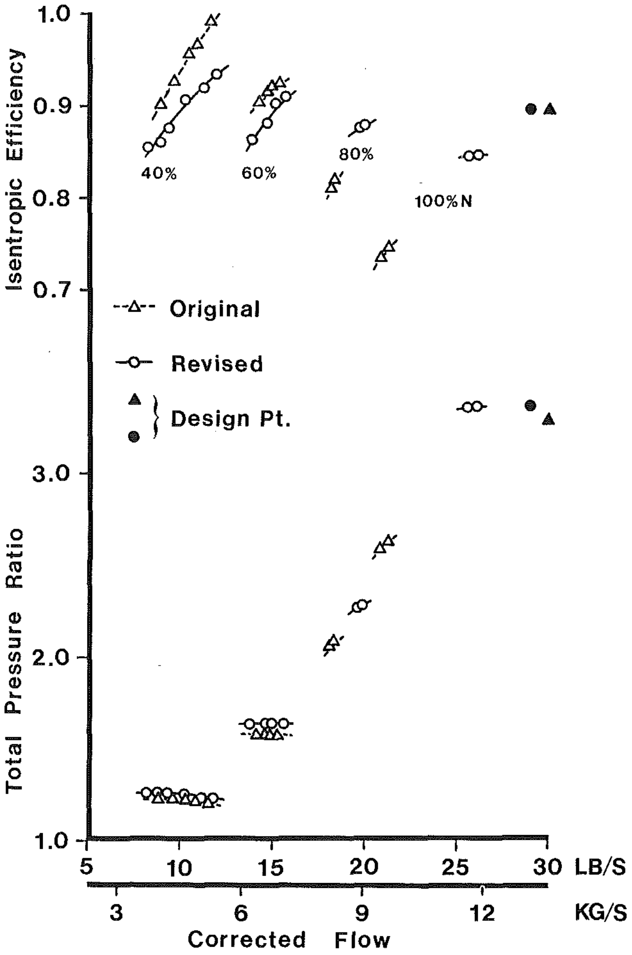

Fig. 4 Comparison of original versus revised rotor performance

jection. During the redesign, an error in the formulation of the continuity equation used with nonradial computing stations was discovered. The error magnitude at the stator leading edge, the most extreme case, was approximately 3 percent. To compensate for this, the new rotor was designed for a flow rate of 29 lb/s (13.2 kg/s) versus 30 lb/s (13.6 kg/s) for the original.

A performance map comparing the revised with the original rotor is shown in Fig. 4. Complete results of this test are presented by Wennerstrom et al. (1975). The high-speed performance has greatly improved at some cost in low-speed performance. Design speed rotor efficiency has now peaked approximately five points below the design value, the peak rotor total pressure ratio at 3.47 is now slightly above the design value of 3.35, and the flow is now approximately 12 percent below the revised design value. Stage performance is still quite poor with the isentropic efficiency 14 points below design and total pressure ratio peaking at 2.77 versus 3.06, respectively. The splitter vanes did appear successful in controlling deviation angle. Midradius rotor deviation, such as plotted in Fig. 2, was now limited to approximately 7–8 deg over the entire speed range. Incidence over the same range now varied from 8 down to 6 deg, with the lowest values now measured at the highest speeds, the reverse of the trend shown in Fig. 2. The original spanwise deviation distribution showed signs of a large hub separation. The hub now appeared very healthy and a large upswing in deviation was now only observed close to the outer casing.

An assessment of rotor losses in relation to a conventional shock plus diffusion loss model was made in the following manner. Holtman et al. (1973) present results of a cascade test of a blade section corresponding to approximately 62 percent span of the rotor. This section was selected because it represented the streamsurface having minimum radius change according to an axisymmetric through-flow calculation. At design-point operating conditions, static pressure along the suction surface of the principal airfoils of the cascade was seen to be nearly constant at the undisturbed free-stream value up to the shock impingement point, indicating that neither precompression nor expansion has occurred upstream of the passage shock wave. Since the compressor stage passed only about 88 percent of design flow, the suction surface Mach number just upstream of the shock wave was assumed to be increased above the free-stream relative value by an amount equal to a Prandtl–Meyer expansion from the relative free-stream Mach number through an angle equal to the difference between actual operating incidence and design incidence. Shock loss was then presumed equal to the total pressure loss through a normal shock having an upstream Mach number equal to the average of the relative free-stream and suction surface Mach number of each streamsurface. These computations were performed for blade sections at 10, 50, and 90 percent span. Shock loss was subtracted from the total loss measured at the same location, and the result was plotted in the form of Total Pressure Loss Parameter versus Diffusion Factor in Fig. 5. Blade solidity was presumed equal to the sum of principal-blade chord plus splitter-vane chord divided by the mean circumferential spacing between principal blades. The three data points are shown superimposed upon the NACA loss correlation presented in Fig. 203 of Johnson et al. (1965) and including the extrapolation of Wennerstrom and Hearsey (1971). At diffusion factors below 0.6, the performance of the blade section (including splitter vanes) appears consistent with past experience. However, at higher diffusion factors, specifically the data point near the tip, the

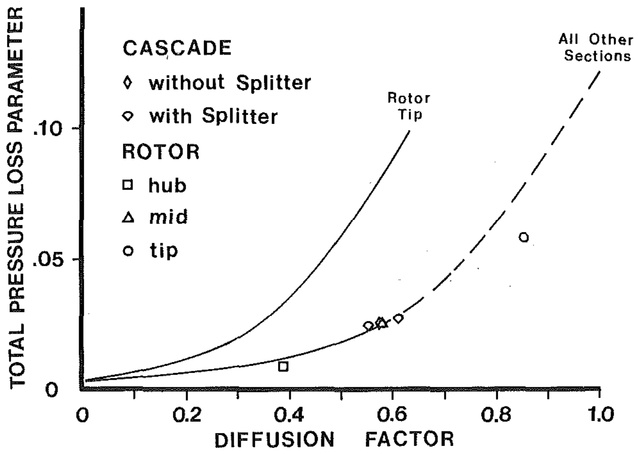

Fig. 5 Rotor and cascade performance relative to Lieblein loss correlation (Johnson et al., 1965)

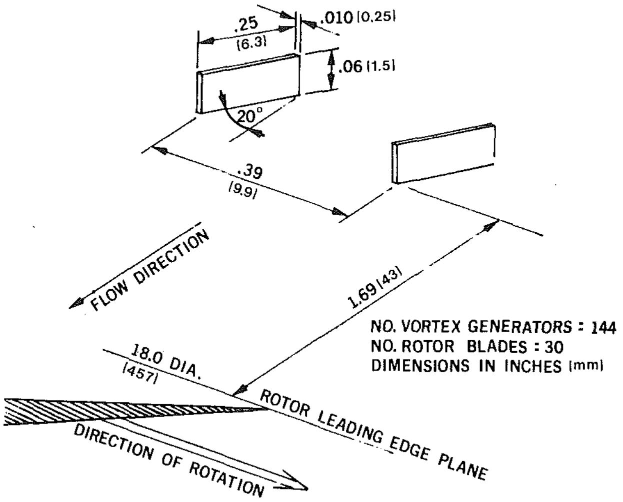

Fig. 6 Casing vortex generator geometry

blade section with splitter vanes performs substantially better than the performance anticipated by the original extrapolation. The absolute values of rotor and cascade performance could not be compared because they did not operate under the same conditions. However, the total pressure loss parameter of the cascade was calculated in the same manner as for the rotor for the two highest static pressure ratios tested at design inlet conditions. These two data points, also shown in Fig. 5, fell almost precisely on the same curve, bracketing the midradius data point of the rotor test.

The deviation angle poses more of a prediction problem. The deviation angle of the cascade just prior to spill was 5.16 deg. This is approximately one half what one would predict using Carter's Rule, and a value of m of 0.41 which was estimated on the basis of a stagger of 52.3 deg and the point of maximum camber at about 65 percent chord. An adjusted solidity was used just as for the loss parameter computation. An alternate approach was examined in which the camber and stagger of the splitter vane are considered dominant. Also, the splitter vane is not far from a circular arc so m for Carter's Rule was drawn from the correlation for circular arcs. Using the same adjusted solidity, a deviation angle of 5.45 deg is predicted which compares favorably with the experimental value of 5.16 deg. At lower static pressure ratios, the experimental deviation rose to a maximum of 6.1 deg, bracketing this alternate predicted value.

Table 2 Comparison of performance at maximum efficiency points with (3) and without (2) vortex generators

PERCENT DESIGN RPM	CONF. NO.	FLOW (LB/SEC)	-----ROTOR----- PRES.RATIO	EFF.	-----STAGE----- PRES.RATIO	EFF.
40	2	10.22	1.250	.907	1.233	.849
40	3	10.27	1.252	.909	1.231	.859
60	2	15.01	1.640	.901	1.569	.816
60	3	15.28	1.637	.917	1.566	.830
80	2	19.69	2.275	.874	2.052	.753
80	3	19.90	2.285	.887	2.080	.776
90	2	21.75	2.697	.845	2.324	.703
90	3	22.19	2.718	.864	2.335	.717
100	2	25.63	3.344	.843	2.708	.674
100	3	25.86	3.418	.859	2.806	.700

Casing Vortex Generators

At this point in the program, the performance of the compressor, although still seriously deficient, was considered adequate to embark upon the program of boundary-layer control modifications originally envisioned. The supersonic compressor of this investigation had very high tip loading plus a strong passage shock wave. Flow separation on the outer casing was considered likely. Thus, the first form of boundary-layer control evaluated was a row of vortex generators placed on the outer casing, upstream of the stage, designed to energize the casing boundary layer across the rotor tip. The configuration employed is illustrated in Fig. 6, and more details of the investigation can be found in Law et al. (1976).

The vortex generators were designed according to the following rationale. Fluid in the vortices was assumed to obey gyroscopic laws of motion. This implies that if a force, such as a pressure gradient, is applied in one direction, the reaction of the vortices will be to deflect in a direction perpendicular to the applied force, left or right depending upon the direction of rotation of the vortices. Considering the periodic rotor pressure gradient from blade to blade to be the applied force, the vortex generators were staggered in the same direction as the rotor blades, as shown in Fig. 6, so that the reaction of the vortices would be to move toward, i.e., to stay on the casing. Should they move away from the casing into the free stream, it was assumed that their effectiveness would be lost. This dictated a corotating design as opposed to counterrotating vortex pairs. Rules for their dimensioning were taken from Lachman (1961). Guidelines from that reference indicate that vortices from a well-designed, corotating configuration will remain effective up to a downstream distance of 80–100 times the generator height; however, they will not become fully effective until reaching a downstream distance of 10–30 times the generator height. Additional considerations were an intuitive judgment to make the vortex generator height at least twice the rotor tip clearance and a desire to reduce the number to a practical minimum because of cost. The final choice was a height of 0.060 in. (1.5 mm). A desirable spacing/height ratio from 4 to 8 was recommended by Lachman (1961). A ratio of 6.5 was chosen leading to 144 generators around the periphery or approximately 4.8 per circumferential blade spacing.

The results achieved by adding casing vortex generators are best summarized by Table 2 (Law et al., 1976) where maximum efficiency operating points with and without vortex generators are compared between 40 and 100 percent corrected speed. In general, both rotor and stage efficiency increased from 1.0 to 2.0 points over the whole speed range, flow increased a comparable amount, and pressure ratio or stall margin increased. An examination of the spanwise performance at the rotor exit indicated that the improvement was not localized at the tip. It appeared distributed over the full

Table 3 Rotor clearance matrix evaluated

	% Chord	% Span
Original Clearance	0.78	1.48
First Modification	0.66	1.25
Second Modification	0.50	0.95

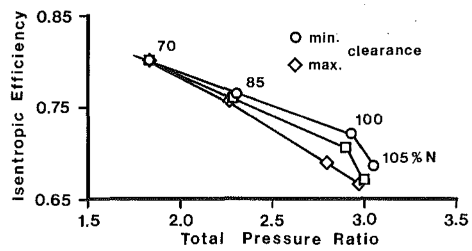

Fig. 7 Influence of rotor tip clearance on stage peak performance

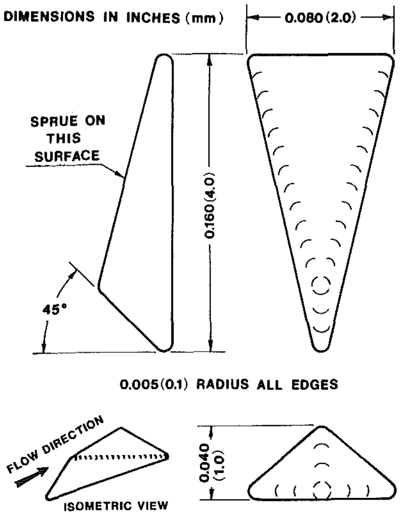

Fig. 8 Rotor vortex generator configuration

span, possibly due to the strong secondary flows characteristic of such a low aspect ratio stage. Another hypothesis is that the strengthening of the casing boundary layer allowed the attainment of a higher back pressure, which improved the operating efficiencies of the other blade elements.

Rotor Tip Clearance

The next phase in the investigation involved a reduction of rotor tip clearance in two steps. The casing over the rotor was conical, converging at a half angle of approximately 9.4 deg, as pictured in Fig. 1. Clearance adjustments were accomplished by shimming the casing forward. The rotor tip diameter was not altered. The clearance matrix evaluated is given in Table 3. The values shown were obtained by subtracting the predicted rotor growth from the measured value of static clearance.

The results obtained are illustrated in Fig. 7, which compares peak stage efficiency versus pressure ratio for 70 to 105 percent corrected speed where peak efficiency increased approximately 3 points and total pressure ratio increased from approximately 2.8 to slightly over 2.9. The shift in stall line was approximately the same as the shift in pressure ratio illustrated for peak efficiency. As with the casing vortex generators, the improvement appeared distributed over the full span rather than being localized at the tip. This is not inconsistent with numerous other investigations, as mentioned by Peacock (1983).

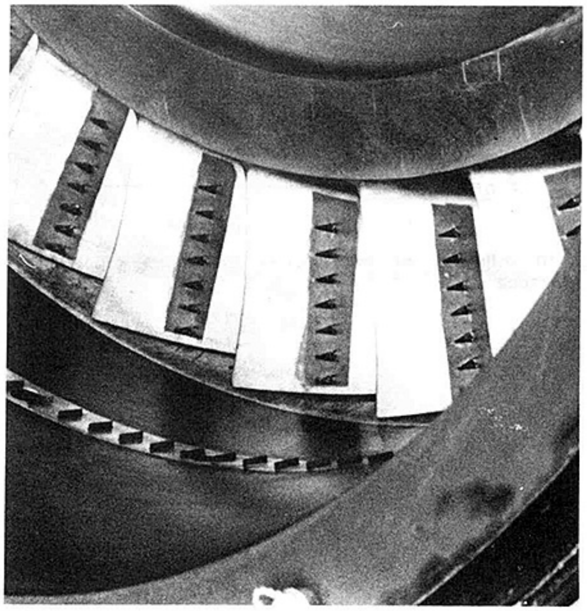

Fig. 9 Rotor vortex generator installation

Rotor Vortex Generators

The last phase of this investigation aimed at enhancing rotor performance involved the installation of vortex generators on the rotor blades. A row of seven, configured as shown in Fig. 8, was placed on the suction surface of each principal rotor blade approximately midway between the leading edge and the impingement line of a normal shock wave. A photograph of the installation is shown in Fig. 9. The height of each vortex generator, 0.040 in. (1 mm), is equivalent to about 1.2 percent of the average chord length of the principal rotor blades. The outer edge of the base of each vortex generator was aligned with the local streamline direction in order to encourage a single large vortex to be produced by the inner surface of each generator rather than a counterrotating vortex pair, if symmetrically oriented. The vortex generators were spaced a distance of six times their height from one another, according to corotating vane design practice, as described by Lachman (1961). The corotating design approach was adopted based upon the assumption that the fluid in the vortices would behave according to gyroscopic laws of motion when reacting to the rotor's environment. Assuming a streamwise momentum deficit relative to the free stream, their tendency in response to radial equilibrium forces would be to move outward. However, the direction of spin of a vortex peeling off the inner surface of each vortex generator is such that the gyroscopic reaction of a radially outward force will cause it to turn toward the blade surface, thus remaining on the airfoil. The vortex generators were pressure molded of glass-reinforced polyimide plastic and bonded to the blades with an adhesive often used to attach strain gages. The design of the vortex generators and the method of installation was identical to that described by Wennerstrom et al. (1982).

The results achieved with rotor-mounted vortex generators were less than rewarding. A minute increase in stage total pressure ratio was achieved at design speed and above, but at a cost in efficiency of nearly one point. It was observed from the spanwise distribution of performance in the rotor exit plane that conditions had improved in the tip region, but had deteriorated near the hub. Considering the results shown in Fig. 5, this was probably not surprising. Only in the vicinity of

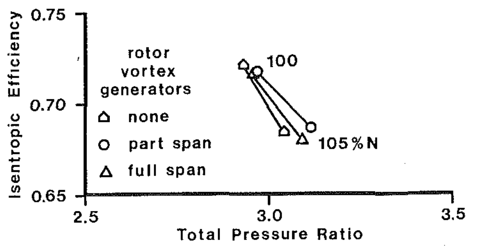

Fig. 10 Influence of rotor vortex generators on stage peak performance

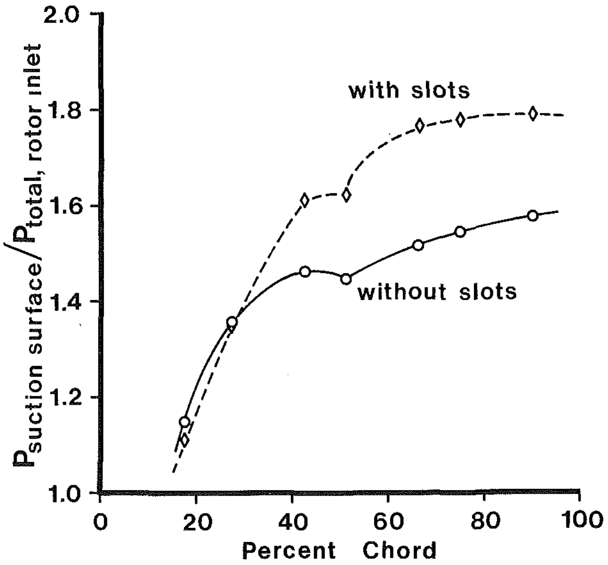

Fig. 11 Stator suction surface pressure distribution

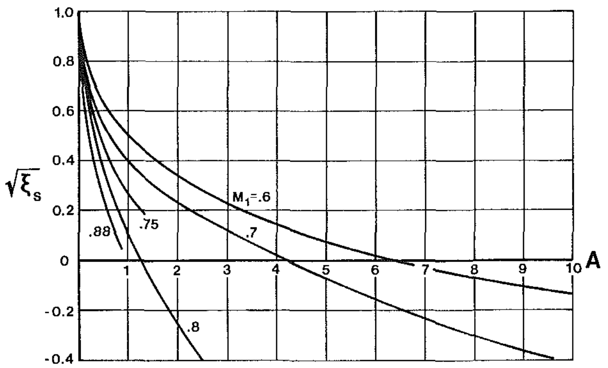

Fig. 12 Slot effectiveness correlation of Griepentrog (Griepentrog, 1970)

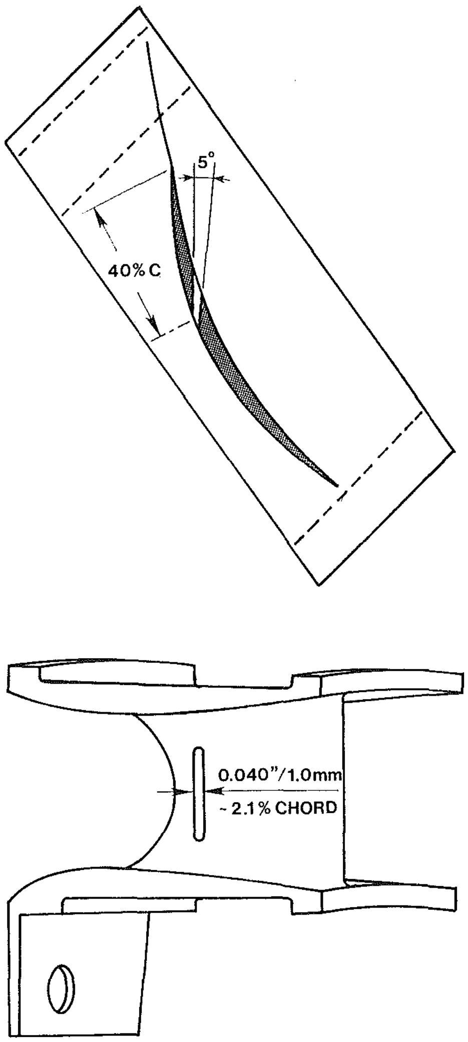

Fig. 13 Stator slot geometry

the tip did Diffusion Factor rise to levels where help of the sort vortex generators might provide was really needed. From midspan inboard, Diffusion Factor remained within a range in which little separation would be expected at this aspect ratio and solidity. Consequently, the stage was tested again with the innermost four vortex generators removed from each blade, leaving the three nearest the tip. This produced the best result; a slight further increase in pressure ratio, and the efficiency approximately restored to the values achieved with no vortex generators. The results are shown in Fig. 10 in the form of peak efficiency versus pressure ratio for 100 and 105 percent corrected speed. At lower speeds, the differences were negligible. The largest improvement was achieved at 105 percent corrected speed. However, it would be difficult to argue that the effort was worthwhile in this case.

Stator Slots

The final variation attempted on this stage was the installation of a slot in each stator vane. It was obvious from the stator suction surface pressure distribution, shown in Fig. 11, that the stator was badly separated from about the third suction surface pressure tap onward. To assess the potential effectiveness of a slot, the slot effectiveness correlation of Griepentrog (1970) was employed. Figure 17 of that reference is reproduced as Fig. 12 of this paper. Slot effectiveness is defined as

$$\xi_s = \frac{\omega - \omega_s}{\omega} \qquad (1)$$

and is plotted against a cascade geometry function

$$A = \phi^{3/2}(AR)^2\sigma \qquad (2)$$

where ω = the plain cascade relative total pressure loss coefficient; ω_s = the value of ω measured with a slot; ϕ = section camber angle (radians); AR = blade aspect ratio; σ = blade solidity. Mach number is shown as a parameter in Fig. 12. The value of the function A for the stator of this stage is 0.358, based upon its averaged geometric properties. Although the mean stator inlet Mach number at design conditions is approximately 1.04, it still appeared likely from Fig. 12 that the slot effectiveness might lie on the positive side of the axis. The slot geometry selected is shown in Fig. 13. The spanwise position of the slot was in the center of the blade and occupies about one half the total span. The slot does not extend into the fillet region at either end wall.

The stage performance achieved with slotted stators is presented in Fig. 14, which shows peak efficiency versus pressure ratio as a function of corrected speed. The improvement was relatively substantial, adding from three to four points to the stage efficiency over the entire speed range. The effect on the suction surface pressure distribution is shown in Fig. 11. An attempt was made to evaluate the slot effectiveness according to equation (1). However, since slotting the blades required sacrificing the stator leading edge total pressure instrumentation, it was necessary to assume that the rotor exit performance had not changed substantially from the unslotted case. The expedient sometimes used of assuming that peak pressures in the exit plane circumferential distribution are equal to rotor exit pressure was not practical in this case. The extremely low stator aspect ratio and high loading produced such strong secondary flow and mixing effects that the improved stator performance showed up as an increase in stator loss coefficient if calculated in this manner. Using the rotor exit total pressures measured without slotted stators and the stage exit plane total pressure and temperature actually measured in each case, the arithmetic average slot effectiveness for the entire stator was calculated to be

$$(\xi)^{1/2} = 0.3774$$

This is a plausible result reasonably consistent with Fig. 12 for a value of $A = 0.358$ and an arithmetic average inlet Mach number of 1.047. The absolute value of the stator total pressure loss coefficient averaged over the span was still extremely high, however, with $\omega = 0.2625$. Whether or not shock loss is taken into account, this still remains large. For the average Diffusion Factor of 0.623, the NACA/Lieblein correlation for stator loss would predict a Loss Parameter value of about 0.03 versus 0.067 corresponding to the measured loss. If the most pessimistic shock loss is assumed, a normal shock at a Mach number corresponding to the lowest pressure measured on the suction surface with the midspan static pressure taps, $M = 1.4$, a shock loss coefficient of $\omega_s = 0.0837$ would result and a diffusion-related Loss Parameter of 0.0454 would be obtained. This is still about 50 percent higher than the value which would normally be predicted for this diffusion level. Whether this was due to extra losses resulting from the extremely low aspect ratio of about 0.43, off-design incidence angles, an optimistic assessment of rotor performance, or yet other factors is not conclusively known. Although the slots significantly improved performance, they simply converted a highly separated blade row into a less separated one, and there is no reason to assume that it should necessarily fall in line with the Lieblein correlation which generally reflects minimum loss conditions for well-designed blade rows. This blade row was not well designed for the actual conditions prevailing during the test. The reader is cautioned that since the slot effectiveness parameter was treated as a lumped parameter for the entire blade row based upon averaged quantities, the foregoing discussion of stator losses also represents arithmetically averaged behavior and not blade element performance.

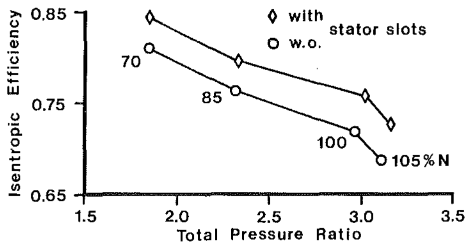

Fig. 14 Influence of stator slots on stage peak performance

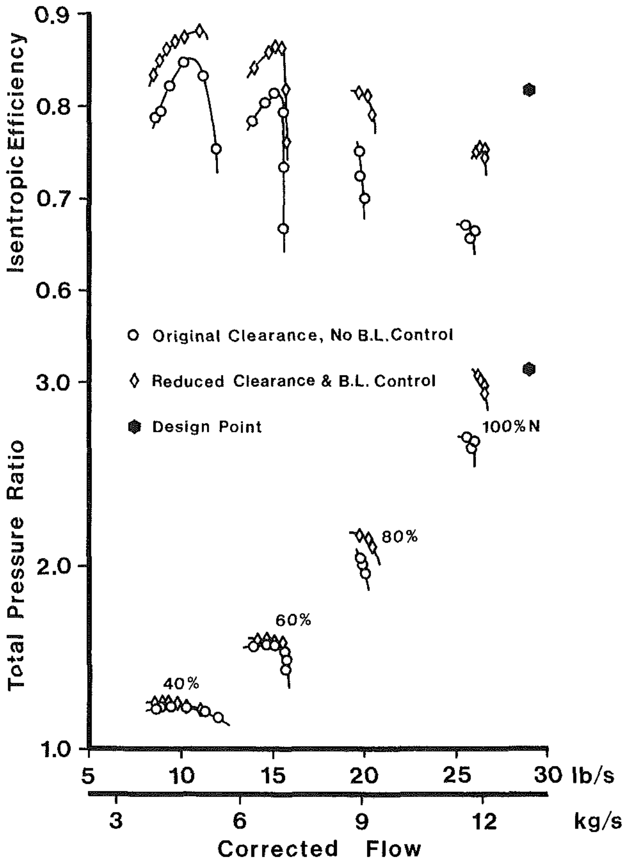

Fig. 15 Improvement in stage performance achieved with reduced rotor clearance and boundary-layer control

Conclusions

Splitter Vanes. The application of splitter vanes to an axial rotor blade row, following similar concepts to those often applied to centrifugal impellers, illustrated potential for satisfactory performance at high diffusion levels. Losses appeared consistent with Lieblein's correlation for rotor and stator diffusion loss or a smooth extrapolation thereof, without the necessity of incorporating added tip loss when shock loss was subtracted and an adjusted solidity used for the computation. Similarly, deviation could be predicted by Carter's Rule if the camber and stagger of the splitter vanes was considered dominant and the same adjusted solidity was employed. This application is structurally limited to rotors of relatively low aspect ratio because of the higher aspect ratio taken on by the splitter vane. However, the present state of the art of flow computation does not currently encourage their use even when it is structurally feasible. In spite of the fact that loss levels appeared consistent with contemporary loss correlations, it was clear from observation of cascade test pressure distributions presented by Holtman et al. (1973) that a design comprised of a splitter vane camber line duplicating the principal blade and placed in midpassage was far from optimum. Significant overexpansion and recompression occurred within the passages. An attempt to optimize splitter vane geometry through an inviscid analysis in the cascade plane, presented by Dodge (1975), was totally unsuccessful. It was concluded that, at the high diffusion levels experienced with this cascade, viscous effects were so strong that an inviscid analysis was incapable of providing useful guidance for optimization of splitter vane shape and position. When full Navier-Stokes analyses or viscid/inviscid interaction analyses are developed to the extent that they become practical design tools for cascade optimization, the application of splitter vanes to axial blade rows may bear re-examination. Considering that the loss levels of the test rotor and cascade appeared consistent with the Lieblein loss correlation and yet the surface pressure distributions were far from ideal, it is clear that a cascade of this type could theoretically be made to operate with significantly lower losses if well designed.

Tip Clearance and Casing Vortex Generators. These two items are grouped because of a similarity of result. Both casing vortex generators and a reduction in rotor tip clearance produced improvements in performance visible over the full span, not localized at the tip. Extremely high diffusion at the tip undoubtedly encouraged separation on both end walls and airfoils. No sign of an optimum clearance was evident at practical levels of running clearance; this result is consistent with the majority of observations, according to Peacock (1983). A potential interaction between clearance and casing vortex generators was not investigated; the casing vortex generators were not removed when clearance was reduced.

Rotor Vortex Generators. In spite of the high rotor diffusion levels, the effect of rotor vortex generators was minimal, contrary to expectations. This is in puzzling contrast to the results reported by Wennerstrom (1984), where an increase in stall margin and also efficiency in much of the operating range was reported for a stage already operating at high efficiency without their assistance. One possible conclusion is that a rotor leading edge flow separation existed with reattachment occurring so close to the vortex generators, or even behind them, that they had no opportunity to act. Minimum rotor incidence at 85 percent speed was about 7 deg at the tip and higher at lower speeds. At 100 percent speed, it was reduced to 5 deg and it continued falling with increasing speed. These levels of incidence are higher than those experienced with the compressor discussed by Wennerstrom (1984). Also, the vortex generators applied to that compressor were in a region of negative camber, encouraging rapid reattachment, whereas in this case the rotor had only positive camber. This conclusion is further supported by results reported by Holtman et al. (1973), where at Mach numbers prevailing outboard of rotor midspan at design speed, lower cascade losses were measured at high static-pressure ratios with vortex generators. However, the cascade ran at the design incidence of 3.4 deg which the rotor was never able to do.

Stator Slots. There have been few instances recorded where slots were effective in improving turbomachine airfoil performance. However, the case reported herein is one of them. The improvement resulting from slots corresponded to an approximately 14 percent reduction in total pressure loss coefficient. This must be qualified by the observation that loss levels with and without the slot were both extremely high as a result of very severe operating conditions and an appreciable mismatch between the design stator inlet conditions and the actual rotor outflow conditions. The improvement achieved by the slots appeared roughly consistent with Griepentrog's correlation.

Overall Design. This compressor, like many supersonic compressors before it, is another example of an overly ambitious design attempted with design tools really not up to the job. At the diffusion levels experienced, viscous computational techniques are really essential to do an adequate job of design optimization. This design also suffered two other significant shortcomings. The original shock loss model employed for the rotor was naively optimistic. It is the author's current view that rotors designed for high static pressure ratios will be unlikely to operate with shock losses significantly less than described by Wennerstrom and Puterbaugh (1984). The other unsuccessful feature was the design approach applied to the stator wherein annulus contraction through the blade row was balanced against camber to achieve a reasonable meridional static pressure distribution as calculated by an axisymmetric solution. The circular arc camber line chosen was, in retrospect, most inappropriate. Annulus contraction cannot fully compensate for camber, particularly upstream of the cascade capture zone, and an airfoil section having less camber forward and more aft is likely to perform much better at Mach numbers approaching sonic and higher. The application of boundary-layer control techniques was partially successful. The overall performance improvement achieved with boundary-layer control and clearance reduction is shown in Fig. 15. In view of the results of Wennerstrom (1984), it appears likely that this level of improvement might still be achieved if the stage were redesigned using more appropriate viscous techniques.

Future Direction. With the progress which has occurred in design technology since this program was performed, there seems little doubt that the original goals could be achieved, and probably exceeded, if one wanted to do so. The development of three-dimensional, viscous computational codes capable of coping with these severe conditions appears imminent, such as the work of Hah (1986). However, they currently are still configured as analysis tools rather than design tools, so their use for design optimization is likely to be time consuming and expensive. Another major question is one of motivation. The applications once envisioned for such stages have not materialized, and it does not appear likely that they will in the near term. Consequently, the major conclusions of value from this effort appear to be that passive boundary-layer control in the form of slots and vortex generators can be used to some practical benefit under the right conditions. These conditions generally include low aspect ratio, relatively high loading, and attached flow in the case of rotor vortex generators. Also, splitter vanes may be of interest for applications involving very high Diffusion Factors. However, their use is not recommended unless accomplished with the benefit of guidance from a good three-dimensional, viscous analysis.

References

Dodge, P. R., 1975, "Transonic Two-Dimensional Flow Analysis of Compressor Cascade With Splitter Vanes," Air Force Aero Propulsion Laboratory, Wright-Patterson Air Force Base, OH, AFAPL-TR-75-110, AD A025921.

Erwin, J. R., 1964, "The Supersonic Compressor, Chapter 1: Early Work on Supersonic Compressors," *Aerodynamics of Turbines and Compressors. High Speed Aerodynamics and Jet Propulsion*, Vol. 10, Princeton, NJ, pp. 368–381.

Ferri, A., 1964, "The Supersonic Compressor, Chapter 2: Aerodynamic Properties of Supersonic Compressors," *Aerodynamics of Turbines and Compressors. High Speed Aerodynamics and Jet Propulsion*, Vol. 10, Princeton, NJ, pp. 381–432.

Griepentrog, H. F. L., 1970, "Performance Prediction for High Turning Low Aspect Ratio Stator Cascades in the Transonic Regime," ASME Journal of Engineering for Power, Vol. 92, pp. 390–398.

Hah, C., 1986, "A Numerical Modeling of Endwall and Tip-Clearance Flow of an Isolated Compressor Rotor," ASME Journal of Engineering for Gas Turbines and Power, Vol. 108, pp. 15–21.

Holtman, R. L., Huffman, G. D., McClure, R. B., and Sinnet, G. T., 1972, "Test of a Supersonic Compressor Cascade (Vol. 1)," Aerospace Research Laboratories, Wright-Patterson Air Force Base, OH, ARL 72-0170, Vol. I, AD 756870.

Holtman, R. L., McClure, R. B, and Sinnet, G. T., 1973, "Test of a Supersonic Compressor Casade With Splitter Vanes," Aerospace Research Laboratories, Wright-Patterson Air Force Base, OH, ARL 73-0142, AD 774549.

Jansen, W., 1967, "The Application of End-Wall Boundary Layer Effects in the Performance Analysis of Axial Compressors," ASME Paper No. 67-WA/GT-11.

Johnson, I. A., Bullock, R. O., et al., 1965, "Aerodynamic Design of Axial Flow Compressors," National Aeronautics and Space Administration, NASA SP-36, p. 248.

Klapproth, J. F., 1961, "A Review of Supersonic Compressor Development," ASME JOURNAL OF ENGINEERING FOR POWER, Vol. 83, pp. 258-268.

Lachman, G. V., ed., 1961, *Boundary Layer and Flow Control*, Vol. II, Pergamon Press, New York, pp. 1281-1286.

Law, C. H., Wennerstrom, A. J., and Buzzell, W. A., 1976, "The Use of Vortex Generators as Inexpensive Compressor Casing Treatment," SAE Paper No. 760925.

Peacock, R. E., 1983, "A Review of Turbomachinery Tip Gap Effects, Part 2: Rotating Machinery," *International Journal of Heat and Fluid Flow*, Vol. 4, pp. 3-16.

Wennerstrom, A. J., and Hearsey, R. M., 1971, "The Design of an Axial Compressor Stage for a Total Pressure Ratio of Three to One," Aerospace Research Laboratories, Wright-Patterson Air Force Base, OH, ARL TR 71-0061, AD 727001.

Wennerstrom, A. J., Frost, G. R., and DeRose, R. D., 1974, "Test of an Axial Compressor Stage Designed for a Total Pressure Ratio of Three to One," Aerospace Research Laboratories, Wright-Patterson Air Force Base, OH, ARL TR 74-0001, AD 778844.

Wennerstrom, A. J., and Frost, G. R., 1974, "Design of a Rotor Incorporating Splitter Vanes for a High Pressure Ratio Supersonic Axial Compressor Stage," Aerospace Research Laboratories, Wright-Patterson Air Force Base, OH, ARL TR 74-0110, AD 786025.

Wennerstrom, A. J., 1974, "On the Treatment of Body Forces in the Radial Equilibrium Equation of Turbomachinery," *Traupel Festschrift*, Juris Verlag, Zurich, pp. 351-367.

Wennerstrom, A. J., Buzzell, W. A., and DeRose, R. D., 1975, "Test of a Supersonic Axial Compressor Stage Incorporating Splitter Vanes in the Rotor," Aerospace Research Laboratories, Wright-Patterson Air Force Base, OH, ARL TR 75-0165, AD A014732.

Wennerstrom, A. J., Law, C. H., DeRose, R. D., and Strain, E. C., 1982, "Investigation of a High-Through-Flow, Single-Stage Axial-Flow Compressor With Tip Clearance Increased 0.020 inch and Rotor Tip Vortex Generators, Configuration 3.1," Air Force Wright Aeronautical Laboratories, Wright-Patterson Air Force Base, OH, AFWAL-TR-82-2071, AD B068098.

Wennerstrom, A. J., and Puterbaugh, S. L., 1984, "A Three-Dimensional Model for the Prediction of Shock Losses in Compressor Blade Rows," ASME JOURNAL OF ENGINEERING FOR GAS TURBINES AND POWER, Vol. 106, pp. 295-299.

Wennerstrom, A. J., 1984, "Experimental Study of a High-Through-Flow Transonic Axial Compressor Stage," ASME JOURNAL OF ENGINEERING FOR GAS TURBINES AND POWER, Vol. 106, pp. 552-560.

Wilcox, W. W., Tysl, E. R., and Hartmann, M. J., 1959, "Resume of the Supersonic-Compressor Research at NACA Lewis Laboratory," ASME *Journal of Basic Engineering*, Vol. 81, pp. 559-568.

H. Pfeil
Professor.

M. Göing
Research Engineer.

Fachgebiet für Thermische Turbomaschinen,
Technische Hochschule Darmstadt,
Darmstadt, Federal Republic of Germany

On the Shear-Stress Integral of Turbulent Boundary Layers

The paper presents an integral method to predict turbulent boundary layer behavior in two-dimensional, incompressible flow. The method is based on the momentum and moment-of-momentum integral equations and a friction law. By means of the compiled data of the 1968 Stanford Conference, the results show that the integral of the turbulent shear stress across the boundary layer, which appears in the moment-of-momentum integral equation, can be described using only two basic assumptions for all cases of flow.

Introduction

For the fluid-mechanical analysis of turbomachine components, methods are required to predict the development of the turbulent boundary layer under the influence of prescribed pressure distributions. As shown by the results of the computations at the 1968 Stanford Conference [1] the behavior of turbulent boundary layer flow is not even known in case of two dimensionality. Differential methods, including modeling of turbulence, e.g., the k-ϵ model of Singhal and Spalding [2], have also failed to predict satisfactorily the boundary layer development, especially for the case of strong positive pressure gradients.

In the present study an integral method is described, in which the equations of motion are reduced to the momentum and moment-of-momentum integral equations. The assumption is that the state of the boundary layer at any x station can be specified by the Reynolds number based on the momentum thickness, the profile shape parameter, the wall shear-stress coefficient, and the nondimensional integral of turbulent shear stress across the boundary layer.

A friction law based on a velocity-profile family gives a relation between the first three of these boundary layer parameters. However, to obtain a closed set of equations, a global assumption is required about the relationship of the shear-stress integral to properties of the mean field. By means of experimental data and the moment-of-momentum integral equation, this closure problem is investigated. Predictions of the turbulent boundary layer development are presented for all compiled flows of the 1968 Stanford Conference [3].

Differential Equations of Motion

Boundary layer theory is based on the continuity equation

$$\frac{\partial}{\partial x}\left[u\phi r\left(1+\frac{y^*}{r}\right)\right]+\frac{\partial}{\partial y}\left[v\phi r\left(1+\frac{y^*}{r}\right)\right]=0 \qquad (1)$$

and the boundary layer equation for the mean flow

$$u\frac{\partial u}{\partial x}+v\frac{\partial u}{\partial y}=-\frac{1}{\rho}\frac{dp_\infty}{dx}$$

$$+\frac{1}{\left(1+\frac{y^*}{r}\right)}\frac{\partial}{\partial y}\left[\frac{\tau}{\rho}\left(1+\frac{y^*}{r}\right)\right] \qquad (2)$$

The mean value of the total shear stress is given by

$$\frac{\tau}{\rho}=\nu\frac{\partial u}{\partial y}-\overline{u'v'} \qquad (3)$$

and the imposed free-stream pressure $p_\infty(x)$ is related to the free-stream velocity $U_\infty(x)$ through Bernoulli's theorem

$$-\frac{1}{\rho}\frac{dp_\infty}{dx}=U_\infty\frac{dU_\infty}{dx} \qquad (4)$$

In equation (2) the fluctuation terms are not included; according to Rotta [4] and McDonald and Stoddart [5] these terms are usually of secondary importance and negligible.

Equations (1) and (2) are valid in the case of *axisymmetric flow* without the restriction $\delta << r$ [6]. Figure 1 shows the coordinate system with the geometric radius $r = r(x)$

$$y^*=y\sqrt{1-\left(\frac{dr}{dx}\right)^2} \qquad (5)$$

The term $\phi = \phi(x)$ in the continuity equation takes possible deviations of the flow from axisymmetry into consideration.

For *plane flows* the terms r and y^*/r in equations (1) and (2), and in the following equations, must be cancelled. $\phi = \phi(x)$ is then the nondimensional lateral width of the flow [7]; the term in equation (1) is a first-order correction for pure lateral divergence (no cross flow). For plane flow ϕ = const; however, in most of the cases in [3] small divergences or convergences of the flow are present, and these lateral effects must be considered in predictive methods.

Integral Equations of Motion

Integral equations can be obtained by multiplying each term

Contributed by the Gas Turbine Division of THE AMERICAN SOCIETY OF MECHANICAL ENGINEERS and presented at the 31st International Gas Turbine Conference and Exhibit, Düsseldorf, Federal Republic of Germany, June 8–12, 1986. Manuscript received at ASME Headquarters Feburary 17, 1987. Paper No. 86-GT-4.

of the boundary layer equation (2) by powers of the velocity u and the wall distance y, and integrating over y

$$\int_{y=0}^{\infty} u^n y^m \left(u \frac{\partial u}{\partial x} + v \frac{\partial u}{\partial y} - U_\infty \frac{dU_\infty}{dx}\right)\left(1+\frac{y^*}{r}\right) dy =$$

$$\int_{y=0}^{\infty} u^n y^m \frac{\partial}{\partial y}\left[\frac{\tau}{\rho}\left(1+\frac{y^*}{r}\right)\right] dy \qquad (6)$$

The velocity component v can be eliminated by application of equation (1). For $n = 0$ and $m = 0$ the *momentum integral equation* can be formulated

$$\delta_2 \frac{d\ln(\delta_2 \phi r)}{dx} + (2+H_{12})\delta_2 \frac{d\ln U_\infty}{dx} = \frac{c_f}{2} \qquad (7)$$

Setting $n = 0$ and $m = 1$ leads to the *moment-of-momentum integral equation*

$$\int_{y=0}^{\infty} \frac{\tau}{\rho}\left(1+\frac{y^*}{r}\right) dy = \frac{d}{dx}(U_\infty^2 A_2) + U_\infty \frac{dU_\infty}{dx}(A_1+A_4)$$

$$+ U_\infty^2 \frac{d\ln(\phi r)}{dx}(A_2+A_3) \qquad (8)$$

where

$$U_\infty A_1 = \int_{y=0}^{\infty} (U_\infty - u) y (1+y^*/r) dy$$

$$U_\infty^2 A_2 = \int_{y=0}^{\infty} (U_\infty - u) u y (1+y^*/r) dy$$

$$U_\infty^2 A_3 = \int_{y=0}^{\infty} (U_\infty - u) \int u (1+y^*/r) dy dy$$

$$U_\infty \frac{dU_\infty}{dx} A_4 = \int_{y=0}^{\infty} (U_\infty - u) \frac{\partial}{\partial x}\left[\int u \left(1+\frac{y^*}{r}\right) dy\right] dy$$

In the case of plane flow, the moment-of-momentum integral equation was derived by McDonald and Stoddart [5] using Coles' velocity-profile family. In this investigation the derivation was repeated for flows with lateral divergence and axisymmetric cases [8].

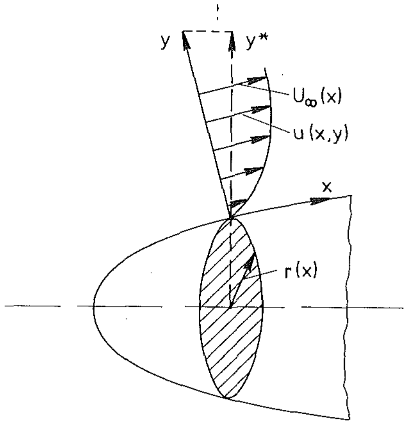

Fig. 1 Coordinate system in axisymmetric case

The term $U_\infty dU_\infty/dx A_4$ in equation (8) requires an evaluation by a velocity-profile model.

Velocity-Profile Family

To describe the velocity profile of the two-dimensional turbulent boundary layer, a model is employed, similar to the Coles profile model [3, 9, 10]. The profile is divided into a wall region and a wakelike outer distribution; however, the abrupt change in slope at the outer edge of the layer is eliminated by an additional term. This model [11] was used to improve the local parameter determination of the boundary layer measurements compiled by Coles and Hirst [3].

Outside the sublayer ($yu_\tau/\nu > 50$) the law of the wall has the form

$$\frac{u}{u_\tau} = \frac{1}{\kappa}\ln\left(\frac{yu_\tau}{\nu}\right) + C + \frac{1}{\kappa}(-2\eta^2 + \eta^3) \qquad (9)$$

with the constants $\kappa = 0.41$ and $C = 5.0$. The last term in this

Nomenclature

A = term in Fig. 2 and equation (12)
A_1-A_4 = coefficients defined by equation (8)
C = constant in equation (9)
c_f = $\tau_w/(\rho/2)(U_\infty^2)$ = local skin friction coefficient
c_τ = nondimensional shear-stress integral defined by equation (18)
$c_{\tau E}$ = value of c_τ in an equilibrium boundary layer defined by equation (23)
H_{12} = δ_1/δ_2 = profile shape parameter
LS = left-hand side of momentum integral equation balance
m, n = exponents in equation (6)
p_∞ = mean value of pressure at the outer edge of the boundary layer
r = geometric radius
r^* = geometric radius defined by equation (17)
Re_δ = $U_\infty\delta/\nu$ = Reynolds number
Re_1 = $U_\infty\delta_1/\nu$ = Reynolds number
Re_2 = $U_\infty\delta_2/\nu$ = Reynolds number
RS = right-hand side of momentum integral equation balance
u, v = mean velocity components in x, y directions
$-\rho\overline{u'v'}$ = Reynolds stress
U_∞ = free-stream velocity
u_τ = $\sqrt{\tau_w/\rho}$ = friction velocity
u_{1m}/U_∞ = profile parameter defined by Fig. 2
w = wake function defined by equation (10)
x = streamwise coordinate
y = direction normal to the surface
y^* = coordinate defined by Fig. 1 and equation (5)
δ = boundary layer thickness
δ_1 = $\int_{y=0}^{\infty}(1-u/U_\infty)\cdot(1+y^*/r)dy$ = displacement thickness
δ_2 = $\int_{y=0}^{\infty}(1-u/U_\infty)u/U_\infty\cdot(1+y^*/r)dy$ = momentum thickness
η = y/δ = nondimensional wall distance
κ = constant in equation (9)
ν = kinematic viscosity
ρ = density
τ = shear stress defined by equation (3)
$\tau_{\max}$ = maximum value of shear stress
τ_w = wall shear stress
ϕ = nondimensional lateral width of flow in equation (1)
ω = u_τ/U_∞ = nondimensional friction velocity

equation results in a steady distribution of the profile at the outer edge of the layer.

The wake function is given by Coles [10]:

$$w(\eta) = \frac{u_{1m}}{U_\infty} \sin^2\left(\frac{\pi}{2}\eta\right) \tag{10}$$

The formulation of the velocity profile results from the superposition of wall and wake region (Fig. 2):

$$\frac{u}{U_\infty} = \frac{\omega}{\kappa}\left[\ln\left(\frac{yu_\tau}{\nu}\right) + C\kappa - 2\eta^2 + \eta^3\right] + \frac{u_{1m}}{U_\infty}\sin^2\left(\frac{\pi}{2}\eta\right) \tag{11}$$

Setting $y = \delta$ and $u = U_\infty$ in equation (11), one obtains

$$1 = A + \frac{u_{1m}}{U_\infty} \tag{12}$$

with $A = (\omega/\kappa)[\ln(\mathrm{Re}_\delta\omega) + C\kappa - 1]$.

Local Friction Law

An implicit skin friction law can be obtained from the description of the turbulent profile to get a relationship in the form $c_f = c_f(H_{12}, \mathrm{Re}_2)$. In [11] good agreement is found between equation (11) and measured profile data in axisymmetric cases, too. So, a relationship $c_f = c_f(H_{12}, \mathrm{Re}_2, \delta/r^*)$ is found in axisymmetric boundary layer flow.

The deduction of the friction law is based on inserting the velocity-profile model into the defining equations of the displacement thickness δ_1 and momentum thickness δ_2. In these integrations the deviations of the sublayer from the logarithmic law are considered using the integral values given by Coles [3]:

$$\int_0^{50}\left(\frac{u}{u_\tau}\right)d\left(\frac{yu_\tau}{\nu}\right) = 541 \tag{13}$$

$$\int_0^{50}\left(\frac{u}{u_\tau}\right)^2 d\left(\frac{yu_\tau}{\nu}\right) = 6546 \tag{14}$$

With these assumptions, δ_1 and δ_2 are given by

$$\begin{aligned}\frac{\mathrm{Re}_1 - 65}{\mathrm{Re}_\delta} &= \left(0.5\,\frac{u_{1m}}{U_\infty} + 0.4167\,\frac{\omega}{\kappa}\right)\\ &\quad + \frac{\delta}{r^*}\left(0.1487\,\frac{u_{1m}}{U_\infty} + 0.05\,\frac{\omega}{\kappa}\right)\end{aligned} \tag{15}$$

$$\begin{aligned}\frac{\mathrm{Re}_1 - \mathrm{Re}_2 - 130}{\mathrm{Re}_\delta} &= \Bigg[0.375\left(\frac{u_{1m}}{U_\infty}\right)^2\\ &\quad + 0.7786\left(\frac{u_{1m}}{U_\infty}\,\frac{\omega}{\kappa}\right) + 0.7623\left(\frac{\omega}{\kappa}\right)^2\Bigg]\\ &\quad + \frac{\delta}{r^*}\Bigg[0.086\left(\frac{u_{1m}}{U_\infty}\right)^2\\ &\quad + 0.0850\left(\frac{u_{1m}}{U_\infty}\,\frac{\omega}{\kappa}\right) + 0.0402\left(\frac{\omega}{\kappa}\right)^2\Bigg]\end{aligned} \tag{16}$$

It must be repeated that the equations are valid for axisymmetric flow. In the case of plane flow, terms with the factor

$$\frac{y^*}{r} = \eta\,\frac{\delta}{r^*} \text{ with } r^* = r\Big/\sqrt{1 - \left(\frac{dr}{dx}\right)^2} \tag{17}$$

must be omitted.

With equations (12), (15), and (16) three equations are available including five parameters: Re_1, Re_2, Re_δ, u_{1m}/U_∞, and ω (respectively c_f); in the case of given Re_2 and H_{12}, the wall shear-stress coefficient can be determined. Furthermore, the boundary layer parameters δ and u_{1m}/U_∞, and thus the velocity distribution (equation (11)), can be computed.

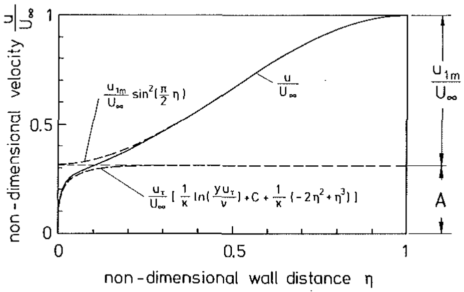

Fig. 2 Velocity profile of the turbulent boundary layer

Model-Specific Moment-of-Momentum Integral Equation

By using the velocity-profile model equation (11), the moment-of-momentum integral equation (8) can be transformed into a nondimensional form. Then, c_τ presents the nondimensional integral of turbulent shear stress across the boundary layer:

$$c_\tau = \int_{\eta=0}^{1} \frac{\tau}{\rho U_\infty^2}\left(1 + \eta\,\frac{\delta}{r^*}\right)d\eta \tag{18}$$

Momentum Balance

Figure 3 shows the left (LS) and right (RS) hand sides of the momentum integral equation balance for typical experiments compiled at the Stanford Conference [3]; at first, the term ϕ is not taken into account in this x-integrated equation (7). For experiments in accelerated flow, e.g., IDNR 1300 (identification number from [3]), the right-hand side exceeds the left one, whereas in constant pressure flow, e.g., IDNR 1400, LS and RS are equal.

In the case of positive pressure gradients, e.g., IDNR 2900 (plane) and 5000 (axisymmetric), a strong momentum imbalance can be recognized. In [3] the discrepancies in momentum balance were computed by Coles and Hirst for each flow. In the literature [3, 8, 12, 13] these discrepancies are attributed to lateral convergence or divergence of streamlines producing small deviations from the two dimensionality of the mean flow. In this investigation these effects are considered in the continuity equation (1) by using the term ϕ as nondimensional lateral width of flow. $\phi(x)$ is determined from measurements and the momentum integral equation (7), and in the following analysis it is assumed to be a known input.

However, it must be assumed that cross-flow effects are of importance for some of the included experiments, e.g., IDNR 1200 and 3500; these effects cannot be considered in this investigation. Besides, in the case of profiles with shape parameters $H_{12} \geq 2.5$ the normal boundary layer measuring technique fails in correct determination of mean velocity and shear-stress distribution near the wall. So, temporal backflow existing in this profile region could not be recognized and the values c_f and H_{12} obtained by measurements seem to be incorrect [14].

Finally, it must be mentioned that no agreement of model equation (11) in comparison with measured data is found for the profiles 3807 (separation), 5202, 5203, 5302, and 5303 (breakdown of the law of the wall equation (9) caused by strong pressure gradients). In these cases the friction law and the moment-of-momentum equation (19) fail to reflect boundary layer behavior.

$$
\begin{aligned}
c_\tau = {} & \delta \frac{d\ln U_\infty}{dx}\Bigg[\left(-0.2974\left(\frac{u_{1m}}{U_\infty}\right)^2+0.5948\left(\frac{u_{1m}}{U_\infty}\right)-0.3784\left(\frac{u_{1m}}{U_\infty}\frac{\omega}{\kappa}\right)+0.2000\left(\frac{\omega}{\kappa}\right)-0.1672\left(\frac{\omega}{\kappa}\right)^2\right)\\
&+\frac{\delta}{r^*}\left(-0.0827\left(\frac{u_{1m}}{U_\infty}\right)^2+0.2285\left(\frac{u_{1m}}{U_\infty}\right)-0.0556\left(\frac{u_{1m}}{U_\infty}\frac{\omega}{\kappa}\right)+0.0388\left(\frac{\omega}{\kappa}\right)-0.0162\left(\frac{\omega}{\kappa}\right)^2\right)\Bigg]\\
&+\delta\frac{d\ln\left(\frac{u_{1m}}{U_\infty}\right)}{dx}\Bigg[\left(-0.2974\left(\frac{u_{1m}}{U_\infty}\right)^2+0.1487\left(\frac{u_{1m}}{U_\infty}\right)-0.1324\left(\frac{u_{1m}}{U_\infty}\frac{\omega}{\kappa}\right)\right)\\
&+\frac{\delta}{r^*}\left(-0.0827\left(\frac{u_{1m}}{U_\infty}\right)^2+0.0653\left(\frac{u_{1m}}{U_\infty}\right)-0.0230\left(\frac{u_{1m}}{U_\infty}\frac{\omega}{\kappa}\right)\right)\Bigg]\\
&+\delta\frac{d\ln\left(\frac{\omega}{\kappa}\right)}{dx}\Bigg[\left(-0.2460\left(\frac{u_{1m}}{U_\infty}\frac{\omega}{\kappa}\right)+0.0500\left(\frac{\omega}{\kappa}\right)-0.1672\left(\frac{\omega}{\kappa}\right)^2\right)\\
&+\frac{\delta}{r^*}\left(-0.0326\left(\frac{u_{1m}}{U_\infty}\frac{\omega}{\kappa}\right)+0.0111\left(\frac{\omega}{\kappa}\right)-0.0162\left(\frac{\omega}{\kappa}\right)^2\right)\Bigg]\\
&+\delta\frac{d\ln(\delta\phi r)}{dx}\Bigg[\left(-0.2112\left(\frac{u_{1m}}{U_\infty}\right)^2+0.2974\left(\frac{u_{1m}}{U_\infty}\right)-0.2934\left(\frac{u_{1m}}{U_\infty}\frac{\omega}{\kappa}\right)+0.1000\left(\frac{\omega}{\kappa}\right)-0.1270\left(\frac{\omega}{\kappa}\right)^2\right)\\
&+\frac{\delta}{r^*}\left(-0.0527\left(\frac{u_{1m}}{U_\infty}\right)^2+0.0980\left(\frac{u_{1m}}{U_\infty}\right)-0.0376\left(\frac{u_{1m}}{U_\infty}\frac{\omega}{\kappa}\right)+0.0167\left(\frac{\omega}{\kappa}\right)-0.0107\left(\frac{\omega}{\kappa}\right)^2\right)\Bigg]\\
&+\delta\frac{d(\delta/r^*)}{dx}\Bigg[\left(-0.0527\left(\frac{u_{1m}}{U_\infty}\right)^2+0.0980\left(\frac{u_{1m}}{U_\infty}\right)-0.0376\left(\frac{u_{1m}}{U_\infty}\frac{\omega}{\kappa}\right)+0.0167\left(\frac{\omega}{\kappa}\right)-0.0107\left(\frac{\omega}{\kappa}\right)^2\right)\Bigg]
\end{aligned}
\tag{19}
$$

Integral of Turbulent Shear Stress

To obtain a closed set of equations for calculating the boundary layer development, a global assumption is required about the relationship of the shear-stress integral c_τ (equation (18)) to properties of the mean field. Investigations of the shear-stress integral were performed by Nash and Hicks [15], McDonald and Stoddart [5], and Granville (Nagel [16]), but no satisfactory formula was found to describe the streamwise behavior of c_τ in strong positive pressure gradients.

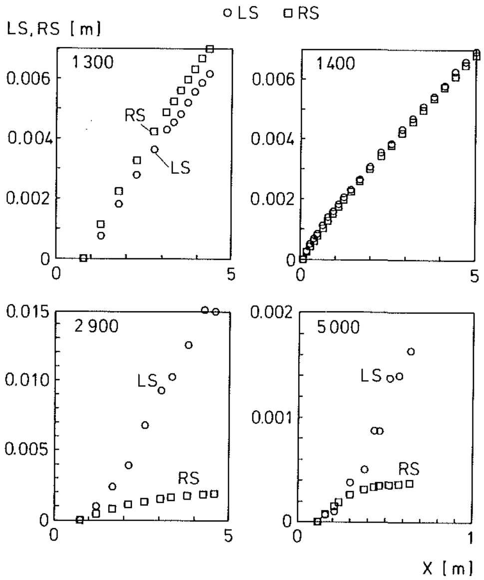

Fig. 3 Momentum integral equation balance

At first, in this study, equilibrium cases, i.e., boundary layers with nearly constant shape parameters H_{12} in the streamwise direction, are investigated. Measurements of the Reynolds shear-stress distribution performed by Bradshaw [17] and East and Sawyer [18] show that the maximum value of the nondimensional turbulent shear stress $\tau_{\max}/(\rho U_\infty^2)$ is only a function of H_{12} in the case of equilibrium (Fig. 4):

$$\frac{\tau_{\max}}{\rho U_\infty^2}=0.023\left(\frac{H_{12}-1}{H_{12}}\right)^2 \tag{20}$$

Theoretical and empirical investigations performed by McDonald and Stoddart [5] and in [8] indicate a relationship of the maximum value to the integral of shear stress across the layer for all cases of flow:

$$c_\tau \simeq 0.6\,\tau_{\max}/(\rho U_\infty^2) \tag{21}$$

Equations (20) and (21) result in formula (22) for the shear-stress integral of equilibrium boundary layers, suggested by Nash and Hicks [15]:

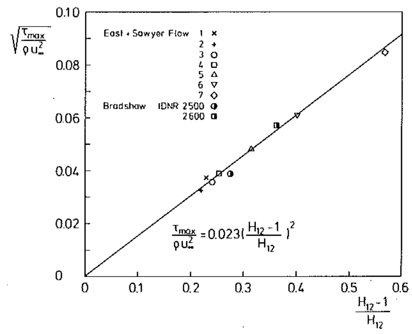

Fig. 4 Relationship of the maximum value of shear stress to the shape parameter H_{12} [18]

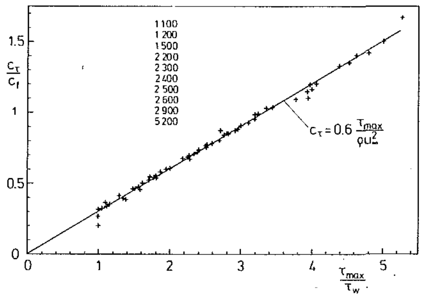

Fig. 5 Relationship of the maximum value to the integral of shear stress across the layer presented in [8]

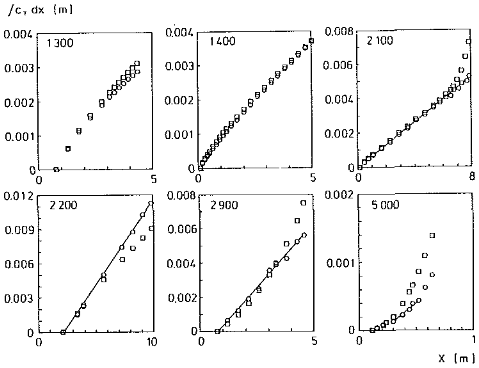

Fig. 6 Comparison of c_τ defined by equation (19) with $c_{\tau E}$ (equation (23)) in x-integrated form; ○ c_τ; □ $c_{\tau E}$

$$c_{\tau E} = 0.0125\left(\frac{H_{12}-1}{H_{12}}\right)^2 \tag{22}$$

This equation is in very good agreement with mixing-length assumptions.

In this investigation, the relationship is used in the following form:

$$c_{\tau E} = 0.0107\left(\frac{H_{12}-1}{H_{12}}\right)^2 \tag{23}$$

Figure 6 shows the shear-stress integral c_τ defined by the moment-of-momentum integral equation (19) in comparison with $c_{\tau E}$ (equation (23)), in x-integrated form.

In the case of accelerated flow (IDNR 1300 and first part of 2100) and constant pressure flow (IDNR 1400), the agreement is very good:

$$c_\tau = c_{\tau E} \tag{24}$$

For mild positive pressure gradients (first x stations of IDNR 2200, 2900, and 5000) good agreement is found, too.

For the case of strong positive pressure gradients, in Fig. 6 a proportionality of $\int c_\tau dx$ to x can be recognized. This means that the shear-stress integral c_τ is constant in the streamwise direction:

$$c_\tau = \text{const} \tag{25}$$

However, the constant is different for each flow. Equation (25) can be applied to describe the c_τ behavior of equilibrium flows (IDNR 2200) as well as of boundary layers with strong gradients of the shape parameter H_{12} (IDNR 2900).

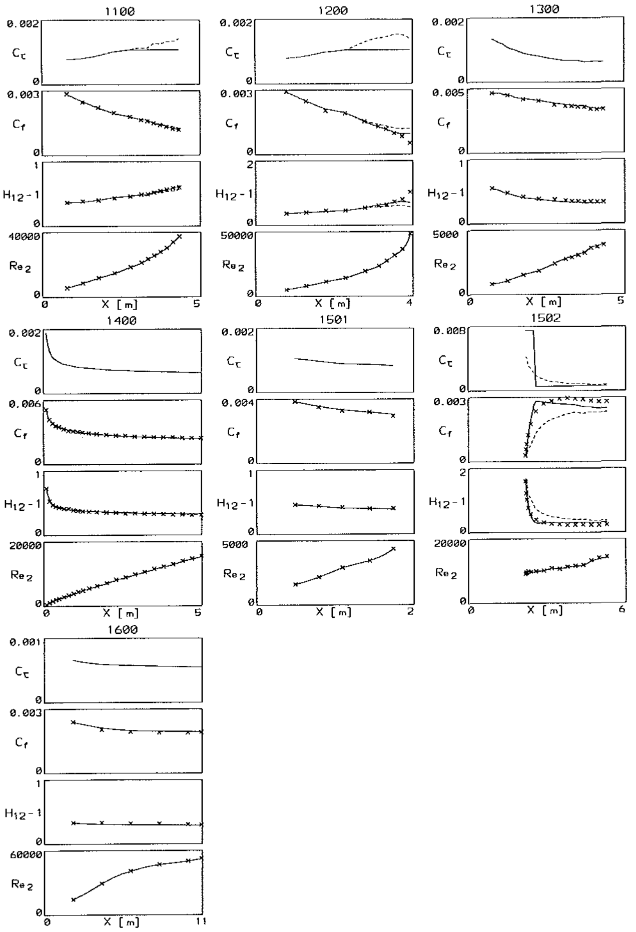

Fig. 7 Predictions of the turbulent boundary layer development: X data according to Coles and Hirst [3]; calculations including closure conditions: ----- $c_\tau = c_{\tau E} = 0.0107\,((H_{12}-1)/H_{12})^2$; ______ according to the plotted c_τ distribution: $c_\tau = c_{\tau E} = 0.0107\,((H_{12}-1)/H_{12})^2$; or c_τ = const (constant adjusted in test calculations; different for each flow)

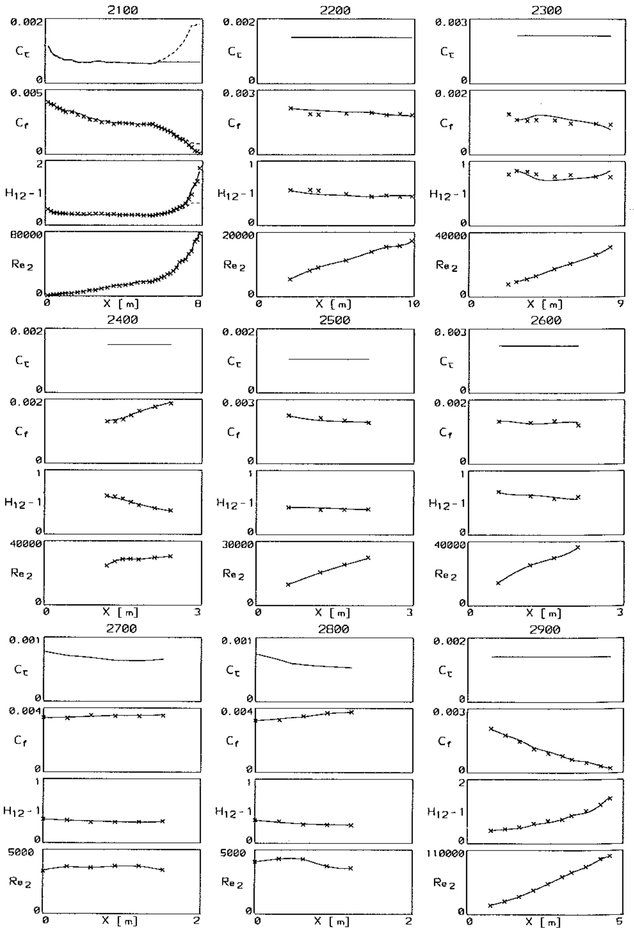

Fig. 7 (cont.)

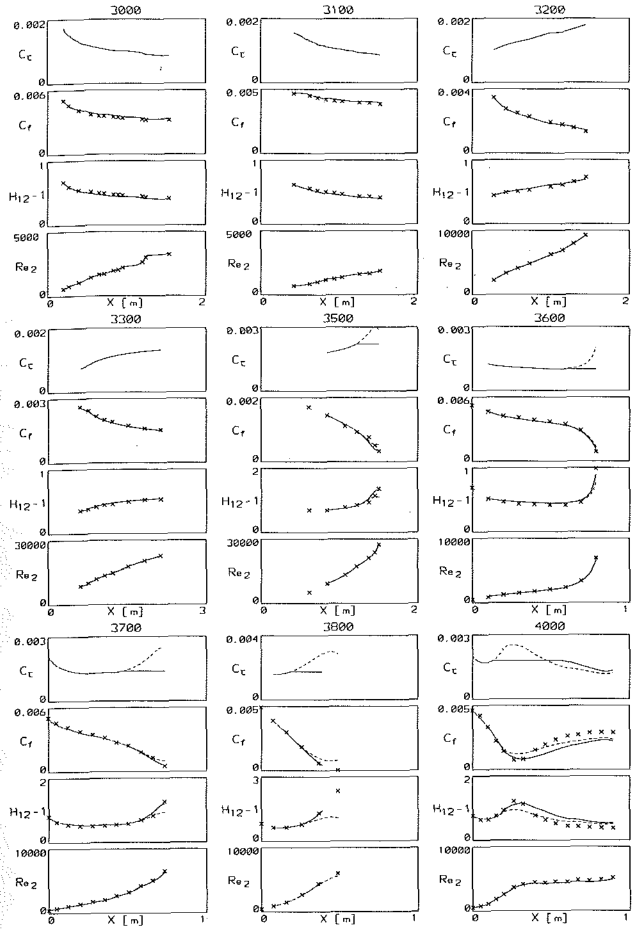

Fig. 7 (cont.)

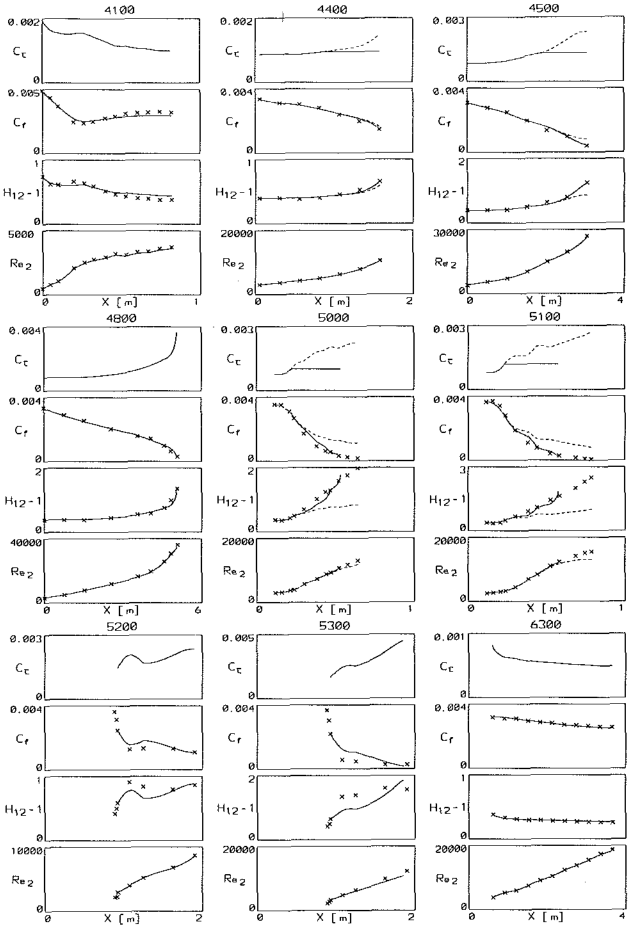

Fig. 7 (cont.)

For flows in rising (mild to strong) positive pressure gradients, c_τ can be defined by equation (24) until it reaches a maximum value; from this point on the shear-stress integral is constant. In case of relaxing flow ($dH_{12}/dx < 0$), c_τ is constant to the end of the relaxation process.

By means of the measurements compiled at the Stanford Conference, it can be assumed that the shear-stress integral c_τ can be described by only two basic assumptions, equation (24) or (25). However, an exact criterion for the change from $c_\tau = c_{\tau E}$ to c_τ = const for flows in positive pressure gradients could not be found. It can be expected that further investigations including the moment-of-momentum integral equation will solve this problem and improve the knowledge on turbulent boundary layer behavior.

Predictions

In Fig. 7 predictions are presented for the 33 experiments compiled at the 1968 Stanford Conference [3]. The calculations are based on the momentum and moment-of-momentum integral equations (7) and (19), the friction law equations (12), (15), and (16), and the closure equation (24) or (25). The free-stream velocity $U_\infty(x)$ and the nondimensional lateral width $\phi(x)$ as well as the values H_{12} and Re_2 of the starting point are assumed to be known input data.

The calculations are performed using the following closure condition (in Fig. 7, solid line): In the case of accelerated flow or constant pressure flow, c_τ is defined by equation (24). For positive pressure gradients, the calculations are performed using the shear-stress integral c_τ to be constant in streamwise direction. However, in some cases, c_τ is described by equation (24) as far as it is equal to a maximum value, and with this value of c_τ the calculation is continued. The different cases are distinguishable in Fig. 7 by the plotted c_τ distributions. For the latter cases the calculations are repeated with the condition $c_\tau = c_{\tau E}$ (Fig. 7, dashed line).

The maximum and/or constant value of the shear-stress integral is also assumed to be a known input, and it was determined in test calculations to get agreeable predictions of the boundary layer parameters. Figure 7 shows the streamwise behavior of c_τ, and the predicted parameters Re_2, H_{12}, and c_f in comparison with measured data.

Summary and Conclusions

In the present study an integral method to predict turbulent boundary layer development is presented. The method is based on the momentum and moment-of-momentum integral equations and a friction law. The required closure equation, i.e., the integral of turbulent shear stress across the layer, can be specified by two basic assumptions:

(*a*) In the case of negative, zero, or mild positive pressure gradients, the shear-stress integral depends on the profile shape parameter. This means that only local parameters of the profile are sufficient to describe the development of c_τ.

(*b*) In the case of strong positive pressure gradients, including high shape parameters and high streamwise gradients of H_{12}, the turbulent shear-stress integral is constant.

By means of the compiled data of the 1968 Stanford Conference, it is shown that these assumptions yield very agreeable predictions of turbulent boundary layer development. It can be assumed that further investigations including the moment-of-momentum integral equation will improve the knowledge on the turbulent boundary layer behavior more reliably and clearly.

Acknowledgments

The authors wish to thank Deutsche Forschungsgemeinschaft (DFG) for supporting the work described in this paper.

References

1 Kline, S. J., Morkovin, M. V., Sovran, G., and Cockrell, D. J., "Computations of Turbulent Boundary Layers," *Methods, Predictions, Evaluations and Flow Structure*, 1968 AFOSR-IFP Stanford Conference, Vol. I, Stanford University, 1969.

2 Singhal, A. K., and Spalding, D. B., "Predictions of Two-Dimensional Boundary Layers With the Aid of the k-ϵ Model of Turbulence," *Computer Methods in Applied Mechanics and Engineering*, Vol. 25, 1981, pp. 365-383.

3 Coles, D. E., and Hirst, E. A., "Computation of Turbulent Boundary Layers," *Compiled Data*, 1968 AFOSR-IFP Stanford Conference Vol. II, Stanford University, 1969.

4 Rotta, J. C., "Turbulent Boundary Layers in Incompressible Flow," *Progress in Aero. Sciences*, Vol. 2, 1962, pp. 1-219.

5 McDonald, H., and Stoddart, J. A. P., "On the Development of the Incompressible Turbulent Boundary Layer," Aero Res. Coun. R&M 3484, 1967.

6 Mayer, M., "Theoretische und experimentelle Untersuchungen über die Zerfaserung thermoplastischer Stoffe in Blasdüsen," Diss. TH Karlsruhe, W. Germany, 1964.

7 Zwarts, F. J., "Turbulent Boundary Layer Predictions Using a Dissipation Integral Method," *Methods, Predictions, Evaluations and Flow Structure*, 1968 AFOSR-IFP Stanford Conference, Vol. I, pp. 154-169.

8 Göing, M., "Untersuchungen über das Impulsmoment turbulenter Grenzschichten und Messungen im Diffusor eines Axialverdichters," Diss. TH Darmstadt, W. Germany, 1985.

9 Coles, D. E., "The Law of the Wall in Turbulent Shear Flow," *50 Jahre Grenzschichtforschung*, F. Vieweg und Sohn, Braunschweig, 1955, pp. 153-163.

10 Coles, D. E., "The Law of the Wake in the Turbulent Boundary Layer," *J. Fluid Mech.*, Vol. 1, 1956, pp. 191-226.

11 Pfeil, H., Amberg, T., and Müller, T., TH Darmstadt, W. Germany, unpublished investigations on turbulent boundary layer data, 1985.

12 Rotta, J. C., *Turbulente Strömungen*, Verlag B.G. Teubner, Stuttgart, 1972.

13 Ludwieg, H., and Tillmann, W., "Untersuchungen über die Wandschubspannung in turbulenten Reibungsschichten," *Ing. Arch.*, Vol. 17, 1949, pp. 288-299.

14 Dengel, P., and Vagt, J.-D., "A Comparison Between Hot-Wire and Pulsed-Wire Measurements in Turbulent Flows," *Fourth Symposium on Turbulent Shear Flow*, Karlsruhe, 1983, pp. 15.12-15.16.

15 Nash, J. F., and Hicks, J. G., "An Integral Method Including the Effect of Upstream History on the Turbulent Shear Stress," *Methods, Predictions, Evaluations and Flow Structure*, 1968 AFOSR-IFP Stanford Conference, Vol. I, pp. 37-35.

16 Nagel, A. L., "A Modified Granville Moment of Momentum Method," *Methods, Predictions, Evaluations and Flow Structure*, 1968 AFOSR-IFP Stanford Conference, Vol. I, pp. 99-104.

17 Bradshaw, P., "The Turbulence Structure of Equilibrium Boundary Layers," *J. Fluid Mech.*, Vol. 29, 1967, pp. 625-645.

18 East, L. F., and Sawyer, W. G., "An Investigation of the Structure of Equilibrium Turbulent Boundary Layers," AGARD CP-217, Paper No. 6, 1979.

H. Pfeil
Professor.

M. Göing
Research Engineer.

Fachgebiet für Thermische Turbomaschinen,
Technische Hochschule Darmstadt,
Darmstadt, Federal Republic of Germany

Measurements of the Turbulent Boundary Layer in the Diffuser Behind an Axial Compressor

This paper presents boundary layer measurements in a diffuser behind a one-stage axial compressor for the case of nearly axial outlet flow direction from the blades. According to the results, three-dimensional effects caused by the compressor blading have a great influence on the character and development of the turbulent boundary layer and must be included in methods to predict the diffuser flow.

Introduction

The fluid mechanical analysis of diffusers behind turbomachines is mainly based on boundary layer calculations for the two-dimensional case [1]. Three-dimensional effects caused by the turbomachine blading are ignored in these predictions of diffuser flow.

In the present study, boundary layer measurements at the outer wall of an annular diffuser behind a one-stage axial compressor are presented to show if the distributions of mean velocities and turbulence intensities can be assumed to be two-dimensional boundary layer distributions or if they are deformed by secondary effects at the blade tips and wake flows behind the stator blades. For the case of deformation, the question is if important boundary layer parameters, e.g., the streamwise wall shear-stress distribution, can still be determined correctly using a two-dimensional procedure.

For the experiments, an axial outlet flow direction from the blades was nearly realized. The development of the turbulent boundary layer was measured at two streamwise lines of traverse positions to obtain information about the axisymmetry of the diffuser flow [2].

Axial Compressor and Diffuser

The cross section of the one-stage axial compressor is shown in Fig. 1; the important geometric data can be taken from this figure. Inlet guide vanes were not used for these investigations. The twisted blades are designed in free vortex and by a two-dimensional design method according to Lieblein [3], and are based on NACA-65-series airfoil shapes. The compressor was designed as follows: 22 rotor and 34 stator blades, shaft power $P_w = 120$ kW, and specific enthalpy increase $\Delta h = 2.5$ kJ/kg. For the speed of rotor $n = 2000$ rpm, the volume flow can be varied from $\dot{V} = 17$ to 30 m^3/s. Camber and stagger distributions, blade thicknesses and chord lengths of the rotor and stator profiles are presented in Tables 1 and 2. More details of design are given in [4]. In [4] an investigation about the influence of the stator blade number and blade chord angle on the performance of this compressor shows that the best performance can be obtained with 25 stator blades and an axial outlet flow direction from the stator blades for a mean volume flow rate.

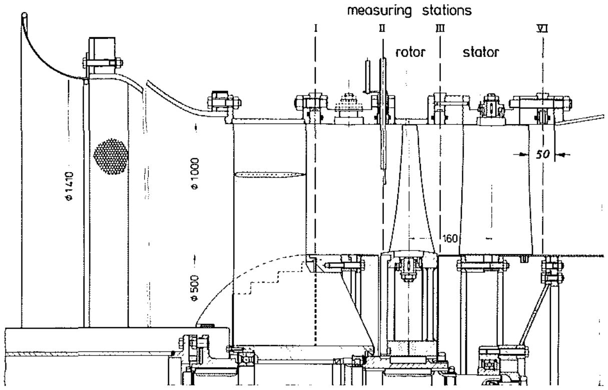

Fig. 1 Cross section of the single-stage axial compressor

In this investigation, diffuser boundary layer measurements are presented for two cases: case *a*: 22 rotor and 25 stator blades; case *b*: 22 rotor and 21 stator blades. For both cases, the stator blade chord angles were restaggered to obtain an axial outlet flow direction for a mean volume flow rate: case *a*: $\gamma_{25} = \gamma_{34} - 6$ deg; case *b*: $\gamma_{21} = \gamma_{34} - 12$ deg. Behind the compressor the air passes through the diffuser, the settling chamber with honeycomb and screens, and the mass flow measuring section.

The diffuser with inner hub was installed very carefully to realize axisymmetric flow. The diffuser is 1 m long (axial length) with an area ratio $AR = 2$ (Fig. 2).

Compressor Performance

To be able to relate the measured diffuser data to a point on the compressor map, plots of total pressure coefficient and volume flow coefficient are shown in Figs. 3 and 4 for case *a*. The measurements were performed using constant speed of rotation ($n = 2000$ rpm; $u_t = 105$ m/s, $r_t = 0.5$ m); the rotor blade chord angles were varied in 4-deg steps:

Contributed by the Gas Turbine Division of The American Society of Mechanical Engineers and presented at the 31st International Gas Turbine Conference and Exhibit, Düsseldorf, Federal Republic of Germany, June 8-12, 1986. Manuscript received at ASME Headquarters February 14, 1986. Paper No. 86-GT-233.

Table 1 Profile data of rotor (22 rotor blades)

r, mm	NACA-65 identification	γ, deg	c, mm	σ
250 (hub)	65-(27) 12	26.2	100.0	1.40
265	65-(24) 11	32.1	98.5	1.30
280	65-(22) 11	37.4	97.0	1.21
300	65-(19) 10	43.1	95.0	1.11
315	65-(17) 10	46.9	93.5	1.04
335	65-(15) 09	50.9	91.5	0.96
355	65-(13) 09	54.2	89.5	0.88
375	65-(12) 08	57.0	87.5	0.82
400	65-(12) 08	60.0	85.0	0.74
425	65-(11) 07	62.4	82.5	0.68
450	65-(11) 07	64.4	80.0	0.62
475	65-(12) 06	66.2	77.5	0.57
500 (tip)	65-(14) 06	67.6	75.0	0.53

Table 2 Profile data of stator (34 stator blades)

r, mm	NACA-65 identification	γ, deg	c, mm	σ
250 (hub)	65-(19) 10	16.5	149.7	3.24
265	65-(19) 10	16.5	147.2	3.00
280	65-(19) 10	16.5	144.9	2.80
300	65-(19) 10	16.4	142.4	2.57
315	65-(18) 10	16.3	140.8	2.42
335	65-(18) 10	16.0	139.0	2.25
355	65-(18) 10	15.7	137.5	2.10
375	65-(18) 10	15.4	136.2	1.97
400	65-(17) 10	14.9	134.8	1.82
425	65-(17) 10	14.5	133.6	1.70
450	65-(16) 10	14.1	132.6	1.60
475	65-(16) 10	13.6	131.8	1.50
500 (tip)	65-(16) 10	13.1	131.1	1.42

$$\gamma_{\text{rotor}} = \gamma_{\text{Table 1}} + \Delta\gamma_{\text{performance map}}$$

In Fig. 3 the performance for the compressor stage is shown based on measurements at the trailing edge of the stator. Figure 4 shows the performance for the compressor stage plus diffuser. Figure 5 shows the swirl angle distributions (averaged values for four circumferential positions, measured by five-hole probes) behind the stator blades for $r = 375$ mm. Compressor performance maps for case b are given in [4].

Diffuser Pressure Recovery

Figure 6 shows the performance chart for annular diffusers given by Sovran and Klomp [5]. With $AR = 2$ and $\bar{L}/\Delta R_1 = 4.04$, the test diffuser falls just above the C_p^* line; the location on this map indicates a pressure recovery coefficient $C_p = 0.56$.

In comparison to this indicated value, Fig. 7 shows the measured pressure recovery distributions for case a, which can be related to the compressor maps, Figs. 3 and 4, and to the distributions of swirl angle α, Fig. 5. For the case of zero diffuser inlet swirl, good agreement is found between the indicated and measured C_p values. This result is in accordance to measurements of Adenubi [6], who used a 10-deg test diffuser with identical values of area ratio AR and nondimensional diffuser length $\bar{L}/\Delta R_1$. The differences between indicated and measured C_p values for the other cases must probably be attributed to the nonzero diffuser inlet swirl, high values of inlet blockage and partially stalled diffuser flow for small volume flow coefficients according to Figs. 10 and 11.

Nomenclature

A = cross-sectional area
AR = area ratio = A_2/A_1
c = blade chord length
$\mathbf{c}$ = mean velocity vector, Fig. 8
c_{ax} = mean velocity component of $\mathbf{c}$ in axial direction, Fig. 8
C = logarithmic law constant in equations (1) and (2)
C_p = pressure-recovery coefficient = $(\bar{p}_2 - \bar{p}_1)/\bar{q}_1$
Δh = specific total enthalpy increase
H_{12} = profile shape parameter = δ_1/δ_2
L = diffuser wall length
$\bar{L}$ = averaged wall length for annular diffusers
$\dot{m}$ = mass flow
M = Mach number based on mass-averaged velocity in the diffuser inlet
n = speed of rotation
p = static pressure
p_o = atmospheric pressure
P_w = shaft power
P_r = bearing losses
$\bar{q}$ = dynamic pressure based on mass-averaged velocity = $\rho/2\ \bar{c}_{ax}^2$
r = geometric radius of diffuser, Fig. 8
r_t = radius of blade tip
ΔR = annulus height = $(r_o - r_i)$
Re = Reynolds number based on mass-averaged velocity in the diffuser inlet = $\bar{c}_{ax_1}\ \Delta R_1/\nu$
s = direction parallel to diffuser hub, Fig. 8
u, v, w = mean velocity components of $\mathbf{c}$ in x, y, z directions, Fig. 8
u', v' = components of velocity fluctuations
u^+ = nondimensional velocity component = u/u_τ
u_t = rotor speed at blade tip
u_τ = friction velocity = $\sqrt{\tau_w/\rho}$
U_∞ = free-stream velocity at outer edge of the boundary layer
V = volume flow
x, y, z = space coordinates, Fig. 8
$y_{\max}$ = maximum value of transverse distance
y^+ = nondimensional wall distance = yu_τ/ν
α = circumferential (swirl) angle of flow, Fig. 8 = arctan (w/u)
$\tilde{\gamma}$ = radial angle of flow, Fig. 8 = arctan $(v/u \cos\alpha)$
γ = blade chord angle, angle between blade chord and axial direction
$\Delta\gamma$ = difference between the realized γ and γ of design point
δ = boundary layer thickness
δ_1 = displacement thickness
δ_2 = momentum thickness
η_i = efficiency = $(\dot{m}\ \Delta h)/(P_w - P_r)$
κ = logarithmic law constant in equations (1) and (2)
ν = kinematic viscosity
ρ = density
σ = solidity, ratio of chord to spacing
τ_w = wall shear stress
ϕ = volume flow coefficient = $\dot{V}/(u_t\ \pi r_t^2)$
ψ_t = total pressure coefficient = $\Delta h/(u_t^2/2)$

Subscripts and Symbols

rotor = rotor blades
t = blade tip
i = diffuser inner wall (hub)
o = diffuser outer wall
1 = diffuser inlet
2 = diffuser outlet
$\bar{\ }$ = time-mean-averaged value (superscript is used only for fluctuation components)
$\bar{\ }$ = mass-averaged

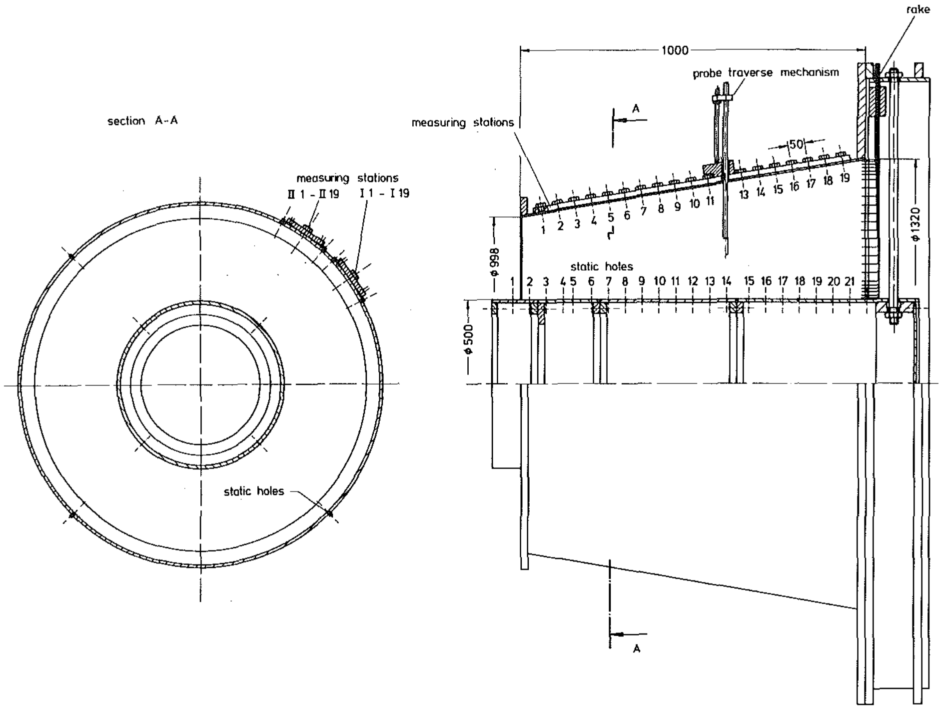

Fig. 2 Annular diffuser with measuring stations

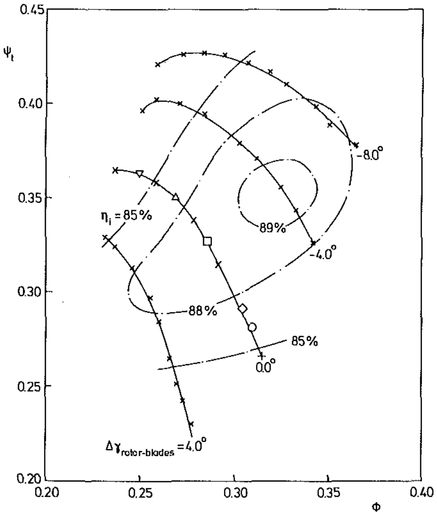

Fig. 3 Compressor performance map (case *a*)

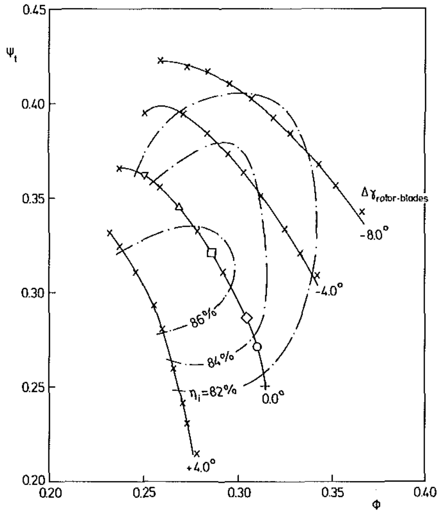

Fig. 4 Compressor performance map (case *a*), stage plus diffuser

Experimental Arrangement

In the inlet and outlet of the diffuser, rakes are installed to determine the axial velocity distribution. The boundary layers presented in this paper were measured at two streamwise lines of traverse positions at the outer diffuser wall. Each line (Fig. 2) includes 19 probe positions disposed in 50-mm intervals in the flow direction; the diffuser flow can be measured normal to the outer wall or normal to the inner hub. At each probe position, there are static taps in the diffuser outer wall (seven circumferential positions, Fig. 2) and hub (four circumferential positions, Fig. 2) to determine the streamwise and circumferential distribution of the static pressure. Figure 8 shows a schematic of the diffuser presenting the coordinate system for boundary layer measurements normal to the outer diffuser wall. The measurements were performed with five-hole probes, single and x hot-wire probes to a maximum value of

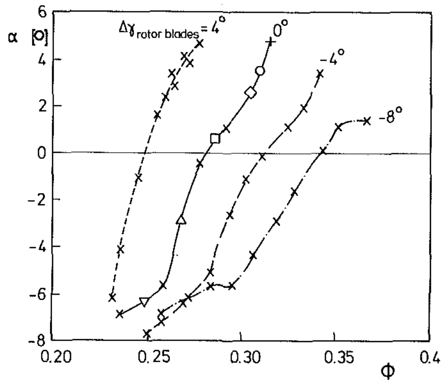

Fig. 5 Distributions of swirl angle α behind the stator blades at 50 percent of passage height (case *a*)

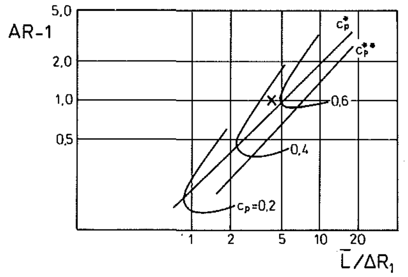

Fig. 6 Performance chart given by Sovran and Klomp [5]

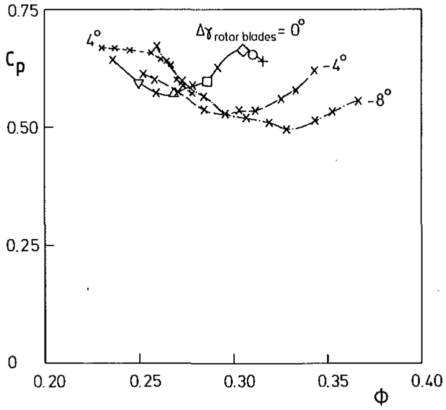

Fig. 7 Pressure recovery coefficients (case *a*)

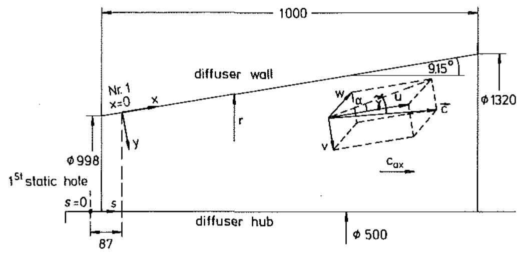

Fig. 8 Coordinate system for the measurements normal to the outer diffuser wall; important geometric data of the diffuser

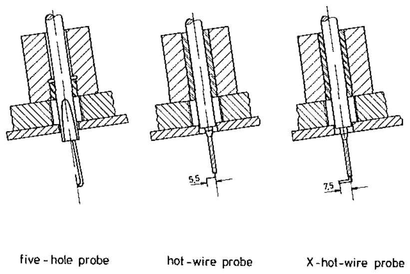

Fig. 9 Probe installation at outer diffuser wall

wall distance y_{max}; in Fig. 9 the installation of the probes at the outer wall is shown.

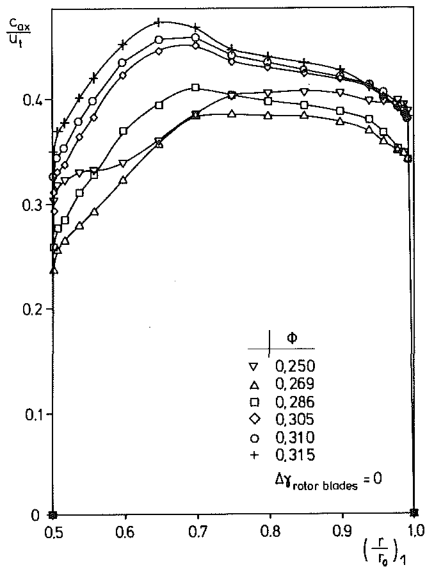

Fig. 10 Axial velocity distributions in the diffuser inlet as a function of the volume flow coefficient ϕ (case *a*)

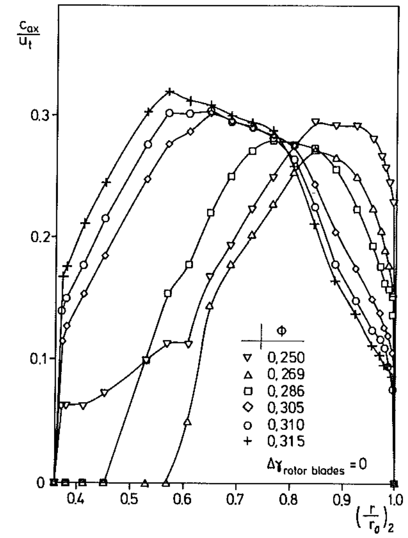

Fig. 11 Axial velocity distributions in the diffuser outlet as a function of the volume flow coefficient ϕ (case *a*)

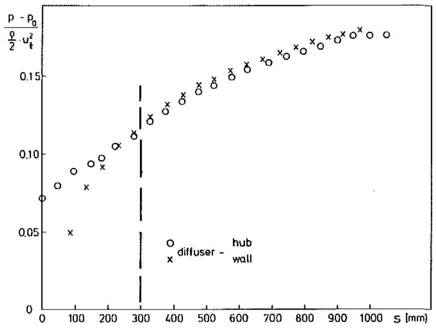

Fig. 12 Pressure distribution at diffuser wall and hub (case *a*: ϕ = 0.310, $\Delta\gamma_{rotor}$ = 0 deg)

Boundary Layer Measurements (Case *a*)

The boundary layer measurements were performed for the case of 22 rotor and 25 stator blades, and the speed of rotor n = 2000 rpm. In Figs. 10 and 11, the axial velocity distributions in the inlet and outlet of the diffuser are shown for one circumferential position downstream between two stator blades as a function of the nondimensional volume flow coefficient ϕ. The profiles can be related to the $\Delta\gamma_{rotor}$ = 0 deg line on the compressor maps, Figs. 3 and 4, the swirl angle distributions, Fig. 5, and the pressure-recovery map of the diffuser, Fig. 7.

In the case of small volume flow, profiles with high shape parameters H_{12} exist near the inner hub because of high blade

Table 3 Measurements for case *a*

- 25 stator blades
- $\Delta\gamma_{\text{rotor}} = 0$ deg
- $n = 2000$ rpm
- $\phi = 0.310$
- $M = 0.13$
- $Re = 6.9 \times 10^5$
- measurements normal to the outer diffuser wall to a maximum wall distance $y_{\max} = 210$ mm
- diffuser: $C_p = 0.65$

loading. In the diffuser outlet, separation of flow can be recognized in that region; for the profile with the smallest mass flow (▽), there is backflow near the inner hub, which is not indicated by the pitot probe. In the case of high mass flow, no separation can be noticed, but the profiles have high boundary layer thicknesses and shape parameters at the outer wall of the diffuser outlet. In this range of mass flow (symbol o in Figs. 3, 4, 5, 7, 10, and 11), the boundary layer measurements were performed with the Reynolds number in the diffuser inlet $Re = 6.9 \times 10^5$ and the Mach number $M = 0.13$.

In Fig. 12 the distribution of static pressure at the outer diffuser wall and inner hub is shown. The pressure is identical for circumferential positions, and from $s = 300$ mm it is equal at wall and hub; five-hole probe measurements confirm that the static pressure is almost constant across the annulus height normal to the hub.

The boundary layer measurements were performed at one line of traverse positions in the wake region behind a stator blade (identification numbers: I1–I19), and another line in the downstream region between two stator blades (II1–II19). Positions with equivalent identification numbers (e.g., I12 and II12) have the same streamwise distance x from the blading, and the axisymmetry of diffuser flow can be examined for the nearly realized axial outlet flow direction from the blades.

To show the repeatability, all measurements were performed twice. In Table 3, the conditions of the following boundary layer measurements are summarized.

Velocity Profiles

The velocity distribution of the turbulent boundary layer near the wall can be described by Spalding's law of the wall [7]

$$y^+ = u^+ + e^{-\kappa C}\left(e^{u^+\kappa} - 1 - u^+\kappa - \frac{(u^+\kappa)^2}{2!} - \frac{(u^+\kappa)^3}{3!}\right) \quad (1)$$

This formula includes the logarithmic law for $y^+ > 50$

$$u^+ = \frac{1}{\kappa}\ln y^+ + C \quad (2)$$

with the constants according to Coles [8]: $\kappa = 0.41$ and $C = 5.0$.

Boundary layer measurements compiled at the 1968 Stanford Conference [8] show that equation (2) is valid in case of axisymmetry, too. The friction velocity u_τ can be determined by a fitting operation of measured profile data with the logarithmic law of the wall.

In Fig. 13 the streamwise development of u_τ is shown for the boundary layers in the wake region behind a stator blade at the outer diffuser wall (positions I2–I18). The agreement between u_τ values determined by different profile measuring techniques is very good to $x = 650$ mm; the skin friction is decreasing. At the last profiles, the five-hole probe measurements indicate smaller values of u_τ, probably caused by the relatively large size of the probe tip measuring in flow near separation. In Figs. 14 and 15 the profiles of the positions I12 and I16 are presented; the velocity u and the wall distance y are related to u_τ according to single hot-wire measurements.

For profile I12 the agreement between different measurements is very good, while differences of profile data near the wall exist for position I16.

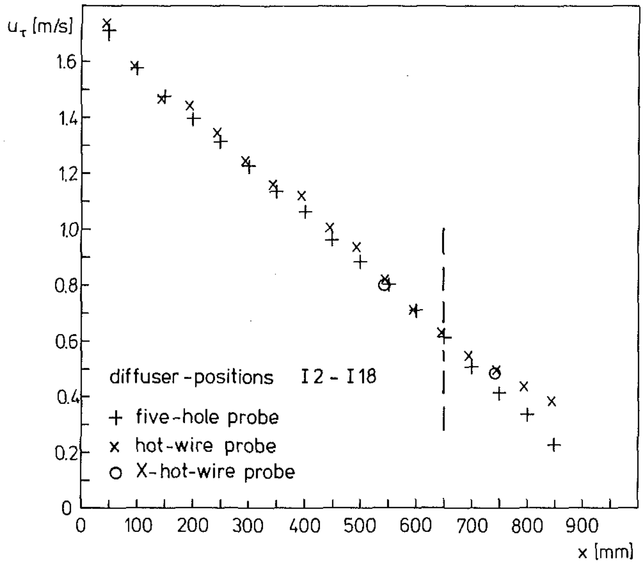

Fig. 13 Distribution of the friction velocity u_τ (case *a*)

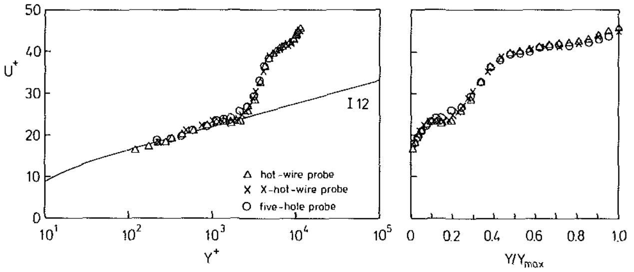

Fig. 14 Velocity distribution of position I12 (case *a*, $y_{\max} = 210$ mm)

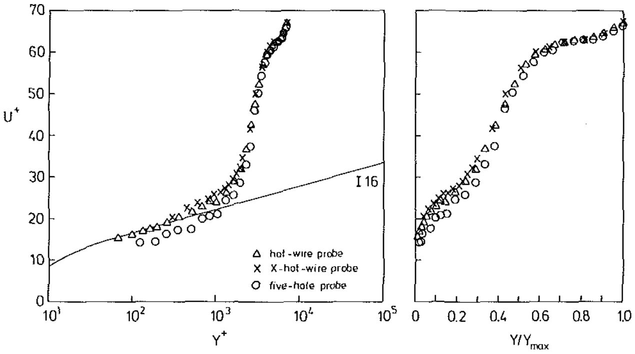

Fig. 15 Velocity distribution of position I16 (case *a*, $y_{\max} = 210$ mm)

In Fig. 16 the streamwise development of the velocity profiles (positions I2–I18) is shown. Caused by the unfavorable diffuser inlet profile (Fig. 10), the velocity u is increasing at the outer edge of the boundary layer; therefore, it is difficult to determine the free-stream velocity U_∞, the displacement thickness δ_1, the momentum thickness δ_2, and a model-dependent boundary layer thickness δ, and thus the velocity distributions can not be described by a profile model for turbulent boundary layers, e.g., Coles' model [8]. In [9] a reduction method for internal flows is presented to determine these unknown boundary layer parameters based on Coles' velocity profile family; because of abnormalities at the middle profile region ($y^+ \simeq 2 \times 10^3$ in Fig. 16), this procedure can not be used for the presented boundary layer measurements.

Good agreement is found between measured profile data

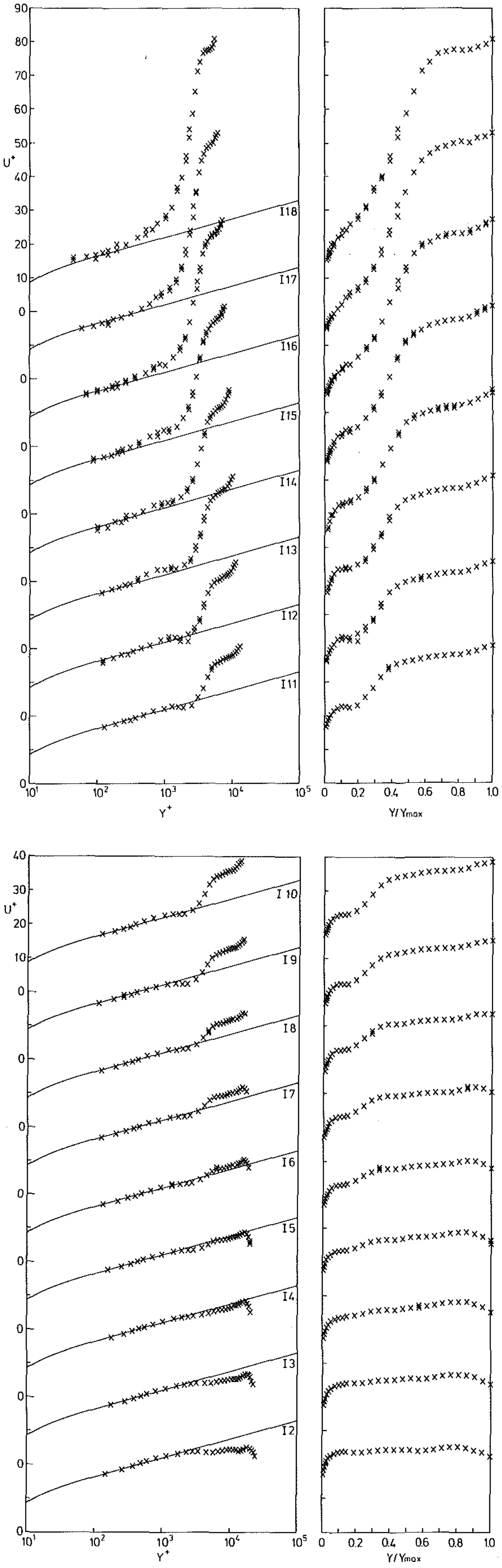

Fig. 16 Velocity profiles of the boundary layers measured in the wake region behind a stator blade at the outer diffuser wall (single hot-wire measurements, case *a*, y_{max} = 210 mm)

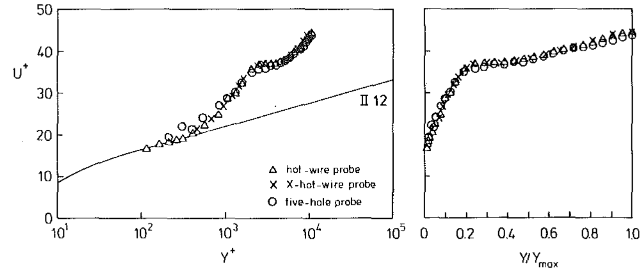

Fig. 17 Velocity distribution of position II12 (case *a*, y_{max} = 210 mm)

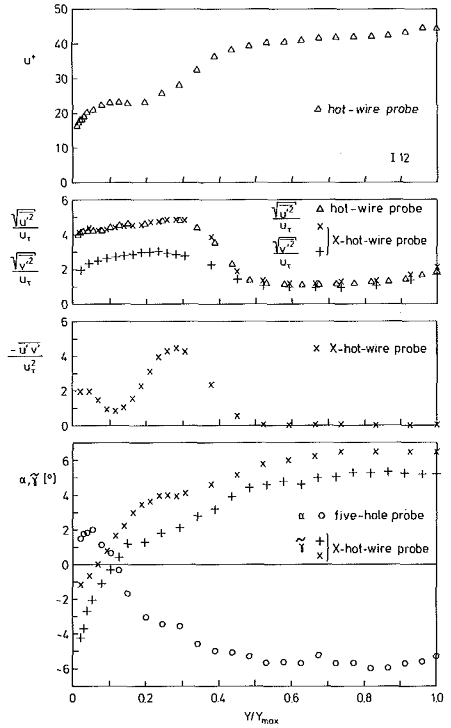

Fig. 18 Experimentally determined distributions (position I12, case *a*, y_{max} = 210 mm)

near the wall and the logarithmic law equation (2); from measuring station I6 an increasing outer profile region (law of the wake) can be noticed. At the positions I5–I13 a region with $\partial u/\partial y \leq 0$ exists ($y^+ \simeq 2 \times 10^3$). In accordance with measurements by East and Hoxey [10], this behavior is an indicator for three-dimensional turbulent boundary flow including strong cross-flow effects. It is remarkable that this important profile abnormality can not be recognized by the u distributions measured by five-hole probes (Fig. 14), probably because of strong velocity fluctuations in that region (Fig. 18) [11].

The streamwise development of the friction velocity for the profiles in the downstream region between two stator blades (II2–II18) is identical to the development measured by hot wire in Fig. 13. As an example, Fig. 17 presents the velocity profile II12. u_τ and the velocity distribution outside the boundary layer are equal to the values of profile I12, but the boundary layer thickness and the shape parameter of profile II12 are relatively small.

Distributions of Reynolds' Stress and Cross-Flow Component

In Figs. 18 and 19 the distributions of mean velocity u, turbulence intensities $\overline{u'^2}$ and $\overline{v'^2}$, Reynolds' stress $-\overline{u'v'}$, and

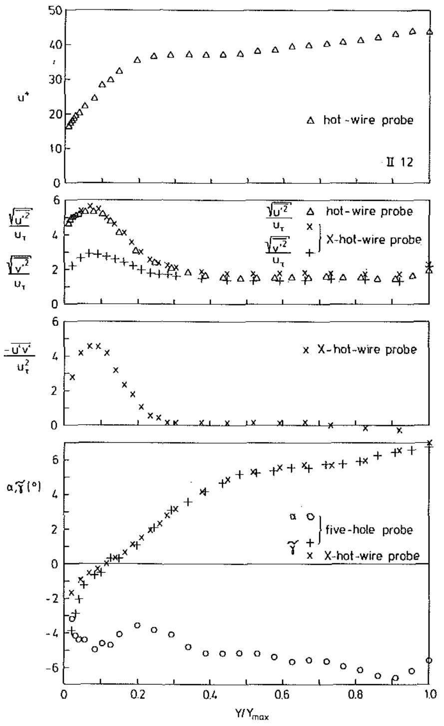

Fig. 19 Experimentally determined distributions (position II12, case *a*, y_{max} = 210 mm)

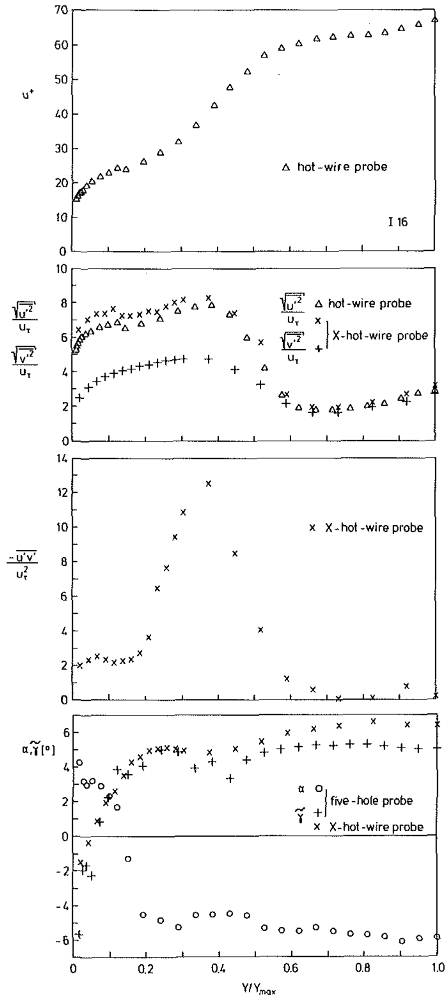

Fig. 20 Experimentally determined distributions (position I16, case *a*, y_{max} = 210 mm)

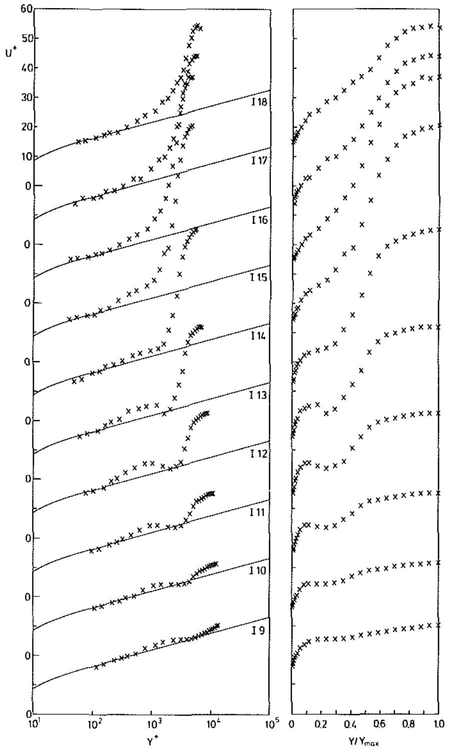

Fig. 21 Velocity profiles (positions I9–I18, case *b*, y_{max} = 170 mm)

the circumferential (swirl) and radial angles α and $\tilde{\gamma}$ are presented as a function of wall distance for the typical measuring positions I12 and II12. The velocities are related to the friction velocity u_τ.

In the downstream region between two stator blades, there are distributions of u, $\overline{u'^2}$, $\overline{v'^2}$, and $-\overline{u'v'}$ with two-dimensional characteristics (Fig. 19). The circumferential (swirl) angle α, a criterion for the cross-flow component w parallel to the wall, is small and nearly constant across the boundary layer.

In the wake region behind a stator blade (Fig. 18), there is three-dimensional flow including strong y gradients of the cross-flow component; the angle α is changing rapidly near the wall. It is remarkable that the turbulence intensities show a wide maximum across the layer, and that $-\overline{u'v'}$ has a local minimum near the wall followed by a strong increase in the region $\partial u/\partial y \leq 0$. Downstream (position I16 in Fig. 20), this behavior and the high y gradients of the cross-flow component w near the wall can also be recognized.

Boundary Layer Measurements (Case *b*)

These measurements were performed under almost unchanged conditions (Table 4). The velocity distributions of the boundary layers at the outer diffuser wall in the wake region behind a stator blade (I9–I18) are shown in Fig. 21. In this case of high blade loading, the indications of three-dimensional turbulent boundary flow, i.e., the middle profile regions with $\partial u/\partial y \leq 0$, become apparent more clearly. The boundary layers at the traverse line in the downstream region between two stator blades show two-dimensional characteristics again.

In Fig. 22 the friction velocity development of the profiles I9–I18 is shown. The skin friction is decreasing, but is increasing for the last three profiles. According to profiles I16–I18 in Fig. 21, it must be assumed that separation of flow exists at the inner diffuser hub, and that this region of separation exer-

Table 4 Measurements for case *b*

- 21 stator blades
- $\Delta\gamma_{rotor} = 0$ deg
- $n = 2000$ rpm
- $\phi = 0.305$
- $M = 0.13$
- $Re = 6.8 \times 10^5$
- measurements normal to the outer diffuser wall to a maximum wall distance $y_{max} = 170$ mm
- diffuser: $C_p = 0.69$

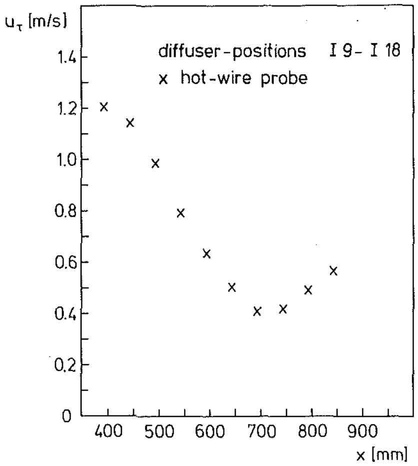

Fig. 22 Distribution of the friction velocity (positions I9–I18, case *b*)

cises an influence on the boundary layer development at the outer wall.

Summary and Conclusions

The measurements presented in this paper were performed particularly to show the character of turbulent boundary layers in a diffuser behind a turbomachine. In literature, there are many papers on measurements describing the global performance of diffusers. In order to reliably predict diffuser flows by calculation, more detailed knowledge is required on the inner flow behavior, especially on the nature and the development of the boundary layer. This paper is meant to be a contribution to that question.

The presented measurements indeed show that the characters of the boundary layers at two lines of traverse positions are different, caused by secondary effects and wake flows of the stator blades. The boundary layers in the downstream region between two stator blades seem to be two dimensional, especially in the law-of-the-wall region. On the other side, the boundary layers behind a stator blade strongly show a three-dimensional character. Further investigations are necessary to ascertain to what extent the asymmetry of diffuser flow is periodic across the blade spacing. Because of this asymmetry, it seems to be questionable to calculate this diffuser flow using two-dimensional theory. However, the behavior of the turbulent boundary layer in a strong pressure gradient and near separation is not well known even in the case of two-dimensional flow as shown by the predictions at the 1968 Stanford Conference [12] and methods using modeling of turbulence, e.g., [13]. Knowledge is required on the shearing stress distribution, otherwise the boundary layer equations can not be used for numerical calculations. According to the differences of the presented $-\overline{u'v'}$ distributions between two and three-dimensional flow (positions I12 and II12), it seems that predictions of flow in a diffuser behind a turbomachine based on boundary layer theory will not be very successful at the present time.

Acknowledgments

The authors wish to thank Deutsche Forschungsgemeinschaft (DFG) for supporting the work described in this paper.

References

1 Stock, H. W., "Compressible Turbulent Flows in Long Circular Cross-Section Diffusers of Large Area Ratio," *J. Flight Sciences and Space Research*, Vol. 9, 1985, pp. 143–155.

2 Göing, M., "Untersuchungen über das Impulsmoment turbulenter Grenzschichten und Messungen im Diffusor eines Axialverdichters," Diss. TH Darmstadt, Federal Republic of Germany, 1985.

3 Lieblein, S., "Experimental Flow in Two-Dimensional Cascades, Aerodynamic Design of Axial-Flow-Compressors," NASA SP-36, Washington, D.C., 1965, pp. 183–226.

4 Pfeil, H., Göing, M., and Sieber, J., "Einfluss der Leitschaufelzahl und -stellung auf das Betriebsverhalten von Axialventilatoren," *Forschungsbericht FG Thermische Turbomaschinen*, TH Darmstadt, Federal Republic of Germany, 1983.

5 Sovran, G., and Klomp, E. D., "Experimentally Determined Optimum Geometries for Rectilinear Diffusers With Rectangular, Conical or Annular Cross-Section," in: *Fluid Mechanics of Internal Flow*, G. Sovran, ed., Elsevier, Amsterdam, 1967, pp. 270–319.

6 Adenubi, S. O., "Performance and Flow Regime of Annular Diffusers With Axial Turbomachine Discharge Inlet Conditions," ASME *Journal of Fluids Engineering*, Vol. 98, 1976, pp. 236–243.

7 Spalding, D. E., "A Single Formula for the 'Law of the Wall'," ASME *Journal of Applied Mechanics*, Vol. 28, 1961, pp. 455–458.

8 Coles, D. E., and Hirst, E. A., "Computation of Turbulent Boundary Layers," 1968 AFOSR-IFP Stanford Conference, Vol. II, *Compiled Data*, Stanford University, 1969.

9 Ball, C. L., Reid, L., and Schmidt, J. F., "End-Wall Boundary Layer Measurements in a Two-Stage Fan," AGARD-CP-351, Sept. 1983, pp. 22-1–22-23.

10 East, L. F., and Hoxey, R. P., "Low-Speed Three-Dimensional Turbulent Boundary-Layer Data," Aero. Res. Coun. R&M 3652, 1969.

11 Herbst, R., "Entwicklung von Grenzschichten bei instationärer Zuströmung," Diss. TH Darmstadt, Federal Republic of Germany, 1980.

12 Kline, S. J., Morkovin, M. V., Sovran, G., and Cockrell, D. J., "Computation of Turbulent Boundary Layers," 1968 AFOSR-IFP Stanford Conference, Vol. I, *Methods, Predictions, Evaluations and Flow Structure*, Stanford University, 1969.

13 Singhal, A. K., and Spalding, D. B., "Predictions of Two-Dimensional Boundary Layers With the Aid of the k-ϵ-Model of Turbulence," *Computer Methods in Applied Mechanics and Engineering*, Vol. 25, 1981, pp. 365–383.

P. Niederdrenk
Research Scientist.

H. Sobieczky
Research Scientist.

Institute for Theoretical Fluid Mechanics,
DFVLR,
Göttingen, Federal Republic of Germany

G. S. Dulikravich
Associate Professor,
Department of Aerospace Engineering,
Pennsylvania State University,
University Park, PA
Mem. ASME

Supercritical Cascade Flow Analysis With Shock-Boundary Layer Interaction and Shock-Free Redesign

This paper describes improvements made in a user-oriented analysis code for steady two-dimensional transonic flows in turbomachinery cascades. The full potential equation is solved by a finite area technique, using a C-type grid and an analytical wake model. Solution adaptive grid clustering refines the inviscid computationally captured shock. The boundary layer is computed by an integral method except in the shock region, where the analytical interaction model of Bohning and Zierep smoothes out the pressure distribution on the airfoil surface. The code is applied in its analysis and design modes to an experimentally tested cascade of airfoils.

Introduction

At high subsonic inlet Mach numbers, transonic cascade flow is usually characterized by local supersonic regions. In order to avoid strong shock losses and minimize viscous losses the blades should be shaped to provide supercritical flow with nearly isentropic recompression at the design point. The general aim is to obtain larger ranges of operating inlet Mach number and incidence angles while keeping the losses acceptably low at the same time. During off-design performance these losses are mainly due to shock waves terminating the supersonic regions and interacting with the boundary layer. Changes in the profile thickness of the order of the boundary layer displacement thickness, particularly in the supersonic region, may shift a shockless cascade flow into a shocked flow.

Thus, careful blade design requires an accurate prediction method including viscous/inviscid interaction effects. Although solving the Navier-Stokes equations in the whole flow field would certainly be the most complete model, we prefer the efficient approach of iterating solutions in different parts of the flowfield to a composite solution until convergence is achieved. At the high Reynolds numbers of practical interest the shear layers are thin and viscous effects can be attributed to an overall viscous/inviscid interaction between boundary layer, wake, and external inviscid flow. The generally weak global interaction may be significantly augmented at transonic speeds by strong local interactions between the shock wave and the turbulent boundary layer as well as between the external inviscid flow and the highly curved streamlines in the near-wake region at the trailing edge. Here we have to account for large normal pressure gradients, which cause the usual boundary layer assumptions to break down.

To describe the local interaction of a normal shock with the turbulent boundary layer we apply the analytical model of Bohning and Zierep [1, 2]. This model yields nonasymptotic small perturbation solutions of the Navier-Stokes equations for a thin viscous sublayer adjacent to the wall and an inviscid shear layer for the main part of the boundary layer. We embedded these solutions in an integral boundary layer method [3] and iteratively coupled them using a displacement thickness concept to an outer potential flow solver [4]. The wake is presently incorporated by a simple analytical model.

Although different in its individual calculation procedures and their coupling, this process may be compared to the "Grumfoil" code developed by Melnik et al. [5]. This work was recently extended by Inger's shock-boundary layer interaction treatment [6]. While the Grumfoil algorithm takes better account of strongly curved near-wake flow, due to the implementation of the results of Melnik and Chow [7], our code is developed for cascade flows and incorporates an extra design option. As outlined already for inviscid cascade flow in [8], the fictitious gas concept is applied to provide modifications of the blade contour necessary to allow for shock-free flow at supercritical operating conditions. It is that flexibility of the code which provides the practicing engineer with a tool to analyze a given cascade's performance and redesign it in order to improve its efficiency.

Computational Grid Generation

Using a finite area technique for the inviscid flow computation the grid does not have to be strictly orthogonal. Therefore, we generate the grid very economically by combining two analytically defined conformal mappings followed by separate coordinate shearing and stretching transformations [10]. This significantly speeds up the overall computation since in our viscous/inviscid coupling procedure the grid has

---

Contributed by the Gas Turbine Division for publication in the JOURNAL OF TURBOMACHINERY. Manuscript received by the Gas Turbine Division November 7, 1984.

to be repeatedly created for each global iteration cycle not only due to the varying displacement thickness but also due to the local grid reclustering at the intermediate shock positions.

When a shock capturing technique is employed, the shock discontinuity is approximated by strong gradients of the flow variables due to artificial viscosity added in the supersonic region. The distance over which the jump is smeared is generally of the same order of magnitude as the shock-boundary layer interaction zone, especially at the high Reynolds numbers of interest. Thus the localization of the smearing yields another reason for smooth grid refinement at the shock.

Our grid-generating procedure requires just the position of the shock along the chord and the distance between two surface points where clustering additional to the leading and trailing edge regions is desired. A detail of the grid around a compressor blade shown in Fig. 1 is depicted in Fig. 2, showing that the grid is clustered on the upper surface at $x/c = 0.33$.

Inviscid Flow Analysis

As already mentioned, we use the full potential equation

$$(1-\Phi_x^2/a^2)\Phi_{xx}+2(\Phi_x\Phi_y/a^2)\Phi_{xy}+(1-\Phi_y^2/a^2)\Phi_{yy}=0 \qquad (1)$$

This may be regarded as the continuity equation for an inviscid isentropic steady flow of an ideal gas. We numerically solve its divergence-free form to treat discontinuous solutions properly

$$(\rho\, u)_x+(\rho\, v)_y=0 \qquad (2)$$

In addition to conservation of mass and energy, we impose constant entropy as a third condition. Thus the momentum equation cannot be satisfied across isentropic shock waves, which means that the preshock Mach number should not be substantially greater than 1.3 to limit the deviations from the correct Rankine–Hugoniot jumps.

As described in earlier papers [4, 8], the finite area technique is used to solve equation (2) subject to uniform flow conditions at the upstream and downstream flow field boundaries.

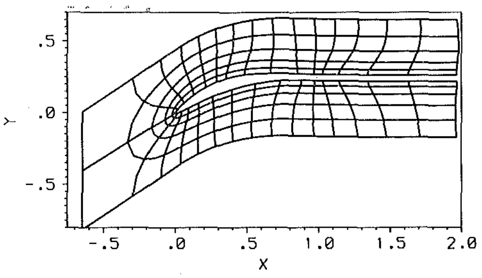

Fig. 1 C-type grid for a staggered compressor cascade with wake included

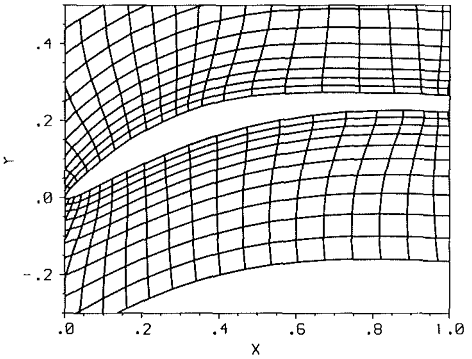

Fig. 2 Local grid clustering at x = 0/0.33/1

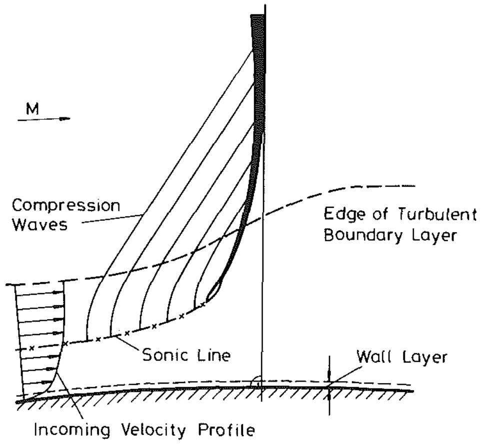

Fig. 3 Sketch of shock-boundary layer interaction model

Treatment of Viscous Layers

For the computation of the boundary layer we employ Rotta's integral dissipation method [3]. It solves simultaneously von Karman's momentum equation and the mechanical energy equation, utilizing additional empirical relations for the shape factors, the skin friction coefficient, and the dissipation coefficient.

When we march under the shock, normal pressure gradients cause a perturbation of the boundary layer. Neglecting the dependence of the undisturbed flow in the streamwise direction within the small interaction region, Bohning and Zierep derived linearized perturbation equations from the continuity, Navier-Stokes, and energy equations. As their model has been already described in the literature [1, 2], only a brief look at some of its essential features will be given here. Following Lighthill's concept the turbulent boundary layer is divided into two compressible layers (see Fig. 3). In the outer layer friction is considered only due to the incoming undisturbed velocity profile while the perturbations lend themselves to an essentially inviscid boundary value problem. Approximating the undisturbed velocity and Mach number profiles by power law functions, the resulting second-order differential equation is solved analytically containing the thickness of the inner wall layer as a yet unknown parameter. Within the inner layer, which turns out to be of the order of 1 percent of the boundary layer thickness, the Mach number typically decreases from

Nomenclature

a = speed of sound
c = cascade airfoil maximum chord length
C_p = pressure coefficient
g = gap distance between leading edges of two neighboring airfoils in the cascade
H_{32} = boundary layer shape factor $= \delta_3/\delta_2$
M = Mach number
Re = Reynolds number
w = velocity
β = flow angle measured from the circumferential direction
β_s = stagger angle
δ_1 = boundary layer displacement thickness
δ_2 = boundary layer momentum thickness
δ_3 = boundary layer energy thickness
ρ = fluid density
Φ = velocity potential
ω = relaxation coefficient
Ω = axial velocity density relation $= (\rho_2 w_2 \sin \beta_2)/(\rho_1 w_1 \sin \beta_1)$

about 0.5 to zero at the wall. A closed-form solution of the linearized compressible boundary layer equations yields on one hand the thickness of this layer and on the other hand – in combination with a suitable law of the wall for the undisturbed profile – the wall shear stress.

As the basic incoming boundary layer quantities are frozen over the streamwise extent of the interaction region, the variations of the perturbations have to vanish at $x \rightarrow \pm\infty$. Thus the solution must exhibit an asymptotic behavior. Actually, because of its exponential decay, the wall pressure perturbation, for example, tends to zero within a few boundary layer thicknesses (typically within 2 percent of chord). Having replaced the assumed analytical structure of the inviscid pressure distribution in the original version by the numerical calculation of the external flow field, we attach the perturbation solution to the ordinary boundary layer calculation at such streamwise locations that the latter will not be subjected to the sharp pressure rise across the shock. These locations, although depending on Reynolds number and grid refinement, are usually given by the extent of potential shock smearing due to artificial viscosity, as mentioned before. At the end of the interaction zone we have all possible integral boundary layer quantities at our disposal. Solving for the displacement thickness we evaluate δ_1 and the shape factor H_{32} at the end of the interaction and submit these quantities to reinitiate the boundary layer code after the shock.

At present we treat the wake as a viscous displacement model of constant thickness given by the sum of the trailing edge and boundary layer displacement thicknesses. Instead of fulfilling the Kutta condition the wake is adjusted to the solution with regard to pressure equality on its upper and lower surfaces by iterating on its curvature only. Within the overall iteration process between inviscid and viscous parts of the flow field this concept can easily be extended to a more appropriate wake treatment including other parameters, e.g., variable wake displacement thickness and/or variable exit flow angle [11].

Viscous-Inviscid Coupling

In transonic flow over an airfoil we are concerned with regions of weak and strong viscous/inviscid interactions. The weak interaction arises from boundary layer displacement and global wake curvature effects. Here we have no convergence problems following the direct global iteration approach: Prescribe the inviscid pressure distribution as a boundary condition for the boundary layer calculation and use the resulting displacement thickness to correct the airfoil contour for blockage effects.

When adverse local pressure gradients cause stronger interaction the direct iteration approach becomes unstable. Damping of the instability is usually provided by underrelaxing the displacement thickness. At the location of very strong pressure gradients due to shock waves or highly curved streamlines in the near wake this procedure would require vanishing relaxation coefficients. At the same time the ordinary boundary layer equations no longer represent the adequate model.

Having partially accounted for this problem by employing the Bohning-Zierep interaction theory at the shock, we still encounter stability problems on the suction surface near the trailing edge. At present we circumvent this shortcoming by linearly extrapolating the pressure distribution to be submitted to the boundary layer code from about 97 percent of the chord up to the trailing edge.

In the potential flow calculation we use a grid-refinement sequence consisting of four consecutively refined grids. In order to save time we could use the ordinary boundary layer integral code on a coarse grid during the first iterations even in the shock region, if the pressure gradient were sufficiently smeared. Hence we introduce a simple analytical function to smear out the pressure rise widely across the inviscid shock during the first two global viscous/inviscid iterations. In fact the adverse velocity gradients predicted by the full potential code in regions of strong interaction are much greater than they will be in the final converged state. So, in anticipation of the qualitative form of the final result, we are able to increase the convergence rate of the global iterative procedure while assuring its stability. Thus the boundary layer code does not signalize separation due to shock-induced strong pressure gradients during the early stage of the iterative process. In order to get a smooth transition to the actually calculated inviscid pressure distribution, which is submitted to the viscous part of the employed local analysis on the third and fourth grid, we also underrelax the pressure. Applying this simple procedure the shock moves only a few grid points during the iterations and convergence is generally obtained after five to seven global cycles.

Results

In order to minimize effects of the trailing edge, where our treatment of the viscous flow still needs substantial improvements, we choose as a first example the symmetric NACA 0012 profile at zero incidence and a free-stream Mach number of 0.77. Starting the iterative cycle on a coarse grid with only 20 grid points along the suction surface, the resulting pressure distribution of the inviscid flow field calculation shown in Fig. 4(*a*) is analytically smeared out over the shock region. Thus the ordinary boundary layer method employed over the whole profile up to the third global iteration does not immediately signal turbulent separation. The resulting displacement thickness (indicated by crosses in Fig. 4*a*) is underrelaxed (solid line in Fig. 4*b*) before it is added to the profile contour. At the third and fourth steps (Fig. 4*c*, *d*) the grid size is halved each time. Near the shock the grid is clustered just to such an extent that unphysical preshock peaks in Mach number are avoided. On the finest grid (Fig. 4*d*, *e*, *f*, *g*) the interaction theory is employed in the shock region and the whole viscous calculation subjected to an underrelaxed pressure distribution. The main effect of relaxing the pressure is again to smear out the streamwise pressure gradient while the shock is still moving during the iteration and thus to stabilize the process of finding stationary positions of the shock and the accompanying boundary layer thickening.

Finally, when global convergence is achieved, the boundary layer is subjected to the correct pressure distribution, its jump across the shock being felt as sharp as provided by the inviscid flowfield calculation in connection with local grid clustering. Due to inviscid potential shock smearing the continuous wall pressure distribution at this high Reynolds number practically coincides with the pressure at the outer edge of the boundary layer. For reasons of clarity only the latter is shown in the figures. Since our finite area inviscid flow analysis code can handle the bumps in displacement thickness produced by the interaction theory, no additional smoothing is needed. Thus the very small change in displacement thickness occurring at transition from laminar to turbulent boundary layer ($x/c = 0.07$) is evident in the pressure distribution (Fig. 4*g*).

When the inviscid flow begins to react with the steeper increase in displacement thickness (Fig. 4*e*, *f*, *g*) the previously observed inviscid postshock expansion at the shock root gradually vanishes. For the pre- and postshock Mach numbers taken from the sample calculation the shock polar diagram (Fig. 5) leads to a deflection angle of 3.85 deg. This value is embedded within the limits given for sonic conditions and maximum deflection at an attached shock, respectively: a feature which is also confirmed by experimental observation.

Changing over to a typical user-oriented problem we analyze an actual supercritical blade section developed and

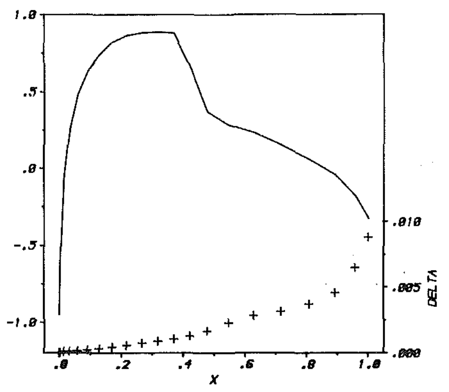

Fig. 4(*a*)

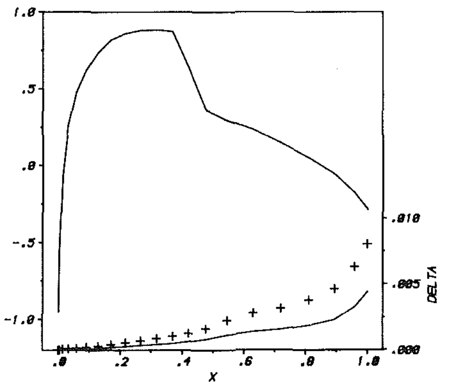

Fig. 4(*b*) $\omega = 0.5$

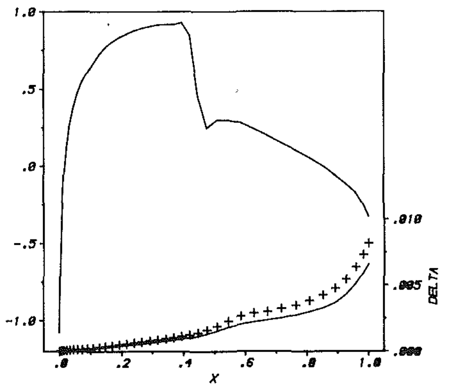

Fig. 4(*c*) $\omega = 0.6$

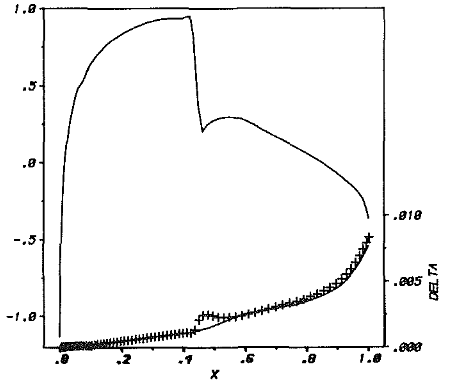

Fig. 4(*d*) $\omega = 0.7$

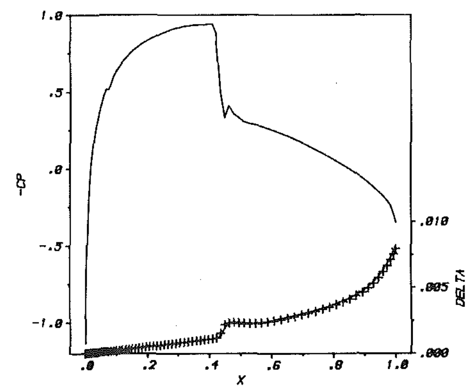

Fig. 4(*e*) $\omega = 0.8$

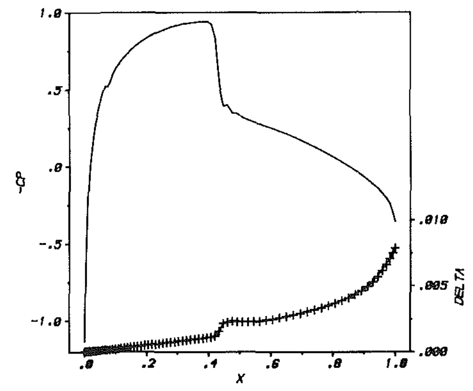

Fig. 4(*f*) $\omega = 0.9$

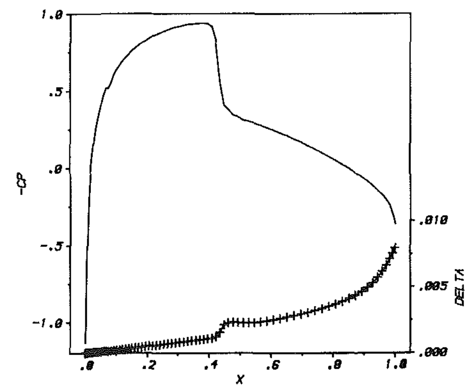

Fig. 4(*g*) $\omega = 1.0$

Fig. 4 Iterative sequence of pressure coefficient and displacement thickness for NACA 0012 profile ($M = 0.77$, $Re = 4.9 \times 10^6$, $\beta = 0$ deg)

tested by Rechter et al. [14] for a transonic compressor cascade at an inlet Mach number of 0.8. The stator is distinguished by a flow turning angle of 37 deg and a gap-to-chord ratio of 0.83. The design was aimed at a shock-free recompression with attached boundary layer and acceptably low losses in the near off-design range. Figure 6 shows the prescribed design Mach number distribution as a solid line together with some measured values from experimental verification. The authors [14] state that the design conditions with $M = 0.8$ and an axial velocity density ratio $\Omega = 1.05$ correspond to measurements around $M = 0.77$ and $\Omega = 1.09$, due to the blockage effects of side wall boundary layers, which are accounted for in different ways in the design process and the experiment. While the discrepancies at the leading edge are due to limitations of Schmidt's design method [15] the disagreement at about 40 percent of chord length was attributed to a laminar separation bubble.

Our analysis is based on $\Omega = 1$ and the profile data given except for the leading edge region, which was rather coarsely

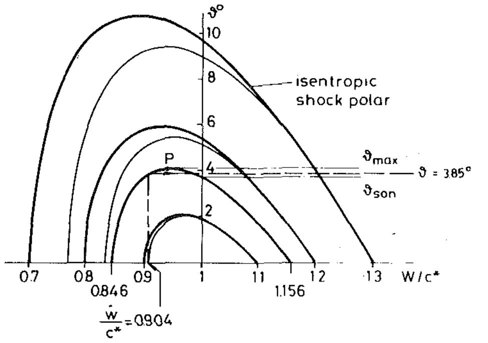

Fig. 5 Velocity deflection angle across shock

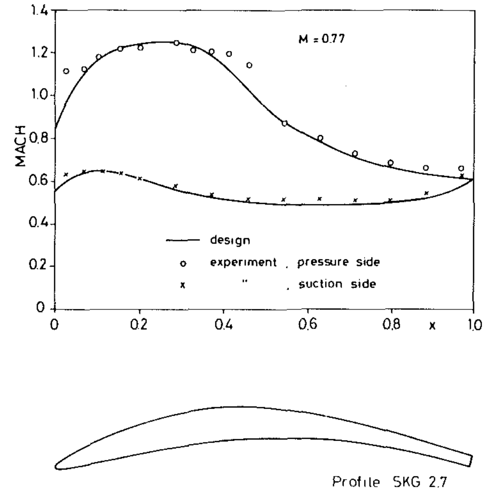

Fig. 6 Prescribed and measured Mach number variation for the SKG 2.7 cascade ([14]: $g/c = 0.821$; $\beta_s = 103.6$ deg; $\beta_1 = 126.7$ deg; $\beta_2 = 90.0$ deg)

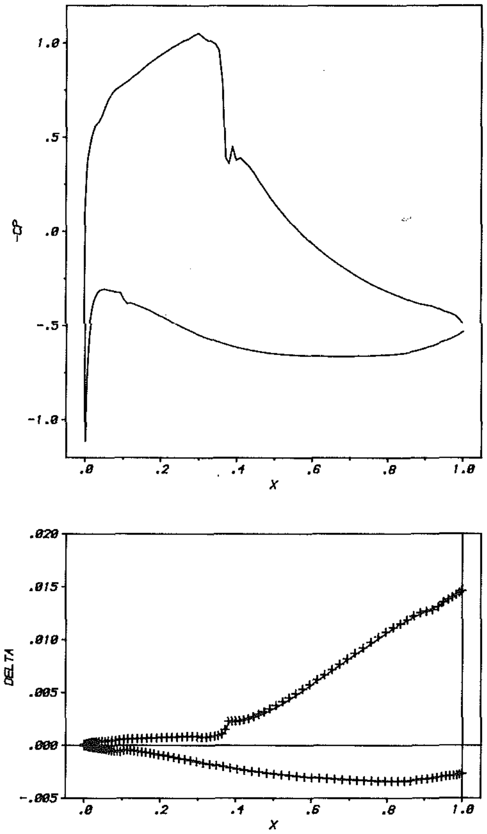

Fig. 7 Analysis of SKG 2.7 cascade at M = 0.8

displayed and needed some modifications. Letting transition take place near laminar separation we encounterd shock-induced transition. As the treatment of shock-transitional boundary layer interaction is beyond the capabilities of our code we specified (with reference to [14]) transition at 30 percent of the chord length. The following results were obtained for Re $= 1.2 \times 10^6$ and $\omega = 0.5$.

At M = 0.8 we encounter a distinct shock impinging on the turbulent boundary layer at $x = 0.36$ (Fig. 7). The shock being again oblique leads to a downstream Mach number just below 1. A further modest increase of inflow Mach number from 0.80 to 0.81 instantaneously caused turbulent boundary layer separation.

It would certainly be unsatisfactory for the practicing engineer to stop at this stage of analysis. Fortunately we can switch over to the design option of the code and apply a semi-inverse solution procedure to the inviscid flow field calculation making use of Sobieczky's fictitious gas concept.

As explained in greater detail in [8, 9] we slightly modify the profile section on the suction surface and perform a fully elliptic potential flow field calculation. The ellipticity of the governing equation is guaranteed by the use of a fictitious gas density-velocity relation, whenever the flow becomes locally supercritical. In extension to the earlier cited publications viscous effects in the design mode are now accounted for by applying the same global iteration procedure as described before for the analysis mode, the only difference being that the pressure coefficient as input variable for the boundary layer calculation is obtained from the fictitious gas analysis result. This approximation leads to an efficient redesign procedure and proves to be appropriate because of the similarity between the isentropic and fictitious gas pressure distributions.

As a consequence of the absence of shocks, the potential flow calculation, which takes most of the overall iteration time, is considerably accelerated. To further speed up the convergence rate, in the design mode the displacement thickness is not only underrelaxed but also locally smoothed, where the rate of smoothing is proportional to the local deviation in displacement thickness between two successive global iterations. Thus smoothing will be reduced while approaching the converged solution.

When convergence of the inviscid/viscous iteration loop is achieved, the initial value problem inside the supersonic bubble is solved by a second-order accurate method of characteristics using now the isentropic gas density-velocity relation. The integration begins at the sonic line and arrives at the new part of the effective airfoil contour which is determined by the condition of its constant value of the stream function. Figure 8 shows the supersonic bubble and the corresponding isentropic gas pressure distribution obtained by the method of characteristics. It should be noted that in striving for an improvement of the blade's performance the chosen example presents a fairly tough test case, because the efficiency of the original design is already not too bad. In carrying out the inverse redesign procedure we encountered a sensitive equilibrium between the avoidance of expansion peaks near the nose and compression shocks terminating the supersonic zone. This may be seen directly from the concentration of characteristic lines in these regions (Fig. 8) and an indentation of the pressure distribution and the sonic line (Fig. 9). This time the finite area method with first-order artificial viscosity was used to calculate the flow through the redesigned cascade with the displacement thickness being added to the profile. This balancing problem is further enhanced by the fact that the flow in the recompression zone over the original blade is already very near to separation. Thus several constraints are

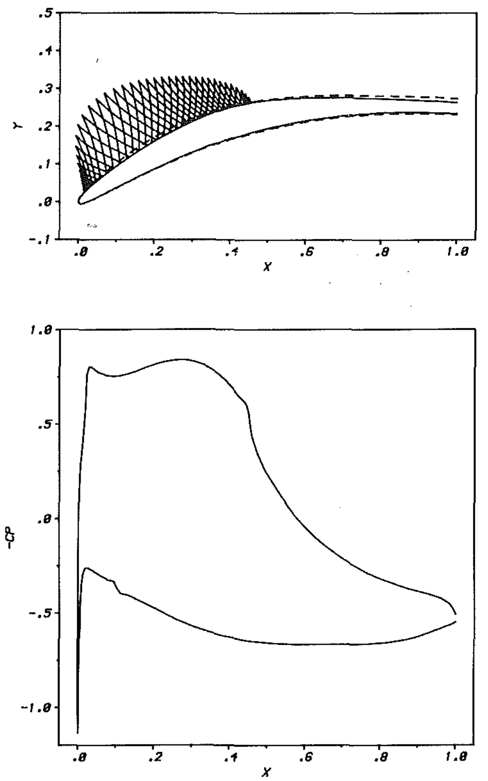

Fig. 8 Redesigned cascade at M = 0.8: supersonic bubble and pressure distribution

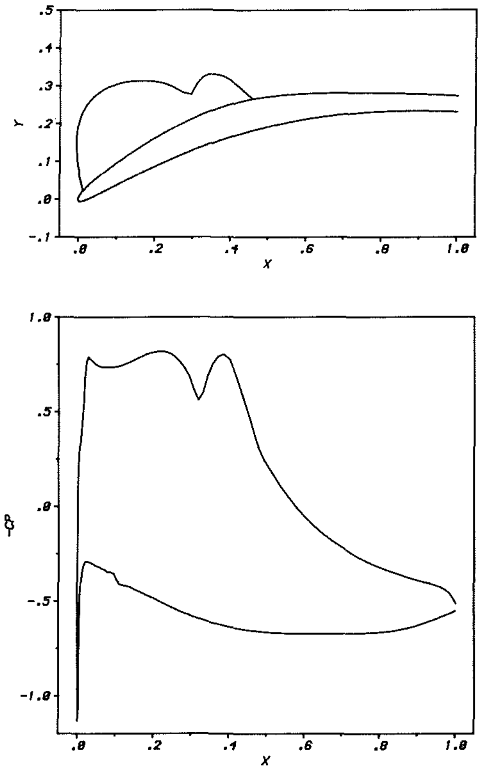

Fig. 9 Analysis of outer inviscid flow around redesigned cascade including displacement thickness at M = 0.8

narrowing down the margin of appropriate contour modifications.

Subtraction of displacement thickness from the effective contour yields the new bare blade shape. The supersonic part of the effective airfoil obtained by the method of characteristics in connection with streamline integration is already smooth. Thus, to avoid slope discontinuities in the new profile contour, we locally smooth the displacement thickness variation over the transition region before subtraction in case boundary layer transition had taken place in the supersonic zone.

To verify the improvements of our redesign we repeat the complete inviscid/viscous flow analysis and in fact recover a

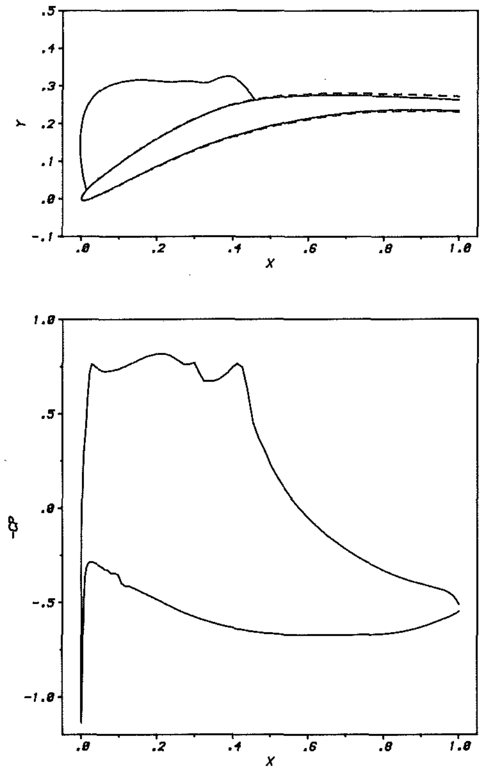

Fig. 10 Complete verification analysis of redesigned cascade at M = 0.8

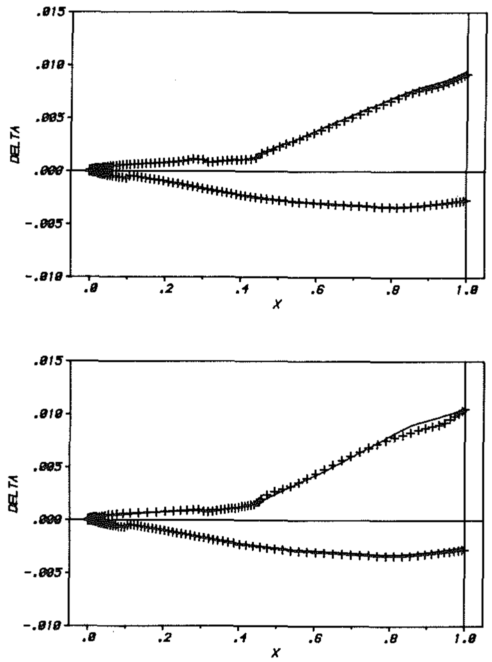

Fig. 11 Comparison of displacement thickness resulting from: (*a*) analysis (upper figure); (*b*) redesign (lower figure) at M = 0.8

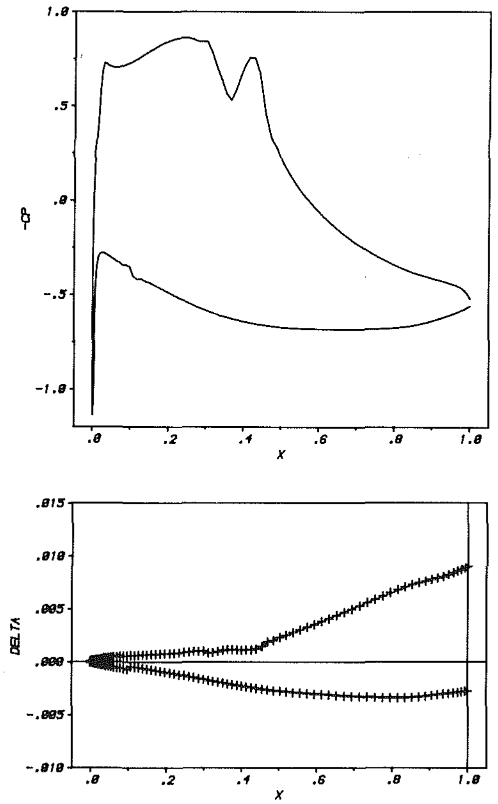

Fig. 12 Analysis of redesigned cascade at M = 0.81

shock-free solution (Fig. 10). As no smoothing technique was applied in the analysis mode the preshock wiggles in the pressure distribution may not only originate from the abovementioned indentation but also from the interaction with the supersonic part of the boundary layer in the course of the iteratively developing solution.

The corresponding displacement thickness is shown in Fig. 11(*a*). There are only small deviations from the displacement thickness obtained by the redesign procedure (Fig. 11*b*). In Fig. 11(*b*) the displacement thickness calculated by the use of the isentropic gas pressure distribution obtained in connection with the method of characteristics (indicated by crosses) is compared to that obtained by the use of the fictitious gas pressure during the last global iteration cycle in the redesign mode (solid line). The smallness of the difference between these two curves in fact confirms the utility of our simplifying approximation for the pressure distribution during iterative redesign; it justifies the use of the fictitious gas pressure as boundary condition for the boundary layer calculation within the supersonic bubble.

Slightly raising the inflow Mach number from 0.8 to 0.81 (Fig. 12) causes again shock losses, but the severe limit of this test case is given by turbulent boundary layer separation, which occurs just beyond M = 0.81.

Conclusion

We have described the extension of an efficient numerical analysis and redesign tool for engineering purposes that takes into account shock-boundary layer interaction for cascades at off-design operating conditions. An easy mapping procedure, a smooth local grid clustering, an analytical solution for the viscous interaction zone, a simple direct coupling and iterative solution technique are the main features of the computational modules contributing to that extension. The flexibility of the code in its analysis and redesign modes has been demonstrated by a user-oriented example calculation. Consideration of quasi-three-dimensional and rotation effects, a more adequate wake modeling, and a refined inviscid shock calculation method belong to further improvements now under development.

References

1 Bohning, R., and Zierep, J., "Der senkrechte Verdichtungsstoss an der gekrümmten Wand," *ZAMP*, Vol. 27, 1976, pp. 225–240.

2 Bohning, R., and Zierep, J., "Normal Shock-Turbulent Boundary Layer Interaction at a Curved Wall," AGARD-CP-291, 17/1–17/8, 1980.

3 Rotta, J. C., "Turbulent Boundary Layer Calculations With the Integral Dissipation Method," *Computation of Turbulent Boundary Layers*, AFOSR-IFP Stanford Conference, Vol. I, 1968, p. 177 (also *Ing. Archiev*, Vol. 38, 1969, pp. 212–222).

4 Dulikravich, D. S., and Sobieczky, H., "Shockless Design and Analysis of Transonic Cascade Shapes," *AIAA Journal*, Vol. 20, No. 11, 1982, pp. 1572–1578.

5 Melnik, R. E., Chow, R., and Mead, H. R., "Theory of Viscous Transonic Flow Over Airfoils at High Reynolds Number," AIAA Paper No. 77-680, 1977.

6 Lekoudis, S. G., and Inger, G. R., "Computation of the Viscous Transonic Flow Around Airfoils With Trailing Edge Effects and Proper Treatment of the Shock/Boundary Layer Interaction," AIAA Paper No. 82-0989, 1982.

7 Melnik, R. E., and Chow, R., "Asymptotic Theory of Two-Dimensional Trailing Edge Flows," NASA SP 317, 1975.

8 Sobieczky, H., and Dulikravich, D. S., "A Computational Design Method for Transonic Turbomachinery Cascades," ASME Paper No. 82-GT-117, 1982.

9 Dulikravich, D. S., and Sobieczky, H., "Design of Shock-Free Cascades Including Viscous Boundary Layer Effects," ASME Paper No. 83-GT-134, 1983.

10 Dulikravich, D. S., "Fast Grid Generation of Three-Dimensional Computational Boundary – Conforming Periodic Grids of C-type," NASA/AFOSR Symposium on Numerical Generation of Curvilinear Coordinate System and Use in the Numerical Solution of Partial Differential Equations, Nashville, TN, Apr. 13–16, 1982.

11 Hobbs, D. E., Wagner, J. H., Dannenhoffer, J. F., and Dring, R. P., "Experimental Investigation of Compressor Cascade Wakes," ASME Paper No. 82-GT-299, 1982.

12 Sobieczky, H., and Stanewsky, E., "The Design of Transonic Airfoils Under Consideration of Shock Wave Boundary Layer Interaction," ICAS Paper No. 76-14; DFVLR Report IB 251-76 A 26, 1976.

13 Jou, W. H., and Murmann, E. M., "A Phemomenological Model for Displacement Thickness Effects of Transonic Shock Wave-Boundary Layer Interactions," AGARD-CP-291, 15/1–15/9, 1981.

14 Rechter, H., Schimming, P., and Starken, H., "Design and Testing of Two Supercritical Compressor Cascades," ASME Paper No. 79-GT-11, 1979.

15 Schmidt, E., "Computation of Supercritical Compressor and Turbine Cascades With a Design Method for Transonic Flows," ASME Paper No. 79-GT-30, 1979.

Unsteady Aerodynamic Interactions in a Multistage Compressor

V. R. Capece

S. Fleeter

Thermal Sciences and Propulsion Center,
School of Mechanical Engineering,
Purdue University,
West Lafayette, IN 47907

The fundamental flow physics of multistage blade row interactions is experimentally investigated, with unique data obtained which quantify the unsteady harmonic aerodynamic interaction phenomena. In particular, a series of experiments is performed in a three-stage axial flow research compressor over a range of operating and geometric conditions at high reduced frequency values. The multistage unsteady interaction effects of the following on each of the three vane rows are investigated: (1) the steady vane aerodynamic loading, (2) the waveform of the aerodynamic forcing function to each vane row, including both the chordwise and traverse gust components.

Introduction

Fan, compressor, and turbine airfoils are susceptible to destructive aerodynamically induced vibrational responses when a periodic aerodynamic excitation source with a frequency equal to an airfoil natural frequency acts on an airfoil row. With the resonant airfoil freqencies accurately predicted with finite element structural models, Campbell diagrams are utilized to determine the rotor speed at which the airfoil row may be susceptible to significant aerodynamically induced vibrational response. However, accurate predictions for the amplitude of the resulting vibration and stress cannot be made due to the inadequacies existing in current state-of-the-art unsteady aerodynamics models for both the aerodynamic forcing function and the resulting airfoil row unsteady aerodynamics.

The most common aerodynamic excitation sources are the wakes shed by upstream blade or vane rows. For example, in the single compressor stage schematically depicted in Fig. 1, the wakes from the upstream rotor are the primary source of the unsteady aerodynamics on the downstream stator vanes, i.e., the exit flow field from the upstream rotor defines the unsteady aerodynamic forcing function to the downstream stator vanes. This aerodynamic forcing function is defined by the velocity components parallel and normal to the vane chord, u^+ and v^+, respectively.

First principles predictive techniques for aerodynamically induced airfoil response require a definition of the unsteady forcing function in terms of its harmonics. The periodic response of the airfoil row to each harmonic is assumed to be comprised of two components. One is due to the chordwise and normal components of the harmonic forcing function being swept past the nonresponding airfoil row, termed the transverse (normal) and chordwise (parallel) gust responses, respectively. The second, the self-induced unsteady aerodynamics, arises when the airfoil row responds to the aerodynamic forcing function.

Gust and self-induced unsteady aerodynamic models have been and continue to be developed [1–7]. These models are inviscid, considering small unsteady perturbations superimposed on a steady throughflow. There are many analytical and physical assumptions inherent in these mathematical models. Unfortunately, at the high reduced frequency values characteristic of turbomachinery, only a very limited quantity of appropriate fundamental unsteady aerodynamic data exists to verify these models. Data have been obtained in single stages of low-speed research compressors. In experiments which considered only transverse gust aerodynamics, the effects of airfoil camber and rotor–stator axial spacing were investigated, with the data demonstrating that the waveform of the aerodynamic forcing function has an important influence on the unsteady aerodynamic gust response of the airfoil row [8, 9]. In [10], the significant effects of steady airfoil loading and the detailed aerodynamic forcing function transverse gust component on the unsteady aerodynamic response of an airfoil row were investigated.

However, the significant effects associated with multistage flow field interactions have not been experimentally (or mathematically) considered. For example, in the single stage depicted in Fig. 1, the wakes from the upstream rotor blades define the unsteady aerodynamic forcing function to the downstream stator vanes, with this forcing function defined by the velocity components parallel and normal to the vane chord. However, in a multistage turbomachine, the aerodynamic forcing function to a downstream vane row is determined by all of the upstream airfoil wakes and the unsteady aerodynamic interactions between the various upstream blade and vane rows.

In this paper, the fundamental flow physics of multistage blade row interactions are experimentally investigated for the first time, with unique data obtained to describe the fun-

---

Contributed by the Gas Turbine Division of The American Society of Mechanical Engineers and presented at the 32nd International Gas Turbine Conference and Exhibit, Anaheim, California, May 31–June 4, 1987. Manuscript received at ASME Headquarters February 17, 1987. Paper No. 87-GT-171.

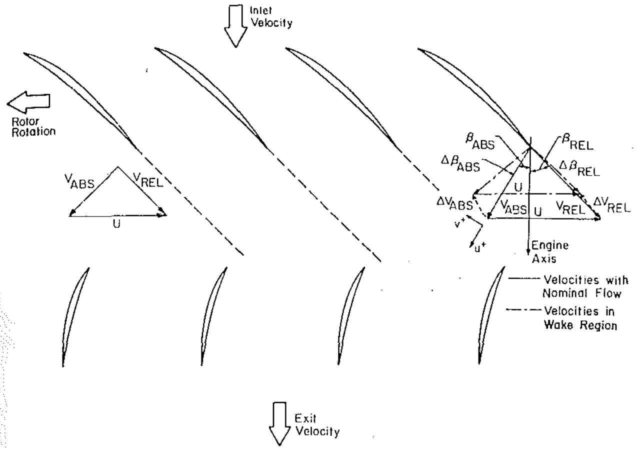

Fig. 1 Schematic of single-stage compressor flow field

damental unsteady aerodynamic interaction phenomena. In particular, a series of experiments is performed which utilize the versatility of the Purdue University Three-Stage Axial Flow Research Compressor to investigate the multistage unsteady interaction effects of the following on each of the three individual vane rows: (1) the steady vane aerodynamic loading, and (2) the waveform of the aerodynamic forcing function to each vane row, including both the chordwise and transverse gust components.

Research Compressor

The Purdue University Axial Flow Research Compressor experimentally models the fundamental turbomachine unsteady aerodynamic multistage interaction phenomena including the incidence angle, the velocity and pressure variations, the aerodynamic forcing function waveforms, the reduced frequency, and the unsteady blade row interactions. The compressor is driven by a 15 hp d-c electric motor over a speed range of 300 to 3000 rpm. Each of the three identical stages contains 43 rotor blades and 41 stator vanes having a British C4 airfoil profile, with the first stage rotor inlet flow field established by a row of variable setting angle inlet guide vanes.

Instrumentation

Both steady and unsteady data are required to quantify the aerodynamics of each of the three vane rows. The steady data specify the overall compressor operating point and the detailed vane surface steady loading. The unsteady data define the time-variant aerodynamic inlet flow field to each vane row, i.e., the individual vane row aerodynamic forcing function, as well as the resulting vane surface unsteady pressure distributions.

Conventional steady instrumentation is used to determine the flow properties throughout the compressor. The steady aerodynamic loading on the surfaces of the vanes is measured with chordwise distributions of midspan surface static pressure taps.

The unsteady aerodynamic inlet flow field to each vane row is measured with a cross hot-wire probe positioned midway between each rotor and stator at midstator circumferential spacing. The probe is calibrated and linearized to 60 m/s and ±35 deg angular variation, with the accuracy of the velocity magnitude and angle of ±4 percent and ±2 deg, respectively. The mean absolute flow angle is determined by rotating the probe until a zero voltage difference between the two linearized hot-wire signals is obtained. This mean angle is subsequently used as a reference for the calculation of the instantaneous absolute and relative flow angles.

The measurement of the midspan vane surface unsteady pressures is accomplished with ultraminiature high response transducers. To minimize the potential of flow disturbances generated by the transducers, the transducers are embedded in the vanes from the backside and connected to the measurement surface by a static tap. These dynamically instrumented vanes are positioned such that a complete flow passage is instrumented in each vane row.

The embedded dynamic transducers are statically and dynamically calibrated. The static calibrations show good linearity and no discernible hysteresis. The dynamic calibrations demonstrate that the frequency response, in terms of gain attenuation and phase shift, is not affected by the transducer mounting. The accuracy of the unsteady pressure measurements, determined from the calibrations, is ±3.5 percent.

Unsteady Data Acquisition and Analysis

The unsteady data of interest are periodic, being generated at rotor blade passing frequency. Thus, a digital ensemble-averaging technique based on the signal enhancement concept of Gostelow [11] is used for the data analysis. The key to this technique is the ability to sample data at a preset time. This is accomplished by an optical encoder mounted on the rotor shaft. The microsecond range square wave voltage signal from the encoder is the data initiation time reference and triggers a high speed A-D multiplexer system. This averaging significantly reduces the random fluctuations superimposed on the periodic signals, with the unsteady signals essentially unchanged when averaged over 75 or more rotor revolutions. For the data presented herein, 200 averages are used.

The resulting ensemble-averaged digital periodic hot-wire and dynamic pressure transducer signals are each Fourier decomposed into harmonics by means of a Fast Fourier Transform (FFT) algorithm. This Fourier analysis determines the magnitude and the phase of the first harmonic of both the inlet flow field to each vane row, i.e., the aerodynamic forcing function, and the resulting vane surface unsteady pressures. These are each referenced to the initiation of the data acquisition. However, the hot-wire probe is positioned upstream of the leading edge plane of the vane row. Thus, it is necessary to time relate the harmonic vane row inlet flow field to the resulting unsteady vane surface pressures.

Nomenclature

c = airfoil chord
$\bar{C}_l$ = steady lift coefficient = $L'/\frac{1}{2}\rho U_t^2 c$
C_p = dynamic pressure coefficient = $\Delta p/\rho V_x v^+$
$\bar{C}_p$ = static pressure coefficient = $(\bar{p} - \bar{p}_{\text{exit}})/\frac{1}{2}\rho U_t^2$
k = reduced frequency = $\omega c/2V_x$
i = incidence angle
L' = steady lift per unit span = $\int_0^c (\bar{p}_p - \bar{p}_s)dx$
$\bar{p}$ = stator vane surface static pressure
$\bar{p}_{\text{exit}}$ = stator vane row exit static pressure
Δp = dynamic pressure difference across vane chordline
u^+ = inlet velocity parallel to vane
U_t = rotor blade tip speed
v^+ = inlet velocity normal to vane
V = absolute velocity
V_x = absolute axial velocity
ω = blade passing frequency

The hot-wire data are analyzed to determine the harmonic unsteady inlet flow angle and velocity to each vane row, in particular, the unsteady velocity components parallel and normal to each vane row, u^+ and v^+ of Fig. 1, which define the unsteady forcing function. The hot-wire probe is positioned upstream of the leading edge of each stator vane row. To relate time-based events measured by the hot-wire probe to the resulting unsteady pressures on the vane surfaces, the following assumptions are made: (1) the wakes are identical at the hot-wire and the vane leading edge planes; (2) the wakes are fixed in the rotor relative reference frame. The rotor blade spacing, the vane spacing, and the axial spacing between the vane leading edge plane and the probe centerline are known.

At a steady operating point for each vane row, the hot-wire data are analyzed to determine the absolute flow angle and the upstream rotor exit relative flow angle. Using the above two assumptions, the wake is located relative to the hot-wire probe and the leading edges of the instrumented vanes. From this, the times at which the wakes are present at various locations are determined.The incremented times between occurrences at the hot-wire and the vane leading edge plane are then converted to phase differences between velocities and the vane surface.

To simplify the experiment–theory correlation, the first harmonic data for each vane row are adjusted in phase such that the transverse inlet velocity component is at 0 deg at the vane suction surface leading edge. From the geometry, the time at which this would occur is calculated and transposed into a phase difference which is then used to adjust the pressure data from the suction surface. An analogous procedure is utilized for the pressure surface data so that the two instrumented stator vanes in each vane row are time related. The pressure difference across the chordline of an equivalent single vane in each row is then determined by the subtraction of these complex time-related vane pressure and suction surface data.

The final form of the unsteady pressure data defines the chordwise variation of the first harmonic pressure difference across the chordline of a stator vane and is presented as a complex dynamic pressure coefficient C_p in the format of the magnitude and the phase lag referenced to a transverse gust at the vane leading edge. As a reference, also presented are predictions obtained from a periodic small perturbation model which considers the inviscid, irrotational flow of a perfect gas [2]. This model analyzes the uniform subsonic compressible flow past a two-dimensional flat plate airfoil cascade, with small unsteady normal velocity perturbations superimposed and convected downstream.

Results

To investigate the rotor wake-generated gust aerodynamics on each vane row of a three-stage axial flow research compressor, including the multistage interactions, a series of experiments were performed. In these, the effects of the following on the unsteady aerodynamics of each vane row were quantified: (1) the steady aerodynamic loading; (2) the detailed waveform of the aerodynamic forcing function, including the chordwise and transverse gust components.

The variations in the steady loading of each vane row were accomplished by adjusting the setting angles of the stators, thereby altering the incidence angle to the vanes. This enables both the aerodynamic forcing function waveform to be maintained while varying the steady aerodynamic loading, and also the matching of the steady vane aerodynamic loading for different aerodynamic forcing functions. The detailed steady aerodynamic loading of the vane rows is specified by the chordwise distribution of the vane surface steady static pressure coefficient $\bar{C}_p$, with the overall loading level given by the incidence angle and the steady lift coefficient $\bar{C}_1$.

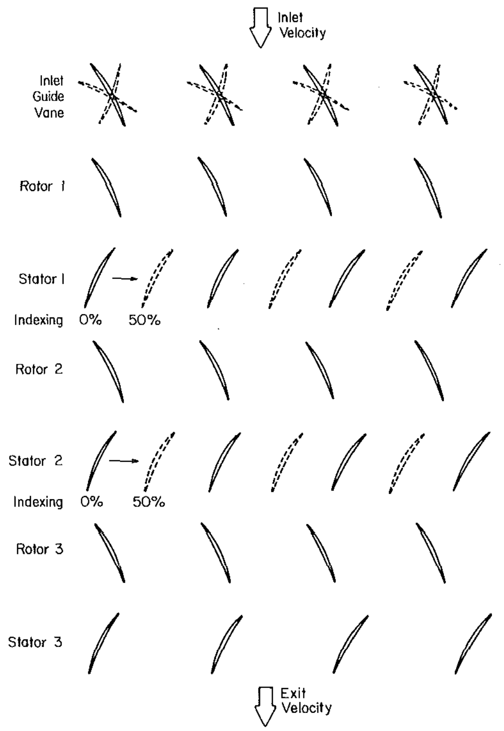

Fig. 2 Schematic of compressor geometry variations to alter the downstream vane row aerodynamic forcing functions

The detailed waveform of the aerodynamic forcing function is specified by the chordwise and transverse gust components, u^+ and v^+. These were experimentally varied as follows. Changing the setting angle of the inlet guide vanes alters the inlet flow to the first stage rotor. This results in a change in the detailed rotor blade exit flow field, in particular the chordwise and transverse gust components. Thus, the variations in the aerodynamic forcing function to the first-stage vane row were accomplished by altering the setting angle of the inlet guide vanes, as schematically depicted in Fig. 2. The forcing function waveform variations for the second and third-stage vane rows were accomplished by independently circumferentially indexing the upstream vane rows relative to one another, as also depicted in Fig. 2. In these cases, the steady aerodynamic loading of the vane row was maintained constant.

First-Stage Vane Row Experiments

Vane Loading Effects. Figures 3 and 4 present the steady vane surface static pressure distributions and the aerodynamic forcing function in the form of the two gust components, respectively, for two relatively low levels of aerodynamic loading. The surface static pressure distributions are smooth and show no indication of flow separation, with the loading differences in the leading edge region due to the differences in the incidence angles. The amplitudes of the chordwise and transverse gust components are different. However, in terms of the first harmonics, these two forcing functions are equivalent. In particular, the ratios of the magnitudes of the first harmonic of these gust components (u^+/v^+) are 0.447 and 0.430 for these two vane loadings. Also, it should be noted that relative to the absolute velocity, these gusts are not small, particularly at -4.7 deg of incidence where the transverse and chordwise gusts are approximately 50 and 20 percent of the absolute velocity. This may have implications regarding the validity of the small perturbation assumption in the various mathematical models.

The resulting chordwise distributions of the dynamic pressure difference coefficient on the first-stage vanes are shown in Fig. 5. Also presented are the predictions from the

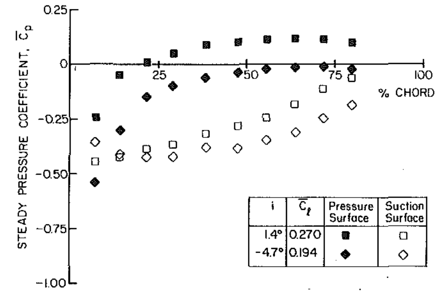

Fig. 3 Chordwise distribution of the first-stage vane surface static pressure coefficient at low loading levels

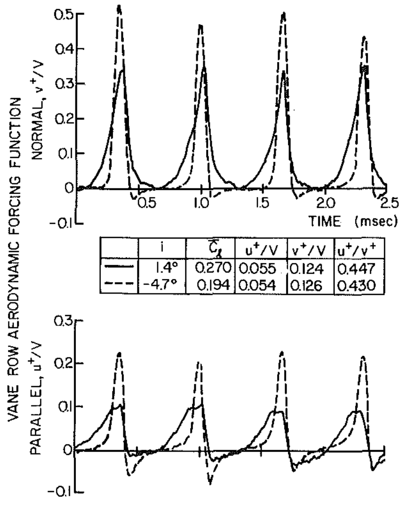

Fig. 4 Aerodynamic forcing function to the first-stage vane row at low loading levels

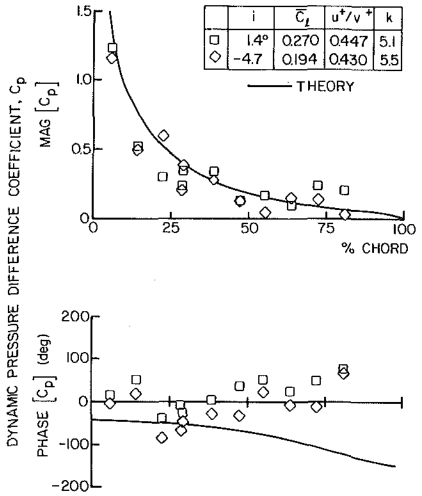

Fig. 5 Chordwise distribution of the dynamic pressure difference coefficient on the first-stage vanes at low loading

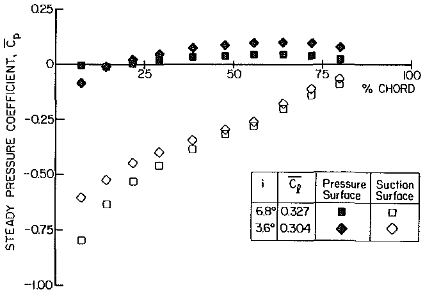

Fig. 6 Chordwise distribution of the first-stage vane surface static pressure coefficient at high loading levels

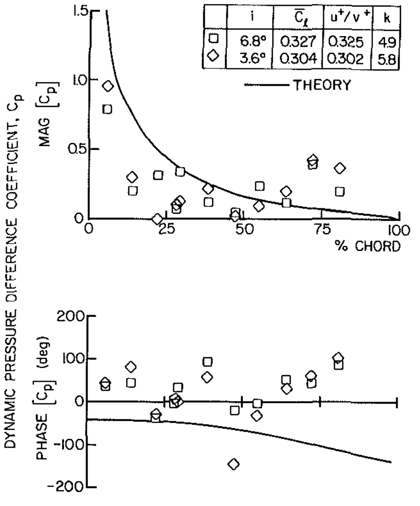

Fig. 7 Chordwise distribution of the dynamic pressure difference coefficient on the first-stage vanes at high loading levels

flat plate airfoil cascade transverse gust model of [2]. The magnitude data exhibit good correlation with the prediction, with both decreasing with increasing chordwise position. As the loading is increased, the magnitude data show an increase above both the prediction and the lower loading data aft of 60 percent chord. The phase of the dynamic pressure difference coefficient data exhibits a somewhat different chordwise distribution than the prediction. This is attributed to the vane camber and the detailed steady chordwise loading distribution on the vane surfaces.

The effects of higher levels of steady aerodynamic loading (Fig. 6) on the first-stage vane row unsteady aerodynamics, with the u^+ and v^+ gust components maintained relatively constant, were also investigated. At these higher loadings, the suction surface distributions are nearly identical over the aft part of the vane, with the differences in the front part of the vane due to the differences in the incidence angles. On the pressure surface, larger variations between the two loading conditions are apparent over the entire vane chord. Again, there is no evidence of flow separation.

The dynamic pressure difference coefficient data for this higher loading case are presented in Fig. 7. A comparison of these high loading data with the corresponding lower loading data of Fig. 5 reveals large differences. As the aerodynamic forcing functions are the same, aerodynamic loading has a significant effect on the unsteady aerodynamics of the vane row. Increasing the aerodynamic loading results in poorer correlation of the dynamic pressure difference coefficient magnitude data with the flat plate cascade prediction, as expected. Also, as the loading is increased, the magnitude data in the trailing edge region of the airfoil are increased in value. As will be shown, the data on the third-stage vane row, the last airfoil row in the compressor, for similar steady loading do not exhibit this increase in the magnitude data in the trailing edge region. Hence, this is most probably a multistage blade row interaction effect.

Thus, the best correlation of the dynamic pressure difference coefficient data and the flat plate cascade predictions is obtained at the low level of steady aerodynamic loading, indicating that the steady loading, not the incidence angle, is a

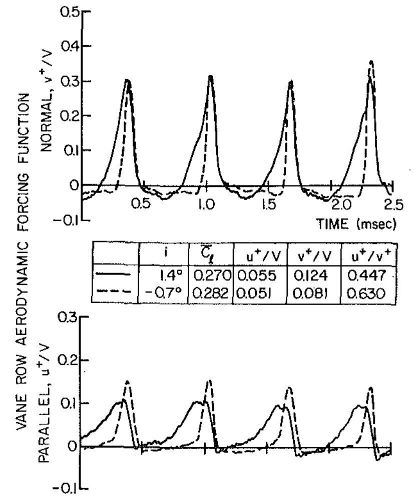

Fig. 8 Variations in the transverse gust aerodynamic forcing function to the first-stage vane row

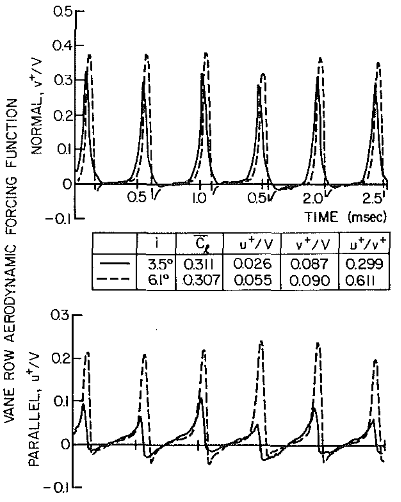

Fig. 11 Variations in the chordwise gust aerodynamic forcing function to the first-stage vane row

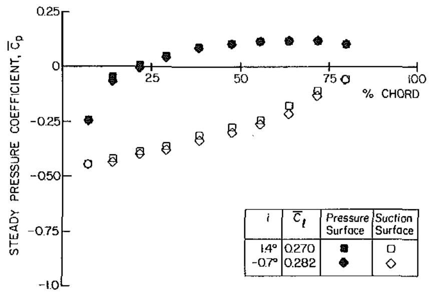

Fig. 9 Effect of the transverse gust aerodynamic forcing function on the first-stage vane surface static pressure coefficient

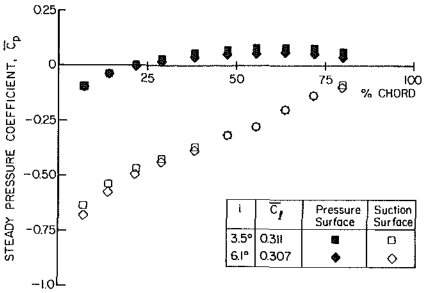

Fig. 12 Effect of the chordwise gust aerodynamic forcing function on the first-stage vane surface static pressure coefficient

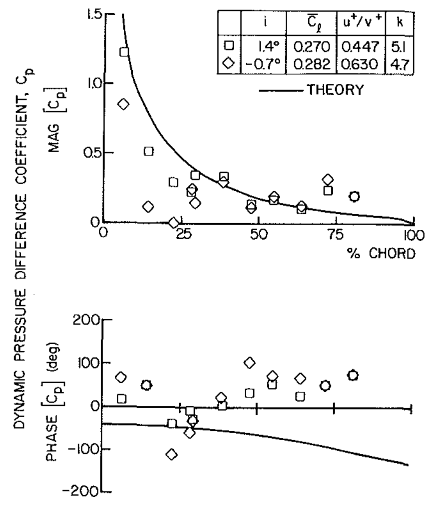

Fig. 10 Variation of the first-stage vane dynamic pressure difference coefficient with transverse gust aerodynamic forcing function

key parameter. Also, the steady loading level and distribution have a significant effect on the unsteady aerodynamics of the vane row.

Aerodynamic Forcing Function Effects. The effects of variations in the aerodynamic forcing function transverse gust component v^+ on the first-stage vane row unsteady aerodynamics are investigated. This is accomplished by means of two configurations such that the chordwise gust component u^+, and the steady aerodynamic loadings are maintained relatively constant. Figure 8 shows these aerodynamic forcing functions, with the ratios of the gust components (u^+/v^+) being 0.447 and 0.630. The chordwise distributions of the steady vane surface static pressure at this moderate loading for these forcing functions are presented in Fig. 9.

The resulting first stage vane chordwise distributions of the dynamic pressure difference coefficient data and the corresponding flat plate cascade prediction are presented in Fig. 10. The magnitude data are decreased in value relative to the prediction over the leading 30 percent of the vane, with the (u^+/v^+) data of 0.630 having a decreased amplitude relative to the (u^+/v^+) data of 0.447. However, in the midchord region, the magnitude data correlate well with each other and with the prediction. Aft of 70 percent of the chord, the magnitude data are increased in value at this moderate level of steady loading, analogous to the previous high steady loading results. The phase data are increased with respect to the prediction over the front part of the vane, becoming nearly constant over the aft half of the vane.

The effects of variations in the aerodynamic forcing function chordwise gust component u^+ on the first stage vane row unsteady aerodynamics are also investigated. This is accomplished by means of two configurations such that the transverse gust component v^+, and the steady aerodynamic loading are maintained relatively constant. The aerodynamic forcing functions are shown in Fig. 11, with the ratios of the gust components (u^+/v^+) being 0.299 and 0.611. The chordwise distributions of the steady vane surface static pressures at this high loading are presented in Fig. 12.

The resulting chordwise distributions of the dynamic pressure difference coefficient data and the corresponding flat

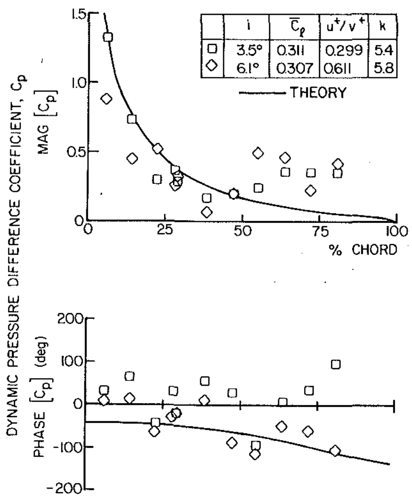

	i	$\bar{C}_\ell$	u^+/v^+	k
□	3.5°	0.311	0.299	5.4
◇	6.1°	0.307	0.611	5.8

Fig. 13 Variation of the first-stage vane dynamic pressure difference coefficent with chordwise gust aerodynamic forcing function

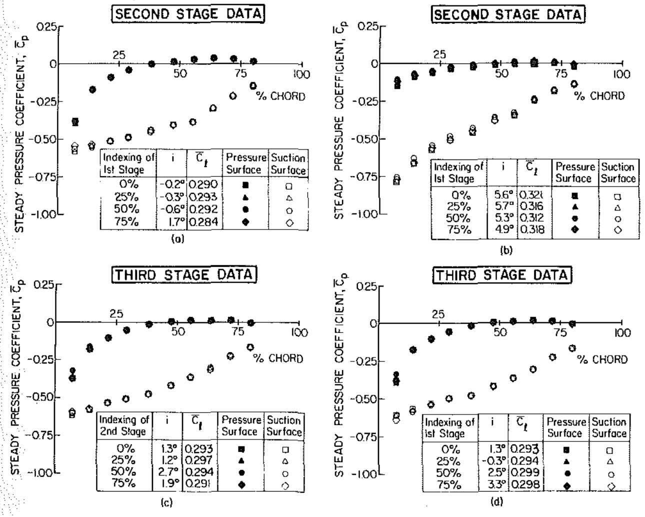

Indexing of 1st Stage	i	$\bar{C}_\ell$	Pressure Surface	Suction Surface
0%	-0.2°	0.290	■	□
25%	-0.3°	0.293	▲	△
50%	-0.6°	0.292	●	○
75%	1.7°	0.284	◆	◇

(a)

Indexing of 1st Stage	i	$\bar{C}_\ell$	Pressure Surface	Suction Surface
0%	5.6°	0.321	■	□
25%	5.7°	0.316	▲	△
50%	5.3°	0.312	●	○
75%	4.9°	0.318	◆	◇

(b)

Indexing of 2nd Stage	i	$\bar{C}_\ell$	Pressure Surface	Suction Surface
0%	1.3°	0.293	■	□
25%	1.2°	0.297	▲	△
50%	2.7°	0.294	●	○
75%	1.9°	0.291	◆	◇

(c)

Indexing of 1st Stage	i	$\bar{C}_\ell$	Pressure Surface	Suction Surface
0%	1.3°	0.293	■	□
25%	-0.3°	0.294	▲	△
50%	2.5°	0.299	●	○
75%	3.3°	0.298	◆	◇

(d)

Fig. 14 Effect of circumferentially indexing the upstream stators on the downstream vane surface static pressure coefficients

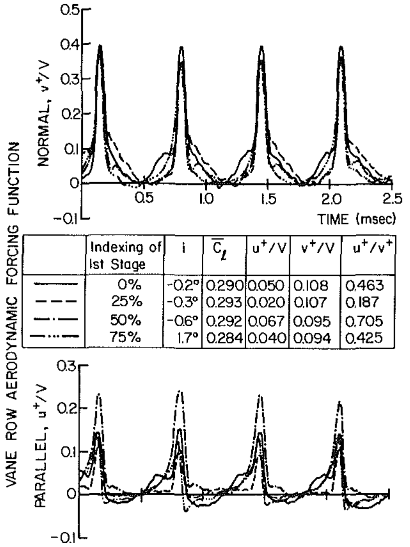

	Indexing of 1st Stage	i	$\bar{C}_\ell$	u^+/V	v^+/V	u^+/v^+
———	0%	-0.2°	0.290	0.050	0.108	0.463
– – –	25%	-0.3°	0.293	0.020	0.107	0.187
—·—	50%	-0.6°	0.292	0.067	0.095	0.705
—···—	75%	1.7°	0.284	0.040	0.094	0.425

Fig. 15 Second-stage vane aerodynamic forcing function variation due to the indexing of the first-stage stators at moderate loading

plate cascade prediction are presented in Fig. 13. The magnitude data both exhibit analogous trends, decreasing over the front part of the vane chord and increasing over the aft part of the vane, analogous to the high and moderate loading cases previously considered. There is good correlaton with the prediction over the front half of the vane for a (u^+/v^+) of 0.299, with the corresponding data for a (u^+/v^+) of 0.611 somewhat decreased in value but exhibiting the same trends. The phase data for a (u^+/v^+) value of 0.299 show trends similar to those obtained with a different aerodynamic forcing function but an analogous high level of aerodynamic loading (Fig. 7).

Thus, the transverse gust component of the aerodynamic forcing function has a larger effect on the phase of the dynamic pressure difference coefficient than either the steady loading or the chordwise gust component. However, both the chordwise and the transverse gust components, and the steady aerodynamic loading, influence the magnitude of the dynamic pressure difference coefficient.

Aft-Stage Vane Row Experiments

To investigate the aft-stage unsteady blade row interactions at a fixed operating point, the upstream stators are indexed circumferentially relative to the downstream instrumented vane rows, as previously noted and depicted in Fig. 2. Figure 14 presents the surface static pressure distributions on the downstream vane rows with the upstream stators indexed circumferentially 0, 25, 50, and 75 percent. The surface static pressure distributions are seen to be nearly independent of the circumferential indexing of the upstream stators, with only small variations apparent near the leading edge. Also, there is no evidence of flow separation.

Unsteady Aerodynamics—Adjacent Vane Row Indexing. The effect of indexing circumferentially (1) the first-stage stators on the second-stage vane row unsteady aerodynamics and (2) the second-stage stators on the third-stage vane row unsteady aerodynamics are considered.

Indexing the first-stage stators has a significant effect on the aerodynamic forcing function to the second-stage vane row. Figure 15 shows that the forcing functions differ significantly from one another and from the previously measured first-stage vane row forcing functions. This variation in the second-stage vane row forcing function at a single operating point is a multistage blade row interaction effect, with the second-stage rotor wake being modulated by the wakes from the upstream inlet guide vanes and the first-stage rotor blades and stator vanes. Also, this indexing is seen to have a larger effect on the amplitude of the chordwise gust than on the transverse gust, indicated by the wide range of values of the ratio (u^+/v^+).

The resulting chordwise distributions of the unsteady pressure difference coefficient on the second-stage vane row are presented in Fig. 16. At this moderate level of steady aerodynamic loading, the effects of circumferential indexing on the magnitude data are primarily found over the front 25 percent of the vane, with these magnitude data coalescing over the aft 75 percent of the chord. In contrast, the indexing affects the phase data over the complete vane chord. Also, the magnitude and phase data exhibit trends analogous to the previously presented first-stage vane row results, with the magnitude data decreased over the front part of the vane and increased over the aft part relative to the prediction. As the steady aerodynamic loading is independent of the indexing of the first stage stators, these effects are attributed to the differences in the chordwise and transverse gust components with indexing.

The effects of steady loading level and circumferential indexing of the first-stage stators are investigated by establishing a new compressor operating point. Figure 17 shows the effect of this indexing on the aerodynamic forcing function to the

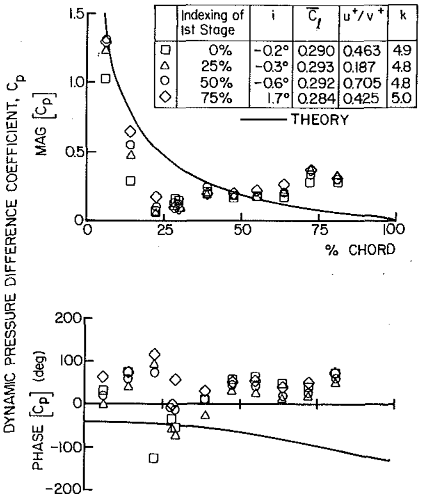

Fig. 16 Effect of first-stage stator indexing on second-stage vane unsteady pressure difference coefficient at moderate loading

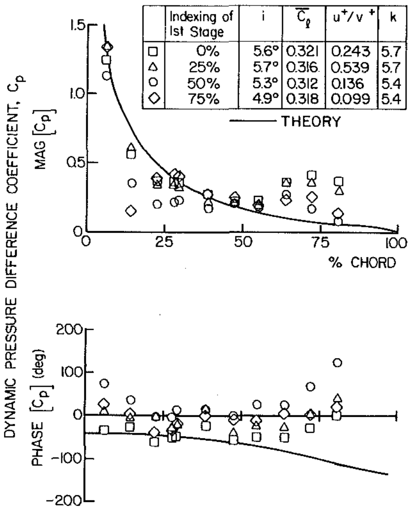

Fig. 18 Effect of first-stage stator indexing on second-stage vane unsteady pressure difference coefficients at high loading

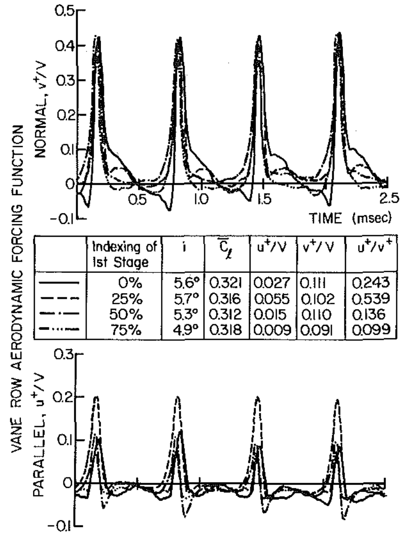

Fig. 17 Second-stage vane aerodynamic forcing function variation due to the indexing of the first-stage stators at high loading

second-stage vane row at this high loading condition. The indexing primarily influences the chordwise gust component, analogous to the lower loading case. Comparing the forcing functions at the two loading levels (Figs. 15 and 17) indicates that the compressor operating point has an effect on the forcing function.

The resulting chordwise distributions of the unsteady pressure difference coefficient in the second-stage vane row associated with these variations in the aerodynamic forcing function at this high loading level are presented in Fig. 18. The effect of this indexing is evident in the magnitude data over the front and aft part of the vane, not just the front as at the lower loading level, with the phase data still affected over the complete vane chord. Also, the magnitude data are decreased over the front and increased over the aft part of the vane as compared to the prediction. However, in the aft chord region, the magnitude data for the 0 and 25 percent indexing differ from that with 50 and 75 percent indexing. Namely, for 0 and 25 percent indexing, the magnitude data continue to increase as the trailing edge is approached relative to the prediction whereas the 50 and 75 percent indexing data decrease and correlate with the prediction in this aft chord region. This magnitude decrease for these two indexing positions is associated with the much smaller magnitudes of the chordwise gust component, as the normal gusts are nearly the same for all indexing positions. Again, the steady aerodynamic loading is independent of the indexing of the first-stage stators. Thus, these effects are attributed to the differences in the chordwise and transverse gust components with indexing.

The effect of indexing the second-stage stators on the aerodynamic forcing function to the third-stage vane row and the resulting chordwise distributions of the unsteady pressure difference coefficient on the third-stage vane row are presented in Figs. 19 and 20, respectively. The magnitudes of the gust components indicated by the values of the (u^+/v^+) ratio are similar to those found for the second stage at the same level of steady loading (Figs. 17 and 19). However, the aerodynamic forcing functions are different than those for the second-stage vane row at the same level of steady loading. This results from the third-stage vane row forcing function being affected by all of the individual component blade rows in the compressor, i.e., the wakes from the inlet guide vanes, the first and second-stage rotor blades and stator vanes, and the third-stage rotor blades.

The resulting third-stage vane row dynamic pressure difference coefficient data show that the forcing function variation with indexing affects the magnitude primarily over the front part of the vane, with the phase affected over the complete vane chord, analogous to previous results. However, these third-stage magnitude data differ from the analogous second-stage data at the same level of steady loading. In particular, the first and second-stage data increase relative to the prediction in the vane trailing edge region, whereas these third-stage data do not and, in fact, exhibit good correlation with the prediction in this region. Since there are no airfoils downstream of the third-stage vane row to influence the unsteady aerodynamics on the aft part of the vane, the increase in the magnitude data relative to the prediction for the first and second-stage vane rows is a multistage interaction effect.

Unsteady Aerodynamics—Upstream Row Indexing. To complete this study, the effect of circumferentially indexing the first-stage stators on the unsteady aerodynamics of the third-stage vane row are considered. The chordwise and transverse gust components defining the aerodynamic forcing function to the third-stage vane row are presented in Fig. 21. The indexing of the first-stage stators affects the third-stage forcing function, with the primary effect being on the chordwise gust component.

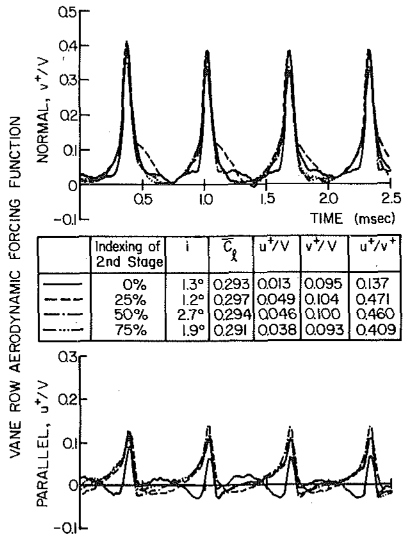

	Indexing of 2nd Stage	i	$\bar{C}_\ell$	u^+/V	v^+/V	u^+/v^+
——	0%	1.3°	0.293	0.013	0.095	0.137
– – –	25%	1.2°	0.297	0.049	0.104	0.471
—·—	50%	2.7°	0.294	0.046	0.100	0.460
—··—	75%	1.9°	0.291	0.038	0.093	0.409

Fig. 19 Third-stage vane aerodynamic forcing function variation due to indexing of the second-stage stators

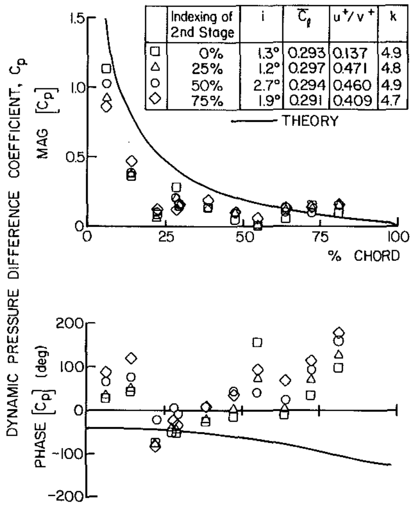

	Indexing of 2nd Stage	i	$\bar{C}_\ell$	u^+/v^+	k
□	0%	1.3°	0.293	0.137	4.9
△	25%	1.2°	0.297	0.471	4.8
○	50%	2.7°	0.294	0.460	4.9
◇	75%	1.9°	0.291	0.409	4.7

Fig. 20 Effect of second-stage stator indexing on third-stage vane unsteady pressure difference coefficient

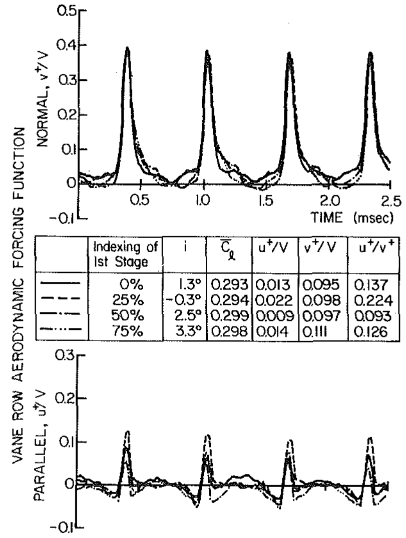

	Indexing of 1st Stage	i	$\bar{C}_\ell$	u^+/V	v^+/V	u^+/v^+
——	0%	1.3°	0.293	0.013	0.095	0.137
– – –	25%	-0.3°	0.294	0.022	0.098	0.224
—·—	50%	2.5°	0.299	0.009	0.097	0.093
—··—	75%	3.3°	0.298	0.014	0.111	0.126

Fig. 21 Third-stage vane aerodynamic forcing function variation due to indexing of the first-stage stators

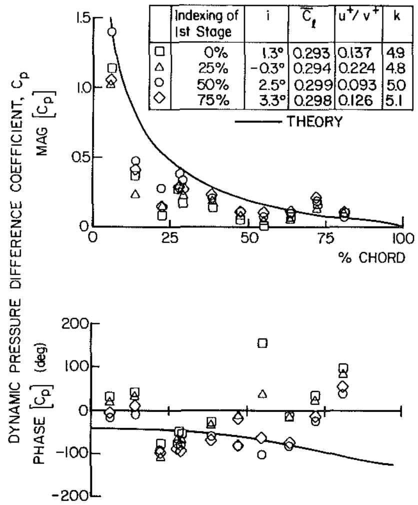

	Indexing of 1st Stage	i	$\bar{C}_\ell$	u^+/v^+	k
□	0%	1.3°	0.293	0.137	4.9
△	25%	-0.3°	0.294	0.224	4.8
○	50%	2.5°	0.299	0.093	5.0
◇	75%	3.3°	0.298	0.126	5.1

Fig. 22 Effect of first-stage stator indexing on the third-stage vane unsteady pressure difference coefficient

The resulting third-stage vane row chordwise distributions of the unsteady pressure difference coefficient are presented in Fig. 22. Again, the effect of the forcing function variation with indexing is evident in the phase data over the complete vane chord, but primarily affects the magnitude data over the front part of the vane. Also, the trailing edge region magnitude data are in good agreement with the prediction.

Summary and Conclusions

The rotor wake generated gust aerodynamics on each vane row of a three-stage axial flow research compressor, including the multistage interactions, were investigated by means of a series of experiments. In these, the effects of the following on the unsteady aerodynamics of each vane row were quantified: (1) the steady aerodynamic loading: (2) the detailed waveform of the aerodynamic forcing function, including the chordwise and transverse gust components.

The best correlation of the dynamic pressure difference coefficient data and the flat plate predictions is obtained at a low level of steady aerodynamic loading, indicating that the steady loading, not the incidence angle, is a key parameter. Also, the steady loading level and chordwise distribution have a significant effect on the unsteady aerodynamics of the vane row.

The transverse gust component of the aerodynamic forcing function has a larger effect on the phase of the dynamic pressure difference coefficient than either the steady loading or the chordwise gust component. However, the steady loading, and the chordwise and transverse gust components all influence the magnitude of the dynamic pressure difference coefficient.

The circumferential indexing of the upstream stators has no effect on the steady aerodynamic loading of downstream vane rows. However, indexing of the upstream vane rows does have a significant effect on the downstream aerodynamic forcing function and resulting chordwise pressure difference coefficient distributions, including the indexing of the first-stage stators affecting the third-stage vane row. The primary effect of the indexing is on the chordwise gust of the aerodynamic forcing function.

Circumferential indexing affects the magnitude of the dynamic pressure difference coefficient data over the front portion of the vane, with the phase data affected over the complete vane chord. The variations in the data as a function of indexing are attributed to the differences in the gust components of the aerodynamic forcing function, primarily the chordwise gust component, since the steady loading is constant.

For moderate levels of steady loading, the dynamic pressure difference coefficient magnitude data increase significantly relative to the prediction in the trailing edge region on the first and second-stage vane rows. However, for the same steady loading, the third-stage vane row data do not show this trend and, in fact, correlate quite well with the prediction. Since there are no blade rows downstream of the third-stage vane row, this increase in the magnitude data relative to the prediction for the first and second stage is a multistage blade row interaction effect.

The variations of the unsteady data with forcing function waveform cannot be predicted by harmonic gust models. This is because the forcing function waveforms and the resulting unsteady pressure distributions have been Fourier decomposed, with the first harmonics of the unsteady data presented. Thus, all of these first harmonic data are correlated with the same prediction curve, i.e., the predictions from these harmonic gust models are identical for all of the forcing function waveforms.

Acknowledgments

Support of this research program by the Air Force Office of Scientific Research, Dr. James Wilson program manager, is gratefully acknowledged.

References

1 Whitehead, D. S., "Force and Moment Coefficients for Vibrating Aerofoils in Cascade," Aeronautical Research Council R&M 3254, Feb. 1960.

2 Fleeter, S., "Fluctuating Lift and Moment Coefficients for Cascaded Airfoils in Nonuniform Compressible Flow," *AIAA Journal of Aircraft*, Vol. 10, Feb. 1973.

3 Naumann, H., and Yeh, H., "Lift and Pressure Fluctuations of a Cambered Airfoil Under Periodic Gusts and Applications in Turbomachinery," ASME JOURNAL OF ENGINEERING FOR POWER, Vol. 95, Jan. 1973.

4 Horlock, J. H., "Fluctuating Lift Forces on Aerofoils Moving Through Transverse and Chordwise Gusts," ASME *Journal of Basic Engineering*, Vol. 90, Dec. 1968.

5 Verdon, J. M., and Caspar, J. R., "Development of an Unsteady Aerodynamic Analysis for Finite Deflection Subsonic Cascades," NASA CR 3455, Sept. 1981.

6 Atassi, H. M., "The Sears Problem for a Lifting Airfoil Revisited—New Results," *Journal of Fluid Mechanics*, Vol. 141, 1984.

7 Englert, G. W., "Interaction of Upstream Flow Distortions With High Mach Number Cascades," ASME Paper No. 82-GT-137, 1982.

8 Fleeter, S., Jay, R. L., and Bennett, W. A., "Rotor Wake Generated Unsteady Aerodynamic Response of a Compressor Stator," ASME JOURNAL OF ENGINEERING FOR POWER, Vol. 100, Oct. 1978.

9 Fleeter, S., Bennett, W. A., and Jay, R. L., "The Time Variant Aerodynamic Response of a Stator Row Including the Effects of Airfoil Camber," ASME JOURNAL OF ENGINEERING FOR POWER, Vol. 102, Apr. 1980.

10 Capece, V. R., Manwaring, S. R., and Fleeter, S., "Unsteady Blade Row Interactions in a Multistage Compressor," *AIAA Journal of Propulsion*, Vol. 2, No. 2, Mar.-Apr. 1986.

11 Gostelow, J. P., "A New Approach to the Experimental Study of Turbomachinery Flow Phenomena," ASME JOURNAL OF ENGINEERING FOR POWER, Vol. 99, Jan. 1977.

The Deposition of Fog Droplets on Steam Turbine Blades by Turbulent Diffusion

K. K. Yau

J. B. Young

Whittle Laboratory,
University of Cambridge,
Cambridge, England

A theoretical approach for calculating the rate of deposition of fog droplets on steam turbine blades by turbulent diffusion is described. The theory is similar to that which has proved successful for predicting deposition of small particles in pipe flow and includes a recent correlation for the inertia-moderated regime. A reliable estimate of the blade surface shear stress distribution is required and is obtained by a quasi-three-dimensional inviscid flow calculation to give the blade surface velocity distribution, followed by a two-dimensional boundary layer calculation. The theory has been applied to two representative case studies. The first involves deposition on the final stage blading of the low-pressure cylinder of an operating 500 MW turbine, and the second concerns deposition in a high-pressure, wet steam turbine. Results are presented showing the effect of fog droplet size, surface roughness, and other flow parameters on the deposition rate. A comparison is made between the rates of deposition by diffusional and purely inertial mechanisms. In low-pressure turbines these are of comparable magnitude, but in high-pressure machines diffusional deposition may dominate.

Introduction

Condensation in wet steam turbines occurs initially by spontaneous nucleation from the vapor phase. The resulting fine homogeneous fog consists of water droplets having radii which, typically, lie in the range 0.05–1 μm. During the expansion of the steam through the latter stages of the turbine some of the fog droplets are deposited on the blade surfaces where they coagulate into films and rivulets and are drawn toward the blade trailing edges by the viscous drag of the steam. From time to time water is stripped off the trailing edges in the form of coarse droplets ($r < 100$ μm) which are accelerated by the steam until they impact onto the leading edge of the following blade row causing erosion damage.

Both inertial impaction and turbulent-diffusional mechanisms are responsible for the deposition of fog droplets onto the blade surfaces. Inertial-impaction is a laminar flow phenomenon and occurs because the droplets, although small, are unable to follow exactly the curved vapor streamlines. Turbulent-diffusional deposition is the process by which droplets entrained in the boundary layers migrate to the blade surfaces under the influence of random fluctuations in the flow.

In this paper, the most recent theories of turbulent-diffusional deposition (developed for pipe flow) are extended to predict the rate of fog droplet deposition on steam turbine blades. In particular, the effect of the variation of the blade surface shear stress is investigated using modern flowfield and boundary layer calculation procedures to obtain the frictional parameters. The results are illustrated using two case studies. The first involves the calculation of deposition rates in the final stage of a conventional fossil fuel, low-pressure turbine, and the second concerns deposition in a high-pressure, nuclear, wet steam turbine.

A search of the literature reveals that diffusional deposition of small particles in turbulent pipe flow has been the subject of a large number of investigations, both theoretical and experimental [1-9]. A good review can be found in [10]. Diffusional deposition in turbomachines, however, has not been studied so extensively. Some early calculations by Gardner [11] were extended in scope by Crane [12] using a more reliable theory for medium-sized droplets, but no simple theory was then available to estimate the diffusional deposition rate of the larger fog droplets. Subsequent investigations have concentrated on small particle deposition in gas turbines [13] and deposition in combustion systems [14]. The only relevant experimental work in turbine cascades is that by Parker et al. [15, 16].

Theory of Diffusional Deposition

In the present application, it is assumed that wet steam consists of a mixture of vapor and monodispersed spherical droplets of radius r. (The extension to polydispersed flows is straightforward if it is assumed that the droplets do not interact with each other.) In passing through a turbine blade passage, a certain number of droplets are deposited on the blade surface by diffusion through the boundary layer. Given c_∞, the volumetric concentration of droplets just outside the boundary layer, the problem is to calculate N, the mass

---

Contributed by the Power Division for publication in the JOURNAL OF TURBOMACHINERY. Manuscript received by the Power Division February 18, 1986.

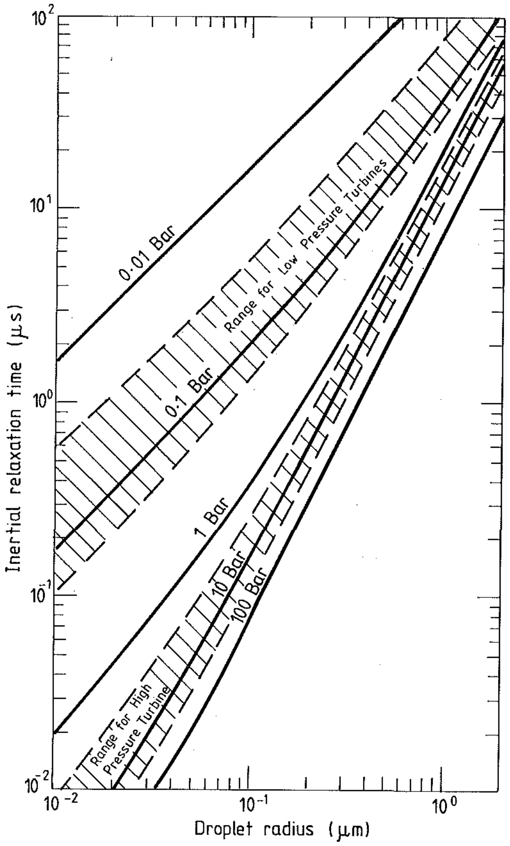

Fig. 1 Inertial relaxation time of monodispersed water droplets in steam

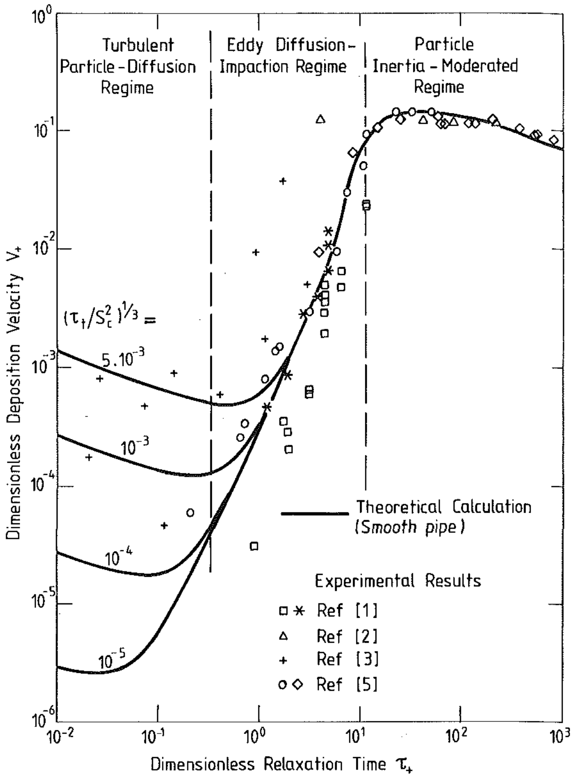

Fig. 2 Diffusional deposition in fully developed turbulent pipe flow: comparison of theory with experiment

transfer rate of droplets to the surface per unit area. Both c_∞ and N may vary with position on the blade surface.

Diffusional deposition data can usefully be correlated in the form

$$V_+ = f(\tau_+) \tag{1}$$

where V_+ $(=N/c_\infty u_*)$ is a dimensionless deposition velocity and τ_+ $(=\tau u_*^2/\nu_g)$ is a dimensionless droplet relaxation time. As shown in [17], the relaxation time τ can be represented with good accuracy by

$$\tau = \frac{2r^2\rho_l}{9\mu_g}(1+2.7\mathrm{Kn}) \tag{2}$$

where Kn $(=l_g/2r)$ is the Knudsen number of a droplet. Equation (2) is a composite formula for spherical droplets based on the Stokes drag law in the continuum regime $(\mathrm{Kn}<<1)$ and on the standard kinetic theory expression in the free molecular regime $(\mathrm{Kn}>>1)$. Figure 1 shows the variation of τ with droplet radius over the range of interest for a number of different steam pressures.

As shown in Fig. 2, three deposition regimes are usually identified. In the *Turbulent Particle-Diffusion Regime* $(\tau_+<0.1)$, particles are transported through the boundary layer by a combination of Brownian and eddy diffusion. The main resistance to mass transfer is in the almost laminar viscous sublayer very close to the surface and hence deposition rates are low and decrease with increasing particle size. In this regime V_+ is not a universal function of τ_+, but depends also on the Schmidt number $\mathrm{Sc}=\nu_g/D$.

For larger particles $(0.1<\tau_+<10)$, experiments show that there is a rapid increase in deposition rate by several orders of magnitude in the *Eddy Diffusion-Impaction Regime.* The

Nomenclature

b_+ = dimensionless displacement of boundary layer origin due to surface roughness = 0.45 k_+
c = volumetric concentration of droplets
c_∞ = value of c in the free stream
c_+ = c/c_∞
D = diffusion coefficient of droplets
F_D = fractional diffusional deposition rate
F_I = fractional inertial deposition rate
F = F_D+F_I
Kn = Knudsen number $=l_g/2r$
k_s = equivalent sand grain roughness height
k_+ = $k_s u_*/\nu_g$
l_g = mean free path of a vapor molecule
N = mass transfer rate of droplets to the surface per unit area
r = droplet radius
r_+ = ru_*/ν_g
Sc = Schmidt number $=\nu_g/D$
s = droplet stop distance
s_+ = su_*/ν_g
u_* = friction velocity (u_*^2 = surface shear stress/vapor density)
V = deposition velocity $=N/c_\infty$
V_+ = V/u_*
v = rms fluctuating component of droplet velocity normal to surface
v_g = rms fluctuating component of fluid velocity normal to surface
y = distance normal to surface
y_+ = yu_*/ν_g
ϵ = eddy diffusivity
μ_g = dynamic viscosity of vapor
ν_g = kinematic viscosity of vapor
ρ_l = density of liquid droplet
τ = inertial relaxation time of droplet
τ_+ = $\tau u_*^2/\nu_g$

transport mechanism here is not well understood and two distinct theories have been proposed, neither of which are well substantiated, but both of which predict the experimental data with acceptable accuracy. The earlier, "inertia-coasting" model [1, 4] assumed that particles diffused through the outer turbulent core of the boundary layer and were then thrown bodily across the viscous sublayer by large eddies in the buffer layer. Unfortunately, a serious physical inconsistency was detected in this model and a second theory [6] was proposed whereby particles are transported to the surface by the intermittent turbulent bursts of fluid which have been observed experimentally to disrupt the sublayer.

For very large particles ($\tau_+ > 10$) the deposition rate is observed to level off and then fall slightly in the *Particle Inertia-Moderated Regime*. Here the transport rate through the turbulent core of the boundary layer is reduced because the high inertia of the particles damps their response to the turbulent eddies.

The various mathematical models used for approximating the deposition characteristics in the three regimes closely follow the recommendations of Wood [9]. Basically, the mass transfer rate of droplets to the surface is calculated by integrating the diffusion equation across the boundary layer. The dimensionless turbulent version of Fick's law is

$$V_+ = \left(\frac{D}{\nu_g} + \frac{\epsilon}{\nu_g}\right)\frac{\partial c_+}{\partial y_+} \tag{3}$$

where $c_+ = c/c_\infty$ and $y_+ = yu_*/\nu_g$. The diffusion coefficient of the droplets D is given by the Einstein formula with a correction for rarefied gas effects

$$D = \frac{kT_g}{6\pi r\mu_g}(1 + 2.7\mathrm{Kn}) \tag{4}$$

Note that in equation (3) it has been assumed that convection effects are negligible.

In the turbulent diffusion and eddy diffusion-impaction regimes, the main resistance to diffusion is in the viscous sublayer ($0 < y_+ < 5$) and buffer layer ($5 < y_+ < 30$). It is, therefore, acceptable to assume the outer limit of integration to be $c_+ = 1$ at $y_+ = 30$. The inner limit of integration near the surface is more difficult to define. In order to model the inertia coasting effect the integration is terminated a distance s from the wall where s is the particle "stop distance." According to Wood this is given, in dimensionless form, by

$$s_+ = \frac{su_*}{\nu_g} = 0.69\tau_+ \tag{5}$$

The constant 0.69 was obtained by Wood by judiciously fitting the theoretical predictions to experimental measurements of deposition in turbulent pipe flow. If the surface is rough, the origin of the velocity profile is displaced a (nondimensional) distance [9]

$$b_+ = 0.45\frac{k_s u_*}{\nu_g} \tag{6}$$

where k_s is the equivalent sand grain roughness of the surface. The inner limit of integration is, therefore, $c_+ = 0$ at $y_+ = s_+ + b_+ + r_+$, where $r_+ = ru_*/\nu_g$.

In order to integrate equation (3), it is necessary to assume a variation of ϵ/ν_g with y_+; the well-known empirical expressions for eddy viscosity due to Lin et al. [18] were adopted.

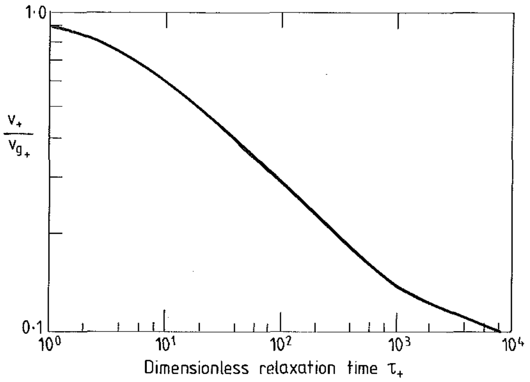

Fig. 3 Variation with τ_+ of the ratio of droplet to gas rms fluctuating velocities normal to a solid surface

These are based on measurements in turbulent pipe flows, but should give a good representation of the eddy viscosity on flat plates and turbine blades as it is the near wall region which is of main interest. The eddy diffusivity of the droplets is assumed equal to the eddy viscosity of the fluid, i.e., the turbulent Schmidt number is unity.

Integration of equation (3) (assuming that V_+ remains constant) gives

$$V_+ = (I_S + I_B)^{-1} \tag{7}$$

where I_S and I_B represent integrals across the sublayer and buffer layer, respectively. The expressions for I_S and I_B are as follows

$$\left.\begin{aligned} I_S &= 14.5\mathrm{Sc}^{2/3}[f(\phi) + g(\phi) - f(\phi_1) - g(\phi_1)] \\ I_B &= 24.2 \end{aligned}\right\} (s_+ + b_+ + r_+) < 5$$

$$\left.\begin{aligned} I_S &= 0 \\ I_B &= 5\ln[25.2/(s_+ + b_+ + r_+ - 4.8)] \end{aligned}\right\} (s_+ + b_+ + r_+) \geq 5$$

$$f(\phi) = \frac{1}{6}\ln\left[\frac{(1+\phi)^2}{1-\phi+\phi^2}\right]$$

$$g(\phi) = \frac{1}{\sqrt{3}}\arctan\left(\frac{2\phi - 1}{\sqrt{3}}\right)$$

$$\phi = 5/a$$

$$\phi_1 = (s_+ + b_+ + r_+)/a$$

$$a = 14.5\ \mathrm{Sc}^{-1/3}$$

Equations (7) are sufficiently accurate for $\tau_+ < 10$. For larger droplets in the inertia-moderated regime, a theory from Reeks and Skyrme [7] is employed. They showed that

$$V_+ = 0.56\eta\,\mathrm{erfc}\left(\frac{4.42}{\eta\tau_+}\right) \tag{8}$$

where η ($= v/v_g$) is the ratio of the droplet and fluid rms fluctuating velocity normal to the surface. For the conditions encountered in steam turbines, η can be related to τ_+ by the universal curve shown in Fig. 3, which is essentially a replotted version of Fig. 1 of [7].

Calculation Procedure

Given values of droplet concentration and radius at the outer edge of the boundary layer, equations (7) and (8) can be used to compute deposition rates if the local value of the friction velocity u_* is known. Unfortunately, fog droplets in steam turbines tend to be in the eddy diffusion-impaction regime and from Fig. 2 it may be deduced that comparatively

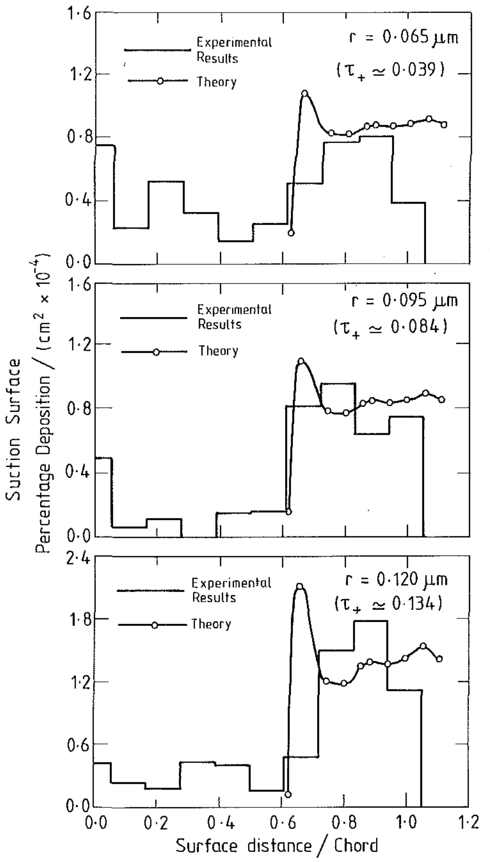

Fig. 4 Comparison of theory with experimental measurements of Parker and Lee [15]

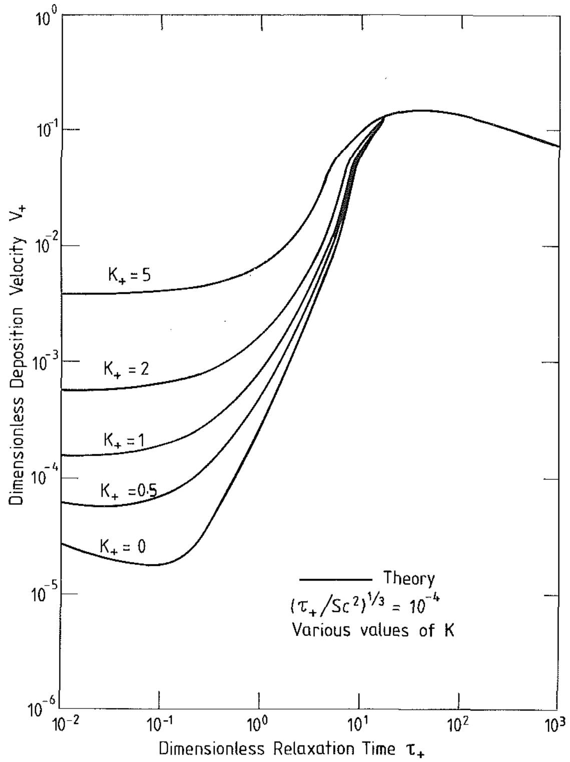

Fig. 5 The effect of surface roughness on diffusional deposition rate

small variations in u_* (and hence τ_+) may result in large changes in V_+. Furthermore, boundary layers on turbine blades are notoriously difficult to compute and, in particular, the difficulty of estimating the laminar-turbulent transition point is well known. Inasmuch as the mass transfer rate by Brownian diffusion through a laminar boundary layer is negligibly small, the accurate prediction of the transition point is obviously crucial to the calculation of deposition rates.

In all the calculations presented below, the friction velocity was obtained using a boundary layer computational procedure written at the National Gas Turbine Establishment and based on the Green Lag Entrainment method [19]. This is as accurate a technique as is available at the present time. The blade surface pressure distribution required as input data for the program was obtained using a quasi-three-dimensional inviscid flow calculation method for subsonic and transonic turbines. This consisted of the application of an axisymmetric streamline curvature throughflow calculation to locate the streamsurfaces of revolution, followed by a blade-to-blade time-marching calculation to give the required pressure distribution. The time-marching technique [20] was quasi-three-dimensional in the sense that it included the effects of change of streamsurface radius and streamtube divergence, but did not take into account the twisting of streamsurfaces within the blade passage. The calculation of the friction velocity distribution was non-iterative, i.e., the throughflow, blade-to-blade, and boundary layer calculations were each performed once only for a particular blade section.

Comparison of Theory With Experimental Data

The bulk of the experimental data available involve measurements of the deposition of suspended particles in turbulent pipe flow. Of these data, the most reliable and comprehensive measurements are those reported in [1-3, 5]. Figure 2 shows a compilation of these results together with the predictions of the theory described above. Good agreement is obtained except for small values of τ_+ where Brownian diffusion through the viscous sublayer dominates, causing the deposition rate to be very low and difficult to measure accurately. In this regime, the deposition rate is also very sensitive to surface roughness [8, 9], but, in the absence of information to the contrary, it was assumed that all the tests represented in Fig. 2 were conducted in hydraulically smooth pipes.

The measurements of Parker et al. [15, 16] are of considerable interest as they comprise the only data available pertaining to the diffusional deposition of small particles on turbine blades. Of particular value is the fact that the distribution of deposition rate over the blade surface is presented for a number of different droplet sizes.

The measured surface velocity distribution of the blade used in the experiments is given in [15] and this was sufficient information to enable values of u_* to be computed by the N.G.T.E. boundary layer program. The pressure surface boundary layer was completely laminar and transition on the suction surface occurred shortly after midchord. A comparison between the experimental results and deposition theory is shown in Fig. 4 for the suction surface of the blade. (Deposition on the pressure surface is negligible.) The agreement is excellent considering the difficulties of the measurements and gives considerable confidence in the calculation procedure, at least for the very small values of τ_+ featured in the experiments.

Effect of Surface Roughness

Figure 5 shows the effect of surface roughness on deposition rate computed using the above theory which, according to [9], is valid for $k_+ < 5$. It is evident that increasing roughness enhances the deposition rate in the turbulent particle-diffusion regime, but has little effect for larger values of τ_+. Typical roughness measurements on machine-shop-polished turbine blades give roughness heights k_s of between 1 and 4 μm,

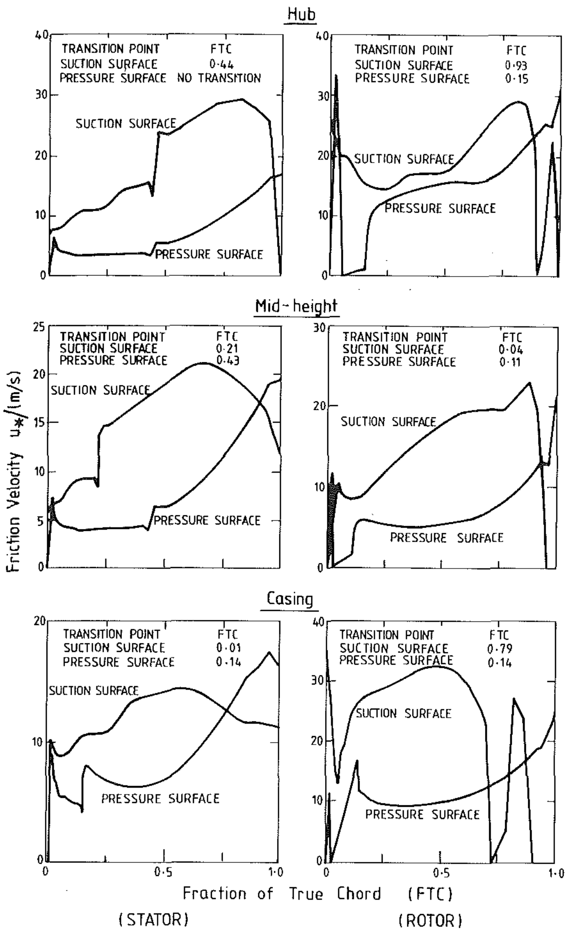

Fig. 6 Friction velocity distributions for the stator and rotor blades of the 500 MW, LP turbine

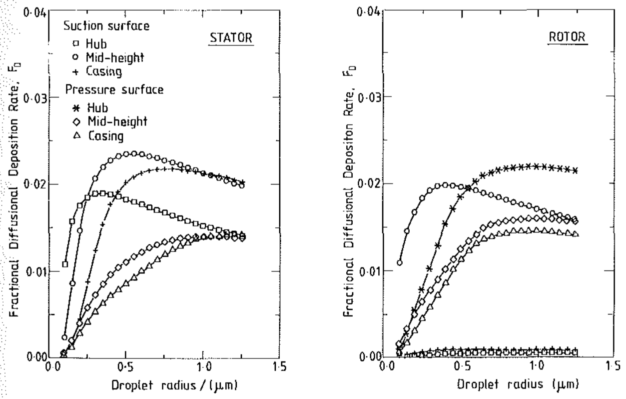

Fig. 7 Diffusional deposition on the stator and rotor blades of the 500 MW, LP turbine (on-design calculation)

which, for low-pressure blading ($\nu_g \cong 10^{-4}$ m^2/s, $u_* \cong 20$ m/s), imply $0.2 < k_+ < 0.8$. For $k_+ < 2$, Fig. 5 shows that V_+ is almost independent of surface roughness for $\tau_+ > 2$. Furthermore, for small droplets such that $\tau_+ < 2$, the rate of deposition is so low as to be quite negligible. It can therefore be concluded that, with the exception of highly eroded blades, diffusional deposition on low-pressure blading is unaffected by surface roughness, and calculations may be performed assuming the blades to be hydraulically smooth.

For high-pressure blading operating in wet steam at a pressure of 50 bar ($\nu_g \cong 10^{-6}$ m^2/s, $u_* \cong 10$ m/s), $10 < k_+ < 40$ corresponding to similar values of k_s. Roughness heights of this magnitude will significantly affect deposition in the eddy diffusion-impaction regime. Fortunately, however, at this pressure, all droplets with radii greater than 0.1 μm fall in the inertia-moderated regime. In this region, a comparison of the smooth wall data of [5] with the rough surface measurements of [2] indicates that deposition rate is largely independent of roughness height.

Case Study 1: Deposition on the Final Stage Blading of the LP Cylinder of a 500 MW Turbine

In order to illustrate both qualitative and quantitative effects of deposition in low-pressure turbines, a complete analysis for the final (sixth) stage of an operating 500 MW turbine was performed. A case study of deposition by inertial-impaction on identical blading is reported in [21] and one of the objectives of the present exercise was to compare the relative importance of the two mechanisms.

The turbine stage selected for analysis was typical of modern design, having long, highly twisted blading and a high casing flare angle. Full details of the geometry and flowfield calculations can be found in [21]. Briefly, however, a quasi-three-dimensional inviscid flow analysis was performed to give detailed blade surface Mach number distributions along three streamsurfaces intersecting each of the stator and rotor blades. These streamsurfaces will be referred to as the hub, midheight, and casing streamsurface, respectively. The six Mach number distributions thus generated formed the input data for the N.G.T.E. boundary layer computer program used to estimate the friction velocity distribution on the six profiles. The results of these calculations can be seen in Fig. 6.

The theoretical predictions of deposition rate are presented as curves of *Fractional Diffusional Deposition Rate* F_D versus droplet radius r. Considering the mass flowrate of water entering a blade row through a streamtube of thickness dR situated a radial distance R from the turbine axis at blade inlet, F_D is defined as the fraction of this water flow rate which is deposited on the blade by diffusional deposition. For deposition by inertial impaction, the *Fractional Inertial Deposition Rate* F_I is defined similarly and the *Total Fractional Deposition Rate* F is equal to $F_D + F_I$.

Calculations were first performed for the on-design condition (i.e., assuming the steam inlet angle equal to the blade inlet angle), and Fig. 7 shows curves of F_D as a function of fog droplet radius for both stator and rotor blades. For droplets with radii lying in the range 0.1–0.5 μm, values of F_D increase rapidly to a maximum of about 2 percent. This corresponds to the eddy diffusion-impaction regime and the exact form of the curves depends on the shear stress distribution as well as the droplet radius. For larger droplets in the inertia-moderated regime, the dependence on both the friction velocity and droplet radius is much less and the curves tend to flatten out. The deposition on the suction surface of the rotor, both near the hub and the casing, is very low because transition is predicted close to the trailing edge.

Inasmuch as the off-design operation of turbine blades affects the blade surface velocity distribution and boundary layer development, the diffusional deposition rate is also affected by variations in the flow inlet angle. In order to investigate this effect, calculations were performed for the midheight streamsurface profile of the stator blade for flow incidence angles of ±10 deg. The results shown in Fig. 8 indicate that, for small negative incidence angles, the deposition rates on both the pressure and suction surfaces are only marginally affected. On the other hand, positive flow incidence angles have a significant effect on the position of the laminar-turbulent transition and this is reflected by large variations in the deposition rates. On the pressure surface, transition is displaced toward the trailing edge resulting in a decrease in the deposition rate, and vice versa on the suction surface. The effects are partially self-cancelling, however, and

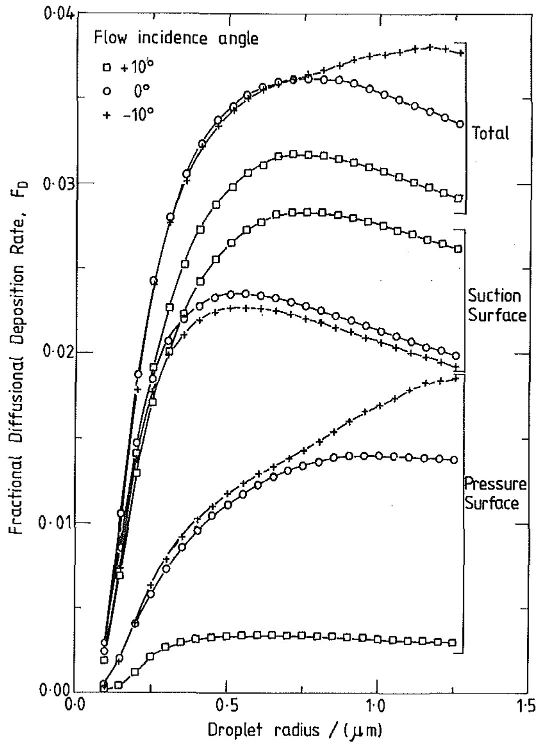

Fig. 8 Diffusional deposition on the stator blade of the 500 MW, LP turbine (midheight streamsurface, off-design calculation)

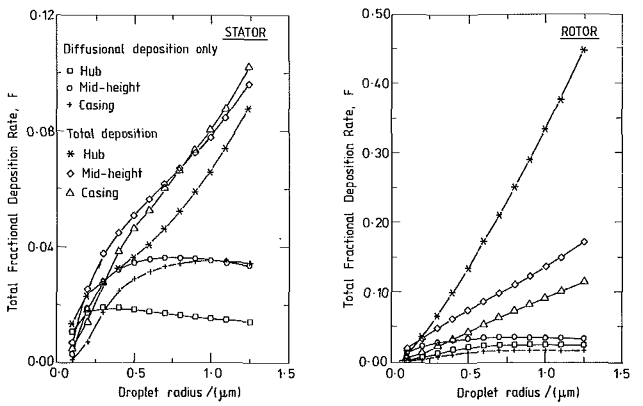

Fig. 9 Total deposition on the stator and rotor blades of the 500 MW, LP turbine (on-design calculation)

the sum total of deposition on both surfaces is not greatly affected.

Figure 9 shows the total fractional deposition rate ($F = F_I + F_D$) for the stator and rotor blades as functions of fog droplet radius, values of F_I being taken directly from [21]. (Note the different ordinate scales for the two graphs of Fig. 9.) Also plotted are curves showing the contribution from diffusional deposition alone. Over most of the range of droplet sizes considered, inertial-impaction and turbulent-diffusional mechanisms make comparable contributions to the overall deposition rate, except near the hub of the rotor where inertial-impaction effects predominate.

Case Study 2: Deposition in a High-Pressure, Wet Steam Turbine

The second case study concerns deposition on a typical stage of the high-pressure cylinder of an operating 500 MW nuclear wet-steam turbine. All stages were composed of the same blade profile with stators and rotors identical. Accordingly only one blade-to-blade analysis was required and this was nominally performed for the midheight streamsurface of the stator of the seventh stage, which occupied a position midway through the 14-stage turbine.

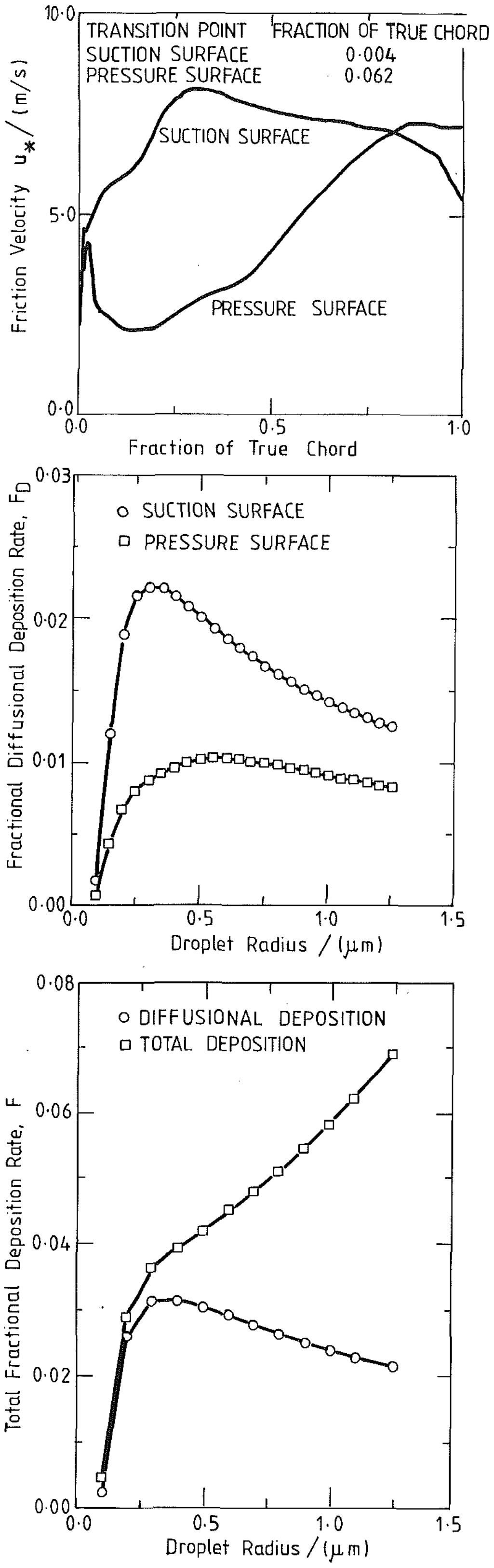

Fig. 10 Diffusional and inertial deposition on the HP stator blade (on-design calculation)

Figure 10 shows the friction velocity distribution generated by the N.G.T.E. boundary layer program and the predicted values of fractional diffusional deposition rate on the suction and pressure surfaces of the blade. In contrast to the low-pressure calculations, even quite small droplets fall within the inertia-moderated regime and consequently the deposition rates vary more uniformly with droplet size. The overall magnitude of F_D is almost unaltered, however, from the maximum values predicted for the low-pressure blading.

The total fractional deposition rate ($F=F_I+F_D$) as a function of droplet radius is also presented in Fig. 10, values of F_I being taken from [21]. It is noteworthy that, for droplets having radii less than 0.5 μm, the deposition is predominantly by diffusion rather than inertial impaction.

Conclusions

1 Deposition of fog droplets on steam turbine blades by turbulent diffusion through the boundary layer is very sensitive to droplet size and blade boundary layer development. Accurate information concerning the location of the laminar-turbulent transition and the variation of surface shear stress in the turbulent boundary layer regions are essential for good predictions. This is particularly important for low-pressure blading where the droplet spectrum tends to span the eddy diffusion-impaction regime. High-pressure blading is less sensitive as droplet sizes usually fall in the inertia-moderated regime.

2 Diffusional deposition through laminar boundary layers is quite negligible.

3 The fractional diffusional deposition rate on either the suction or pressure surface of a blade is unlikely to exceed 2 percent even in the inertia-moderated regime. This is true for both low and high-pressure blading. Deposition rates on the suction surface tend to be higher than on the pressure surface because of the higher turbulence levels.

4 The effect of surface roughness on deposition on low-pressure blading is negligible providing the equivalent sand grain roughness of the blade is less than 20 μm. On high-pressure blading it is possible that typical levels of roughness may significantly affect deposition rates.

5 Over the range of droplet sizes found in low-pressure steam turbines, diffusional deposition rates are comparable to those by inertial impaction. In high-pressure machines diffusional deposition may predominate.

Acknowledgments

The work was carried out at The Whittle Laboratory, University of Cambridge, and was supported by a grant from the Central Electricity Research Laboratories, Leatherhead. One of the authors (KKY) was supported by a Croucher Foundation Scholarship during the course of the work.

References

1 Friedlander, S. K., and Johnstone, H. F., "Deposition of Suspended Particles From Turbulent Gas Streams," *Ind. Eng. Chem.*, Vol. 49, 1957, pp. 1151–1156.

2 Chamberlain, A. C., "Transport of Lycopodium Spores and Other Small Particles to Rough Surfaces," *Proc. Roy. Soc.*, Vol. 296A, 1967, pp. 45–70.

3 Montgomery, T. L., and Corn, M., "Aerosol Deposition in a Pipe With Turbulent Airflow," *J. Aerosol Science*, Vol. 1, 1970, pp. 185–213.

4 Beal, S. K., "Deposition of Particles in Turbulent Flow on Channel or Pipe Walls," *Nuclear Sci. and Eng.*, Vol. 40, 1970, pp. 1–11.

5 Liu, B. Y. H., and Agarwal, J. K., "Experimental Observation of Aerosol Deposition in Turbulent Flow," *J. Aerosol Science*, Vol. 5, 1974, pp. 145–155.

6 Cleaver, J. W., and Yates, B., "A Sub-layer Model for the Deposition of Particles From a Turbulent Flow," *Chem. Eng. Sci.*, Vol. 30, 1975, pp. 983–992.

7 Reeks, M. W., and Skyrme, G., "The Dependence of Particle Deposition Velocity on Particle Inertia in Turbulent Pipe Flow," *J. Aerosol Science*, Vol. 7, 1976, pp. 485–495.

8 El-Shobokshy, M. S., and Ismail, I. A., "Deposition of Aerosol Particles From Turbulent Flow Onto Rough Pipe Wall," *Atmospheric Environment*, Vol. 14, 1980, pp. 297–304.

9 Wood, N. B., "A Simple Method for the Calculation of Turbulent Deposition to Smooth and Rough Surfaces," *J. Aerosol Science*, Vol. 12, 1981, pp. 275–290.

10 Hidy, G. M., and Heisler, S. L., in: *Recent Developments in Aerosol Science*, D. T. Shaw, ed., Wiley Interscience, New York, 1979.

11 Gardner, G. C., "Events Leading to Erosion in the Steam Turbine," *Proc. Instn. Mech. Engnrs.*, Vol. 178, 1963–64, p. 593.

12 Crane, R. I., "Deposition of Fog Drops on Low Pressure Steam Turbine Blades," *Int. J. Mech. Sci.*, Vol. 15, 1973, pp. 613–631.

13 Menguturk, M., and Sverdrup, E. F., "A Theory for Fine Particle Deposition in Two-Dimensional Boundary Layer Flows and Application to Gas Turbines," ASME JOURNAL OF ENGINEERING FOR POWER, Vol. 104, 1982, pp. 69–76.

14 Rosner, D. E., and Seshadri, K., "Experimental and Theoretical Studies of the Laws Governing Condensate Deposition From Combustion Gases," *Eighteenth Int. Symp. on Combustion*, 1980, pp. 1385–1393.

15 Parker, G. J., and Lee, P., "Studies of the Deposition of Submicron Particles on Turbine Blades," *Proc. Inst. Mech. Engnrs.*, Vol. 186, 1972, pp. 519–526.

16 Parker, G. J., and Ryley, D. J., "Equipment and Techniques for Studying the Deposition of Submicron Particles on Turbine Blades," *Proc. Instn. Mech. Engnrs.*, Vol. 184, Part 3C, 1969–70, pp. 43–51.

17 Gyarmathy, G., "Bases of a Theory for Wet Steam Turbines," Bull. 6, Inst. for Thermal Turbomachines, Federal Technical University, Zurich, 1962.

18 Lin, C. S., Moulton, R. W., and Putnam, G. L., "Mass Transfer Between Solid Wall and Fluid Streams," *Ind. Engng. Chem.*, Vol. 45, 1953, p. 636.

19 Herbert, M. V., and Calvert, W. J., "Description of an Integral Method for Boundary Layer Calculation in Use at N.G.T.E., With Special Reference to Compressor Blades," National Gas Turbine Establishment, Memo M82019, 1982.

20 Denton, J. D., "An Improved Time-Marching Method for Turbomachinery Flow Calculation," ASME *Journal of Engineering for Power*, Vol. 105, 1983, pp. 514–524.

21 Young, J. B., and Yau, K. K., "The Deposition of Fog Droplets on Steam Turbine Blades by Inertial Impaction," submitted to ASME *Journal of Engineering for Gas Turbines and Power*.

Particle Transport Across the Transpired Turbulent Boundary Layer

H. Kozlu
Graduate Student.

J. F. Louis
Professor.

Department of Aeronautics
and Astronautics,
Massachusetts Institute of Technology,
Cambridge, MA 02139

The results of the experimental and theoretical investigation are presented to determine the effects of surface inclination and density of particulates on deposition control by transpiration. Effects of the particle size and injection rate were reported in a recent paper by Kozlu and Louis (1986). The purpose of this work is to obtain a better insight into the deposition process by investigating the different aspects of the problem. An application of the work is the control of deposition of small particles (0.5-3 μm) contributing most of the mass of the solid carryover entering turbines burning fuels derived from coal. Experimental study is carried out in a wind tunnel facility containing a porous transpired section. Similar flows and particle motions are achieved by choosing the proper Reynolds and Stokes numbers which are representative of the conditions found in industrial gas turbines. The study after reviewing the effects of size and injection rates on deposition determines the interaction between transpiration and the inertial impaction of particulates using the glass particles. Tests were also conducted on the inclined plate with coal particles to determine the density effects on the particle concentration profiles and consequently on the arrival rates. Experimental data are used to predict the concentration profiles of particulates for different density values. For inclined plate experiments, the turbulent Schmidt numbers obtained from the experiments are in agreement with the theoretical prediction of Tchen (1947) as found in the flat plate.

Introduction

Deposition is one of the major phenomena which could hamper the operating life and performance of coal-fired gas turbines. The chemical variability of coal, the complexity of its combustion and ash behavior, the intricacy of deposition and surface physics and chemistry plus the requirements of turbine part-load operation make the problems associated with coal burning gas turbines look almost insurmountable. A careful consideration of the key phenomena of deposition suggests solutions which could greatly reduce or eliminate the deleterious effects of burning coal in industrial gas turbines. It is believed that the direct solution method is to avoid the deposition of particulates using transpiration.

Transpiration cooling is one of the most important schemes for air cooling. However, until today it has been studied to reduce high heat fluxes. An extensive study of transpiration cooling is presented by Georgiou and Louis (1985). The purpose of the present research is to control the deposition of particulates using transpiration, which could create enough momentum to prevent deposition.

Particle deposition depends on the gas composition, temperature, particle size, blade configurations, and surface temperature. Under the conditions of highly cooled blades, deposits will be in solid phase at the metal surface and will be swept away in the regions of high shear existing around the leading edge and the pressure side of blades. Therefore, deposits are likely to be formed in the regions of low shear existing on the suction sides of blades. When the large particles depositing by inertial impaction are removed by cyclones or other devices, deposition occurs by diffusion processes. Under these conditions, particles carried over in industrial gas turbines are in the size range of 0.5-3 μm.

The turbulent diffusion process is mainly determined by the particle Stokes number. This important dimensionless number is defined as the ratio of particle relaxation time τ_p to the turbulent fluctuation time τ_f. The present paper focuses on the particles which have a Stokes number between 1 and 3.5, which is chosen as representative of industrial gas turbine conditions. The turbulent Schmidt number associated with turbulent diffusion of such particles obtained from Tchen's (1947) analysis in the case of homogeneous turbulence is in the range of 2-6.

It is expected that transpiration could avoid the deposition of particles having a Stokes number of 1-3.5. Kozlu and Louis (1986) studied the effects of transpiration rate and of particle size on deposition control strategy. The purpose of the present paper is to extend the previous work to analyze the effects of particulate density and inclination on deposition control.

The study first reviews the effect of the particle size. Then, based on the analysis and available data, density effects on

---

Contributed by the Gas Turbine Division of THE AMERICAN SOCIETY OF MECHANICAL ENGINEERS and presented at the 32nd International Gas Turbine Conference and Exhibit, Anaheim, California, May 31-June 4, 1987. Manuscript received at ASME Headquarters February 27, 1987. Paper No. 87-GT-265.

concentration profiles and consequently on the arrival rates are presented. Effect of inclination is also determined in an experimental setup using an inclined transpired plate. Measurements allow a determination of the turbulent particle Schmidt number using the Tchen equation.

Experiment

The objective of the experiment is to measure the concentration profiles over a transpired porous plate for different particle sizes and densities and injection rates. Similar flows and particle motions are achieved by choosing the correct Reynolds and Stokes numbers which simulate those of industrial gas turbines (e.g., $T_{gt} = 1200$ K, $U_{gt} = 330$ m/s, and static pressure = 6 atm). Since the experimental wind tunnel operates at pressures and temperatures close to ambient, for a velocity of 25 m/s equality of Reynolds numbers yields a length scale of $L_{\text{exp}}/L_{gt} = 10$. Identity of Stokes numbers requires the ratio of particulate density of $\rho_{Pgt}/\rho_{P\text{exp}} = 1.5$. The spherical glass particles having a density of 2.42 g/cm^3 in the size range of 5-30 μm and coal particles of density of 1.27 g/cm^3 in the size range of 5-14 μm are used in the experiment to represent a particulate-laden flow found in the typical gas turbines. The density of the ash particles from coal varies from 1.3 to 5 g/cm^3 depending on the type of coal and temperature-time history. Therefore, the tests with glass particles correspond to the particles of 3.63 g/cm^3 density on the heavy end of the ash density scale. Coal particles are used to simulate the tests on the light end of the ash density scale. The classification of glass microbeads is performed using the available "MAJAC-ACUCUT Air Classifier" and their size distributions are obtained by utilizing the optical microscope.

I Experimental Setup

Figures 1 and 2 illustrate the schematic drawings of the experimental facility with a wind tunnel capable of providing a flow of 50 m/s in a 0.31 × 0.31 m cross-sectional test unit. The experimental facility includes an entrained fluidized particle feeder system, a mixing section with a diffuser, a coolant injection system, a test section, and an existing exhaust section.

Particles are injected in the main flow by an entrained fluidized particle feeder system. Particles are fed from a bunker to the base of the fluidization section using a screwfeeder driven by an electric motor with a feedback control (Fig. 1). Air flow rate is adjusted by a throttle valve and measured by a Fisher flowmeter. The entrained fluidized particle feeder system enables us to regulate the particle feed rate continuously and precisely while achieving uniform injection. The particle-laden flow is injected at the tunnel throat, which is followed by a section designed to achieve complete mixing. The coolant injection system is used to introduce an uniform transpiration fluid into the main flow. It is made of a coolant injection box consisting of two porous plates to provide an uniform transpired injection through the porous plate installed in the test section (Fig. 1). The air for transpiration is supplied from an existing compressor and the line pressure is controlled by a Watts pressure regulator. The desired flow rate is achieved using a throttle valve and determined by a Fisher flowmeter. The test section, which has a cross section of 0.31 × 0.31 m, is connected to the mixing section of the experimental facility. It uses a 0.10 × 0.25 m size, sintered bronze, rectangular transpiration plate of 1/8 in. thickness. The porous transpiration plate is a 103A type plate from Thermit Co., MA. This type was selected because of its very small roughness of average 4 μm, measured by Talisurfmeter. The Reynolds number based on the plate length is 1.6×10^5 for the flow velocity of 25 m/s. The test section also contains a vertical positioning system (Fig. 2) to traverse the boundary layer in the vertical direction. This system is made very rigid by the use of a moving aluminum frame.

II Measurement Techniques

(a) Turbulence Intensity Measurements. The turbulence intensity of the wind tunnel is measured by using the hot-wire anemometer of TSI Model 1051-2, which applies a constant temperature arrangement. Measured turbulence intensity of

Nomenclature

b = injection parameter = (F/St_o) or $(2F/C_{fo})$
C = mean value of particle concentration
$\tilde{C} = C/C_\infty$ = dimensionless mean value of particle concentration
C_f = skin friction coefficient
C_{ow} = measured mean value of particle concentration at the wall
$\tilde{C}_{ow} = C_{ow}/C_\infty$ = dimensionless measured mean value of particle concentration at the wall
C_p = specific heat at constant pressure
d_m = particle mean diameter
D = diffusion coefficient
F = injection rate = $((\rho V)_w/(\rho U)_\infty)$
I = attenuated beam intensity
I_o = nonattenuated beam intensity
$\text{Sc}_T = \nu_T/D_T$ = turbulent Schmidt number
$\text{St}k = \rho_p d_m^2 U_\infty/18\mu\delta$ = particle Stokes number
U = mean value of streamwise velocity
$\tilde{U} = U/U_\infty$ = dimensionless mean value of streamwise velocity
V = transpiration velocity
x = streamwise coordinate
y = transverse coordinate
$\tilde{y} = y/\delta_c$ = dimensionless transverse coordinate
δ_c = concentration boundary layer thickness
δ_m = momentum boundary layer thickness
η = similarity variable
μ = fluid dynamic viscosity
ν_T = turbulent kinematic viscosity
ρ = fluid density
ρ_p = particle density
σ = standard deviation
τ_f = turbulent fluctuation time
$\tau_p = \rho_p d_m^2/18\mu$ = particle relaxation time

Subscripts

exp = experiment
gt = gas turbine
f = fluid
o = solid wall
p = particle
T = turbulent
w = at the wall
∞ = free-stream conditions

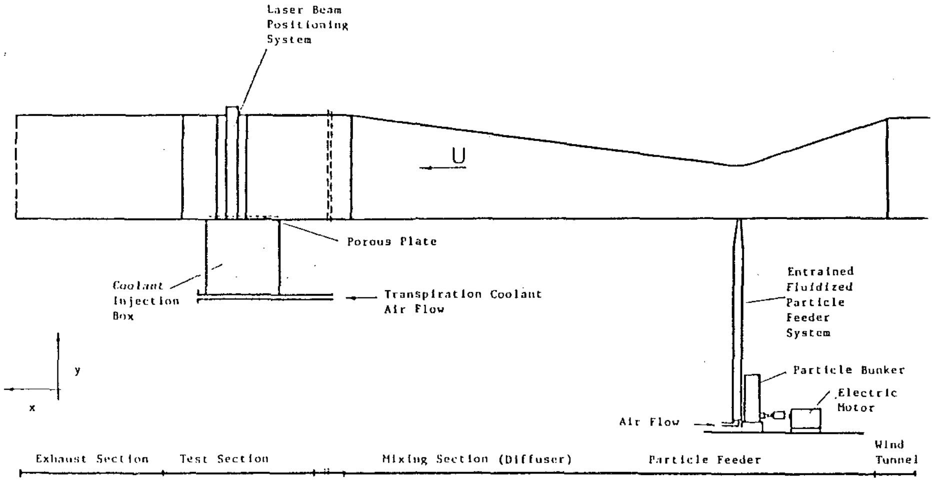

Fig. 1 Schematic drawing of the experimental facility

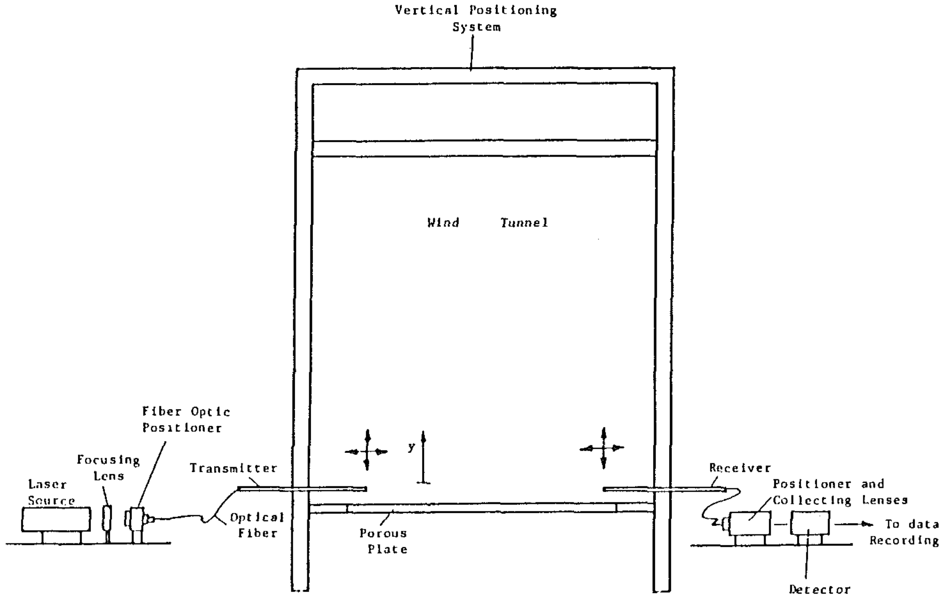

Fig. 2 Schematic drawing of the laser beam positioning system

the tunnel is about 2.85 percent for the wind tunnel speed of 25 m/s.

(b) Particle Concentration Measurements. A laser system is developed to determine the distribution of particle concentration within the boundary layer near the transpired plate (Fig. 2). The laser light emitted from a helium neon laser (6328 Å) of 1 mW is coupled into the single-mode optical fiber of core diameter of 4 μm using the Newport precision fiber coupler F-915 so that the single-mode fiber coupling efficiency is maximized by matching the incident optical field distribution to the fiber mode profile. The ends of the optical fibers are polished. A well-collimated laser beam is obtained from the single-mode optical fiber through a Selfoc microlens installed at the end of the transmitter. Selfoc is a cylindrical lens which has a refraction index decreasing as the square of the radial distance from the optical axis. Because of this parabolic index of refraction, it performs the same optical function as a spherical lens although it has a flat end surface. The Selfoc microlens has a diameter of 2.0 mm and a length of 16 mm and a divergent angle of less than 0.06 deg when used in conjunction with a single-mode fiber. The well-collimated laser beam of about 0.5 mm diameter emitted from the transmitter traverses the boundary layer parallel to the porous plate and perpendicular to the approaching flow. The attenuated beam is picked up by a receiver using a multimode fiber of core diameter of 1 mm and its intensity is measured by a EMI-GENCOM photomultiplier. Since, for monosize particles, the variation of the beam intensity is related to the particle concentration through the relation

$$\frac{dC}{C}=\frac{d\ln I/I_0}{\ln I/I_0} \tag{1}$$

the attenuation of the beam gives an indication of the particle concentration in the boundary layer. The coupling of both the transmitter and the receiver to the positioning frame is made by using the Newport precision positioners FP-2. A second identical stationary beam is located just upstream of the moving beam at 3 cm from the transpired wall to verify the uniformity of the particle loading of the mainstream.

Experimental Results and Analysis

(a) Effect of Particle Size. As indicated in Kozlu and Louis

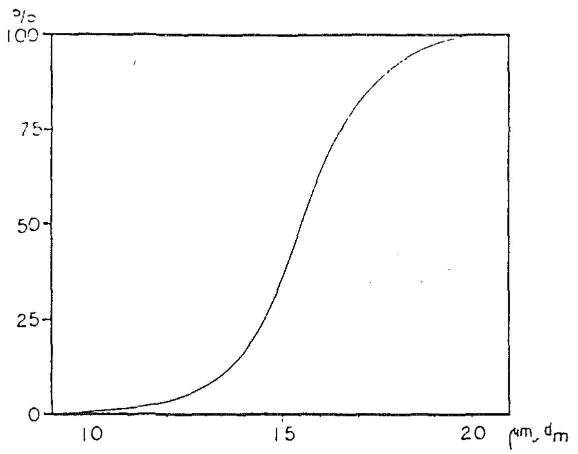

Fig. 3(*a*) Cumulative particle size distribution curve

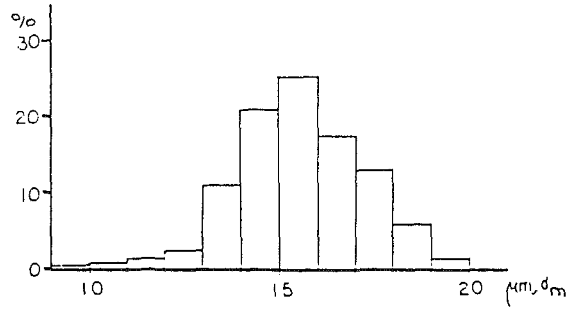

Fig. 3(*b*) Frequency distribution curve for number of particles with respect to particle size (based on 468 particles): $d_m = 16.03$ μm; $\sigma = 1.73$ μm

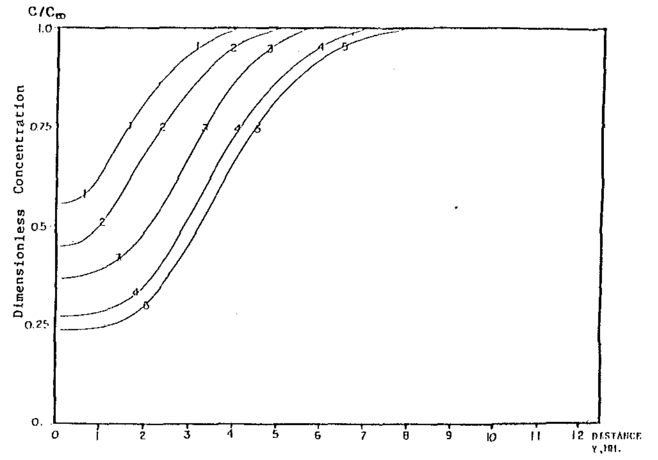

Fig. 4 Particle concentration profiles for different particle sizes and for the injection rate of 2.09 percent: (1) $d_m = 24.17$ μm, $\sigma = 2.40$ μm; (2) $d_m = 20.60$ μm, $\sigma = 2.53$ μm; (3) $d_m = 18.88$ μm, $\sigma = 2.047$ μm; (4) $d_m = 16.03$ μm, $\sigma = 1.73$ μm; (5) $d_m = 14.09$ μm, $\sigma = 1.824$ μm

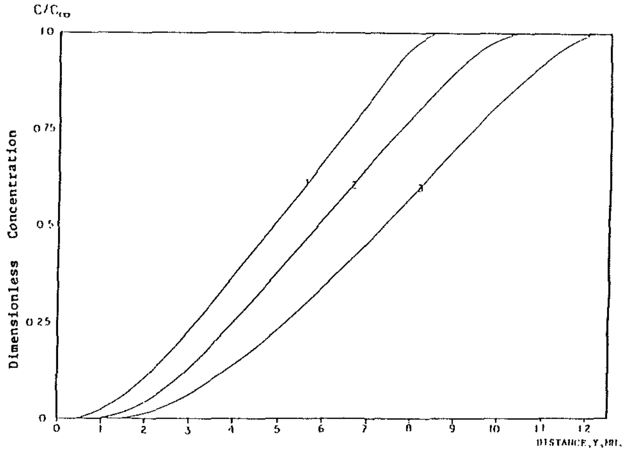

Fig. 5 Particle concentration profiles for different particle sizes and for the injection rate of 2.76 percent: (1) $d_m = 22.36$ μm, $\sigma = 3.32$ μm; (2) $d_m = 18.59$ μm, $\sigma = 1.892$ μm; (3) $d_m = 15.81$ μm, $\sigma = 1.731$ μm

(1986), using the glass particles with a narrow size distribution (Fig. 3*a*, 3*b*), the measurements of particle concentration profiles clearly indicate an effect of particle size on the local concentration for the given injection rates of 2.09 and 2.76 percent, as shown in Figs. 4 and 5. It can be seen that the concentration at the wall increases with the size of the particles (or Stokes numbers of particles) and that the thickness of the concentration boundary layer decreases with the increasing particle diameter (or Stokes number).

For the theoretical analysis of effects of particle size or Stokes number on deposition process, an integral method for the species conservation equation has been applied in a control volume chosen in the transpired-turbulent boundary layer. For a planar, transpired-turbulent steady flow with constant properties the integral equation can be written as follows:

$$\frac{\partial}{\partial x}\,\delta_c\int_0^1 \tilde{U}(\tilde{C}-1)d\tilde{y} = -\frac{V}{U_\infty} \tag{2}$$

The dimensionless velocity profile $\tilde{U}$ is matched to be a linear function of $\tilde{y}$ using the experimental profiles within the concentration boundary layer. Figure 6 shows the obtained dimensionless concentration profiles from the measurements. It can be seen that the profile follows the same curve and dimensionless concentration profile, $(\tilde{C}-\tilde{C}_{ow})/(1-\tilde{C}_{ow})$, which is approximated by a cosine function of $\tilde{y}$. Then equation (2) is integrated over the concentration boundary layer thickness. As a result of the integration over the concentration boundary layer, C_{ow} is found to be as follows:

$$\tilde{C}_{ow} = 1 - 6.734\,\frac{V}{U_\infty}\,\frac{(x-x_o)}{\delta_c} \tag{3}$$

where x_o is the effective origin of the concentration boundary layer thickness. When the incident flow laden with particles is subjected to the transpired turbulent boundary layer, the particles' inertia will induce a transition length before the concentration boundary layer grows linearly with the streamwise coordinate. This transition length can be estimated from the equation of particle motion. The equation of motion for a single particle following the path of the particle can be written as follows:

$$\left(\frac{\rho_p d_m^2}{18\mu}\right)\frac{dU_p}{dt} + U_p = U_F \tag{4}$$

Using the time response techniques in control theory, we conclude that the response time for a particle will be proportional to τ_p, particle relaxation time. Hence, the transition length for particles will be proportional to $\tau_p U_\infty$ or $x_o = a\tau_p U_\infty$ where a is the proportionality constant. Since τ_p changes with particle diameter and density for larger and/or heavier particles, the response time is longer and the transition distance increases. Based on the experimental results, the transition length x_o has been calculated for different particle diameters (or Stokes numbers) as presented in Fig. 7. Since we are dealing with an inertial response, the results are based on the Stokes number instead of particle diameter. Figure 8

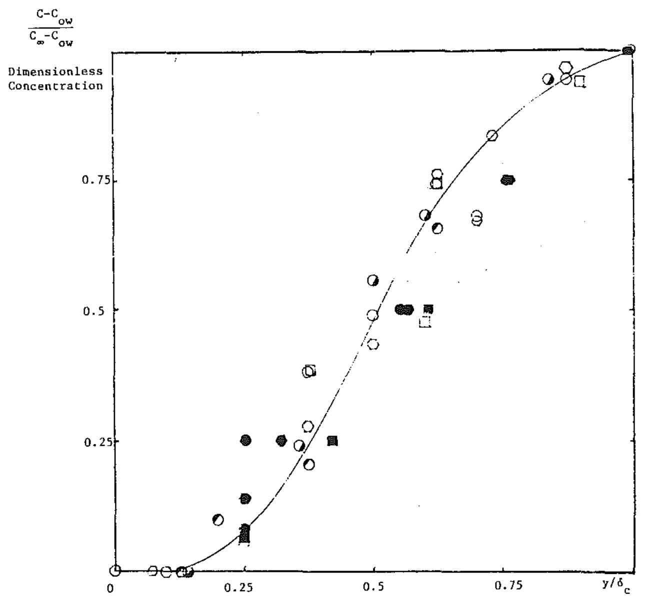

Fig. 6 Dimensionless concentration versus dimensionless distance normal to the plate

Symbol	Sc_T	F, percent
■	2.77	2.76
●	3.5	2.76
⬢	4.54	2.76
○	6.	2.09
□	4.6	2.09
⬡	3.97	2.09
◐	2.54	2.09
◑	3.1	2.09

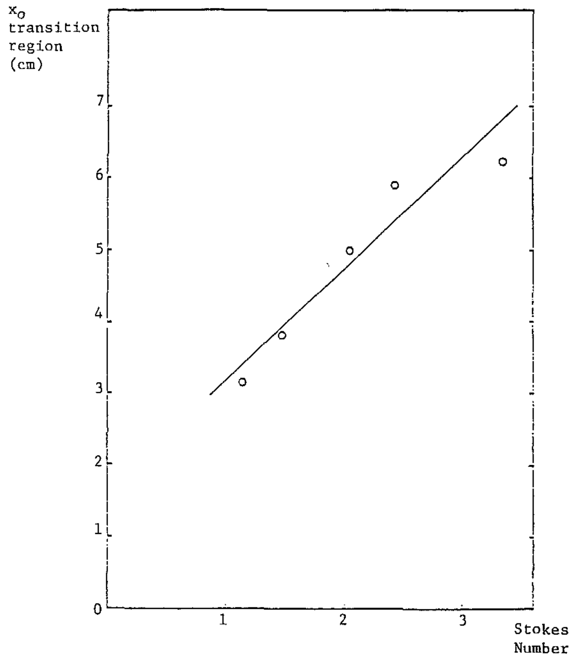

Fig. 7 x_0 versus Stokes number for injection rate of 2.09 percent

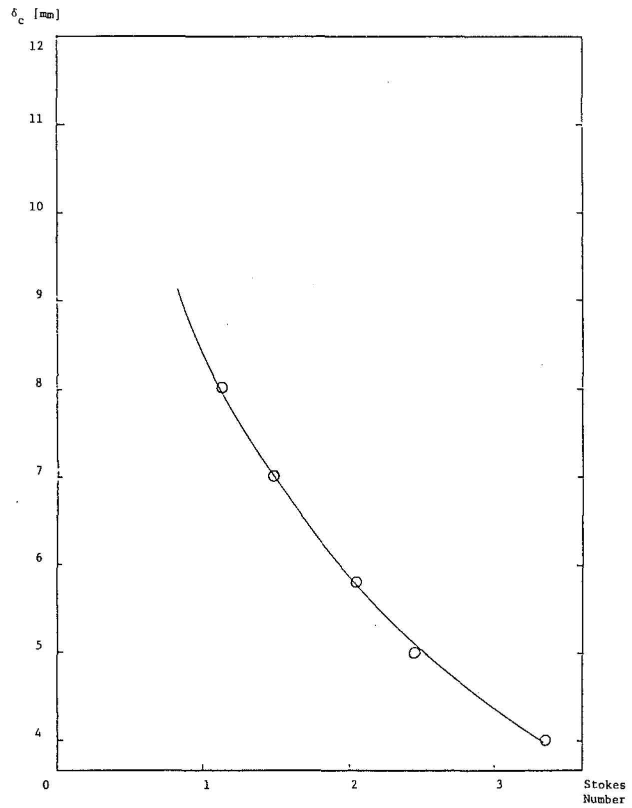

Fig. 8 δ_c versus Stokes number for injection rate of 2.09 percent

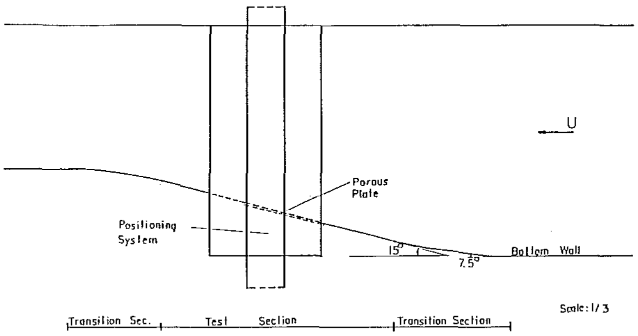

Fig. 9 Schematic drawing of the inclined plate at 15 deg angle relative to the main flow

shows the dependency of concentration boundary layer thickness on the Stokes number. As expected, when the Stokes number increases, the concentration boundary layer decreases.

(*b*) **Effect of Inclination.** The interaction between transpiration and inertial impaction of particles is determined in an experimental setup using an identical inclined transpired plate. As illustrated in Fig. 9, the angle of inclination is 15 deg relative to the main flow. To avoid separation of the flow, in the transition regions hand-made wood pieces are used. Since the pressure along the inclined plate changes due to the inclination, the coolant injection box is divided into four separate sections to achieve uniform transpiration flow and each section is connected to the main reservoir through the choked orifices. Figure 10 gives the results of the concentration profiles for four different injection rates on the inclined plate with the unclassified particles. As it can be seen, the concentration boundary layer is very thin and even for very high injection rates there is a concentration at the wall due to the inertial (impaction) effects of the particles. Figure 11 illustrates the results of measurements for four different particle sizes and a specific injection rate of 3.1 percent. The measurements clearly indicate that particle concentration at the wall is a function of the particle diameter (or Stokes number). As expected, the transpired flow is more effective to reduce the con-

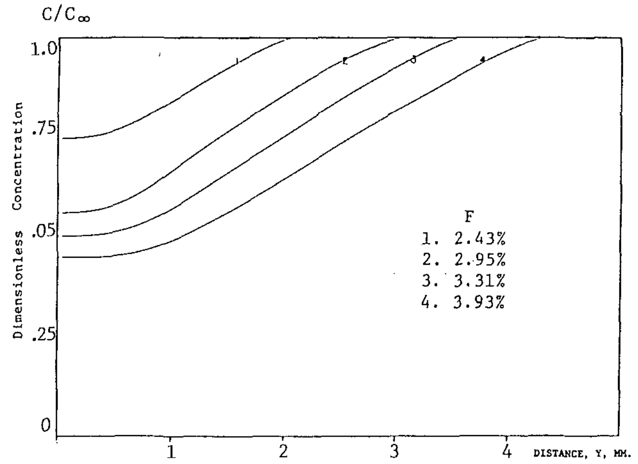

Fig. 10 Concentration profiles of glass particles ($d_m = 16.29$ μm; $\sigma = 5.25$ μm) for different injection rates on the inclined plate

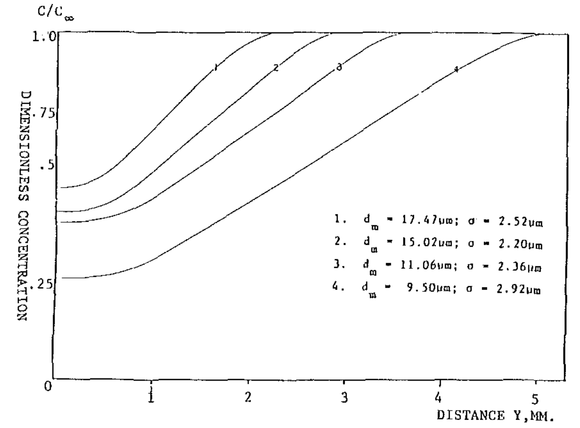

Fig. 11 Particle concentration profiles for classified glass particles on the inclined plate for the injection rate of 3.1 percent

centration of the smaller particles close to the wall. Comparisons of flat and inclined plate measurements show that the effectiveness of the transpiration is decreased due to the inertial effects of the particles close to the wall. High momentum by transpired flow in the normal direction to the wall is needed to overcome the higher particle inertial effects. However, transpiration is again effective in reducing the wall concentration and consequently the arrival rate of particulates to a transpired inclined plate can be much reduced when compared to the case of the solid inclined plate.

(*c*) **Effect of Density of Particulates.** Based on the above analyses and the available data, the effect of the density of particulates on the concentration profiles and consequently on the arrival rates can now be predicted. As mentioned before, particles contributing most of the mass of the solid carryover entering turbines have a Stokes number between 1 and 3.5, and the density of such particles varies from 1.3 to 5 g/cm^3 depending on the type of coal and temperature-time history. For the present analysis, particle diameter and the injection rate are fixed, while the particle density is changed in the range of interest. Hence, knowing the diameter and injection rate, Stokes numbers can be calculated for different particle density values. Figures 7 and 8 enable us to obtain the transition distance x_0 and the thickness of concentration boundary layer δ_c for the calculated Stokes numbers for the injection rate of 2.09 percent. Then, dimensionless wall concentration $\bar{C}_{0w}$ is obtained from the derived equation (3). The exact profiles can be predicted by using Fig. 6, which indicates that the nondimensional concentration profiles can be approximated by the cosine shape curve. Figure 12 gives three curves obtained for different densities as a result of such analysis. It clearly shows an effect of the particle density on concentration profiles: As density increases the wall concentration increases and the concentration boundary layer decreases. This is mainly a result of the heavier particles, due to their high inertia, needing a high-momentum transpired flow to be blown away from the surface.

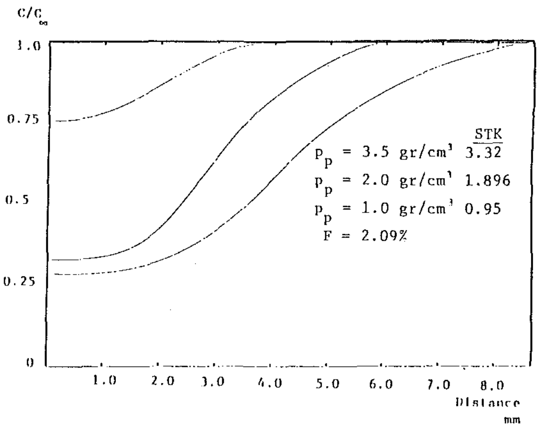

Fig. 12 C/C_∞ versus y (distance) for different densities

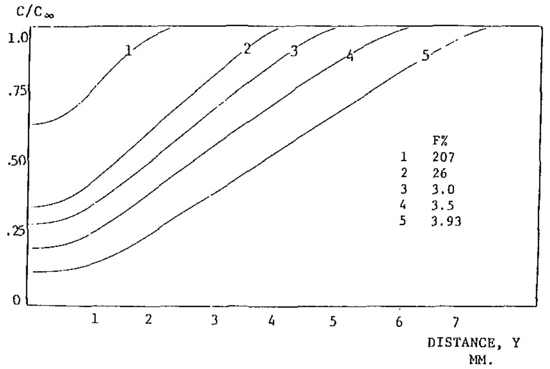

Fig. 13 Concentration distribution of coal particles for different injection rates

To determine the density effects, the tests were conducted over the inclined transpired plate with unclassified coal particles (5–14 μm) with a density of 1.27 g/cm^3 simulating ash particles of 1.9 g/cm^3 in a gas turbine. Figure 13 gives the concentration profile for different blowing rates. Comparisons of tests involving two different densities indicate that the concentration at the wall is smaller and the concentration thickness larger than for glass particles of the same diameter. Figure 14 compares the experimental concentration profiles of coal particles of about 14 μm and glass particles of 9.5 μm – having the same Stokes numbers – for nearly the same blowing rate. As expected, they are found nearly identical.

Calculation of Turbulent Schmidt Numbers

Tchen (1947) derived an expression for the turbulent Schmidt number of monosize particles influenced by an homogeneous turbulence field. It is expected that the expression derived by Tchen gives a correct order of Schmidt number for the transpired turbulent boundary layers operating with high injection rates. The Tchen equation is given as follows:

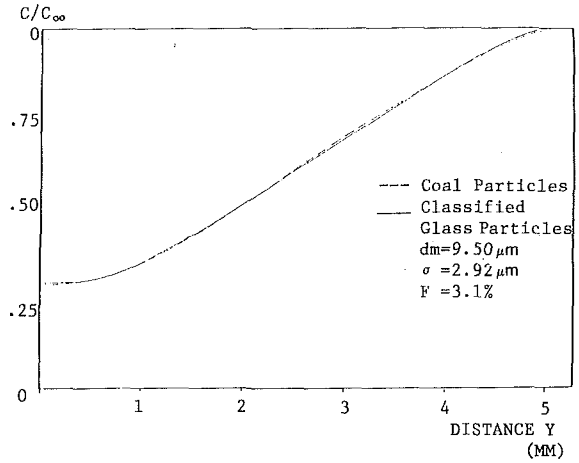

Fig. 14 Comparisons of concentration curves for coal and glass particles

$$\mathrm{Sc}_T^{-1} = 1 + \left[\frac{1}{(\tau_f/\tau_p)^2}\right]\left[\frac{\exp(-t/\tau_p)-\exp(-t/\tau_f)}{1-\exp(-t/\tau_f)}\right] \qquad (5)$$

In a transpired turbulent boundary layer with high injection, thickness of the layer is in order of the size of the turbulent eddies. Thus, residence time for a particle in this region will be order of τ_f. Consequently, for $t=\tau_f$, equation (5) becomes:

$$\mathrm{Sc}_T^{-1} = 1 + \frac{\exp\left(-\frac{\tau_f}{\tau_p}+1\right)-1}{1.72\left[\left(\frac{\tau_f}{\tau_p}\right)^2 - 1\right]} \qquad (6)$$

which is applicable to the transpired turbulent boundary layers operating with large injection rates.

When a reasonable value for the turbulent time scale is assumed, the ratio of velocity to concentration boundary layer thicknesses δ_m/δ_c, obtained in Fig. 11, is found to vary quasi-linearly with the calculated Schmidt number (Fig. 15) as in the case of a flat plate (Kozlu and Louis, 1986).

Conclusions

The following conclusions can be drawn from the results of the present study:

1 Using the experimental data, a theoretical prediction based on the Stokes number is developed to predict the effect of density. The latter is found to be important, which is confirmed by experiments.

2 For a given transpiration rate, the effectiveness of transpiration is decreased due to inertial (impaction) effects of the particles for inclined surfaces relative to the approaching flow.

3 Measurements determine the turbulent Schmidt number for different particle Stokes numbers of interest. Experimental *results are in agreement with the theoretical prediction of* Tchen.

Acknowledgments

This work was performed under contract DE-AC21-83-MC20334 from the Department of Energy, Morgantown Energy Technology Center.

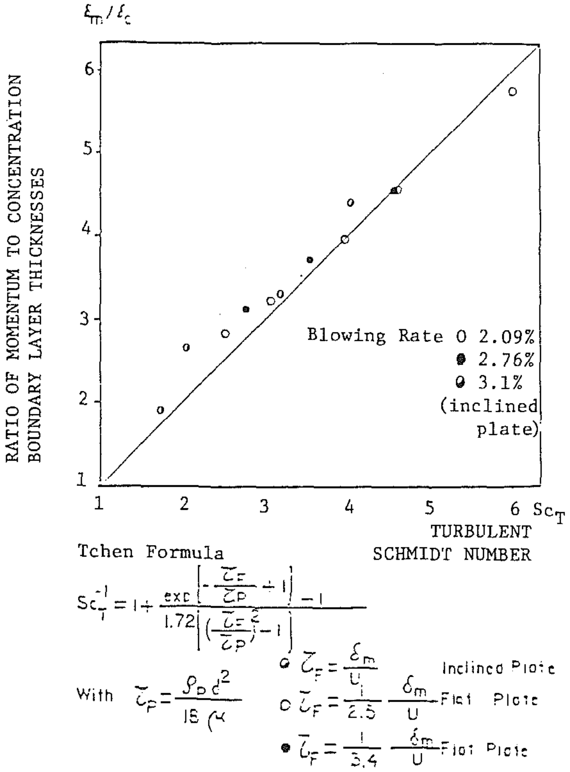

Fig. 15 δ_m/δ_c versus calculated Schmidt number for flat and inclined plates

References

Beal, S. K., 1970, "Deposition of Particles in Turbulent Flow on Channel or Pipe Walls," *Nucl. Sci. and Eng.*, Vol. 40, pp. 1-11.

Davies, C. N., 1966, *Aerosol Science*, Academic Press, New York, Chap. XII.

Friedlander, S. K., 1977, *Smoke, Dust and Haze—Fundamentals of Aerosol Behavior*, Wiley, New York.

Friedlander, S. K., and Johnstone, H. F., 1957, "Deposition of Suspended Particles From Turbulent Gas Streams," *Ind. and Engrg. Chem.*, Vol. 49, No. 7, p. 1151.

Fuchs, N. A., 1964, *The Mechanics of Aerosols*, Pergamon Press, Chap. 6.

Georgiou, D. P., and Louis, J. F., 1985, "The Transpired Turbulent Boundary Layer in Various Pressure Gradients and the Blow-off Condition," ASME JOURNAL OF ENGINEERING FOR GAS TURBINES AND POWER, Vol. 107, pp. 636-641.

Gökoğlu, S. A., 1982, "Thermophoretically Enhanced Deposition of Particulate Matter Across Non-isothermal Boundary Layers," Ph.D. Thesis, Chemical Engineering Department, Yale University.

Hinze, J. O., 1975, *Turbulence*, 2nd ed., McGraw-Hill, New York, Chap. 5.

Im, K. H., and Chung, P. M., 1983, "Particulate Deposition From Turbulent Parallel Streams," *AIChE Journal*, Vol. 29, p. 498.

Kozlu, H., and Louis, J. F., 1986, "Deposition Control Using Transpiration," ASME Paper No. 86-GT-260.

Liu, B. Y. H., and Ilori, T. A., 1974, "Aerosol Deposition in Turbulent Pipe Flow," *Env. Sci. and Tech.*, Vol. 8.

Raj, R., 1983, "Deposition Results of a Transpiration Air-Cooled Turbine Vane Cascade in a Contaminated Gas Stream," ASME JOURNAL OF ENGINEERING FOR POWER, Vol. 105, pp. 826-833.

Raj, R., and Moskowitz, S., 1978, "Transpiration Air Protected Turbine Blades—An Effective Concept to Achieve High Temperature and Erosion Resistance for Gas Turbines Operating in an Aggressive Environment," ASME Paper No. 78-GT-100.

Sehmel, G. A., 1971, "Particle Diffusivities and Deposition Velocities Over a Horizontal Smooth Surface," *Journal of Coll. and Interface Sci.*, Vol. 37.

Tchen, C. M., 1947, "Mean Value and Correlation Problems Connected With the Motion of Small Particles Suspended in a Turbulent Fluid," Ph.D. Dissertation, Delft.

Heat Transfer and Fluid Mechanics Measurements in Transitional Boundary Layers on Convex-Curved Surfaces

T. Wang
Department of Mechanical Engineering,
Clemson University,
Clemson, SC

T. W. Simon
Department of Mechanical Engineering,
University of Minnesota,
Minneapolis, MN

An experimental investigation of the effects of convex curvature and free-stream turbulence on momentum and heat transfer in a boundary layer undergoing natural transition was performed. The test section was designed for providing a two-dimensional boundary layer flow on a uniformly heated curved surface. The unique feature of the test wall was its flexibility to be bent to various radii of curvature R. *Three cases of* $R = \infty$, *180 cm, and 90 cm, are presented, each with two free-stream turbulence intensity levels, 0.68 and 2 percent. Mean velocity and temperature profiles and local Stanton number data were taken in a heated flow and streamwise Reynolds normal stress profiles were taken in an isothermal flow. Mild convex curvature* ($R = 180$ *cm*) *is shown to delay transition. Bending the test wall to a smaller radius of curvature, 90 cm, results in no significant further delay of transition. Cases with both curvature and higher free-stream disturbance effects show a pronounced dominance of the latter. Heat transfer rates and mean temperature profiles are shown to change more slowly after transition than wall shear stress values and velocity profiles. This can be observed as higher values of turbulent Prandtl number and lower values of the Reynolds-analogy factor,* $2St/C_f$, *in the transitional and early-turbulent flows than values known to apply for mature turbulent flows. The results of this study increase the data base for development of transition prediction models which can be used in gas turbine blade design.*

Introduction

Transition from laminar to turbulent boundary layer flow significantly increases local wall shear stress and convective heat transfer rates. These increases must be appropriately factored into the design of many types of equipment, e.g., compressor and gas turbine blades. Presently, the poor predictability of the location and streamwise coverage of transition on gas turbine blades results in either reduced longevity of the blades or reduced performance of the engine below design objectives. For most commercial gas turbines, a 35 percent error in the heat transfer coefficient prediction results in a wall temperature error of 56°C and an order-of-magnitude decrement in vane life [1]. It is common that as much as 50–80 percent of a typical gas turbine blade suction (convex) surface is covered by flow undergoing transition [2]. The inability to predict transition is partially due to a lack of experimental data, both heat transfer and hydrodynamic, which isolate the separate effects that influence transition. Some of these effects are: free-stream turbulence, acoustic disturbances, surface vibration, surface roughness, streamwise acceleration, cross-stream straining, film cooling, boundary layer separation, compressibility, body forces, and streamwise curvature. An earlier paper [3] by the present authors discussed free-stream turbulence effects on a flat wall; the present paper investigates the convex-curvature effect at two free-stream turbulence levels. Characteristics of transition such as three dimensionality, unsteadiness, and nonlinear interaction of several influences, tend to exacerbate the difficulty in understanding the fundamentals. Consequently, a program of systematic, well-controlled experimental studies designed to isolate separate effects, then combine them in a controlled fashion, is needed to provide the data base necessary for developing improved transition prediction models.

Previous Studies

Curvature Effects. Boundary layer flow is stabilized by convex curvature. Van Dyke [4] gave the following theoretical result for the skin-friction coefficient C_f in a low-speed constant-pressure laminar flow: $C_f = C_{f0}\ (1 - 1.24\ \delta/R)$, where C_{f0} is the skin-friction coefficient on a flat plate. For most laminar flows, δ/R is very small, and the curvature effect is minimal. The curvature effect is amplified in turbulent boundary layer flow, however. Thomann [5] showed the effect of longitudinal surface curvature on Stanton numbers in a supersonic turbulent boundary layer; on the convex surface,

---

Contributed by the Gas Turbine Division and presented at the National Heat Transfer Conference, Denver, Colorado, August 4–7, 1985. Manuscript received at ASME Headquarters February 16, 1987. Paper No. 85-HT-60.

heat transfer rates were reduced about 20 percent from plane-surface values and, on the concave surface, heat transfer was enhanced about 20 percent. Bradshaw [6, 7] pointed out that this large influence of curvature in turbulent flow corresponds to a large effect of curvature on Reynolds stresses: roughly ten times as much as the observed changes in viscous stresses. Recent studies on the influence of curvature on turbulent boundary layer flows include: So and Mellor [8], Hoffmann and Bradshaw [9], Ramaprian and Shivaprasad [10], Mayle et al. [11], Gillis et al. [12], Simon and Moffat [13, 14], and Gibson et al. [15, 16]. The general conclusions are:

1 The introduction of convex surface curvature reduces significantly the turbulence length scale with an accompanying reduction of turbulence intensity, shear stress, skin friction, and Stanton number.

2 Turbulent heat fluxes and Stanton numbers are more sensitive to wall curvature than are Reynolds stresses and skin friction coefficients – the stabilizing effect of convex curvature affects heat transfer more than momentum transfer [13–16].

3 Curvature does not affect the near-wall layer as much as it does the outer region of the boundary layer.

4 The production of turbulence decreases steeply with distance from the wall outside of the viscous region of the convex-curved boundary layer and has been shown to approach zero [8] and reverse sign [12] in the outer regions of the boundary layers; larger eddies are destroyed by compression of the active turbulence production region.

More on curved flow can be found in [6, 17, 18].

Very little research has dealt with the curvature effect on boundary layer flows undergoing laminar-to-turbulent transition. Pioneering work was done by Clauser and Clauser [19] on a low free-stream turbulence boundary layer flow which started at the beginning of the curved section. Important conclusions were: (1) The critical Reynolds number was doubled on the convex wall and reduced to one-half on the concave wall (compared with the straight wall). (2) There was a point of maximum turbulence intensity in the laminar boundary layer profiles that were near transition. This maximum shifted away from the wall with increasing streamwise distance on the convex wall and shifted toward the wall with increasing streamwise distance on the concave side. (3) There were two maximum values in the turbulence profiles for boundary layers on convex walls, a double hump, but only one maximum value on the concave wall. Liepmann [20] investigated effects of curvature, streamwise pressure gradient, and roughness on transition. He concluded that transition was not affected by convex curvature for $\theta/R < 0.001$, but a pronounced effect on transition was found for concave surfaces. To the authors' knowledge, very little research on the curvature effect on transition has been done since these two early studies. Recently, Simon and Moffat [13] conducted "separate effects" heat transfer experiments in convex-curved boundary layers. In a study of the effect of momentum boundary layer maturity, convex curvature was introduced to laminar and early-transitional flows. Heat transfer results showed that the curvature effect was weaker in the laminar boundary layer than in the early transitional boundary layer, and that the curvature apparently delayed and retarded the transition process.

The curvature effect on transition is not well understood. The present study responds to a need for more fundamental measurements in curved, transitional flows.

Free-Stream Disturbance Effects. The effect of free-stream disturbance on planar boundary layer flows has been the topic of many researchers. Reference [3], written by the present authors, summarizes these works in detail and presents some experimental results by the authors. These results were taken in the same facility as, and serve as baseline data to, the present curvature study. The following are some important findings from previous research.

A forced-oscillation method for investigating boundary layer transition was introduced by Schubauer and Skramstad [21] to demonstrate the growth and evolution of disturbances in laminar flows. They concluded that when the free-stream turbulence intensity exceeds 0.1 percent, transition is caused directly by random disturbances and is not precluded by selective amplification of sinusoidal oscillations, as with low-disturbance flows. Dyban et al. [22] investigated the structure of laminar boundary layers developing under elevated free-stream turbulence intensities from 0.3 to 25.2 percent. They found a peak in the rms streamwise velocity fluctuation profile which is believed to be caused by the penetration and amplification of free-stream disturbances. The waveform of this oscillation was not sinusoidal but more turbulentlike with energy distributed across a wide range of frequencies. They called the late-laminar boundary layers which show this behavior "pseudo-laminar" to separate them from laminar and transitional boundary layer behavior, considered to be fundamentally different. Except for early data by Clauser and Clauser [19] and Liepmann [20] for late-laminar and transitional flows, no other experiments were presented which document in detail the development of this "turbulence" for natural transition of boundary layers: laminar, "pseudo-laminar," transitional, and turbulent.

Recently, Blair [23] conducted several tests on a uniformly heated flat wall where free-stream turbulence intensity was varied over the range of 0.7 to 6.0 percent. He concluded that fully turbulent mean velocity profiles were established faster

Nomenclature

$C_f/2$ = skin friction coefficient
C_p = specific heat
Pr = Prandtl number
Pr_t = turbulent Prandtl number
$\dot{q}''$ = wall heat flux
R = radius of curvature
Re_x = x Reynolds number
St = Stanton number = $\dot{q}''/(\rho C_p U_{pw}(T_w - T_\infty))$
TI = free-stream turbulence intensity
T^+ = mean temperature in inner coordinates = $(T_w - T)u^*/(\dot{q}''/\rho C_p)$
U^+ = mean velocity in inner coordinates = U/u^*
U_{pw} = potential flow velocity at the wall
u' = instantaneous streamwise velocity relative to mean
u^* = friction velocity = $\sqrt{\tau_w/\rho}$
Y = distance from the wall
Y^+ = distance from the wall in inner coordinates = Yu^*/ν
Y_{cl}^+ = conduction layer thickness in inner coordinates = $Y_{cl}u^*/\nu$
δ = boundary layer thickness based on 99.5 percent of potential flow velocity
δ^* = displacement thickness
θ = momentum thickness
Λ_θ = Pohlhausen pressure parameter = $(\theta^2/\nu)(dU_{pw}/dx)$
τ = shear stress

Subscripts

∞ = at the freestream
w = at the wall

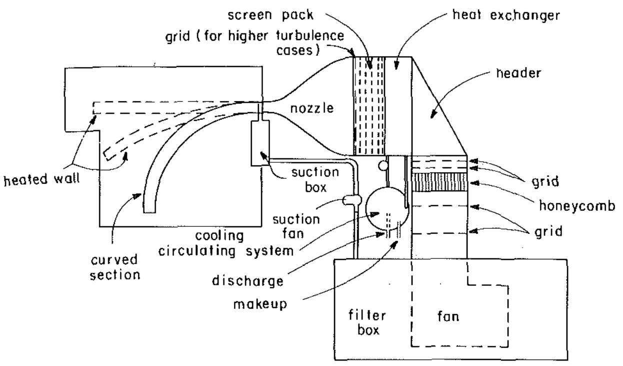

Fig. 1 Curved boundary layer facility

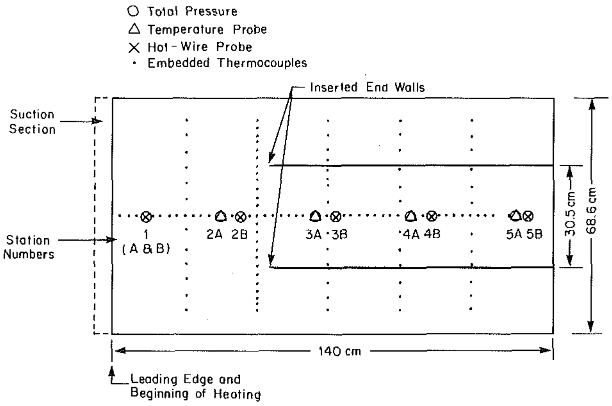

Fig. 2 Measurement locations for total pressure tubes, temperature probe, hot-wire probe, and embedded thermocouples. Stations "A" are for heated flow, and stations "B" are for adiabatic flow.

than fully turbulent mean temperature profiles. This results in a breakdown of Reynolds analogy and a larger effective turbulent Prandtl number in the very early turbulent flow than observed in mature turbulent flows. He also showed that transition Reynolds number is insensitive to acceleration as large as $\Lambda_\theta < 0.08$ for flows with this high turbulence intensity range, as predicted by the Van Driest–Blumer model [24]. In a study of the influence of free-stream turbulence on turbulent boundary layer heat transfer, Blair [25] concluded that both the Stanton number and the skin friction coefficient increase with increasing free-stream turbulence intensity and that the Reynolds analogy factor $2\text{St}/C_f$ increases linearly with increased free-stream turbulence.

The present experiment was undertaken in a low-speed, open-circuit wind tunnel. Thermal and hydrodynamic boundary layers were grown on a uniformly heated test wall which is capable of being bent to various radii of curvature. The primary objective is to isolate two factors that influence transition: convex streamwise curvature and free-stream disturbance level. The following parameters characterize the experimental runs of the present study:

TI, percent	*R*, cm	Description
0.68	180	45-deg bend, low-turbulence case
0.68	90	90-deg bend, low-turbulence case
2.0	180	45-deg bend, high-turbulence case
2.0	90	90-deg bend, high-turbulence case

The Experimental Facility. The test facility in the present study was especially designed and constructed for two-dimensional boundary layer flow research. Details of the facility are given in [3, 26]; the following summarizes:

The test program employed the boundary layer heat transfer facility shown in Fig. 1. This is an open-circuit, blown-type wind tunnel. Air is drawn through filters, then forced through a heat exchanger and screen pack to enter the test region. Four coarse grids and a honeycomb section were installed downstream of the blower to eliminate fan swirl and to make the velocity uniform across the flow section. Selection of the grids and honeycomb was based on the experience of Metha [27] and Loehrke and Nagib [28]. The heat exchanger was inserted upstream of the nozzle to effect a uniform and constant free-stream temperature. The screenpack, consisting of five screens, was installed between the heat exchanger and the contraction. Each screen is 24 mesh; the screen–screen spacing is 76.2 mm (about 400 screen-wire diameters) allowing the wakes of the wires sufficient streamwise distance to decay. A large open-area ratio (67.2 percent) was chosen consistent with the recommendations of [29–31].

Free-stream nominal velocities, ranging from 12 m/s to 35 m/s, were shown to be uniform to ±0.2 percent, and the free-stream temperature, nominally 25°C, was shown to be uniform to ±0.05°C and constant to ±0.2°C. A coarse grid was installed at the entrance of the contraction section for the higher turbulence cases. This gave free-stream turbulence intensities which decay from 2.1 to 1.9 percent over the test length – nominally 2.0 percent in the transition region. The grid, designed according to [32], was fabricated using 14 gauge, 2.54-cm-wide aluminum strips with 10.2 cm center spacing. The three-dimensional contour of the 10.7:1 area-ratio contraction was constructed as two intersecting cubic curves. Strong suction was applied at the exit of the contraction section over the entire span of the test wall through a 3.8 cm streamwise length suction slot covered with a perforated plate with 2.38 mm diameter staggered holes. A centrifugal fan draws approximately 1/8-1/10 of the primary air mass flow rate through the perforated plate and returns it to the filter box. Because of this strong suction, a new boundary layer starts just upstream of the heated test wall simulating the sharp leading edge configuration. The smoothness and flatness of the joint between the perforated plate and the heated wall was very important and great care was taken in its construction.

The test region is rectangular in cross section, 11.4 cm × 68.6 cm, and 1.4 m long. One side wall of dimensions 68.6 cm by 1.4 m is heated to nominally 10°C above the incoming air temperature with a heat flux of 150–240 W/m^2 uniform to ± 1 percent. The heated wall is flexible so that it can be bent to varying degrees of streamwise curvature. Embedded in the heated wall is a flexible heater and 122, 3-mil, chromel-constantan thermocouples. The thermocouples are distributed along the wall centerspan, with a 2.54-cm streamwise spacing, and are uniformly distributed across the span at five streamwise locations (Fig. 2). Covering the thermocouples, in contact with their junctions and bonded to the wall, is a 0.1-mm-thick sheet of stainless seel. Bonded to the stainless steel and providing the test surface is a 25-μm-thick sheet of reflective film. This film was added to reduce the uncertainty attributable to radiation exchange. To keep the heated wall flat while in the straight configuration, it was necessary to insert end walls and clamp the tunnel assembly together. These inserted end walls began 50 cm downstream of the test wall leading edge, and are 15 cm above and below the tunnel centerspan (Fig. 2). The end walls were removed for curved-wall cases; bending holds the composite heated wall assembly firmly together.

The outer wall (observing side) was made of 4.8-mm-thick Lexan sheet. Six probe access holes were drilled uniformly spaced along the centerline and in cross-span arrays giving the probe traversing stations shown in Fig. 2.

Instrumentation. Mean velocity measurements were taken with total pressure tubes in both heated and isothermal flows. A shear displacement correction was made according to Young and Maas [33]. Pressures were read with a diaphragm differential pressure transducer or a micromanometer. Static pressure taps were arranged on the top wall 5.71 cm (nominal half-width of the test section) away from the test wall. Pressure transducer signals were digitized with about 5000 samples over a sampling period of about 30 s, then averaged. The transducer was calibrated against a micromanometer which has a stated precision of 0.01 mm H_2O. Calibration to pressures larger than 5.0 cm H_2O was done with a cathetometer having a precision of 0.1 mm H_2O. Hot-wire measurements were taken in an isothermal flow. Streamwise normal stresses were obtained with a horizontal hot wire. Two thousand samples were collected in a period of 45 s for each data point and averaged. Because the digitizer had a very fast "up-front" sample hold, each sample was nearly instantaneous (within 1 μs). Linearization and other processing was done in the laboratory minicomputer. The hot wires were calibrated against total pressure tubes read with a micromanometer.

Mean temperature profiles were read with a two-dimensional boundary-layer temperature probe constructed following the design of Blackwell and Moffat [34]. EMF values were measured with a digital multimeter. Two-hundred samples were taken over 40 s and averaged for each position in the profile. All thermocouples were calibrated against a calibrated thermister reference inside the tunnel with a flow of 32 m/s and the test wall unheated. The uncertainty of this calibration is estimated to be ± 2.5 μV (0.04°C). Data were acquired and processed by the laboratory minicomputer. Corrections to the velocity and temperature profiles were made for property variations due to humidity, atmospheric pressure, and film temperature effects. Displacement and momentum thicknesses were computed using the potential velocity distribution in the irrotational flow following the method of Honami and Johnston [35] for curved flows. Skin friction coefficients were deduced from velocity profiles by forcing the data to pass through either the laminar correlation ($Y^+ = U^+$) in a laminarlike profile or the turbulent correlation ($U^+ = 2.44 \ln Y^+ + 5.0$) in a turbulentlike profile – the Clauser technique [36]. The uncertainty in this deduced skin-friction coefficient is estimated to be about ± 5 percent where the boundary layer is clearly laminar or turbulent. Mean temperature profiles were plotted in Y^+ versus T^+ coordinates. In the turbulent flow, the data were expected to follow $T^+ = \mathrm{Pr} \cdot Y^+$ near the wall and $T^+ = Y_{cl}^+ \mathrm{Pr} + \mathrm{Pr}_t/0.41 \ln (Y^+/Y_{cl}^+)$ [37] in the turbulent core. The conduction layer thickness Y_{cl}^+ and the turbulent Prandtl number Pr_t were considered free variables. Local Stanton number values were computed from the local wall temperature (at each thermocouple location), the free-stream temperature, the measured heater power, and the measured free-stream velocity. Corrections were made for heat transfer through the backside insulation, radiation exchange, streamwise conduction within the heated wall, and recovery effects. Usually five samples of each wall thermocouple reading, taken over a period of 15 min, were averaged. A complete uncertainty analysis of the Stanton number measurement was made employing the Kline and McClintock [38] methodology for computing the propagation of uncertainties and the Moffat [39] methodology for incorporating known contributors to bias error; details are given in [26, 40].

The test facility was first qualified by conducting an all-laminar boundary layer test. Then the baseline cases to the present study were taken on a straight wall. Details of these tests are discussed in [3, 26]. Some results which are important to this study are summarized below.

Flat-Wall Laminar Qualification Case. Stanton number data taken at momentum thickness Reynolds numbers in excess of 400 were shown to be unsteady; the time-averaged Stanton number values followed the laminar correlation well, however. Mean velocity and mean temperature profiles were shown to be laminarlike. A thermal energy balance applied over the entire test length assuming two-dimensional flow showed closure to within 3 percent.

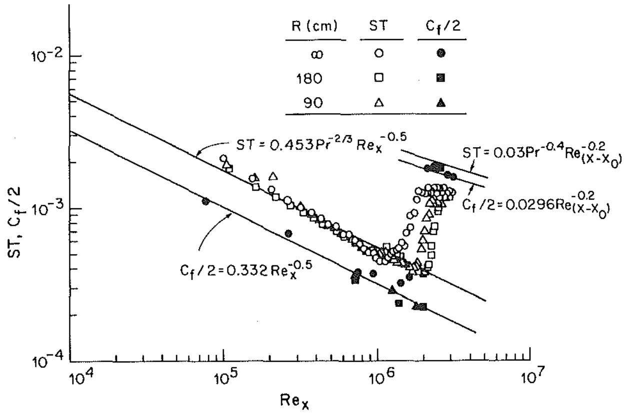

Fig. 3 Convex curvature effect on transition: comparison of the baseline and the two curved cases ($R = 180$ cm and 90 cm) at $TI = 0.68$ percent

Flat-Wall Baseline Cases. The free-stream velocity was controlled to move the location of the beginning of transition to about one-third of the test length. The resulting free-stream turbulence intensity became 0.68 percent without the turbulence-generating grid and 2.0 percent with it. Transition for the lower turbulence case, taken to be the beginning of the dramatic increase in heat transfer coefficient and shear stress, is at an x Reynolds number of 1.2×10^6 (Fig. 3) and a displacement thickness Reynolds number of 1890. Transition for the higher turbulence case began at $\mathrm{Re}_x = 2.1 \times 10^5$ and $\mathrm{Re}_\theta = 788$ (Fig. 11). Transition at these locations is consistent with previous data and the McDonald–Fish prediction model [41]. In the early turbulent flow, skin friction coefficient values were found to be higher than Stanton number values. This indicates a slower response of the heat transfer data after transition than that of the hydrodynamic data. The turbulent Prandtl number in the low-Reynolds-number turbulent flow is considerably larger than 0.9, the value measured for mature turbulent boundary layers. Spanwise distributions of local Stanton number for the lower turbulence case showed earlier transition near the end wall followed by a migration of the onset of transition toward the centerspan for progressively downstream locations. The higher-turbulence case displayed a nearly two-dimensional behavior throughout the test section length, including the transition region. The heat transfer runs were found to be repeatable to within 1 percent over a 6-hr test period, beginning after the standard 10-hr equilibrium period, and repeatable to within 3 percent over a period of one month.

Straight lines were drawn to fit data in the log regions of the mean temperature profiles. Optimum fits were found with $Y_{cl}^+ = 20$ and $\mathrm{Pr}_t = 1.20$ and 1.15 in the early-turbulent flow of the lower intensity case. For the higher turbulence intensity cases, $Y_{cl}^+ = 14.5$, 16, and 16 and $\mathrm{Pr}_t = 1.36$, 1.24, and 1.19, for progressively downstream profiles. These data support the conclusion, also made by Blair [23], that Reynolds analogy is severely violated in the low-Reynolds-number turbulent boundary layer. This also shows that the conduction layer is thicker in the low-Reynolds-number turbulent flow than the $Y_{cl}^+ = 13.2$ observed in higher Reynolds number flows. Note that the conduction layers were thinner for the higher-turbulence case than for the lower-turbulence case. Profiles of Reynolds normal stresses, taken upstream of transition, show some turbulencelike characteristics although the mean velocity and temperature profiles and the Stanton numbers at these streamwise positions are clearly laminarlike. The anemometer output signals were viewed on a storage oscilloscope. At the

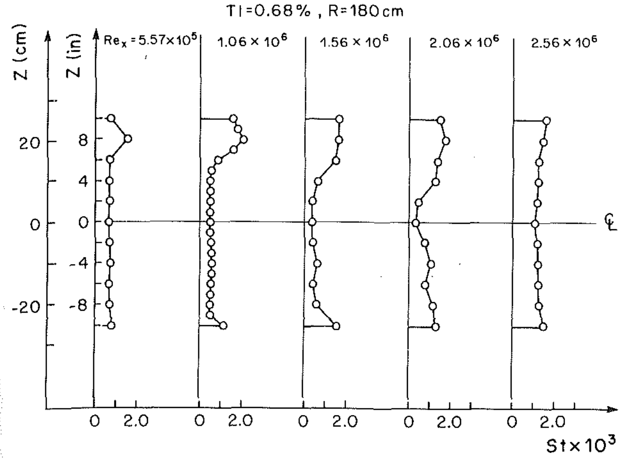

Fig. 4 Spanwise distribution of local Stanton number for the case of $R = 180$ cm and $TI = 0.68$ percent

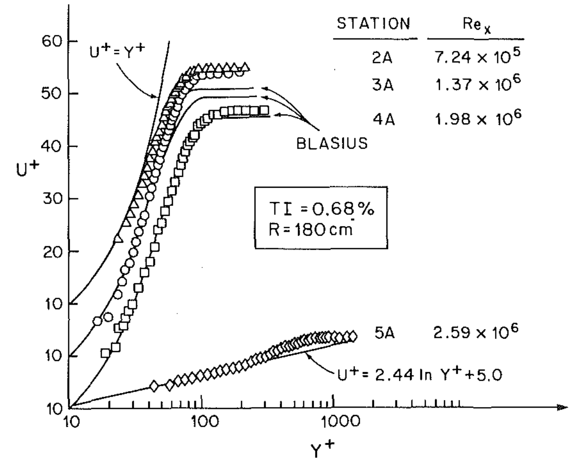

Fig. 5 Mean velocity profiles for the case of $R = 180$ cm and $TI = 0.68$ percent

peak value, i.e., $Y/\delta^* = 1.3$ for the first station, the waveform was turbulentlike, indicating a distribution of energy over a large range of frequencies. No intermittent non-turbulent behavior was observable. At the innermost possible Y position, $Y/\delta^* = 0.3$, some intermittency was observed where a quiet signal was present about 5 percent of the time. These findings are consistent with the results of Dyban et al. [22]. They termed such a boundary layer "pseudo-laminar." Transition is observable in the normal stress profiles as an increase in peak turbulence intensity concentrated near the wall where it is believed that turbulent bursts are agitating the flow. The residue of the laminar profile peaks continues to move outward from the wall, in successive downstream profiles, and soon becomes overshadowed by the near-wall activity. Profiles at the end of the test section (low-Reynolds-number turbulent flow) had reached an equilibrium shape similar to that measured in a mature turbulent boundary layer by Klebanoff [42]; turbulence characteristics are established almost immediately after transition.

Results and Discussion

Lower Free-stream Disturbance Study ($TI = 0.68$ percent). Two convex-curved cases were studied: the first with a radius of curvature of 180 cm and the second with a radius of curvature of 90 cm. Local Stanton numbers and skin friction coefficients taken along the channel centerspan are plotted with those from the baseline case in Fig. 3. The onset of transition is delayed from $\mathrm{Re}_x = 1.2 \times 10^6$ in the baseline case to 2.0×10^6 for the curved wall cases.

The 180 cm Radius-of-Curvature Case. Local Stanton numbers in the laminar flow follow the correlation and are essentially the same as those measured for the baseline case. A small increase of heat transfer coefficient for this case is observed in the range between $\mathrm{Re}_x = 0.9 \times 10^6$ and 1.3×10^6. The distinct hump at $\mathrm{Re}_x = 1.3 \times 10^6$ may suggest a local trend toward transition which is suppressed by the stabilizing effect of convex curvature. It is interesting to know that the position of minimum Stanton number before the hump, $\mathrm{Re}_x = 1.2 \times 10^6$, is at the same location as the transition point for the baseline case. A plausible explanation follows: The curvature effect, which scales as δ/R in the laminar boundary layer, is small in the early laminar flow; the amplification of disturbances in the thin laminar boundary layer is without a significant curvature effect. As the boundary layer thickens, δ/R increases and the effect of convex curvature becomes more significant. Stanton numbers continue to be depressed by curvature until the instability which leads to transition overcomes the stabilizing curvature effect and transition proceeds. The reproduction of the flat-wall Stanton number data in the early laminar flow demonstrates that no significant bias errors were introduced as the heated wall was bent.

In the very early turbulent flow the heat transfer coefficient is smaller than that of the baseline case. The test section is not sufficiently long to observe the remainder of the trend, however. The slower response of the heat transfer coefficient after transition compared to the skin friction coefficient, as mentioned earlier in the baseline case discussion, is observed again in this curved case.

The spanwise distribution of Stanton number is shown in Fig. 4. A streak of high local heat transfer coefficient is observed at about 20.3 cm above the centerspan at the $\mathrm{Re}_x = 5.57 \times 10^5$ location. This is identical to that observed in the all-laminar qualification case and the straight-wall baseline case [3]. Two dimensionality in the ± 15.2-cm band along the centerspan is maintained until transition starts ($\mathrm{Re}_x = 2.0 \times 10^6$). This indicates that secondary flow, present to some degree in all curved-flow studies, is not directly influencing the measurements taken along the centerspan, for this case. The severe cross-span variation at the beginning of transition is observable at the fourth station ($\mathrm{Re}_x = 2.06 \times 10^6$). The two dimensionality is quickly restored at $\mathrm{Re}_x = 2.56 \times 10^6$ where turbulent cross-span diffusivity has smoothed the cross-span velocity and temperature gradients.

The first three velocity profiles (Fig. 5), Stations 2A, 3A, 4A (see Fig. 2 for measurement locations), are laminarlike. The deviation from the Blasius profile at Stations 2A and 3A indicates a lower value of $C_f/2$ than predicted by laminar flat plate theory, as can be seen in Fig. 3. The good agreement with the Blasius profile at Station 4A is presumed to be due to the stabilizing effect of convex curvature countering the rising trend of $C_f/2$ in transition. Note that Station 4A is in the early stage of transition (Fig. 3). The profile at Station 5A, $\mathrm{Re}_x = 2.59 \times 10^6$, already appears to be a fully turbulent flow; the law of the wall is clearly seen from $Y^+ = 40$ to 200. The skin friction coefficient deduced by the Clauser technique at this station is 1.8×10^{-3}, which is higher than the corresponding Stanton number value (Fig. 3). Mean temperature profiles are shown in Fig. 6. The first three profiles (Stations 2A, 3A, and 4A) are laminarlike. The last profile, at $\mathrm{Re}_x = 2.59 \times 10^6$, is similar to those observed in the baseline study. The best fit of the data shows a conduction layer thickness Y_{cl}^+ of 16.5 and a turbulent Prandtl number Pr_t of 1.47. This indicates that the flow has not developed to a fully mature state (characterized by $Y_{cl}^+ = 13.4$ and $0.9 < \mathrm{Pr}_t < 1.2$ [14]) on the convex surface.

Streamwise-normal Reynolds stress profiles (Fig. 7) show a profound influence of curvature. The peak in the laminar

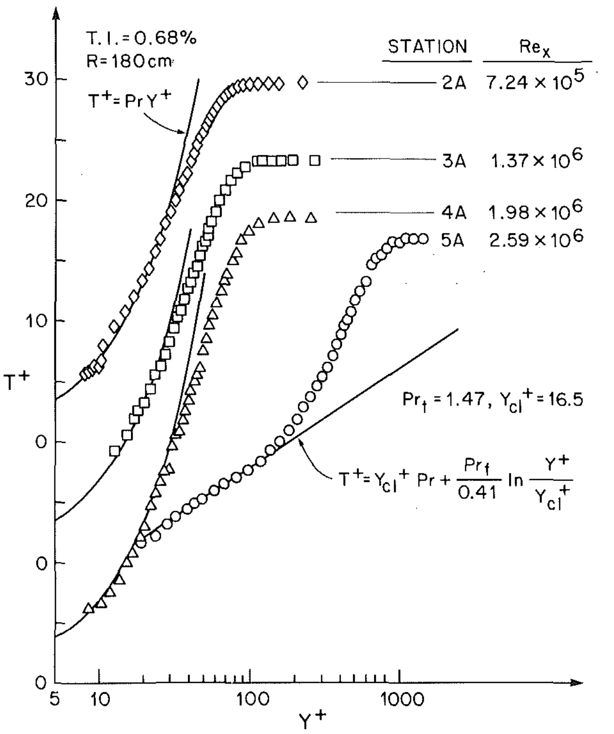

Fig. 6 Mean temperature profiles for the case of $R=180$ cm and $TI=0.68$ percent

boundary layer does not grow as the flow progresses downstream (as was observed in the flat-wall cases – see Fig. 8 from the baseline study for comparison). Instead, the peak is confined to around $\sqrt{\overline{u'^2}}/U_{pw}=3.7$ percent. At Station 3B the Reynolds normal stress profile is further depressed. Values close to the wall ($y/\delta^*=0.1$) are nearly the same as those of Stations 1B and 2B, but at the outer part of the boundary layer, the values are depressed by curvature to less than those of Stations 1B and 2B. Despite the stabilizing effect of convex curvature, which obviously delays transition, disturbances eventually grow and the flow undergoes transition. As shown in profile 4B, the streamwise-normal Reynolds stresses become very large. Because the profiles are sparse and because the state in the near-wall region of the boundary layer is changing rapidly near transition, it is not possible to assess the influence of curvature on this near-wall peak by comparing Figs. 7 and 8. The second peak, which is believed to be the residue of the peak appearing in the upstream laminar boundary layers, is clearly influenced by curvature; it is widened and flattened. The downstream profile at Station 5B is in the early turbulent region. This profile compares well with the flat-plate data in the region of $y/\delta^*<3$, but shows reduced values, due to curvature, in the outer two-thirds of the profile. This indicates that the convex curvature effect is most strongly felt on the outer part of the turbulent boundary layer.

The normal stress profiles, shown in Fig. 7, document important flow behavior of boundary layers undergoing transition. Free-stream disturbances are amplified within the boundary layer after a critical Reynolds number is exceeded. They develop unstable, three-dimensional waves and vortices. In the region where the boundary layer is too thin for curvature effects to be felt, the amplification process is similar to that on a plane surface. However, when the boundary layer thickens, the curvature effect becomes significant and the increasing stabilizing effect results in a subsequent reduction of the disturbance level. The stabilizing effect on a convex surface is eventually overcome by the hydrodynamic instability which leads to turbulent spots and transition. The disturbance levels increase to very high values in the transitional boundary layer, possibly due to a much higher production rate than dissipation rate. They are then reduced to those of an equilibrium profile in the turbulent flow as dissipation grows to equal production of turbulence.

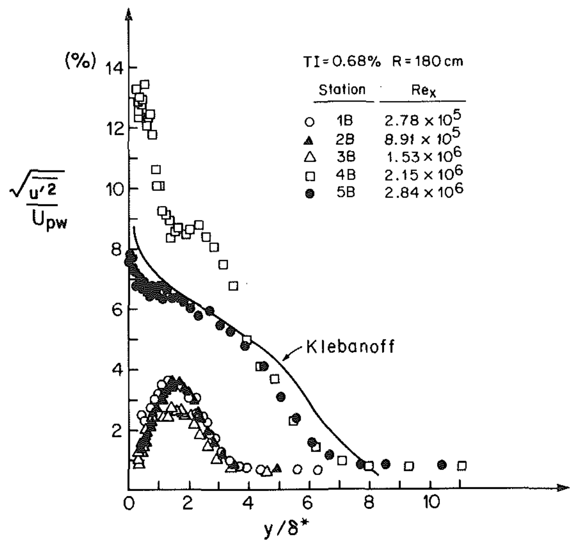

Fig. 7 Streamwise Reynolds normal stress for the case of $R=180$ cm and $TI=0.68$ percent

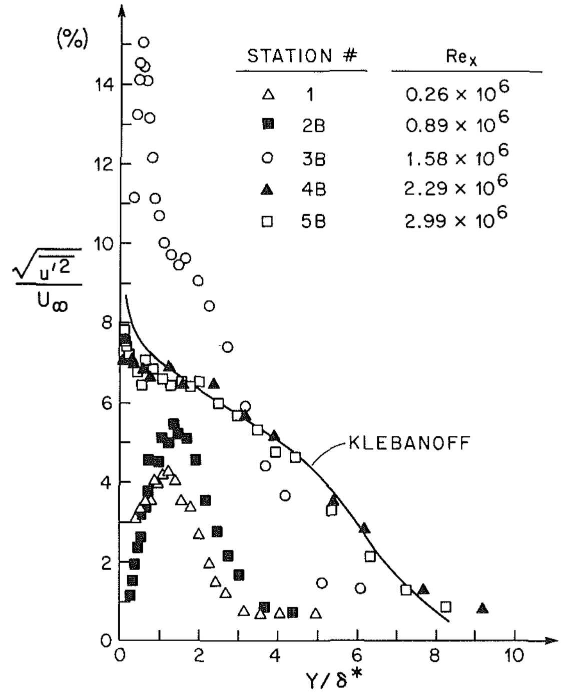

Fig. 8 Reynolds streamwise-normal stress profiles for the baseline case ($TI=0.68$ percent)

Momentum and thermal energy balances show energy closure to within 10 percent from the leading edge to Station 4A and to within 23 percent from the leading edge to Station 5A. Poor closure between 4A and 5A is probably due to three dimensionality in the transition region.

The 90 cm Radius-of-Curvature Case. Local Stanton numbers taken along the centerspan for this case are shown in Fig. 3. They are very similar to those for the $R=180$ cm case. The important finding in this case is that the transition point is not further delayed as the strength of curvature is increased from $R=180$ cm to $R=90$ cm. The transition starts at $Re_x=1.8\times10^6$, which is slightly upstream of the previous case's

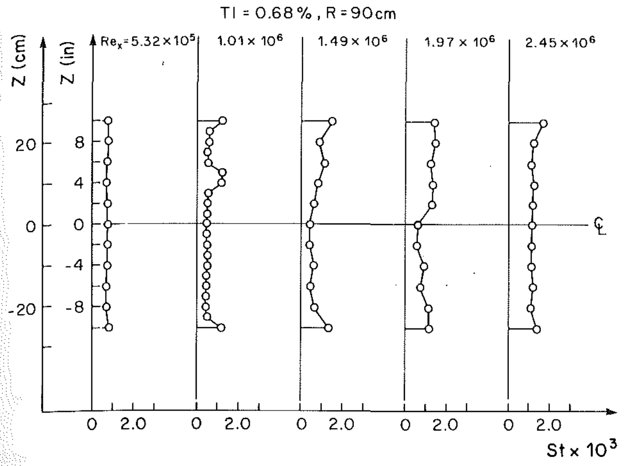

Fig. 9 Spanwise distribution of local Stanton number for the case of $R = 90$ cm and $TI = 0.68$ percent

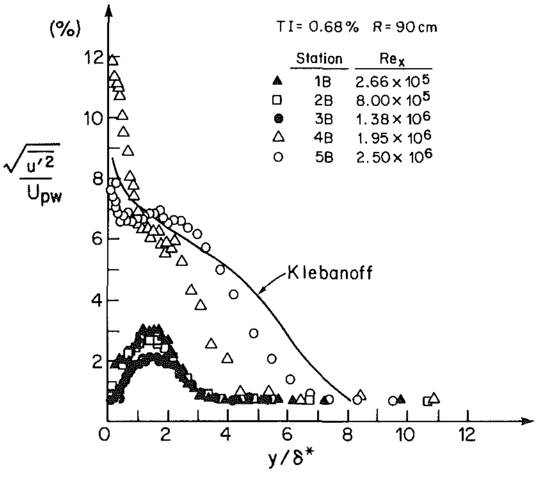

Fig. 10 Reynolds streamwise-normal stress profiles for the case of $R = 90$ cm and $TI = 0.68$ percent

transition point. One plausible explanation is that the large Taylor–Görtler vortices on the opposite concave surface exert an acoustic influence which expedites transition. No direct influence from the concave wall was detected, however; hot-wire measurements showed that a potential core remained over the full test length (~2 cm thick at the exit). Another possible reason for the earlier transition is that the secondary flow is slightly stronger for this case than for the mild-curved case (R = 180 cm). This secondary flow, generated by the slower boundary layer flow on the top and bottom walls being influenced by the cross-stream pressure gradient, enhances the migration of transition toward the centerspan with increasing streamwise distance. This effect of secondary flow is not indicated in the spanwise distributions of local Station number shown in Fig. 9, however, and Conrad probe measurements showed no significant spanwise mean velocity component. The important point is that the smaller radius of curvature of this case does not show an increased effect of curvature on either the fluid mechanics or the heat transfer behavior. No particular significance is placed on the slightly earlier transition Reynolds number for this case.

Mean velocity and temperature profiles are very similar to those of the R = 180 cm case. The best fit of the mean temperature profile in the turbulent core at Station 5A shows a conduction layer thickness Y_{cl}^+ of 16.0, which is about the same as in the milder-curved case, and a turbulent Prandtl number Pr_t of 1.22, which is somewhat less.

The most noticeable influence of the relatively stronger curvature can be seen in Fig. 10. In the laminar region, the streamwise disturbance is suppressed further by the increased curvature. The magnitude of the peak values of Stations 1B, 2B, and 3B are all less than those of corresponding stations in the R = 180 cm case. This effect is most obvious in profile 3B. The peak in the near-wall region of the transitional flow (Station 4B) is closer to the wall than the corresponding stations in the baseline case and the 180-cm radius case. In the baseline case (Fig. 8), the streamwise turbulence intensity decreases toward the wall from the peak; in the mild-curved case (R = 180 cm), the region of decreasing values of $\sqrt{\overline{u'^2}}/U_{pw}$ is also observable (Fig. 7), but in the present case (Fig. 10) it is not. Apparently this region was too thin in this case to be measured by the hot wire used in the present study. At the outer part of profile 4B ($y/\delta^* > 1$) the values of Reynolds normal stress are below the fully turbulent profile at Station 5B. This is thought to be due to the stabilizing effect of convex curvature. The second peak, the residue of the peaks in the laminar profiles around $y/\delta^* = 2$, is very small. The collapse of streamwise Reynolds stress is believed to be caused by the organizing effect of convex curvature. The influence of convex curvature continues to be seen in the fully turbulent profile of Station 5B. The outer part of profile 5B ($y/\delta^* > 4$) of both cases (Figs. 7 and 10) shows lower values of normal stress than those from Klebanoff [42]. This is an indication of reduced turbulence production in the outer part of the boundary layer due to convex curvature.

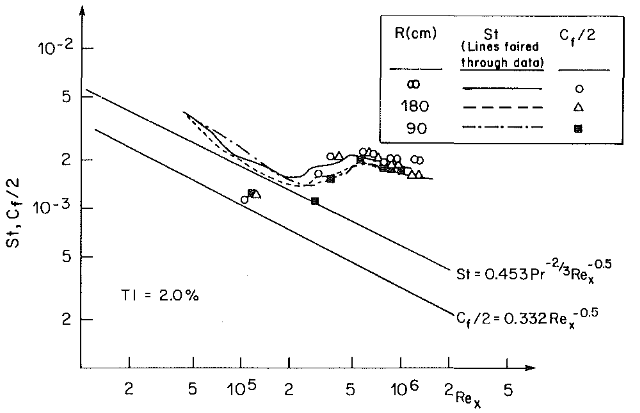

Fig. 11 Comparison of convex curvature effects on transition in the high free-stream turbulence flow ($TI = 2.0$ percent)

Momentum and thermal energy balances showed closure to within 7 percent to Station 4. The transition region between Stations 4 and 5 drives the lack of closure of the integral momentum and energy balances to 22 percent.

A comparison of boundary layer growth shows no noticeable effect of curvature in the laminar region and only a 3–5 percent increase of shape factor due to curvature. In the transition and turbulent regions the curvature effect retards the boundary layer growth.

The "Reynolds Analogy Factor," $2St/C_f$, for the two curved cases is about 15 percent lower than that of the baseline case in the early-turbulent flow. This indicates a stronger stabilizing effect of convex curvature on heat transfer than on hydrodynamics as was previously found and documented in [13, 16, 18].

Higher Free-Stream Disturbance Study (TI = 2.0 percent). The previous results in the low free-stream turbulence flows show that convex curvature can stabilize the flow, suppress the mixing activity, reduce the turbulence production in the boundary layer, and delay transition, whereas the effect of increased free-stream turbulence is the opposite. The following discusses the combined effects of these two. Figure 11 shows lines faired through the local Stanton number data for the

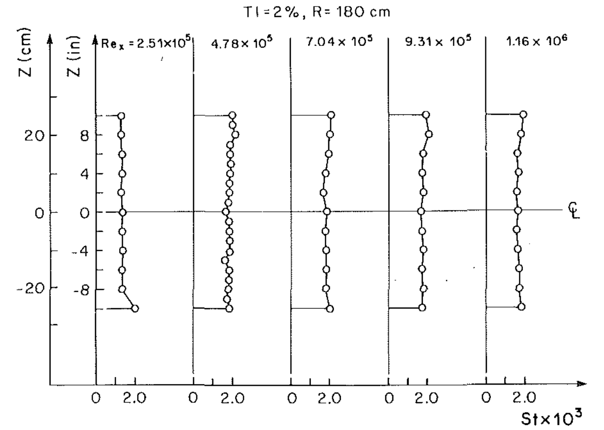

Fig. 12 Spanwise distribution of local Stanton number for the case of $R = 180$ cm and $TI = 2.0$ percent

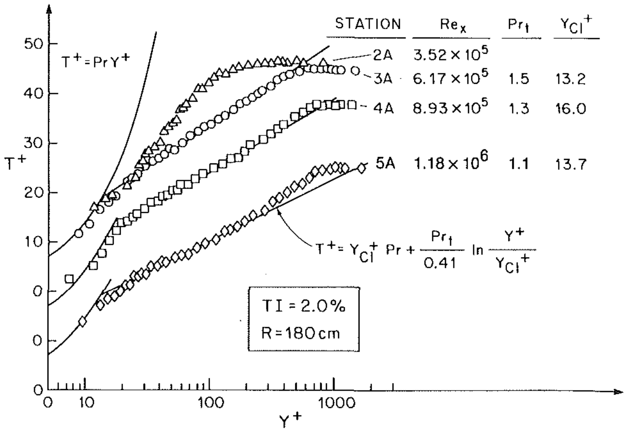

Fig. 14 Mean temperature profiles for the case of $R = 180$ cm and $TI = 2.0$ percent

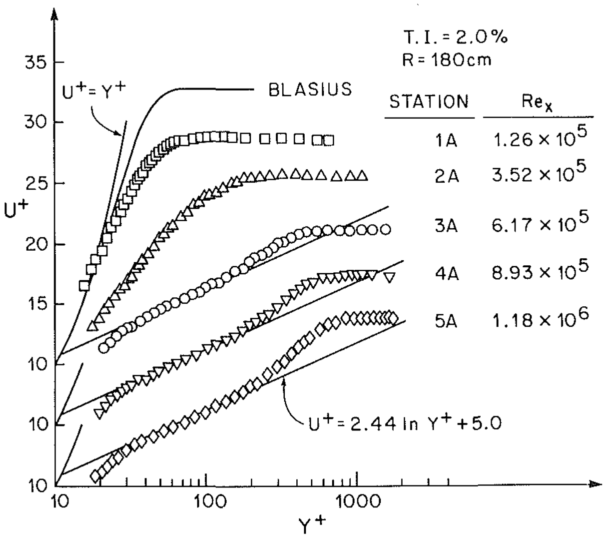

Fig. 13 Mean velocity profiles for the case of $R = 180$ cm and $TI = 2.0$ percent

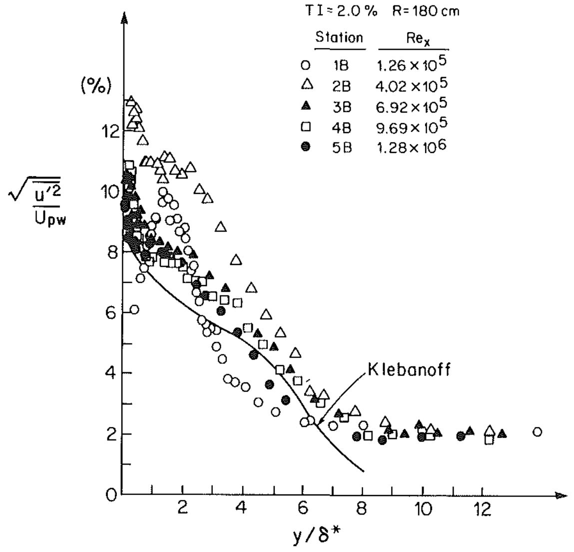

Fig. 15 Reynolds streamwise-normal stress profiles for the case of $R = 180$ cm and $TI = 2.0$ percent

three higher free-stream turbulence cases with $R = \infty$, 180 cm, and 90 cm. The influence of free-stream turbulence seems to dominate the transition process. Convex curvature only slightly delays transition, from $Re_x = 2.1\times10^5$ of the plane wall case to about 2.5×10^5 for the mildly curved case of $R = 180$ cm. A continued reduction of the radius of curvature to 90 cm results in no clear further delay of transition. The following section presents this study.

The 180 cm Radius-of-Curvature Case. The transition point of this case is slightly downstream of that for the high turbulence straight-wall case, and much earlier than that of the low turbulence mild curvature case; the free-stream turbulence effect is much more pronounced than the convex curvature effect. Although the Stanton number is apparently unaffected by curvature in the laminar flow, it is about 10 percent lower than the straight-wall case in the transitional and turbulent regions. In the late transitional and early turbulent regions, the skin friction coefficients are higher than the corresponding Stanton numbers ($2St/C_f < 1$) as was previously observed in the lower turbulence case. The spanwise distribution of local Stanton numbers, Fig. 12, shows two-dimensional behavior throughout the entire test length, in contrast to the low-disturbance level case.

Mean velocity profiles, Fig. 13, differ from the Blasius profile in the laminar regime, a higher-turbulence effect. Station 2A, in the transition region, and the other downstream stations (3A, 4A, and 5A) are turbulentlike, each with a longer log-linear region and a stronger wake than the last. The increase of wake strength is evidence of a convex curvature effect on the outer part of the boundary layer, as previously observed by Simon and Moffat [14]. In the straight-wall case of [3], the wake strength is decreased by the higher free-stream turbulence level. Mean temperature profiles at Stations 3A and 4A (Fig. 14) show a reduced wake strength due to the higher free-stream turbulence. The appearance of the wake at Station 5A, which was not observed in the higher turbulence straight-wall case [3], is considered a convex curvature effect. The turbulent Prandtl number ranges from 1.5 at Station 3A to 1.1 at Station 5A. This is consistent with the increasing value of the Reynolds analogy factor $2St/C_f$ from 0.78 to 0.95.

The streamwise Reynolds normal stress values in the laminar and transition regions (Stations 1B and 2B) (Fig. 15) are very similar to their counterparts in the straight wall case: No curvature effect is apparent. The curvature effect, which has been shown to be an order of magnitude larger in turbulent flows than in laminar flows, manifests its influence on the outer part of the turbulent boundary layer profiles. A comparison of the straight-wall and the mild-curved wall ($R = 180$ cm) profiles at Station 5B (Fig. 16) shows that in the region $y/\delta^* > 3$ the magnitude of disturbance is reduced by streamwise curvature; in the inner part $y/\delta^* < 3$, these two profiles are similar. The streamwise Reynolds normal stress

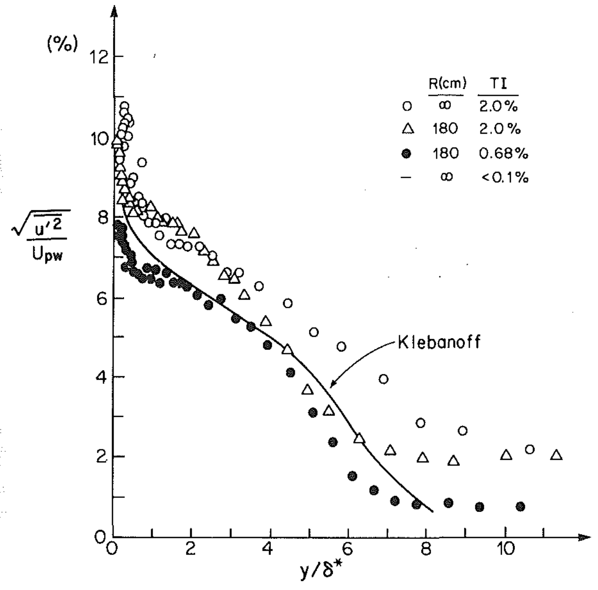

Fig. 16 Comparison of Reynolds streamwise-normal stress profiles for the three cases

profile at Station 5B on a curved surface (R = 180 cm) but with low free-stream turbulence level (TI = 0.68 percent) is also plotted in Fig. 16. The free-stream turbulence penetrates deeply into the boundary layer and elevates the turbulence level throughout – no exception for the convex surface.

Because of the higher free-stream turbulence and enhanced transport, the higher turbulence cases are more two dimensional than the lower disturbance cases. The momentum integral balance from the first station to the last shows a closure to within 8 percent; the thermal energy balance is within 12 percent.

The 90-cm Radius-of-Curvature Case. Local Stanton numbers shown in Fig. 11 indicate that transition starts around $\mathrm{Re}_x = 2.6 \times 10^5$ for the stronger-curved case which is slightly downstream of the mild-curved case transition point ($\mathrm{Re}_x = 2.5 \times 10^5$). The small influence of curvature in this higher free-stream turbulence case is expected. As with the 180-cm case, spanwise distributions of the heat transfer coefficient show two-dimensional behavior. Three dimensionality in the transition region is smoothed by effective turbulent transport.

Mean velocity and temperature profiles are similar to those of the mild-curved case. Integral momentum and energy balances along the centerline closed to within 12 percent.

Conclusions and Recommendations

This study presents results showing the effects of convex curvature at two levels of free-stream turbulence on a boundary layer undergoing natural transition from laminar to turbulent flow. Because of the design of the bendable test wall, all tests were run in a single facility. Therefore, uncontrolled variations from case to case were minimized. The following conclusions were drawn:

(*a*) Mild convex curvature delays transition. The transition x Reynolds number for the mild convex curvature case is twice the straight-wall value when the free-stream turbulence intensity is low (0.68 percent). Convex curvature delays transition slightly in the higher free-stream turbulence intensity cases (2.0 percent).

(*b*) A relatively stronger curvature of 90 cm radius does not significantly delay transition further.

(*c*) Free-stream turbulence effects dominate convex curvature effects on transition, for the cases studied.

(*d*) Although free-stream turbulence effects dominate, the curvature effect is observable in the flow. This can be seen in the wall measurements, the profiles of mean velocity and temperature, and the turbulence intensity profiles.

(*e*) No noticeable curvature effects on the skin friction coefficient and heat transfer coefficient were observed in the early laminar flow.

(*f*) A 5 to 10 percent decrease of heat transfer coefficient due to convex curvature was observed in the late-transitional and early turbulent regions.

(*g*) The Reynolds analogy factor $2\mathrm{St}/C_f$ in the early-turbulent region of the curved flow is about 15 percent lower than that in the flat-wall case; convex curvature reduces the heat transfer coefficient more than it does the skin-friction coefficient.

(*h*) Convex curvature strengthens the wake region of turbulent velocity and temperature profiles while increased free-stream turbulence reduces it.

(*i*) Reynolds normal stresses are suppressed by convex curvature in the late-laminar boundary layer. Normal stresses are amplified after the critical Reynolds number is exceeded, then reduced by the stabilizing effect of convex curvature. Downstream, when transition begins, normal stress values grow very rapidly.

(*j*) The near-wall peak in normal stress profiles within the transitional flow regime moves toward the wall as the strength of curvature is increased. The second peak, the residue of the disturbance in the laminar boundary layer, is flattened by convex curvature. In the turbulent region, the outer part of the boundary layer has lower values of normal stress in the convex-curved flow than on the straight wall. Increased free-stream turbulence elevates the streamwise turbulence intensity throughout the boundary layer.

Acknowledgments

This study was supported by NASA-Lewis Research Center grant No. NAG 3-286. The grant monitor is Dr. Raymond Gaugler. Additional support was provided by the Graduate School of the University of Minnesota and by the AMOCO foundation.

References

1 Graham, R. W., "Fundamental Mechanisms That Influence the Estimate of Heat Transfer to Gas Turbine Blades," NASA TM-79128, 1979; ASME Paper No. 79-HT-43, 1979.

2 Turner, A. B., "Local Heat Transfer Measurements on a Gas Turbine Blade," *J. of Mech. Engr. Sci.*, Vol. 13, No. 1, 1971, pp. 1-12.

3 Wang, T., Simon, T. W., and Buddhavarapu, J., "Heat Transfer and Fluid Mechanics Measurements in Transitional Boundary Layer Flows," ASME JOURNAL OF ENGINEERING FOR GAS TURBINES AND POWER, Vol. 107, 1985, pp. 1007-1015.

4 Van Dyke, M. D., "Higher-Order Boundary Layer Theory," *Annual Rev. Fluid Mech.*, Vol. 1, 1969, pp. 265-292.

5 Thomann, H., "Effect of Streamwise Wall Curvature on Heat Transfer in a Turbulent Boundary Layer," *J. Fluid Mech.*, Vol. 33, 1968, p. 283.

6 Bradshaw, P., "Effects of Streamline Curvature on Turbulent Flow," AGARDograph No. 169, 1973.

7 Bradshaw, P., "Review – Complex Turbulent Flows," *Trans. ASME*, June 1975, pp. 146-154.

8 So, R. M. C., and Mellor, G. L., "An Experimental Investigation of Turbulent Boundary Layers Along Curved Surfaces," NASA-CR-1940, Apr. 1972.

9 Hoffmann, P. H., and Bradshaw, P., "Turbulent Boundary Layers on Surfaces of Mild Longitudinal Curvature," Imperial College, Aero. Rept. 78-04, 1978.

10 Ramaprian, B. R., and Shivaprasad, B. G., "The Structure of Turbulent Boundary Layers Along Mildly Curved Surfaces," *J. Fluid Mech.*, Vol. 85, 1978, pp. 273-303.

11 Mayle, R. E., Blair, M. F., and Kopper, F. C., "Turbulent Boundary Layer Heat Transfer on Curved Surfaces," ASME *Journal of Heat Transfer*, Vol. 101, No. 3, 1979, pp. 521-525.

12 Gillis, J. C., Johnston, J. P., Moffat, R. J., and Kays, W. M., "Ex-

perimental Data and Model for the Turbulent Boundary Layer on a Convex, Curved Surface," NASA-CR-3391, Mar. 1981.

13 Simon, T. W., and Moffat, R. J., "Turbulent Boundary Layer Heat Transfer Experiments – A Separate Effects Study on a Convexly-Curved Wall," ASME *Journal of Heat Transfer*, Vol. 105, No. 4, 1983, pp. 835–840.

14 Simon, T. W., and Moffat, R. J., "Convex Curvature Effects on a Heated Turbulent Boundary Layer," *Proceedings of the VIIth Int'l. Heat Transfer Conf.*, Vol. 3, 1982, pp. 295–301.

15 Gibson, M. M. Verriopoulos, C. A., and Vlachos, N. S., "Turbulent Boundary Layer on a Mildly Curved Convex Surface, Part 1: Mean Flow and Turbulence Measurements," *Exp. in Fluids*, Vol. 2, 1984, pp. 17–24.

16 Gibson, M. M., and Verriopoulos, C. A., "Turbulent Boundary Layer on a Mildly Convex Surface, Part 2: Temperature Field Measurements," *Exp. in Fluids*, Vol. 2, 1984, pp. 73–80.

17 Muck, K. C., "Turbulent Boundary Layers on Mildly Curved Surfaces," Ph.D. Thesis, Dept. of Aeronautics, Imperial College, 1982.

18 Simon, T. W., Moffat, R. J., Johnston, J. P., and Kays, W. M., "Turbulent Boundary Layer Heat Transfer Experiments: Convex Curvature Effects, Including Introduction and Recovery," Stanford University, Dept. of Mech. Engr., Thermalsci. Div. Rept. HMT-32, 1980; NASA CR-3510, 1982.

19 Clauser, M., and Clauser, F., "The Effect of Curvature on the Transition From Laminar to Turbulent Boundary Layer," NACA TN No. 613, 1937.

20 Liepmann, H. W., "Investigations on Laminar Boundary-Layer Stability and Transition on Curved Boundaries," NASA Wartime Rept. Advance Confidential Rept. 3H30, Aug. 1943.

21 Schubauer, G. B., and Skramstad, H. K., "Laminar Boundary Layer Oscillations on a Flat Plate," NACA Rept. No. 909, 1948.

22 Dyban, Ye. P., Epik, E. Ya., and Suprun, T. T., "Characteristics of the Laminar Boundary Layer in the Presence of Elevated Free-Stream Turbulence," *Fluid Mech. – Soviet Research* (in English), Vol. 22, No. 5, 1980, pp. 213–228.

23 Blair, M. F., "Influence of Free-Stream Turbulence on Boundary Layer Transition in Favorable Pressure Gradients," ASME JOURNAL OF ENGINEERING FOR POWER, Vol. 104, Oct. 1982, pp. 743–750.

24 Van Driest, E. R., and Blumer, C. B., "Boundary Layer Transition: Freestream Turbulence and Pressure Gradients Effects," *AIAA J.*, Vol. 1, No. 6, June 1963, pp. 1303–1306.

25 Blair, M. F., "Influence of Free-Stream Turbulence on Turbulent Boundary Layer Heat Transfer and Mean Profile Development, Part I – Experimental Data," ASME *Journal of Heat Transfer*, Vol. 105, Feb. 1983, pp. 33–40; "Part II – Analysis of Results," pp. 41–47.

26 Wang, T., "An Experimental Investigation of Curvature and Free-Stream Turbulence Effects on Heat Transfer and Fluid Mechanics in Transitional Boundary Layer Flows," Ph.D. Thesis, Mech. Engr. Dept., Univ. of Minnesota, Dec. 1984.

27 Mehta, R. D., "The Aerodynamic Design of Blower Tunnels With Wide-Angle Diffusers," *Prog. Aerospace Sci.*, Vol. 18, 1977, pp. 59–120.

28 Loehrke, R. J., and Nagib, H. M., "Control of Free-Stream Turbulence by Means of Honeycombs: A Balance Between Suppression and Generation," ASME *Journal of Fluids Engineering*, Vol. 98, Sept. 1976, pp. 342–353.

29 Bradshaw, P., "The Effect of Wind Tunnel Screens on Nominally Two-Dimensional Boundary Layers," *JFM*, Vol. 22, 1965, p. 679.

30 Mehta, R. D., and Bradshaw, P., "Design Rules for Small Low Speed Wind Tunnels," *Aeronautical Journal*, Nov. 1979, pp. 443–449.

31 Loehrke, R. J., and Nagib, H. M., "Experiments on Management of Free-Stream Turbulence," AGARDograph, R-598, 1972, Ad-749-891.

32 Baines, W. D., and Peterson, E. G., "An Investigation of Flow Through Screens," *Trans. ASME*, Vol. 73, July 1951, pp. 467–480.

33 Young, A. D., and Maas, J. N., "The Behavior of a Pitot Tube in a Transverse Total-Pressure Gradient," R&M No. 1770, Aero. Res. Council, London, 1936.

34 Blackwell, B. F., and Moffat, R. J., "Design and Construction of a Low-Velocity Boundary-Layer Temperature Probe," ASME *Journal of Heat Transfer*, Vol. 97, May 1975, pp. 313–315.

35 Honami, S., and Johnston, J. P., "A New Definition of Integral Thickness for Boundary Layer Flow Over Longitudinally Curved Surfaces," *Thermosci. Div. Mech. Engr. Dept.*, Stanford Univ., Rept. IL-26, 1980.

36 Clauser, F. H., "The Turbulent Boundary Layer," *Advances in Applied Mechanics*, Vol. IV, 1956, Academic Press, New York, pp. 1–51.

37 Kays, W. M., and Crawford, M. E., *Convective Heat and Mass Transfer*, 2nd ed., McGraw-Hill, New York, 1980.

38 Kline, S. J., and McClintock, F. A., "Describing Uncertainties in Single-Sample Experiments," *J. of Mech. Engr. Sci.*, Vol. 75, 1953, pp. 3–8.

39 Moffat, R. J., "Contributions to the Theory of Single-Sample Uncertainty Analysis," ASME *Journal of Fluids Engineering*, Vol. 104, 1982, pp. 250–260.

40 Wang, T., and Simon, T. W., "Uncertainty Analysis and Experimental Program Development," Univ. of Minnesota, Heat Transfer Laboratory Report, Jan. 1984.

41 McDonald, H., and Fish, R. W., "Practical Calculations of Transitional Boundary Layers," *Int. J. Heat Mass Transfer*, Vol. 16, 1973, pp. 1729–1744.

42 Klebanoff, P. S., "Characteristics of Turbulence in a Boundary Layer With Zero Pressure Gradient," NASA Rept. 1247, 1955.

Journal of Turbomachinery
Formerly included in the Journal of Engineering for Gas Turbines and Power.

Book Reviews

Thermodynamics and Fluid Mechanics of Turbomachinery, edited by A. S. Ucer, P. Stow, and C. Hirsch. Martinus Nijoff Publishers, 1985.

Most textbooks on turbomachinery tend to be fairly basic in nature. While they are valuable and essential for educational purposes, they tend not to reflect the real state of the art as defined by aircraft turbine engine technology. Consequently, they are rarely used by the practicing engineer working at that technological level. The subject two-volume text, however, is different. It is the first book to come along in years which reflects current aircraft turbine engine turbomachinery design practice in many areas normally found only in widely scattered technical literature. As such, it is a book which will not only be of interest to professors and graduate students. It will also be of interest and value to engineers in industry desiring a convenient reference to the present state of the art in this area.

The book concentrates primarily on what can be accomplished with analytical and computational methods. It covers the complete hierarchy of mathematical models from inviscid to viscous, two-dimensional and three-dimensional, throughflow and blade-to-blade, and includes inviscid-viscous interaction methods. The various methods available are described and in many cases presented in detail. End-wall as well as airfoil boundary layers are covered. The book also presents such modern concepts as the superposition of spanwise mass transport and mixing effects on axisymmetric solutions as a means of incorporating three-dimensional effects in practical design computations. Examples are shown in many cases comparing the different levels of computation with experimental data.

Only a few empirical correlations are presented and those that are, tend to be the more classical. However, the book recognizes that empiricism is still a very important factor in turbomachinery design and the presentations generally make it evident where and how this is introduced. A few chapters are largely qualitative in nature, such as those describing secondary flows, overall design methods, and performance prediction. However, these chapters give a good picture of what is going on in the flow field and what methods are most commonly used and they are well equipped with references for more detailed study. Three chapters are devoted to describing some of the more important aspects of modern measurement technology as applied to turbomachinery research. Two concluding chapters introduce unsteady flows and provide a good survey of flow instabilities in turbomachines. Most of the emphasis is on axial turbomachines but two chapters do address radial turbomachinery specifically. Turbine cooling is not covered.

The authors of the various chapters are too numerous to mention. However, they represent a distinguished and international group whose names are conspicuous in the published literature of this field. In my opinion, this two-volume book would represent a worthwhile addition to the library of anyone interested in the fluid mechanics of sophisticated turbomachinery.

Reviewed by:
A. J. Wennerstrom
Aero Propulsion Lab (AFWAL/POTX)
Wright-Patterson AFB, OH 45433-6563